

Using single-molecule microscopy to investigate macromolecular complexes from NER to Translation

Antoine Paris

**Submitted to the University of Kent for the Degree of Doctor of Philosophy in
Biochemistry**

School of Biosciences, October 2023, 231 pages

No part of this thesis has been submitted in support of an application for any degree or other qualification of the University of Kent, or any other University or Institution of learning.

Acknowledgements

I would like to thank my supervisors Neil and Tobias for their constant support, help and most of all patience. This PhD would have been much harder and way less fun without the people that supported me throughout it. As such I would like my lab mates: Jamie for his exceptional welcome to the lab, Alex for her kind help throughout my first years, and James for being everyone's dad and who took such good care of the rest of us. A special thanks to Rob, Lorenzo, Roman and Matt who I am not sure if they made me win or waste a lot of time in the lab, but they definitely made it a fun experience.

I would like to thank my friends Rafaella, Sam, Ane, Antonio, Kirtika, Marie-Claire, Sara, Ilyaas, Diego, Elise and Polina without which I wouldn't have been able to make it through. I also must mention my friends who encouraged me to do a PhD: Pauline, Nettie, Sophie, Jérémie, and Thomas.

I would also like to thank my grandparents for always seeing the best in me and my parents who probably are still thinking that I am doing a master's degree and wondering what is taking me so long. My cousin Margaux deserves a specific mention for the endless London parties. I would like to thank my sister Johanna and her partner Adrien for everything they did for me, and my two little sisters Mégane and Gaëtane who are just the best.

Disclaimer

The COVID-19 pandemic significantly affected this work due to the closure of the university research laboratories, limited access and lab rotations after restrictions were lifted, delays in deliveries, quarantines, etc. All the above led to a limited amount of time conducting research as well as disruptions of experiments, reducing the outcome of this Ph.D.

TABLE OF CONTENTS

USING SINGLE-MOLECULE MICROSCOPY TO INVESTIGATE MACROMOLECULAR COMPLEXES FROM NER TO TRANSLATION	1
ACKNOWLEDGEMENTS	3
DISCLAIMER	4
LIST OF FIGURES AND TABLES	11
LIST OF ABBREVIATIONS	15
ABSTRACT	18
CHAPTER I: INTRODUCTION	19
1.1 DNA INTEGRITY NEEDS TO BE MAINTAINED	20
1.2 NUCLEOTIDE EXCISION REPAIR	21
1.2.1 <i>Simple layout</i>	21
1.2.2 <i>DNA damage recognized by NER.</i>	22
1.2.3 <i>Structure and function of UvrA</i>	24
1.2.4 <i>Structure and functions of UvrB.</i>	27
1.3 BRIEF OVERVIEW OF OTHER DNA DAMAGE REPAIR PATHWAYS.....	31
1.3.1 Base Excision Repair.....	32
1.3.2 Mismatch repair.....	34
1.3.4 Homologous Recombination and Non-Homologous End-Joining	36
1.4 THE NECESSITY FOR NEW ANTIMICROBIALS.....	37
1.4.1 <i>Interest in using NER as a target for antimicrobials.</i>	38
1.5 TRANSLATION AND RIBOSOME SPEED	39
1.5.1 <i>Antibiotics and the central part played by ribosomes</i>	39
1.5.2 <i>Regulation of gene expression</i>	40
1.5.4 <i>Ribosome Structure</i>	40
1.5.5 <i>Transfer RNA structure</i>	42
1.5.6 <i>Initiation of translation</i>	44
1.5.7 <i>Elongation of translation</i>	46
1.5.7.1 <i>Decoding</i>	47
1.5.7.2 <i>Protein bond formation</i>	48
1.5.7.3 <i>Translocation</i>	48
1.5.7.4 <i>Nascent protein folding</i>	49
1.5.8 <i>Termination of translation</i>	49
1.5.9 <i>Cognate, near-cognate and non-cognate tRNAs</i>	50
1.5.9.1 <i>Cognate tRNA</i>	50
1.5.9.2 <i>Near-cognate tRNA</i>	50
1.5.9.3 <i>Non-cognate tRNA</i>	51

1.5.10 Ribosome speed	51
1.5.10.1 Importance of working on ribosome speed	51
1.5.10.2 Impact of cognate, near-cognate and non-cognate populations of tRNA on ribosome speed	52
1.5.10.3 Impact of nascent peptide chain folding and sequence on ribosome speed	53
1.5.10.4 Secondary mRNA structures	53
1.6 PHD AIM	54
CHAPTER II: GENERAL MATERIALS AND METHODS.....	55
2.1 Lysate preparation	56
2.2 Protein purification	57
2.3 UV damage to DNA.....	60
2.4 Data analysis.....	60
2.4.1 Kymographs	60
2.4.2 Trackmate	60
2.4.3 Calculation of the On-rate.....	61
2.4.4 Calculation of the Off-rate	61
2.4.5 Comparison of the affinity of UvrA to the DNA strand calculations	62
2.4.6 Calculation of the distance to the transition state.....	63
CHAPTER III: APPLYING TENSILE FORCES TO DNA AFFECTS PROKARYOTIC NER <i>IN VITRO</i>	66
3.1 INTRODUCTION	67
3.1.1 The importance of forces within cells	67
3.1.2 Binding of proteins to DNA.	68
3.1.3 UvrA and UvrB kinetics in single molecule studies.....	70
3.1.4 Importance of single-molecule studies	71
3.1.5 Project aim.....	72
3.2 MATERIAL AND METHODS	73
3.2.1 The C-Trap system.....	73
3.2.2 Optical traps	74
3.2.3 Laser tweezers allow for the tethering of DNA strands.	77
<p><i>The binding of UvrA to DNA is a complex phenomenon. Its free energy landscape can be approximated as presented here in black where collisional binding occurs resulting in UvrA-ATP molecules binding to the DNA (On-rate). This is followed by hydrolysis of ATP which helps UvrA to release from the DNA (Off-rate) (48). Unbinding of UvrA-ADP from the DNA is very quick and therefore not rate-limiting. TS1 and TS2 are the two transition states that divide the free energy landscape.</i></p>	
3.2.4 Medial and lateral flow affects the DNA strand.	82

3.2.5 Widefield, Total Internal Reflection Fluorescence, and Oblique Angle Fluorescence microscopy.....	83
3.2.6 Lysate preparation.....	86
Lysate was prepared as described in chapter II. 3.2.7 Protein purification	86
3.2.8 UV damage to DNA.....	86
3.2.9 Nick translation.....	87
3.2.10 General Data analysis.....	87
3.3 RESULTS	88
3.3.1 UvrA-mNeonGreen binds to tethered DNA.....	88
3.3.2 UvrA binding is influenced by the flow.....	90
3.3.4 Increases in tension show higher decoration of UvrA-mNeonGreen to the DNA strand.	95
3.3.5 Tensile force affects both the On-rate and the Off-rate of lysate UvrA-mNeonGreen in the presence or absence of UV damage to the DNA.....	96
3.3.6 UvrA-mNeonGreen's binding is affected by fluorescein-damaged DNA.....	100
3.3.7 Effect of Tension and UV Damage on UvrB's Recruitment by UvrA.....	104
3.3.8 A high concentration of purified UvrA-mScarlet x2 shows little difference in behaviours upon UV damage and tension changes	109
3.3.9 Purified UvrB-mNeonGreen behaviour with undamaged and UV-damaged DNA substrates under various DNA tensions.	112
3.4 DISCUSSION.....	119
3.4.1 UvrA binding is influenced by DNA tension, UV damage and Fluorescein lesions.	119
3.4.1.1 UvrA's binding is influenced by DNA tension.	119
3.4.1.2 UvrA's binding in the presence of UV damage shows conflicting results.	120
3.4.1.3 UvrA's binding in the presence of Fluorescein shows an effect on the off-rate but not on the attachment rate.....	121
3.4.1.4 Bell fitting of UvrA-mNeonGreen's binding.	122
3.4.2 UvrB's binding is influenced by DNA tension and UV damage.	126
3.4.3 Kinetics discrepancies with literature.	128
3.5 CONCLUSION	129
3.5.1 Future work.....	129
3.5.2 Future optimisations.....	129
CHAPTER IV: UNDERSTANDING THE MECHANISM OF ANTIMICROBIAL ACTION: THE EFFECT OF NER INHIBITORS ON UVRA'S DNA BINDING ABILITY.....	131
4.1 INTRODUCTION	132
4.1.1 Project aim.....	133

4.1.2 Compounds background: ATBC.....	134
4.1.3 Compounds background: L-Thyroxine, Dienestrol and Aprotinin	134
4.1.4 Compounds background: Bemcentinib	135
4.1.5 Structures of Compounds.....	136
4.1.6 Effect of various compounds on the ATPase activity of UvrA	136
4.2 MATERIAL AND METHODS.....	138
4.2.1 Origin and purity of compounds	138
4.2.2 Lysis preparation.....	138
4.2.3 DNA tethering	138
4.2.4 Video capture parameters	138
4.2.5 Workflow for picture generation of the effect of compounds on UvrA-mNeonGreen binding to DNA.....	138
4.2.6 Workflow for quantification of the effect of ATBC on UvrA-mNeonGreen binding	141
4.2.7 Workflow for quantification of the effect of Aprotinin on UvrA-mNeonGreen binding	143
4.2.8 Workflow for quantification of the effect of Bemcentinib, L-Thyroxine and Dienestrol on UvrA-mNeonGreen binding.....	143
4.3 RESULTS	145
4.3.1 Snapshot of the effect of various NER inhibitors on UvrA's binding to undamaged DNA	145
4.3.2 Kinetics of UvrA while in the presence or absence of NER inhibitors	146
4.3.2.1 ATBC reduces the number of binders of UvrA to tethered DNA.....	147
4.3.2.2 Bemcentinib decreases both the attachment rate and the lifetime of UvrA on tethered DNA.....	147
4.3.2.3 Aprotinin increases both the attachment rate and the lifetime of UvrA on tethered DNA.....	148
4.3.2.4 L-Thyroxine decreases the attachment rate of UvrA on tethered DNA.....	148
4.3.2.5 Dienestrol decreases the attachment rate of UvrA on tethered DNA.....	148
4.3.3 Differences in the data depending on the order of compound exposition.....	150
4.3.6.1 The first use of a DNA strand has a higher attachment rate constant than the second use of a DNA strand.....	151
4.3.6.2 The first exposure of the DNA strand shows the impact of the compound on the binding.....	152
4.3.6.3 Binding of compounds to the DNA strand.....	152
4.4 DISCUSSION.....	157
4.4.1 ATBC is inhibiting UvrA-mNeongreen's ability to bind to DNA.....	157

4.4.2 L-Thyroxine, Dienestrol and Aprotinin affect UvrA-mNeongreen's ability to bind to DNA.....	157
4.4.3 Bemcentinib	158
4.5 CONCLUSION	160
4.5.1 Future work.....	160
CHAPTER V: STALLING OF RIBOSOMES ON SPECIFIC CODONS	163
5.1 INTRODUCTION	164
5.1.1 Project aim.....	164
5.1.2 Principle	164
5.2 MATERIALS AND METHODS	168
5.2.1 TnT® Coupled Reticulocyte Lysate Systems typical reaction	168
5.2.2 PURExpress typical reactions	168
5.2.3 Amino-Acid mix preparation	169
5.2.4 One-glo™ luciferase assay	169
5.2.5 Gibson assembly of pls7.....	170
5.2.6 Colony PCR	170
5.2.7 Single-molecule glass slide and coverslip treatment	171
5.2.8 Flow cell chamber assembly	171
5.2.9 Flow cell chamber passivation	172
5.2.10 Single-molecule sample preparation	173
5.2.11 Single-molecule experimental setup.....	173
5.3 RESULTS	174
5.3.1 APCT2 allows expression of functional luciferase using a TNT rabbit reticulocyte coupled system	174
5.3.2 Removing one amino acid doesn't prevent the expression of luciferase	175
5.3.3 Using different amino acid mixes or different DNA doesn't prevent the expression of luciferase in the absence of one amino acid	176
5.3.4 Amino-acid contamination is present in all the lysate aliquots	177
5.3.5 Exhausting the amount of amino acids doesn't show an increase in luciferase expression when complemented with said amino acid	178
5.3.6 APCT2 doesn't allow the expression of functional luciferase when using the PURExpress kit	179
5.3.7 The PURExpress kit doesn't allow expression of luciferase using the pls7 construct but does allow expression of the DHFR control plasmid	180
5.3.8 Pls7 plasmid does allow expression of luciferase when using the TNT rabbit reticulocyte kit	182

5.3.9 RNase contamination in miniprep samples prevents the expression of protein...	182
5.3.10 Stalling of ribosomes is possible when using an amino-acid mix with a minimized amount of KOH in the absence of one amino acid.....	186
5.3.11 Stalled ribosomes seem to bind to the surface	187
5.4 DISCUSSION	191
5.5 CONCLUSION	193
CHAPTER VI: DISCUSSION.....	194
6.1 MECHANISM OF ACTION OF UvRA AND UvrB RECOGNITION OF DNA DAMAGE.....	195
6.2 EFFECT OF VARIOUS INHIBITORS ON UvRA'S BINDING TO DNA	197
6.3 RIBOSOME STALLING	200
APPENDIX	201
7.1 APPENDIX 1: CODE FOR IMPACT OF TIME AND PROTEASE INHIBITOR ON THE BINDING OF UvRA-MNEONGREEN	202
7.2 APPENDIX 2: CODE FOR THE TENSION DEPENDENCY OF UvRA-MNEONGREEN	204
REFERENCES	206

List of figures and tables

Figure 1: Schematics of Nucleotide Excision Repair in prokaryotes.....	22
Figure 2: Typical lesions recognized by NER.	23
Figure 3: Structure of <i>Bacillus stearothermophilus</i> 's UvrA dimer (2R6F).....	27
Figure 4: Structure of <i>Bacillus caldotenax</i> 's UvrB (1D9Z)	29
Figure 5: Structure of UvrB's beta-hairpin going through double-stranded DNA (6O8F).....	30
Figure 6: Structure of UvrA2B2 heterotetramer in <i>Geobacillus</i> sp. Y412MC52 (3UWX).....	31
Figure 7: Mutagenic sources and related repair pathways	32
Figure 8: Base Excision Repair general pathway.....	33
Figure 9: Mismatch repair.....	35
Figure 10: Homologous repair.	37
Figure 11: Crystal of a ribosome with its 3 sites occupied and with EF-Tu.	42
Figure 12: Cloverleaf and tertiary structure of tRNA.	44
Figure 13: Translation initiation of Shine-Dalgarno-led genes.	46
Figure 14: Translation elongation.	47
Figure 15: Illustration of the different factors acting on ribosome speed.	53
Figure 16: Plasmid maps of proteins used.	57
Figure 17: SDS page gel of UvrA-mNeonGreen purification.	59
Figure 18: Typical data analysis pathway.....	64
Figure 19: Different modes of DNA scanning by proteins.	69
Figure 20: The C-Trap system.....	74
Figure 21: Schematics of an optical trap.....	76
Figure 22: Example of calibration curve.....	77
Figure 23: Schematic of a strand of biotinylated DNA tethered to streptavidin beads, captured by optical traps.....	78
Figure 24: Representation of a Force Distance (FD) curve for dsDNA.....	80
Figure 25: Simplified free energy landscape of UvrA binding to DNA.	82
Figure 26: Difference between Lateral and Medial flow.	83

Figure 27: Difference between Widefield, TIRF and OAF microscopy.....	86
Figure 28: Nt.BspQI nick translation result and corresponding Lambda map.....	87
Figure 29: Exposure synchronisation:	88
Figure 30: UvrA-mNeonGreen binds to tethered DNA.	89
Figure 31: The presence of 0.1 Pa of flow greatly increases the binding of UvrA to the DNA strand.....	91
Figure 32: Impact of time and protease inhibitor on the binding of UvrA-mNeonGreen.....	94
Figure 33: Kymograph of Increase of tension shows a higher decoration of UvrA-mNeonGreen to the DNA strand.	96
Figure 34: Experimental set-up for tension dependency study.....	97
Figure 35: UvrA-mNeonGreen lifetime is affected by both tension and UV damage.	99
Figure 36: Bell-fits of k_d , k_a and K_D of the binding of UvrA-mNeonGreen to undamaged and UV-damaged DNA under various forces.	100
Figure 37: Fluorescein affects the lifetime of UvrA-mNeonGreen but not its on-rate.	103
Figure 38: Example of experimental data.	105
Figure 39: UvrA's kinetic in the presence of UvrB.	106
Figure 40: Kinetics of Lysate UvrB-mNeonGreen at 45 pN in the absence or presence of UV damage.	107
Figure 41: Recruitment of UvrB by UvrA depending on tension.	108
Figure 42: A high concentration of purified UvrA shows an unclear effect of tension and UV damage on UvrA's binding.	110
Figure 43: Effect of tension and UV damage to UvrA-mScarlet x2's dwell time on DNA.	112
Figure 44: Purified UvrA's kinetics in the presence of purified UvrB.....	115
Figure 45: Kinetics of purified UvrB-mNeonGreen.	116
Figure 46: Effect of Tension and UV on UvrB-mNeongreen's binding to DNA...	117

Figure 47: Effect of tension and UV damage on the recruitment of UvrB by UvrA.	118
Figure 48: Free energy landscape of UvrA-mNeonGreen lysate when using undamaged or UV-damaged DNA as substrate.	124
Figure 49: Chemical structure of ATBC, Bemcentinib, L-Thyroxine, Dienestrol and secondary structure of the Aprotinin peptide.	136
Figure 50: UvrA shows a reduction in ATPase activity when in the presence of various compounds.	137
Figure 51: Breakdown of the workflows used to generate pictures of the effect of compounds on UvrA-mNeonGreen binding to DNA.	140
Figure 52: Workflow for quantification of the effect of compounds on UvrA-mNeonGreen binding.	142
Figure 53: Compounds affect the binding of UvrA-mNeonGreen to the DNA.	146
Figure 54: UvrA-mNeongreen's attachment rate to DNA is greatly reduced in the presence of ATBC, Bemcentinib, L-Thyroxine and Dienestrol, but not in the presence of Aprotinin where the binding is increased.	149
Figure 55: Bemcentinib and Aprotinin affect greatly the lifetime of UvrA-mNeonGreen.	150
Figure 56: Experimental set-up highlights potential carryover of compound on the DNA strand.	154
Figure 57: Principle of ribosome stalling.	165
Figure 58: Schematic of a single molecule experimental set-up:	167
Figure 59: Luciferase reaction.	169
Figure 60: Colony PCR of Gibson reaction.	171
Figure 61: Flow chamber construction.	172
Figure 62: Expression control of DHFR.	181
Figure 63: Miniprep pDNA doesn't allow for the expression of DHFR within the PURExpress kit.	184
Figure 64: The addition of RNase Inhibitor allows for miniprep DHFR expression within the PURExpress kit.	185

Figure 65: Flow cell surface passivation.....	189
Table 1: Associated values from Figure 54.	155
Table 2: TNT Rabbit Reticulocyte coupled system luciferase expression control.	175
Table 3: Removing one amino acid doesn't prevent the expression of luciferase.	176
Table 4: The use of a different amino acid mix doesn't change the outcome of luciferase expression.....	177
Table 5: Use of a different plasmid miniprep with different amino acid mix doesn't change the expression of luciferase.	177
Table 6: The different lysates don't affect luciferase expression in the absence of amino acids.	178
Table 7: The exhaust experiment doesn't show differences in luciferase expression.	178
Table 8: The PURExpress kit doesn't express luciferase.	180
Table 9: Pls7 doesn't show luciferase expression in the presence of the kit's amino- acid mix.	181
Table 10: TNT rabbit reticulocyte luciferase activity check.	182
Table 11: The use of a minimized KOH amino-acid mix lacking leucine allows for stalling of ribosomes within the PURExpress kit.....	187
Table 12: Effect of compounds on UvrA's ability to bind to DNA.....	199

List of Abbreviations

NER: Nucleotide Excision Repair

DNA: DeoxyRibonucleic Acid

RNA: Ribonucleic Acid

mRNA: messenger RNA

tRNA: transfer RNA

UV: Ultra-Violet light

Pol I: Polymerase I

UVA, UVB, and UVC: Sub-categories of UVs

CPD: Cyclobutane Pyrimidine Dimers
6-4PP: 6-4 pyrimidine-pyrimidone
PhotoProducts

BER: Base Excision Repair

dR: 2-deoxyribose

NBD: Nucleotide Binding Domain

MMR: MisMatch Repair

NHEJ: Non-Homologous End Joining

HR : Homologous Recombination

SSB: Single Strand Binding Protein

IF: Initiation Factor

EF: Elongation Factor

RF: Release Factor

SSU: Small Sub-Unit

LSU: Large Sub-Unit

E-site: Exit-site

P-site: Peptidyl-site

A-site: Aminoacyl-site

aa: amino acid

SD: Shine Dalgarno

RRF: Ribosome Recycling Factor

MFD: Transcription Repair Coupling Factor (or TRCF)

WLC: Worm Like Chain

TS: Transition state

TIRF: Total Internal Reflection Fluorescence

OAF: Oblique Angle Fluorescence

Tris: Tris(hydroxymethyl)aminomethane

EDTA: Ethylenediaminetetraacetic acid

DTT: Dithiothreitol

DMSO: Dimethyl sulfoxide

4NQO: 4-Nitroquinoline 1-Oxide

mPEG: Poly(ethylene glycol) monomethyl ether

BSA: Bovine Serum Albumin

SDS: Sodium Dodecyl-Sulfate

kbp: kilobase pair

LAP: Linear Assignment Problem

k_a : Attachment rate constant

k_d : Detachment rate constant

K_D : Dissociation constant

Abstract

DNA is subjected to many forces within cells. In prokaryotes, those range from the supercoiling of the DNA to the impact of macromolecular complexes like the replisome. Lesions on DNA induce changes in DNA structure and/or flexibility. Some of those are recognized and repaired by Nucleotide Excision Repair (NER). NER is a DNA damage repair pathway composed of a few proteins but can recognize and process a plethora of lesion types. It has been proposed that NER recognizes local changes in the structure or flexibility of the DNA at lesion sites. This thesis aims to assess the effect of structural modifications of the DNA on the ability of NER proteins to recognize the damage, as well as assess the effect of newly found inhibitors on the binding of a NER protein. By using optical traps, we were able to alter the tension applied to a single molecule of double-stranded DNA and assess how DNA distortion affects the kinetics of NER proteins at the single-molecule level. Those changes in the tension altered the binding of fluorescently tagged UvrA and UvrB, the first two responders to damage in NER. The more tension applied to the DNA strand, the faster the attachment and the longer the lifetime of UvrA on the DNA. Similarly, UvrB is recruited more often by UvrA when the tension is increased. This sheds light, for the first time, on how these proteins recognise DNA damage, suggesting these proteins recognize changes in the structure of the DNA in a systemic manner instead of specific alterations for each lesion type. Furthermore, we assessed the effect of various NER inhibitors on the binding of UvrA to the DNA and highlighted potential modes of action. Aprotinin increased the affinity of UvrA to the DNA, while ATBC, Bemcentinib, L-Thyroxine and Dienestrol decreased the affinity of UvrA to the DNA. Interestingly, Dienestrol seems to have a dual mode of action by binding to the UvrA molecule and reducing its affinity for the DNA, as well as binding to the DNA molecule, hindering UvrA binding. Prokaryotic NER inhibitors are of great interest as they could be used as a novel family of antimicrobials and potentially be exploited in cancer therapy in combination with DNA-damaging agents to inhibit the growth of bacterial infections. The discovery of novel antimicrobials is of the foremost importance as antimicrobial resistance is rapidly spreading. With most antibiotics targeting the ribosome, a third aim of this thesis was to deepen the understanding of one understudied aspect of translation which is the impact of near-cognate tRNA in the elongation step of the translation. In this thesis I outline a series of experiments that allowed us to stall ribosomes at a specific codon, the first step to assess codon/near-cognate tRNA interactions.

Chapter I: Introduction

1.1 DNA integrity needs to be maintained

DNA is the epicentre of genetic information and its integrity is essential for cell fitness. However, DNA is constantly under attack by a myriad of DNA-damaging agents from a multitude of sources. For example, DNA is particularly sensitive to the exposure to high-energy electromagnetic waves such as UV-light, X-rays and gamma rays, which have severe effects on the DNA ranging from the creation of bulky adducts to double-strand breaks (1,2). An excess of DNA damage is detrimental to the cell and can lead to cell death (3). Thankfully, several repair pathways have evolved to be able to deal with most forms of damage. However, no pathway is 100 percent efficient, therefore, some DNA damage will remain undetected leading to changes in the sequence of the DNA (4). Such changes can be detrimental in various ways. First, a large number of mutations are toxic for the cell (5). Second, mutations of genes can induce big changes in the phenotype of the organism. In humans, a wide variety of diseases originate from DNA damage or faults done by the DNA damage repair machineries. Those includes mutations in somatic cells that can lead to cancer, and mutations in gametic cells that can affect the progeny and lead to genetic diseases. For example, cystic fibrosis is caused by mutations within the CFTR gene (6). This gene is responsible for the expression of an ion channel that expels chloride within the airways, which in turn attracts water which allows for cilia to expulse both mucus and germs within(7). Defects in the CFTR protein leads to difficulty in breathing because of the lack of expulsion of mucus, and a susceptibility to lung infections. Many mutations of the CFTR gene are responsible for this phenotype, the most common one being a deletion of the F508 which causes the protein to fold incorrectly (8). Interestingly, mutations within DNA damage repair pathways genes often have drastic effects. It is the case for mutations of Nucleotide Excision Repair (NER) proteins which can lead to xeroderma pigmentosum. By disturbing NER, it renders individuals much more sensitive to UV light and is linked to a high likelihood of developing skin cancer at a young age (9).

However, the incorporation of novel mutations into an organism's genome can sometimes be beneficial. Indeed, mutations are at the heart of the evolution process and can result in phenotypes that are sometimes valuable to respond to changes in the environment. In higher eukaryotes, mutations affect evolution if they happen within gametic cells while mutations that occur within somatic cells affect the individual (10). In prokaryotes, all mutations can be carried over to the progeny. Fine-tuning is however required as too much DNA damage will lead to cell death, and too few mutations at a population level will make colonies less efficient at adapting to their environment (11). This fine-tuning is done at several levels with on one side the spontaneous mistakes made by the replicative machinery and on the other side, the efficiency of the DNA damage repair pathways to repair DNA lesions before they get processed by the replication machinery. DNA damage repair pathways therefore play a central role in the maintenance of genome integrity.

1.2 Nucleotide Excision Repair

1.2.1 Simple layout

Several DNA damage repair pathways are present in prokaryotes. One of them, Nucleotide Excision Repair is involved in repairing a wide variety of lesion types. In prokaryotes, Nucleotide Excision Repair (NER) involves only a few proteins. Despite its apparent simplicity, it is far from understood. The general mechanisms illustrated in Figure 1 start with UvrA binding to damaged DNA with a stronger binding affinity than undamaged DNA (12). UvrA functions as a dimer that will then recruit UvrB to the lesion (13,14). UvrA either binds to DNA as a homodimer or is already complexed with UvrB in an A₂B or A₂B₂ complex (15–17). Transfer of the lesion to UvrB is thought to occur as a result of hydrolysis of UvrA's bound ATP which in turn will dissociate from the DNA (18,19). Subsequently, UvrC is recruited to the lesion site and immobilized UvrB and will nick the damaged strand, first 5 bases in 3' then 7 or 8 bases in 5' of the lesion (20). The helicase UvrD in combination with DNA polymerase I will stimulate the displacement of both UvrB

and UvrC as well as the damaged nicked strand (21,22). It is unclear if UvrB and UvrC are removed at the same time or sequentially. Then DNA polymerase I will synthesize a new strand using the undamaged strand as a template. Finally, a ligase ligates the newly synthesized strand (23).

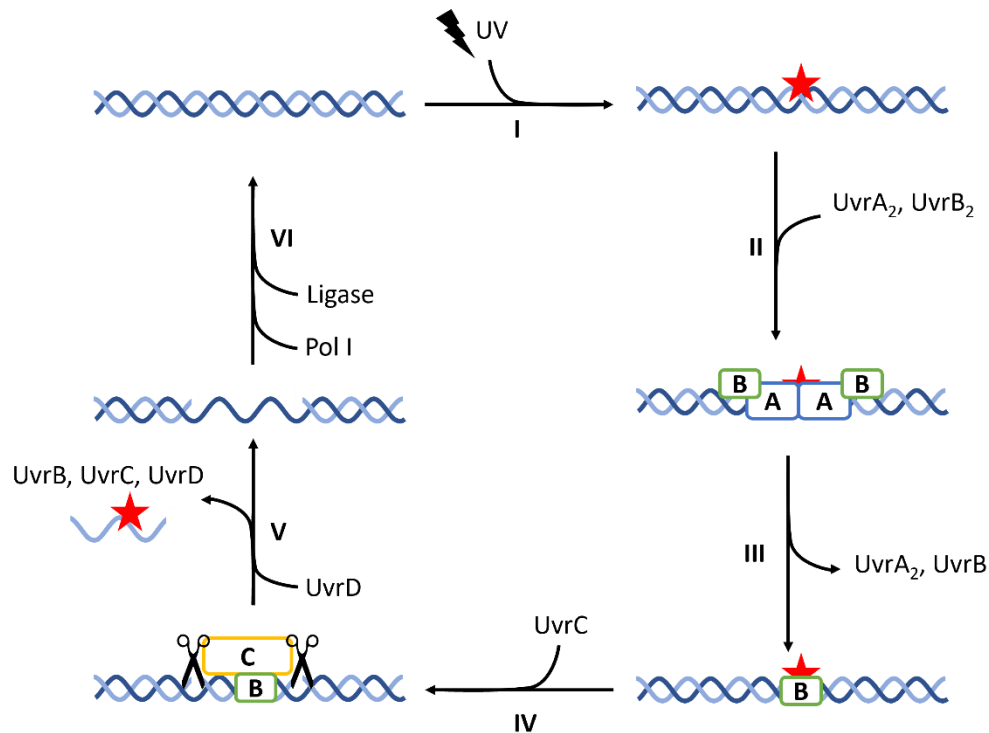


Figure 1: Schematics of Nucleotide Excision Repair in prokaryotes. Adapted from (24). **I:** UV damages DNA. UV lesion is represented as a red star. **II:** UvrA₂B₂ locates and binds to DNA on the damage site. **III:** UvrB verifies the damage which leads one UvrB and two UvrA to leave the DNA. **IV:** UvrC is recruited by UvrB and will excise both 5' and 3' of the lesion. **V:** UvrD is recruited which will kick out both UvrB and UvrC as well as the damaged oligo thanks to its helicase activity. It is unclear if UvrB and UvrC are removed together or sequentially. **VI:** Pol I resynthesis the nicked DNA strand and a ligase will remove the nick.

1.2.2 DNA damage recognized by NER.

The NER proteins UvrA, UvrB, and UvrC got their name from their ability to recognize and repair UV lesions. Such lesions are caused by UV rays. UV rays are classified into three categories. UVA ranges between 320 nm and 400 nm. UVB range from 280 nm to 320 nm and UVC ranges from 200 nm to 280 nm. The ozone layer in the atmosphere absorbs most UVB and all UVC from reaching living

organisms. However, most UVA still passes through the ozone layer (25). UVB and UVC are absorbed by DNA and result in Cyclobutane Pyrimidine Dimers (CPDs) and 6-4 pyrimidine-pyrimidone photoproducts (6-4PP; structures shown in Figure 2). Following exposure to sunlight, CPDs represent 70 to 80 percent of the lesions while 6-4PP represents 20 to 30 percent of the lesions (26). UVA and UVB induce oxidative DNA damage (8-oxoguanine) (1,25,27). However 8-oxoguanine damage is repaired by Base Excision Repair (BER) (28). Even though NER is well known to repair UV damage, it is also responsible for repairing a plethora of lesions. Amongst those are cis-platinum adducts caused by cisplatin treatments, protein-DNA crosslinks etc.

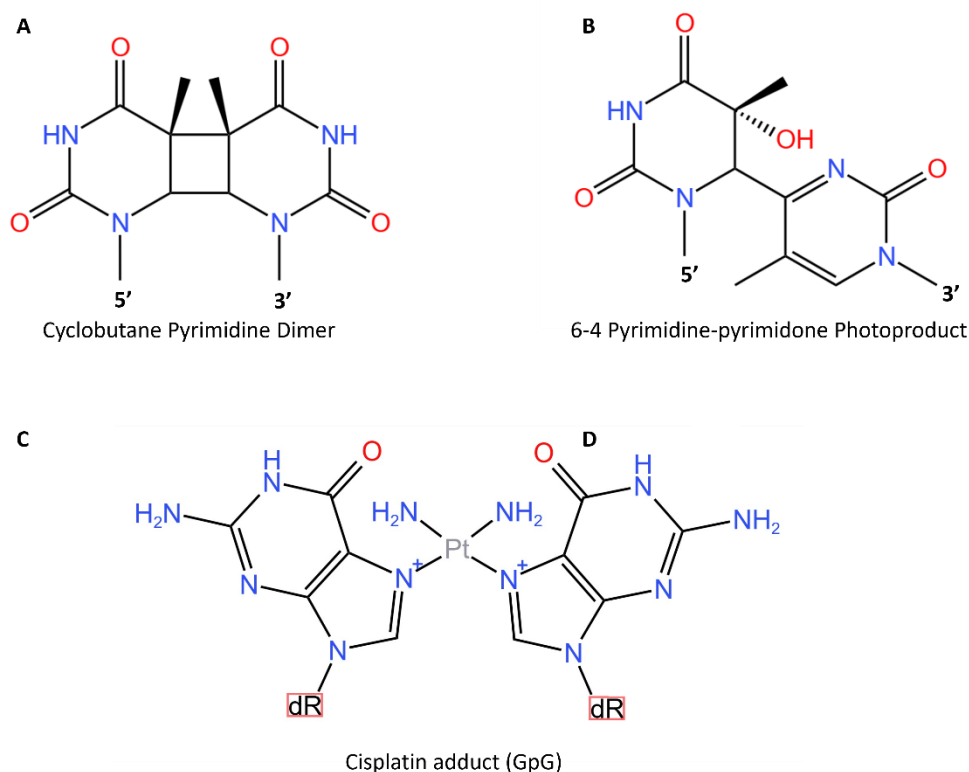


Figure 2: Typical lesions recognized by NER. UV can damage DNA in various ways. The two most common lesions are **A**: CPD and **B**: 6-4PP. Both lesions are recognized and repaired by NER, and so are the lesions produced by **C**: cisplatin where each cisplatin binds covalently to DNA. dR stands for 2-deoxyribose. Cisplatin can form that kind of adduct within the same strand (intra-strand crosslink) or with the opposing strand (inter-strand crosslink) (29). (Inspired by (30))

1.2.3 Structure and function of UvrA

UvrA is the first protein involved in NER in prokaryotes and binds as a dimer to DNA with an UvrA-DNA dissociation constant of 10 nM for UV damaged DNA, with the binding being 1000 to 10000-fold weaker for undamaged DNA (14). However, those values are debated as it was also shown that this difference was of only 6-fold using fluorescein damaged DNA (31). UvrA has the same ATP binding cassette as the ABC transporter superfamily which mostly contains transmembrane transporter proteins (32,33). UvrA has two of those nucleotide-binding cassettes, namely NBDI (Nucleotide Binding Domain I) and NBDII (Nucleotide Binding Domain II). NBDI contains the ATP binding domain I (in red in Figure 3), the signature domain I (in green in Figure 3), the UvrB binding domain (in pink in Figure 3) and the insertion domain (in yellow in Figure 3). The last two are unique to UvrA when compared with other proteins of the ABC transporter superfamily. NBDII contains the ATP binding domain II (in orange in Figure 3) and the signature domain II (in blue in Figure 3). Both ATP binding domains are homologous through the ABC transporter superfamily ATP binding domains and contain Walker A and Walker B motifs, a Q-loop, a D-loop, and an H-loop (34,35). Most ABC proteins require two nucleotide-binding domains for their functions and obtain those by either acting as dimers with each protein possessing one NBD or as monomers with two NBDs. UvrA is unique since each monomer possesses two NBDs and still functions as a dimer, making for the presence of four NBDs per dimer (34,36).

ATP binding domain I will be called the proximal ATPase site throughout this thesis while the ATP binding domain II will be called the distal ATPase site (37). The Q-loop of the ATP binding domains has been suggested to be responsible for conformational changes when ATP binds (35,38). The UvrB binding domain is essential for the interaction with UvrB (36,39) while the insertion domain is involved in DNA binding (40).

DNA binds to the ventral part of the UvrA dimer (which is concave), with multiple points of interactions in the insertion domain, the zinc bindings, the signature

domain I and the signature domain II (37,39,40). The latter is of greater importance. Indeed, when Lys680 and Arg691, two positively charged amino acids, both of them predicted to be important for DNA binding, are mutated to alanine, a 37-fold decrease in UvrA's ability to bind to DNA was observed (41). Interestingly, it only had a minor impact on DNA damage recognition by the UvrA₂B₂ complex (41). Those two amino acids are located within the signature domain II.

UvrA has 3 Zinc fingers that play a role in DNA binding. Initially, only 2 zinc fingers were expected from sequence analysis (34), but the crystal structure of *Bacillus stearothermophilus*'s UvrA dimer has shown the presence of 3 zinc fingers (36) which are believed to play an important structural role (42–44). The first zinc is located between the signature domain I and the UvrB binding domain. The second Zinc is located between the signature domain I and the insertion domain. Finally, the third Zinc is located between the signature domain II and the dimer interface. This last one is essential for UvrA's ability to differentiate damaged from non-damaged DNA (42) and is namely the C-terminal Zinc-finger. Interestingly, this Zinc finger changes location depending on the conditions, with the two of them adopting a close conformation when bound to ADP or an open conformation when bound to DNA (31,45).

Upon binding of UvrA to DNA, the insertion domain forms a clamp around the DNA stabilizing the UvrA on the DNA. This movement will push the DNA in contact with other surface regions. In this position, the two zinc-fingers are connected through phenylalanines, positioning the zinc-finger alpha helixes in a way that prevents the hydrolysis on the proximal ATPase site. Once in contact with DNA damage, rearrangement of the DNA binding regions occurs, moving the Zinc fingers and disrupting the phenylalanines. This moves the alpha helixes which in turn, allows for hydrolysis of the ATP (43,45).

Both ATPase domains were shown to be able to independently hydrolyse ATP on their own when the protein was split in half by inserting a collagenase recognition

sequence in between those domains (46). Interestingly, in a dimer, the proximal ATPase sites of one protomer are in close proximity to the distal ATPase sites of the other protomer (36). It is an intricate system where hydrolysis of the proximal and distal ATPs is possible with a lot of intermediates depending on the presence or absence of DNA or damaged DNA (47). ATPase rates and lifetimes of UvrA were correlated and it was shown that the ATPase rate of UvrA didn't vary when using undamaged or damaged DNA. However, the lifetime of UvrA tripled in the presence of damage. It was proposed that in the absence of damage, ATP hydrolysis induces UvrA to leave while in the presence of damage, ATP hydrolysis activates the other ATPase. This reconciles the difference in lifetime observed with the lack of difference in ATPase activity in the presence of damage and is indicative of negative cooperativity (48). It was also proposed that proper ATPase activity of those ATPase sites is a requirement for the recruitment of UvrB (49).

It was shown that there is an asymmetric allosteric effect upon binding of native DNA where the proximal site undergoes significant change and the distal site less so. However, upon binding to damaged DNA, both the proximal and the distal sites undergo significant and distinct changes in their ATPase mechanisms. It is proposed that UvrA binds to damaged DNA by keeping an ATP in the proximal site while having turnover of ATP hydrolysis at the distal site with both of them allowing for the recruitment of UvrB to the lesion (13,47).

It was shown by mutating the ATPase sites that recruitment of UvrB was reduced when the proximal ATPase site was mutated and further reduced when the distal ATPase site was mutated (50). Through an *in vitro* FRET experiment, it was shown that the mutation on the distal ATPase site allowed loading of UvrB to the lesion with a slightly slower rate while the mutation on the proximal site or the double mutant was shown to still be able to load UvrB to the lesion, but at a much smaller rate (51).

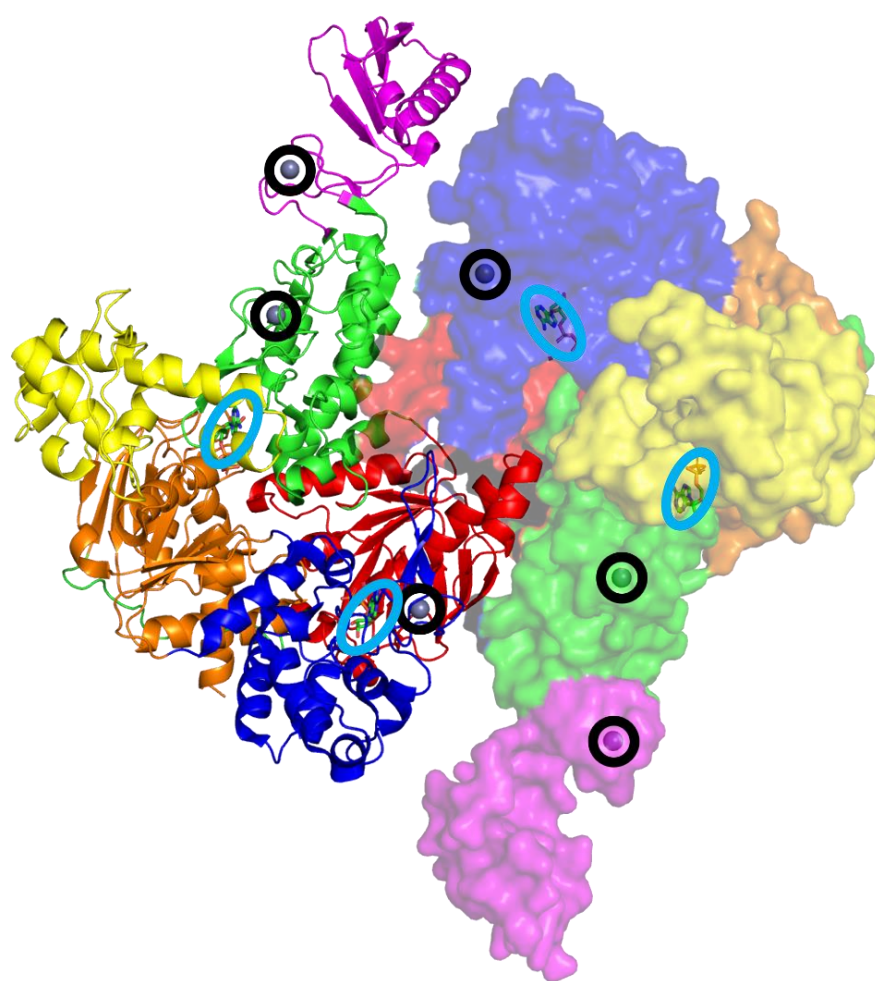


Figure 3: Structure of *Bacillus stearothermophilus*'s UvrA dimer (2R6F) (36). One monomer is shown in cartoon on the left side of the picture while the other monomer is shown with its surface. Proximal and distal ATPase domains are coloured in red and orange respectively. Signature domain I is coloured in green while signature domain II is shown in blue. The UvrB binding domain is shown in pink, and the insertion domain is shown in yellow. Teal ovals are highlighting ATP molecules bound to ATPase cassettes. Black circles highlight zinc within zinc fingers. The structure was generated using Pymol.

1.2.4 Structure and functions of UvrB.

UvrB is a DNA helicase part of the helicase II superfamily. UvrAB complexes have a 5' to 3' helicase activity. That activity is inhibited by UV photoproducts (52). UvrB is constituted of domain 1a (in green in Figure 4), domain 1b (in red in Figure 4), domain 2 (in yellow in Figure 4), domain 3 (in cyan in Figure 4) and domain 4 (not

shown in Figure 4) as well as a beta-hairpin (in magenta in Figure 4). The beta-hairpin bridges the gap between domain 1a and domain 1b (53). The 115-250 residues located after show homology with the transcription repair coupling factor (TRCF). TRCF was shown to be able to recruit UvrA to DNA, therefore the UvrB residues that share homology with TRCF were put forward as being the region where UvrA binds (54). UvrB's ATP binding site is located in-between domains 1a and 3 which are both structurally related to helicases (53). UvrB's ATP hydrolysis is a requirement for the creation of the pre-incision complex but isn't for binding to UvrA or for the binding of UvrA₂B₂ to undamaged DNA (15,51,55). Furthermore, it was shown that domain 4 of UvrB was acting as an auto-inhibition domain where its truncation led to an increase of ATPase activity and UvrA-independent damage-specific incision with an UvrC homolog (Cho) (56). A recent study by Kraithong has shown that the dissociation of UvrA from the UvrAB-DNA complex does not require, but is accelerated by ATP hydrolysis by UvrB, contradicting older studies (51,55,57).

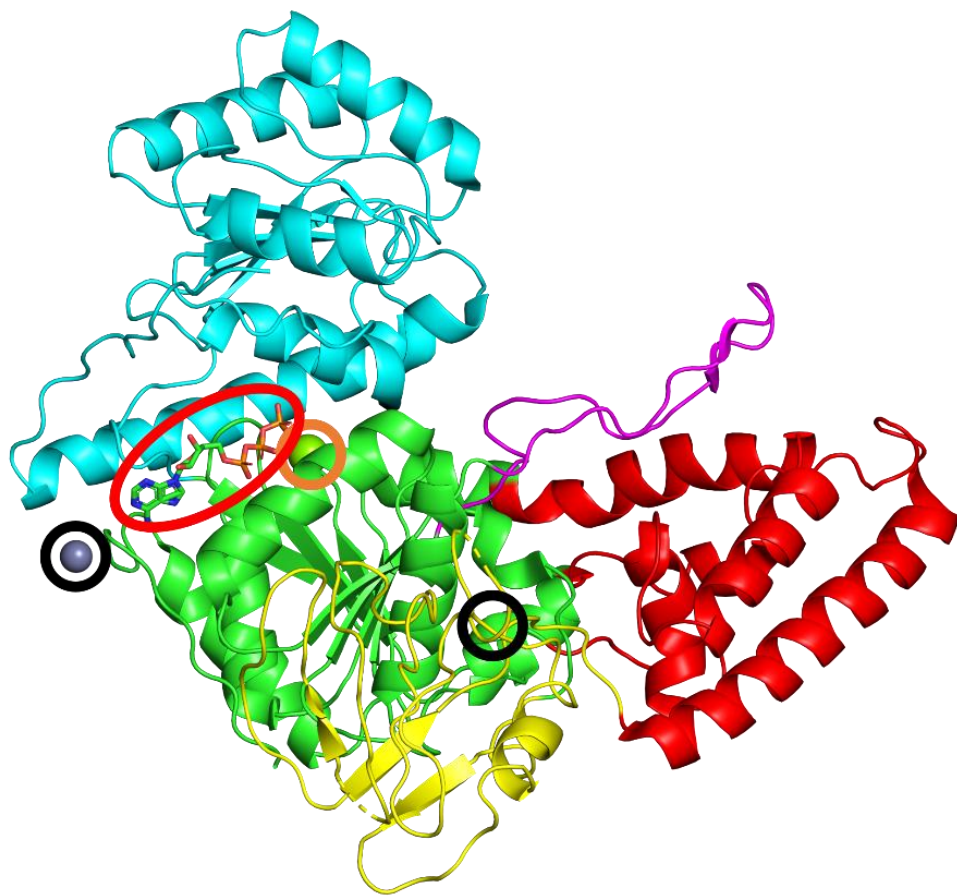


Figure 4: Structure of *Bacillus caldotenax*'s UvrB (1D9Z) (53). Domain 1a is shown in green. Domain 1b is shown in red. Domain 2 is shown in yellow. Domain 3 is shown in cyan. Finally, the beta-hairpin is shown in magenta. Domain 4 is not shown as its structure wasn't resolved. Black circles highlight the location of Zinc within zinc fingers while the orange circle highlights Magnesium. The red oval shows the location of ATP within the ATPase cassette of UvrB. The structure was generated using Pymol.

The beta-hairpin is rich in hydrophobic residues and is crucial for damage validation and UvrB's interaction with DNA. As shown in Figure 5, the beta-hairpin goes in between the DNA strands with the tip of the beta-hairpin interacting with domain 1b. Mutations in hydrophobic residues at different locations in the beta-hairpin greatly affect UvrB's function, by preventing damage recognition, formation of UvrB/DNA pre-incision complexes or by promoting undamaged DNA nicking (58,59).

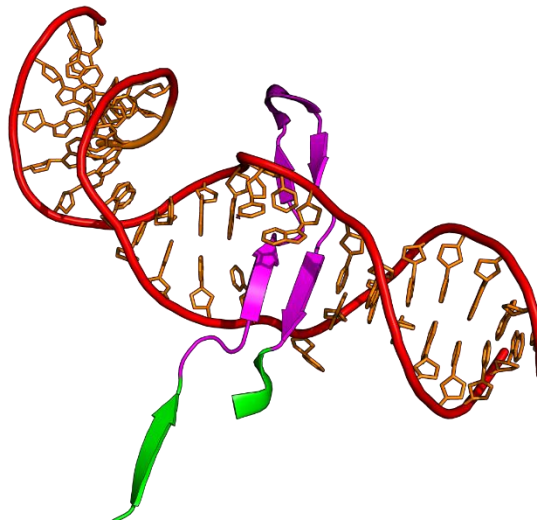


Figure 5: Structure of UvrB's beta-hairpin going through double-stranded DNA (6O8F)

(24). Residues 83-118. The structure was generated using Pymol.

For long it was believed that one molecule of UvrB binds to UvrA dimers to form UvrA₂B complexes. However, evidence has shown that two UvrB binds to UvrA dimers (Figure 6), and that allows both DNA strands to be checked for damage by UvrB (17,37). It is thought that both UvrBs have a 3' translocation activity which allows for the UvrB of the damaged strand to stall at the lesion while the other UvrB is kicked out (37,60).

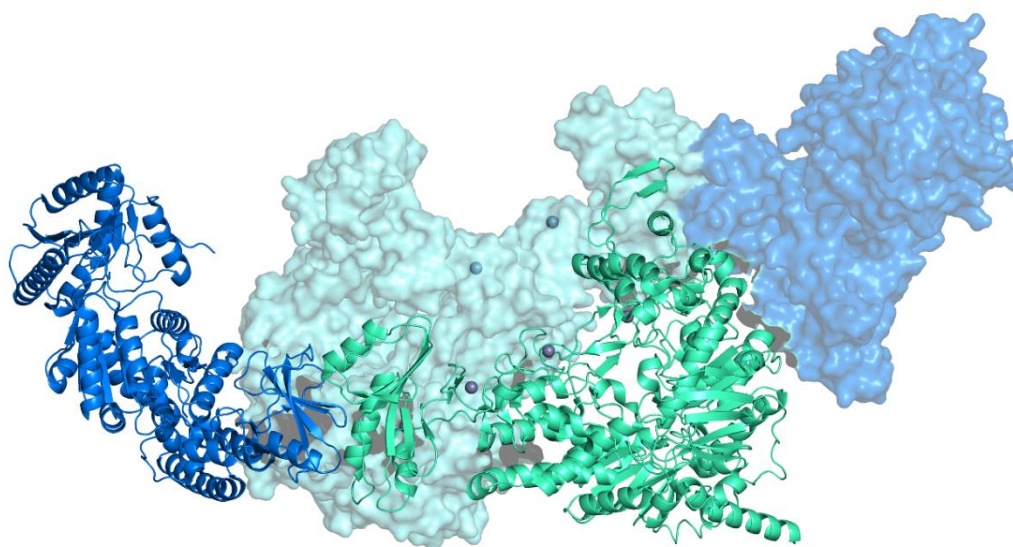


Figure 6: Structure of UvrA2B2 heterotetramer in *Geobacillus* sp. Y412MC52 (3UWX)

(37). This heterotetramer has a BAAB structure with UvrB in the extremities (represented in dark blue) and UvrA in the centre (represented in teal). The structure was generated using Pymol.

The C-terminal part of UvrB is required for binding to UvrC (61). Once recruited at the lesion, UvrC performs two nicks on the DNA, first 5 bases 3' to the lesion, then 7 or 8 bases 5' to the lesion (18,20). Although UvrC is capable of binding to DNA, it requires interactions with UvrB to undergo structural changes that allow for incisions (62). Furthermore, the presence of UvrA is also a requirement to allow for the incision of damaged DNA as UvrB and UvrC alone are not sufficient to incise damaged DNA (62).

1.3 Brief overview of other DNA damage repair pathways.

DNA is constantly getting damaged. To preserve cell fitness, DNA needs to be repaired. This thesis focusses on NER in prokaryotes. NER can handle a plethora of DNA damage ranging from UV photoproducts to protein-DNA crosslinks (20,63). However, there are numerous ways that DNA can be damaged and NER is not

equipped to deal with all types of damage. Figure 7 illustrates various DNA lesions and the associated DNA damage repair pathway.


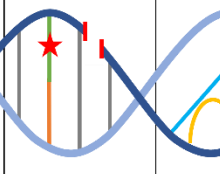
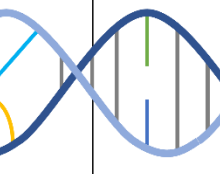
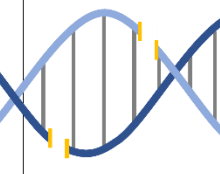
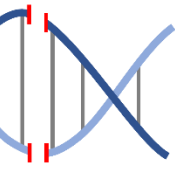
Repair pathway	BER	NER	MMR	NHEJ	HR
					
DNA lesion	Base modifications Abasic site Single strand break	Intra-strand crosslink Inter-strand crosslink Bulky adducts (CPDs, 6-4PPs)	Mismatch Indels	Double strand breaks	
Mutagenic source	Oxygen radicals Intercellular reactions Alkylating agents Ionizing radiation	UV light Crosslinking agents	Replication errors	Replication stress Alkylating agents Ionizing radiation	

Figure 7: Mutagenic sources and related repair pathways DNA is subjected to a plethora of mutagenic sources which alter DNA. Illustrated here are DNA lesions (represented on the double helix) and the related mutagenic sources and repair pathways. Base modifications (repaired by BER) are represented here by a red star while DNA nick is represented by the two red lines. Nucleotide Excision repair (NER), as previously described, is involved in repairing a The wide variety of DNA damages repaired by NER ranging from intra- (represented here in yellow) inter- (represented here in blue) strand crosslink as well as bulky adducts. Mismatches (repaired by MMR) are represented here by a green and a blue base that are not able to pair. Double-strand breaks can either have blunt ends (represented here with the red bars) or sticky ends (represented here with the yellow bars). Those are classically repaired by Homologous Recombination (HR) or by Non-Homologous End Joining (NHEJ). However, the latter is not present in *E. coli*. Adapted from (64).

1.3.1 Base Excision Repair

Base modifications such as oxidation, deamination, and alkylation are repaired by Base Excision Repair (BER) (65). BER is initiated by glycosylases, which are enzymes that cleave the bond between a base and the deoxyribose. Each glycosylase is specialised in recognizing specific lesions on the DNA. As such, the process of BER varies depending on the lesion involved (66). A well-described lesion recognized and repaired by BER is the 8-oxo-7,8-dihydroguanine modification of guanine and this lesion is recognised by the glycosylase MutM in prokaryotes (also called FPG) (67). The pathway of the repair is presented in Figure 8 where MutM acts as a

glycosylase and excises the modified base from its deoxyribose which leaves an abasic site (AP site) on the DNA (Figure 8II). This is followed by cleavage of the phosphodiester bond on the 3' side of the AP site via a β -elimination reaction thanks to the AP lyase activity of MutM (Figure 8III). Similarly, MutM cleaves the 5' side of the 3'-incised AP-site, freeing the related deoxyribose (Figure 8IV). The 3' phosphate group is removed by an AP-endonuclease/3'-phosphodiesterase (Either EndoIV or ExoIII). Steps III and IV can also happen at the same time as shown in Figure 8V. Finally, a polymerase comes and synthesis the lacking nucleotide (Figure 8VI). The resulting nick is ligated by a ligase.

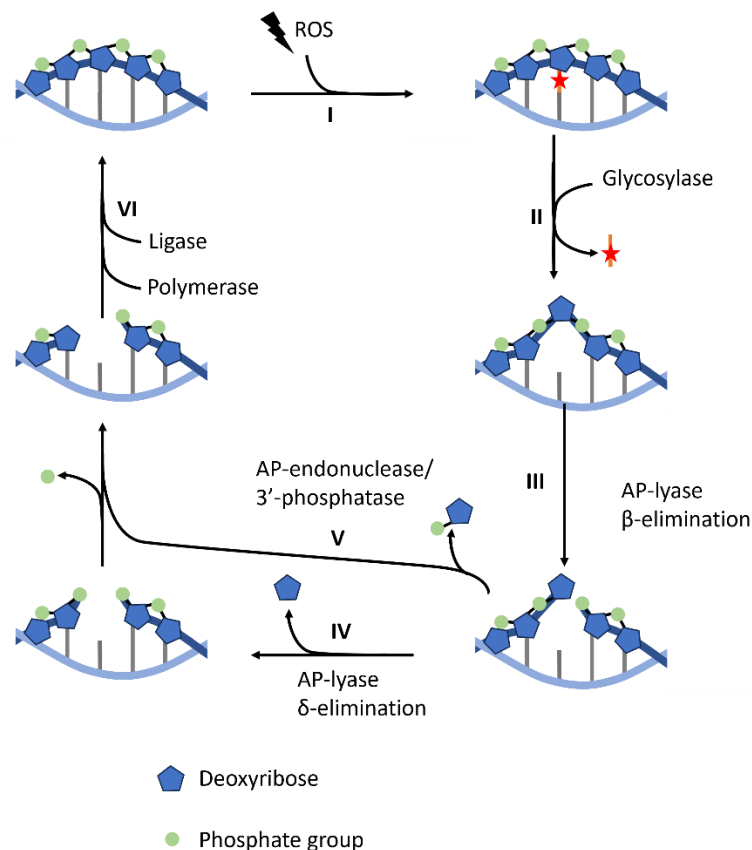


Figure 8: Base Excision Repair general pathway. I: Reactive Oxygen Species can create lesions on DNA. A typical lesion repaired by BER is 8-oxo-7,8-dihydroguanine. **II:** A glycosylase that can recognise the lesion will bind and cleave the damaged base from the DNA strand, resulting in an abasic site, also called AP-site. **III:** An AP-lyase will be able to cleave the DNA strand 3' of the AP-

site. **IV:** This is followed by an AP-lyase cleaving the DNA strand 5' of the AP-site, freeing the deoxyribose that was initially connected to the damaged base. **V:** The 3' phosphate is removed which allows for **VI:** priming of a polymerase that will synthesise the lacking nucleotide and a ligase that will ligate the resulting nick (67).

1.3.2 Mismatch repair

Mismatch Repair (MMR) is a DNA damage repair pathway that recognizes and repairs insertions, deletions, and substitutions that arise during replication. In *E. coli* the frequency of those mutations is of the order of 10^{-5} to 10^{-6} (68). The better-described pathway is the methyl-directed DNA mismatch repair which involves MutS, MutL, MutH and UvrD. This pathway allows for recognition of the template DNA which is methylated and newly synthesized DNA which is not methylated yet (69). It relies on MutH binding to a DAM site (the unmethylated strand of a newly replicated GATC site) at relative proximity to the mismatch as well as the capability of MutS to bind to mismatches (70) (Figure 9II). MutS recruits MutL and they move as a complex alongside the DNA strand in both directions until they come into contact with MutH. They form a new complex that induces MutH to cleave the newly synthesized DNA strand (Figure 9III). Upon cleavage, the complex dissociates from the DNA (Figure 9IV). This leaves room for a new MutS-MutL complex to come in proximity to the nick, recruiting UvrD to the nick (Figure 9V). Through the 3' to 5' helical activity of UvrD, the newly synthesised strand will get uncoupled to the template strand and is cleaved by exonucleases while the template strand is protected by single-strand binding proteins (SSB) (69) (Figure 9VI). As a result, the template DNA is now single-stranded and ready for a polymerase to synthesize the lacking DNA strand (Figure 9VII) (69,71).

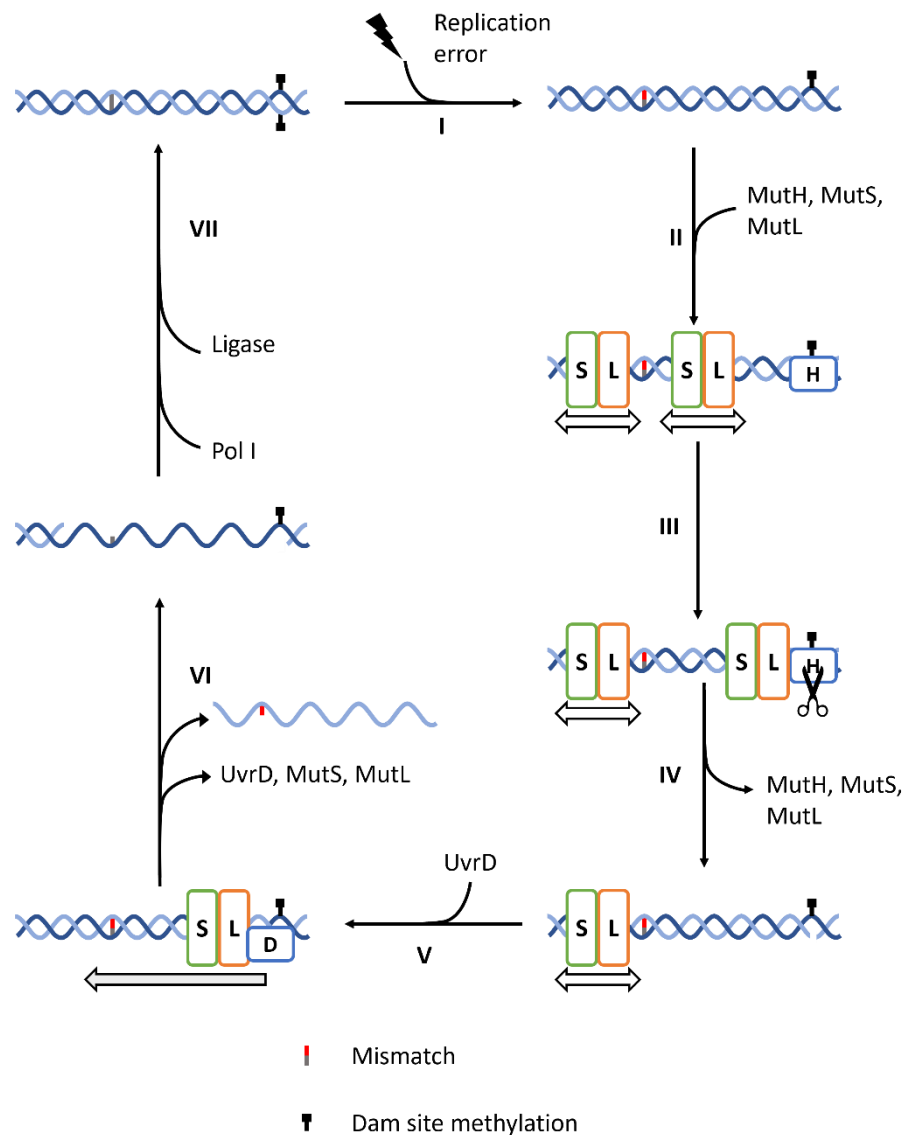


Figure 9: Mismatch repair. *I: During replication, errors can occur which can lead to mismatches. Thankfully, the mismatch repair pathway is well-equipped to restore the original base. II: MMR relies on MutH being able to bind to hemimethylated Dam site at relative proximity to a mismatch site as well as MutS binding to mismatches and recruiting MutL. III: MutSL complexes diffuse freely on the DNA until they come into contact with MutH at the Dam site. IV: Once in a MutSLH complex, MutH get activated and nick the DNA. This causes the newly formed complex to dissociate from the DNA. V: Another MutSL complex that is diffusing on the DNA will be able to recruit UvrD to the nick. VI: UvrD 3' to 5' helicase activity dissociates the mismatched strand and an exonuclease gets rid of it. VII: As a result, a polymerase can come resynthesize the lacking strand, using the unchanged DNA strand as a template. (72).*

1.3.4 Homologous Recombination and Non-Homologous End-Joining

Homologous recombination (HR) is used to repair double-strand breaks by using the homology between sister chromatids to repair the break. In *E. coli*, several proteins are involved. First, RecB, RecC and RecD bind to a double-strand break as a RecBCD complex (Figure 10II). Thanks to a helicase and a nuclease activity, the complex digests both strands of the DNA as it slides down (Figure 10III). Once RecBCD reaches a Chi sequence, it slows down and starts to protect the 3' terminated strand (73). A Chi sequence is an 8-base pair sequence that is very common in *E. coli* (up to one Chi site every 5 kbp). The presence of single-stranded DNA allows for single-strand binding protein (SSB) to bind (Figure 10IV). RecA is loaded by RecB until it covers the single-stranded DNA portion (74) (Figure 10V). This RecA/DNA complex can search and find DNA sequences of a double-stranded DNA that are homologous to its single-stranded DNA (75–77). A strand exchange of the newly-found homologous double-stranded DNA is used to repair the damaged DNA (78,79) (Figure 10VI). Interestingly, Non-Homologous End Joining (NHEJ) is a repair pathway that is not present in *E. coli*. As such, *E. coli* relies entirely on homologous recombination to fix double-strand breaks.

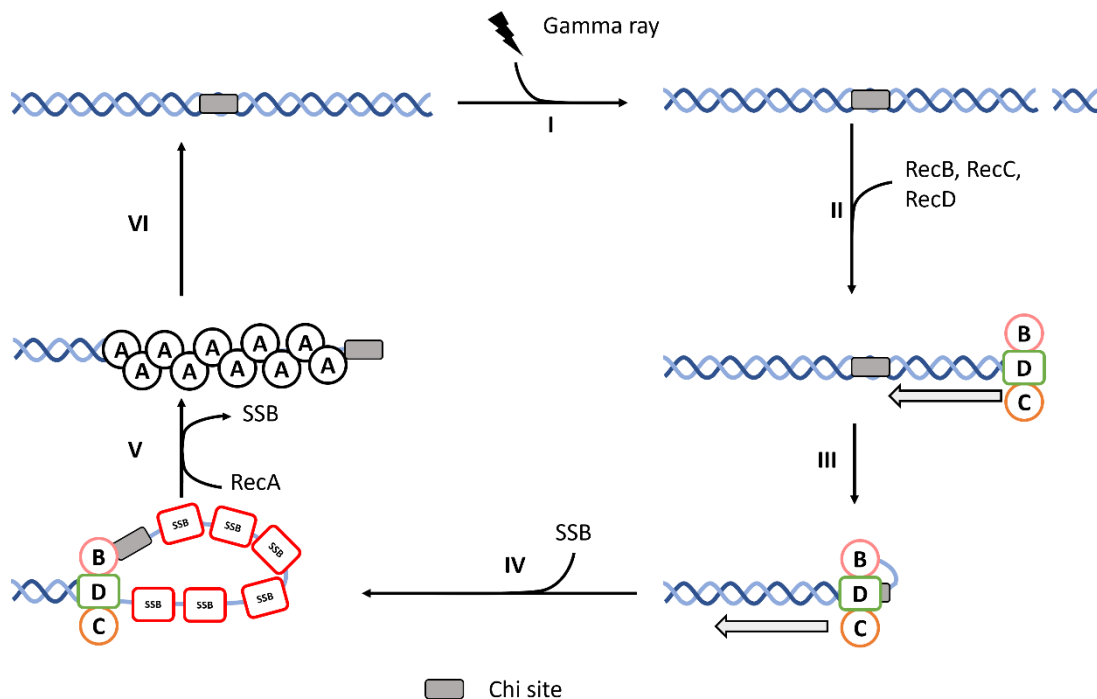


Figure 10: Homologous repair. I: Gamma rays can induce double-strand break. In *E. coli*, RecB, RecC and RecC bind to the break site. II: Together as a complex they digest both strands until reaching a Chi site (an 8 bp sequence that is spread every 5 kbp in *E. coli*, represented as a grey box here). III: This causes the complex to slow down and RecB will protect the 3' end while the complex keeps sliding down and degrades the 5' end. IV: Single Strand Binding proteins (SSB) bind to the newly formed single-stranded DNA and protect it. V: RecA is recruited to the DNA and replaces the SSB proteins. VI: The RecA/DNA complex finds a double-stranded DNA that is homologous to its single-stranded DNA and a strand exchange occurs to repair the damaged DNA. Adapted from (80).

1.4 The necessity for new antimicrobials.

Microorganisms were first described in the 17th century with the invention of microscopy (81,82). It took around 250 years to discover the first antibiotics (83,84). This together with better nutrition, clean water, sanitation and vaccination have changed the global life expectancy from 48 to 71 years and from 53 to 76 years in males and females respectively between 1950 and 2017 (85). However, within two years of the mass production of penicillin, the first cases of antibiotic resistance were already appearing (86). Presently, around 25,000 and 63,000 patients die every year in Europe and the United States because of

multidrug-resistant bacterial infections (87). The World Health Organisation has described antimicrobial resistance as one of the biggest threats to global health, with worries of returning to a pre-penicillin world where infections will get deadlier, and with a massive impact on the health system (88). The cost of antimicrobial resistance has been estimated to be between 21 to 34 billion American dollars for the US alone. This is because patients are required to stay longer in hospitals and the use of more expensive antimicrobials becomes a necessity. Those numbers are wildly contested because antimicrobial resistance is a vast field with a plethora of diseases and related antimicrobials being affected, and adding to the complexity are socio-economic factors (89). Microbes are becoming increasingly resistant to antimicrobials, and finding new classes of antimicrobials is extremely challenging. As a result, the classic research methods haven't found new classes in the past 30 years (87).

Antimicrobials target essential mechanisms of action, and therefore greatly affect cell fitness. The most common mechanisms targeted are protein synthesis, nucleic acid synthesis as well as cell wall synthesis and metabolic pathways (90). Some of the work presented in this thesis have been completed in collaboration to propose Nucleotide Excision Repair (NER) as a potential new class of antimicrobials. In addition, this thesis also seeks to develop a better understanding of protein synthesis, one of the most common targets for antimicrobials.

1.4.1 Interest in using NER as a target for antimicrobials.

NER is a great candidate as an antimicrobial target for several reasons. First, NER proteins are structurally very different between prokaryotes and eukaryotes despite having similar functions. Therefore, inhibitors of prokaryotic NER shouldn't affect eukaryotic NER. Second, UvrA recognizes a plethora of lesions, and therefore inhibiting UvrA would diminish NER for various lesions origins. The proposed antimicrobial effect is due to the combinational effect with DNA damaging agents. Such damaging agents can be a wide range of DNA damage sources; a great example of DNA damaging agents is cisplatin which is very

common in the treatment of cancers and UV light that is used in UV light therapy. Both induce DNA damage that is repaired by NER. Importantly, NER is not essential for the fitness of the cells when there is no external damage (91). All the above makes a great case for the use of prokaryotic NER inhibitors in combination with DNA-damaging agents.

The idea of inhibiting DNA repair pathway as an antimicrobial or an accessory to antimicrobials is not new. Firstly, many antimicrobials induce oxidative damage to DNA strands as a side effect, and therefore a lot of emphasis has been brought forward into inhibiting the SOS response, hence limiting the capabilities of microbes to repair damage in combination with antibiotics (92–95). It was also put forward that NER proteins were responsible for the majority of mutations that occurs during the transcription (96). Inhibiting NER could also help prevent bacteria from becoming antibiotic resistant.

1.5 Translation and ribosome speed

1.5.1 Antibiotics and the central part played by ribosomes

There is a plethora of mechanisms of action targeted by antibiotics but a central one is translation with ribosomes inhibitors representing more than half of the medicine used to treat infection (97). Mechanisms of actions of those antibiotics are very varied and depend on the location of the binding of the compound to the ribosome, either on the large or on the small sub-unit, and range all of the steps of the translation from initiation to elongation to termination (97,98). As an example of antibiotics, Edeine acts on the initiation by binding to the P-site of the small subunit of the ribosome and as a result prevents the binding of fMet-tRNA^{fMet} (99). Spectinomycin acts on the translocation by interacting with the 16S part of the small sub-unit, limiting the 30S head rotation and therefore preventing translocation (100). Another interesting example is Kirromycin which reduces the affinity of EF-Tu for aminoacyl tRNAs (101). Ribosomes are targeted by many antibiotics that affect many of the ribosome functions. However, despite being

studied extensively in the past decades, there is still a lot of unknown in some of the translation steps. Elucidating those steps could help provide an understanding of the way that some antibiotics work. One of those is the impact that near-cognate tRNAs have on ribosome speed, one of the ways that gene expression is regulated. This thesis shows work that was done on developing a single-molecule method to assess the effect of various near-cognate tRNA/codons interactions.

1.5.2 Regulation of gene expression

Regulation of gene expression is essential for the fitness of any cells. Any changes can have dramatic effects. Regulation occurs at all stages of gene expression and spans from epigenetic DNA modifications to translation regulation as well as post-translational regulation. Regulation at the DNA level encapsulates DNA modifications (methylcytosine, 5 hydroxy-methylcytosine, etc.) as well as histone modifications in eukaryotic cells (methylation, acetylation, etc.). Both affect the availability of the DNA for the transcription machinery and therefore have an impact on the overall mRNA population (102–104). Regulation at the messenger RNA (mRNA) level goes through both the transcription rates and the mRNA degradation rate as they will both vary depending on the mRNA (105,106). Remarkably, in prokaryotes, translation starts simultaneous to the transcription event, and genes are often present as polycistronic mRNA. At the translation level, the most studied factor of regulation is the initiation phase where initiation sites are blocked preventing the recruitment of the translation machinery (107). Lesser-studied aspects of the regulation of gene expression are events that occur during the elongation, where mRNA sequence and tRNA populations will have a strong impact on the speed at which ribosomes generate new proteins (108–111). Ribosomal speed is of particular importance as it helps regulate the quantity of each protein within the cell as well as the fitness of those proteins.

1.5.4 Ribosome Structure

Prokaryotic ribosomes are large complexes of roughly 2.5 Megadaltons with a diameter of around 20 nm and make up for 28% of the dry mass of fast-growing *E.*

coli (112–114). They are composed of two subunits. A large subunit (LSU, in salmon in Figure 11) and a small subunit (SSU, in magenta in Figure 11) with sedimentation coefficients of 50S and 30S respectively. Both of those are themselves composed of ribosomal RNA (rRNA) and proteins with the LSU having 31 proteins, the 5S and the 23S rRNA while the SSU has the 16S rRNA and 19 proteins. There are numerous sites of interactions in-between the two sub-units named inter-subunit bridges that are responsible for many translational events such as subunits joining, ribosome recycling, translocation, and peptide release through the rotation between the two subunits (115). Ribosomes possess three sites that span in-between the two sub-units where tRNA will be located throughout translation: the Exit-site (E-site) within which is positioned the green transfer RNA (tRNA) in Figure 11, the Peptidyl-site (P-site) within which the orange tRNA is positioned in Figure 11 and the Aminoacyl-site (A-site) where the red tRNA bound to EF-Tu in Figure 11 is located. The exit tunnel of the ribosome is a structure present on the LSU that is 9.6 nm long and contains from 30 to 40 amino acids of the nascent protein chain (116–120). Some peptides can stall the ribosome by folding within the exit tunnel. Two common examples are the SecM protein and polyproline sequences. SecM proteins stall the ribosomes by interacting with the exit tunnel and altering the configuration of the A-site and the P-site of the ribosome (121). Nascent proteins containing three consecutive prolines also stall the ribosomes by the unique proline structure within the different amino acids and require the action of EF-P to stop the dwelling of the ribosomes (122,123).

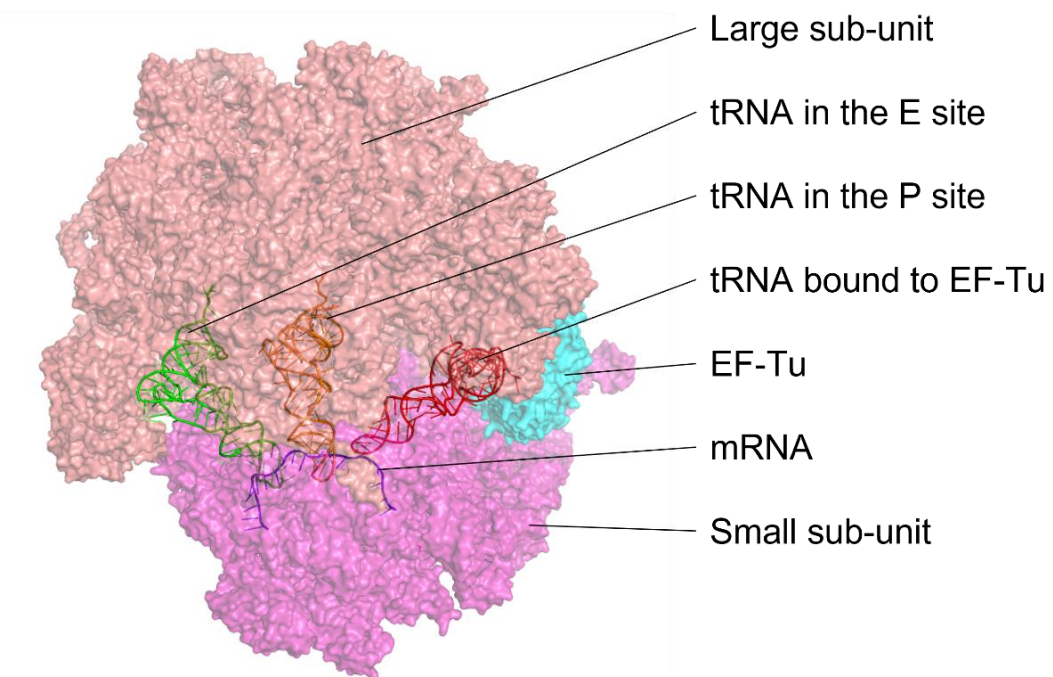


Figure 11: Crystal of a ribosome with its 3 sites occupied and with EF-Tu. This shows a fully assembled ribosome with its three sites occupied. Its E-site and P-site are occupied by tRNAs represented in green and orange respectively. A tRNA-EF-Tu complex is within the A-site with the tRNA represented in red and EF-Tu represented in teal. The large and small ribosomal subunits are represented in salmon and magenta respectively while the mRNA is represented in dark blue.

1.5.5 Transfer RNA structure

In *E. coli*, tRNAs are composed of 76 to 95 nucleotides with their secondary structure showing four arms in a clover leaf structure (Figure 12A) and their tertiary structure folded in an L-shape fashion (Figure 12B) (124–126). As shown with the clover leaf structure, the tRNA is composed of 5 main parts. Firstly the acceptor stem contains both the 5' start and the 3' end of the tRNA sequence with a three-nucleotide CCA overhang in the 3'. The amino acid is added to the final 3' hydroxyl group of the tRNA by aminoacyl tRNA transferases (or tRNA ligases, aaRS) to form aminoacyl-tRNA (aa-tRNA). There are 46 different tRNA in *E. coli* but only 21 aaRS, one for each amino acid that will be used for elongation plus an extra one for lysine (127,128). Recognition of tRNAs by aaRS happens mainly through nucleotide 73 in the acceptor stem and the anticodon bases 35 and 36. However, it is variable for each tRNA and recognition of the correct tRNA can be helped by

core nucleotides as well as through nucleotide modifications (129). aa-tRNAs are recognized by EF-Tu which binds each cellular aa-tRNAs with a different affinities. Interestingly that affinity is inversely proportional to the number of aminoacyl-tRNA for each species present in the cell (130). EF-Tu interacts with the acceptor stem and T-arm as shown for both $_{\text{phe}}\text{tRNA}^{\text{phe}}$ and $_{\text{cys}}\text{tRNA}^{\text{cys}}$ (Figure 12B)(126,131). The interaction relies on base pairs nucleotides 49/65, 50/64 and 51/63 (132). tRNAs are heavily modified and show a higher level of modifications on the anticodon arm especially on nucleotides 34 and 37 of the tRNA affecting its decoding activity. The three nucleotides shown in blue in Figure 12A and B are the anticodon, spanning from nucleotide 34 to nucleotide 36. The anticodon is responsible for recognising the mRNA codon that is present within the A-site of the ribosome. Modifications outside of the anticodon arm often have structural roles (133–135). Mature tRNAs can be fragmented in a variety of ways producing short 16-35 nucleotides tRFs (fragmented tRNA) or tiRNA (tRNA halves). Such RNAs are involved in a variety of regulation processes (136). From inhibition of tRNA synthetase, stress adaptation, involvement in disease, inhibition of protein synthesis, etc (136–141). Interest is increasing for tRFs and tiRNAs effects as functional RNA but also to which extent they impact translation.

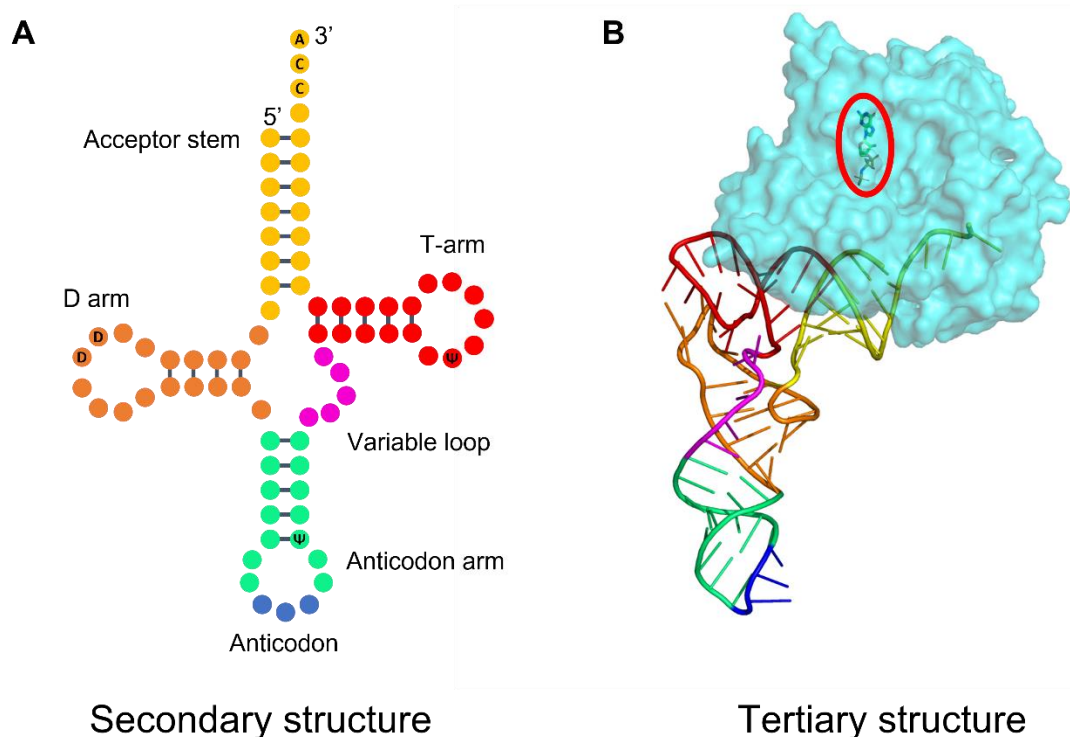


Figure 12: Cloverleaf and tertiary structure of tRNA. Adapted from (126). **A:** Secondary structure of generic tRNA where the RNA adopts a cloverleaf structure with four arms and a variable loop. Notable structures are the acceptor stem (represented in yellow), the three nucleotides (CCA) overhang, the D arm (represented in orange), the anticodon arm (represented in green) containing the anticodon (in blue), the variable loop (represented in pink, and finally, the T-arm (represented in red) **B:** Tertiary structure of tRNA bound to EF-Tu (crystal structure 1TTT, *Thermus aquaticus*). When folded, tRNA adopts an L-shape 3D structure. Once loaded with the corresponding amino acid, the tRNA will form a complex with EF-Tu (represented in teal here) which will allow for the newly formed complex to interact with the ribosome. The colour code for the tRNA is kept from Figure 12A. The localisation of EF-Tu's GTP cassette is circled in red with a GDP being bound. The tRNA represented here is *phe*tRNA^{Phe}.

1.5.6 Initiation of translation

There are various ways that the initiation of translation can start. Notably, Shine-Dalgarno (SD) led, non-SD led, within polycistronic mRNA or leaderless mRNA. The most studied initiation process is within SD-led genes and is one that will be described today. However, not all mRNA have a Shine Dalgarno sequence, and there is huge variability between species from 11.6 % to 90.8 % of genes containing

a SD sequence with *E. coli* standing at 61 % (142). Shine Dalgarno is a specific sequence located 8 to 10 bases upstream of the start codon AUG with the conserved sequence of AGGAGG (AGGAGGU for *E. coli*). This is closely related to the complementary sequence CCUCCU (ACCUCCU for *E. coli*) within the 16 S ribosomal RNA (143). This motif is called the anti-SD sequence and allows for the recruitment of the 30S subunit to the mRNA in SD-led genes by base-pairing with the SD sequence within the mRNA. Initiation Factors 1, 2 and 3 (IF1, IF2 and IF3) are recruited to the 30S subunit as well as the initiator tRNA ${}^{\text{fMet}}\text{tRNA}^{\text{fMet}}$. The recruitment of the initiation factors, the initiator tRNA and the mRNA can happen in a multitude of ways and in a non-linear fashion (144,145). However, there is a kinetically favoured assembly pathway where IF2 and IF3 are the first factors to assemble onto the 30S, followed by IF1 which locks the factors in a stable 30S PIC, ${}^{\text{fMet}}\text{tRNA}^{\text{fMet}}$ is then recruited (144). Once they are all recruited, they form the 30S Initiation Complex (IC). Recruitment of the large 50S sub-unit leads to the release of the initiation factors and accommodates the initiator tRNA in the P site of the ribosome forming the 70S initiation complex that is ready for elongation as shown in Figure 13.

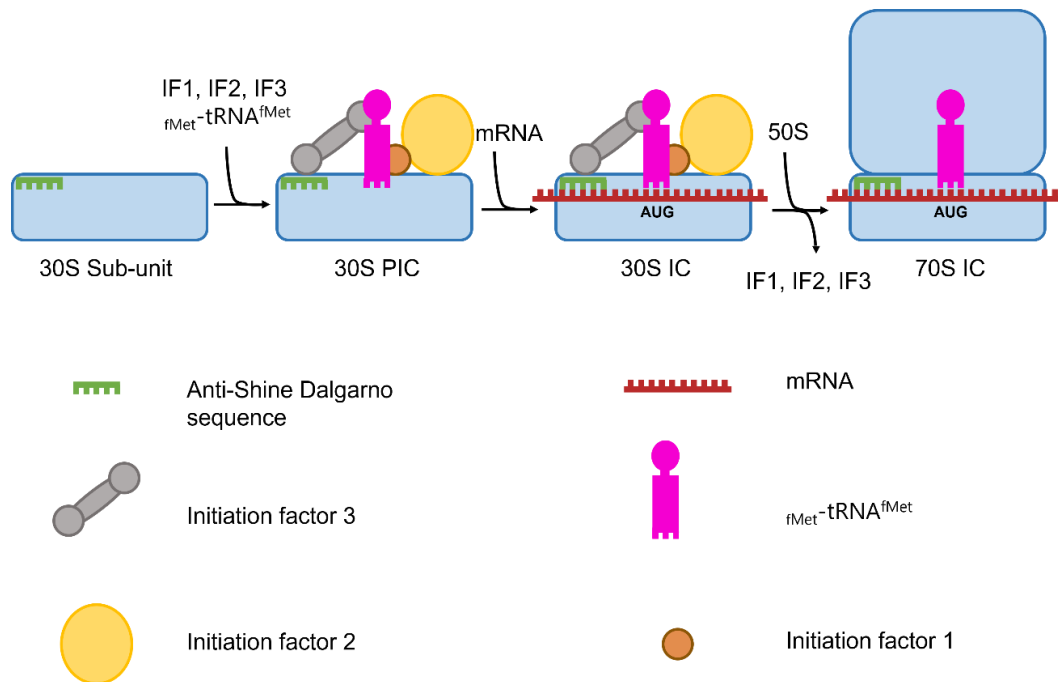


Figure 13: Translation initiation of Shine-Dalgarno-led genes.

The 30S ribosomal sub-unit recruits the initiation factors 1, 2 and 3 as well as the initiator $fMet-tRNA^{fMet}$ to form the 30S Pre-Initiation Complex. The anti-SD motif within the 16S ribosomal RNA will help the loading of the mRNA by interacting with its SD motif. The loading of the different initiation factors, tRNA and mRNA can proceed in any order. Once $fMet-tRNA^{fMet}$ recognizes the start codon it will lead to the recruitment of the 50S ribosomal sub-unit as well as kicking out the initiation factors, ultimately forming the 70S initiation complex with the $fMet-tRNA^{fMet}$ located at the P site of the ribosome.

1.5.7 Elongation of translation

The elongation is a cyclic process that happens through three repeating steps: decoding, peptide bond formation and translocation as illustrated in Figure 14. It starts as soon as the A-site of the ribosome is free for elongator tRNA docking and stops when the ribosome reaches a stop codon.

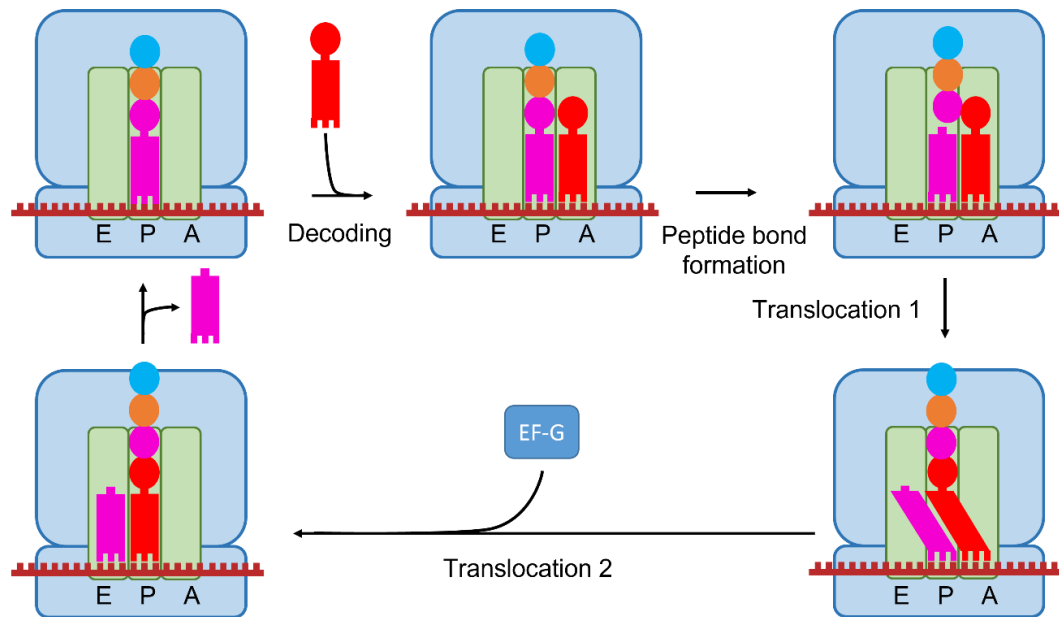


Figure 14: Translation elongation. During the elongation of the translation, the nascent protein chain is bound to the peptidyl-tRNA located in the P site of the ribosome. Novel aa-tRNA insert themselves within the A-site of the ribosome until the cognate tRNA properly decodes the codon located on the A-site. This leads to peptide bond formation between the amino acid carried by the cognate tRNA and the nascent protein chain. The novel nascent protein chain is transferred to the tRNA located in the A-site during this process. A first event of translocation will force both tRNAs into hybrid P/E and A/P states where the decoding part of the tRNA is still within the P-site and A-site while the rest has been moved within the E-site and P-site respectively. With the help of EF-G, both the mRNA and the tRNAs will be translocated as well. Finally, the tRNA located within the E-site will be able to exit the ribosome and the elongation of the translation can keep proceeding until reaching a stop codon. Each cycle adds one amino acid to the nascent protein chain.

1.5.7.1 Decoding

During decoding, the codon of the mRNA will be recognized by the anticodon part of incoming tRNA which will lead to the selection of the proper tRNA and therefore proper amino acid for subsequent elongation events. This happens in a succession of events. First, the aminoacyl-tRNA arrives bound to $\text{GTP} \cdot \text{EF-Tu}$ as a complex and binds to the small sub-unit without base pairing happening. This is followed by anticodon and codon pairing with each others. Importantly the ribosome stays in open conformation which allows the GTP binding pocket of EF-Tu to stay distant

from the large sub-unit (146). The GTPase activity of EF-Tu depends on its interaction with the 23S rRNA of the large sub-unit (147), in particular its sarcin-loop. Once the codon-anticodon interaction has occurred, the 16S rRNA within the decoding centre change their orientation (148) leading to the small sub-unit closure and rapprochement of the aa-tRNA-GTP-EF-Tu complex and subsequently to GTP hydrolysis. Hydrolysis has for consequences the dissociation of the EF-Tu from the aa-tRNA and accommodation of the aa-tRNA within the A site of the ribosome. Proper codon recognition will be discussed further below.

1.5.7.2 Protein bond formation

Once a codon has been properly recognized by the appropriate elongator-tRNA, peptide bond formation will occur in between the amino acid of the elongator-tRNA in position A and the last added amino acid of the nascent protein chain carried by the peptidyl-tRNA in position P. The entropy of this reaction is lowered by the ribosome by ordering water molecules, positioning of rRNA and tRNA residues by a factor of $2 \cdot 10^7$ (149–151). Nucleophilic attack of the amino group of the elongator-tRNA on the carbonyl carbon of the ester bond in peptidyl-tRNA leads to peptide bond formation. This leaves the peptidyl-tRNA in the P site to be unloaded of its peptide while the elongator-tRNA in the A site is now in possession of the peptide.

1.5.7.3 Translocation

Translocation is the event that moves both the empty tRNA and the peptidyl-tRNA from the P-site and the A-site to the E-site and the P-site respectively. It also moves the mRNA by three bases to allow decoding of the following codon. This occurs through rotations of the large and small subunits with each other and allows positioning of the empty tRNA and the peptidyl-tRNA in a P/E and A/P hybrid state respectively (152,153). In those hybrid states, the codon/anticodon of the mRNA/tRNAs stay in the original binding sites P and A while the rest of the tRNA moves to the E-site and P-site. It's Elongation factor G (EF-G) that comes and assists the mRNA/tRNA movement on the small subunit at the cost of GTP

hydrolysis (154). The peptidyl-tRNA is now located in the P-site and is ready for a new elongation cycle. The tRNA that is now located in the E-site will spontaneously leave the ribosome. However, it has been shown that tRNA exit of the ribosome is also dependent on the arrival of a new aa-tRNA binding in the A-site in early cycles of protein elongations (155).

1.5.7.4 Nascent protein folding

Nascent protein folding occurs as the mRNA is translated. At first, the nascent protein chain is within the ribosome exit tunnel and the folding will be limited by the lack of space within that tunnel. Indeed, the exit tunnel is only 10 nm long and can accommodate only 30 to 40 amino acids. Once all domains emerge from the ribosome, the final stage of folding can occur. It has been suggested a bridge between ribosome speed and protein folding, where rare codons slow down the translation, resulting in different folding of proteins (156–158).

1.5.8 Termination of translation

Termination will occur once the ribosome reaches a stop codon. Termination is divided into three steps, the first one is the recognition of the stop codon, the second is the hydrolysis of the ester bond of the peptidyl-tRNA and finally, the last step is the dissociation of the release factors (159). Recognition of the stop codon occurs through the release factor (RF) RF1 (UAG/UAA) (160,161) and RF2 (UGA/UAA) (162,163) and is due to the presence of conserved recognition motifs which both have structures allowing specific recognition of the three bases. Hydrolysis of the ester bond of the peptidyl-tRNA is catalysed by the peptidyl transferase centre of the ribosome with the help of the GGQ motif of RF1 or RF2 which leaves the free peptide and deacylated tRNA (164). Once the hydrolysis happens, RF3 will come to release RF1 or RF2 from the ribosome and finally, RF3 will hydrolyse its GTP to dissociate itself from the ribosome (165). To recycle the ribosomes, bacteria use two proteins. The ribosome recycling factor (RRF) occupies the A-site of the ribosome and it stabilizes a fully rotated state of the ribosome, EF-G pushes the RRF against an inter-subunit bridge at the cost of a GTP

hydrolysis, leading to subunit splitting and release of deacylated tRNA and mRNA (166,167).

1.5.9 Cognate, near-cognate and non-cognate tRNAs

During codon-decoding, aa-tRNA will be presented to the A-site of the ribosome by EF-Tu. Each aa-tRNA presented will be assessed by its capacity to decode the codon. Codon nucleotides 1, 2 and 3 will be decoded by anticodon nucleotides 36, 35 and 34 respectively. There are three potential cases. Either the anticodon corresponds to a cognate, near-cognate or non-cognate relative to the codon.

1.5.9.1 Cognate tRNA

A cognate tRNA is a tRNA that can base pair the A-site codon with its anticodon. The two first bases of the anticodon will form a Watson-Crick base pair (A-U or G-C) and the third base will either form a Watson-Crick or a wobble (G-U, I-U, I-A, or I-C, I stands for Inosine) base pair (168,169). Interestingly, the I base is only found in one *E. coli* tRNA (${}_{\text{ICG}}\text{tRNA}^{\text{arg}}$) reading three different codons (170). Wobble base pairing allows for some flexibility in the pairing and enables the decoding of several codons by the same tRNA (169) and explains why there are only 46 tRNA and not 61 (for 64 codons, minus the stop codons). Wobble pairing is possible because two Watson-Crick base pairings are enough to hold the tRNA in place (171). This however comes at a cost as those wobble-base interactions will proceed at a slower rate and will have a higher probability of being rejected than the non-wobble ones (110,172). The rules of what is a wobble anticodon have been changed over time as tRNA modifications have been shown to affect it.

1.5.9.2 Near-cognate tRNA

A near-cognate tRNA is a tRNA that carries a non-matching amino acid compared to the codon, but that has some complementarity with it. A functional definition has been put forward as near-cognate tRNA being capable of forming a mRNA:tRNA mini-helix which is not the case for non-cognate tRNAs (173). Near-cognate tRNA can do the same reactions as cognate tRNA but with less favourable ratios of forward-to-reverse rate constants (174). Near-cognate can be misread by

the ribosome, leading to the incorporation of the wrong amino acid into the sequence. Interestingly, stop codons have near-cognate tRNA and it has been shown that upon metabolic stress, stop codons can be read through resulting in protein variants with extended C-termini. This results in heterogeneity between cells that have the same genetic code and might be linked to adaptation to environmental changes (175).

1.5.9.3 Non-cognate tRNA

A non-cognate tRNA is a tRNA that carries a non-matching tRNA and has not more than one base of complementarity with the codon. It is not capable of forming mRNA:tRNA mini-helices in the A-site of the ribosome.

1.5.10 Ribosome speed

1.5.10.1 Importance of working on ribosome speed

Despite being extensively studied, Translation still has a lot of unknowns. In industrial settings, codons of proteins are optimised to ensure an increase in product yield in various expression systems (176–179). A better understanding of translation will help further optimisation of medicine production, hence decreasing production costs. Defects of various stages of translation elongation have been shown to result in diseases in humans, from mutations in aminoacyl-tRNA synthetases leading to genetic diseases (180,181), post-translational modifications of the elongation factor eEF2 are involved in Alzheimer's and Parkinson disease (182,183) as well as cancer (184) and upregulation of tRNAs are linked to an increase in mortality in prostate cancer (185). Those discoveries are primordial as they highlight novel potential targets for therapeutic applications. The study of prokaryotic translation also comes with therapeutic interests as many antimicrobials are focused on translation. Notably within the elongation phase with a few examples being chloramphenicol binding within the A-site of the ribosome, preventing tRNA from presenting their anticodon, erythromycin binding within the exit tunnel, or spectinomycin inhibiting translocation (98). Regulation of ribosomal activity is at the convergence of modern therapeutics challenges,

from the recent discoveries on implications in various diseases to antimicrobial resistance. In-depth study of all translation processes is required to ensure better understanding of their implication and potential neo-target for future therapeutic treatments.

1.5.10.2 Impact of cognate, near-cognate and non-cognate populations of tRNA on ribosome speed

Despite thoughts that regulation was occurring mostly during the initiation, more and more evidence shows the importance of elongation and ribosome speed for translational control (186,187). Ribosome speed is the speed at which the ribosome processes the mRNA and produces the peptide. This speed is influenced by several factors as illustrated in Figure 15. Most notably it is strongly affected by the efficiency of the decoding process where the concentration of cognate, near-cognate and non-cognate aa-tRNA as well as the base pair formed in the wobble position play a major part in the elongation speed (108). 64 combinations of 3 nucleotides form the genetic code and will be translated into 20 amino acids using 46 different tRNAs. Each tRNA has different concentration and diffusion constants. Most importantly each codon (excluding stop codons) will have from 1 to 3 cognate tRNA and from 0 to 8 near-cognate tRNA (in *E. coli*). Each near-cognate tRNA binding to the ribosome will slow down the translation of the corresponding codon resulting in a complicated network of relationships that links individual tRNA concentration, diffusion constant, ability to act as near-cognate for specific codons, and mRNA sequence. It was shown that the average synthesis rate at 24.5°C and 37°C are 4.4 and 12.9 amino-acids per second (188) and the average time to insert an amino acid from a cognate aa-tRNA is 9.06 ms (174,189). Delays induced by the binding of near-cognate and non-cognate amino acids are estimated to be 10.48 ms and 0.5 ms respectively when using mathematical models (189,190). This model uses only one set of data to get the rates of elongation steps using ${}^{\text{phe}}\text{tRNA}^{\text{phe}}$ and ${}^{\text{leu}}\text{tRNA}^{\text{leu}}$ while assessing the codons UUU (coding for phe) and CUC (coding for leu) (174). More data is required to have

more precise models of ribosome speed. Especially assessing near-cognate rates of more codons/tRNAs couples.

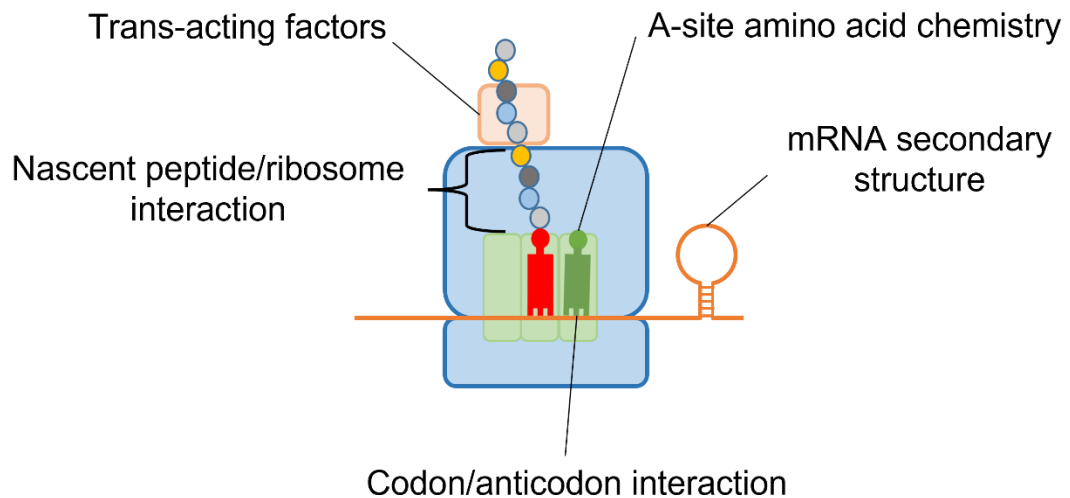


Figure 15: Illustration of the different factors acting on ribosome speed. Several factors impact ribosome speed. From mRNA topology that slows or stops the ribosome, the slow rate constant of peptidyl transfer reactions in the A-site, the action of trans-acting factors, the interaction of the nascent peptide with the ribosome that can slow down or even stop translation and finally the overall cognate/near-cognate tRNA concentration and the base pair formed in the wobble position which both act as the principal factor of ribosome speed. Adapted from (108)

1.5.10.3 Impact of nascent peptide chain folding and sequence on ribosome speed

The composition of the Nascent peptide chain can have a big impact on ribosome speed. As mentioned earlier, three consecutive prolines are sufficient to stall the ribosome and some peptides are capable of doing the same (121–123). Additionally, positively charged amino acids do interact with the ribosome exit tunnel, slowing down translation (191,192).

1.5.10.4 Secondary mRNA structures

The topology of the messenger RNA can affect translation by slowing down ribosomal speed. However, mRNA secondary structures have also been reported to be correlated with higher protein expression in *S. cerevisiae* (193,194).

1.6 PhD aim

It is thought that NER recognizes alterations in the structure of the DNA in proximity to DNA lesions (195–197). However, this hypothesis was not totally proven. We aim to understand how distortion of the DNA can impact the kinetics of NER proteins. Insights on how NER proteins interact with damage sites is of great interest as we also aim to assess if NER inhibitors could be used as a novel family of antimicrobials. Antimicrobial resistance is in steep increase and it is imperative to find new ways to defend ourselves against unfriendly germs. With most antibiotics targeting the ribosome, we aim to deepen the understanding of one understudied aspect of translation which is the impact of near-cognate tRNA in the elongation.

Chapter II: General Materials and Methods

2.1 Lysate preparation

A pJB-derived plasmid with UvrA-mNeonGreen containing a His-tag on the C-terminus, and driven by a T5 promoter and a resistance marker (CamR) (**Error! Reference source not found.A**) was transformed into a BL21 *E. coli* expression strain where the genes expressing UvrA and UvrB were deleted (BL21 $\Delta uvrA \Delta uvrB$). A single colony was isolated and grown at 37 °C in a 1L LB flask supplemented with chloramphenicol at 150 rpm. Once the OD₆₀₀ reached 0.4-0.6, 1 mM IPTG was added, allowing the expression of the protein. The protein was expressed at 18 °C overnight at 150 rpm. The cells were then spun down at 5000 rpm for 20 minutes. The pellet was re-suspended in resuspension buffer (50 mM NaH₂PO₄, 300 mM NaCl, 15 mM imidazole), supplemented with protease inhibitor (Pierce Protease inhibitor tablets, A32963, Thermofisher). The cells underwent lysis by sonication (12 minutes, 30 seconds ON, 59 seconds OFF, 55% amplitude). This is followed by centrifugation at 20000 rpm for 30 minutes. The supernatant is then filtered and aliquoted. Lysates for UvrA-mScarlet, UvrA-mScarlet x2 (meaning that the protein is made of UvrA and two successive mScarlet proteins as shown in **Error! Reference source not found.C**) and UvrB-mNeonGreen were prepared similarly. Concentration of UvrA-mNeonGreen and UvrB-mNeonGreen within the lysate were estimated by measuring absorbance at 506 nm (Extinction coefficient: 116,000 M⁻¹.cm⁻¹). Plasmid maps are presented in **Error! Reference source not found.**

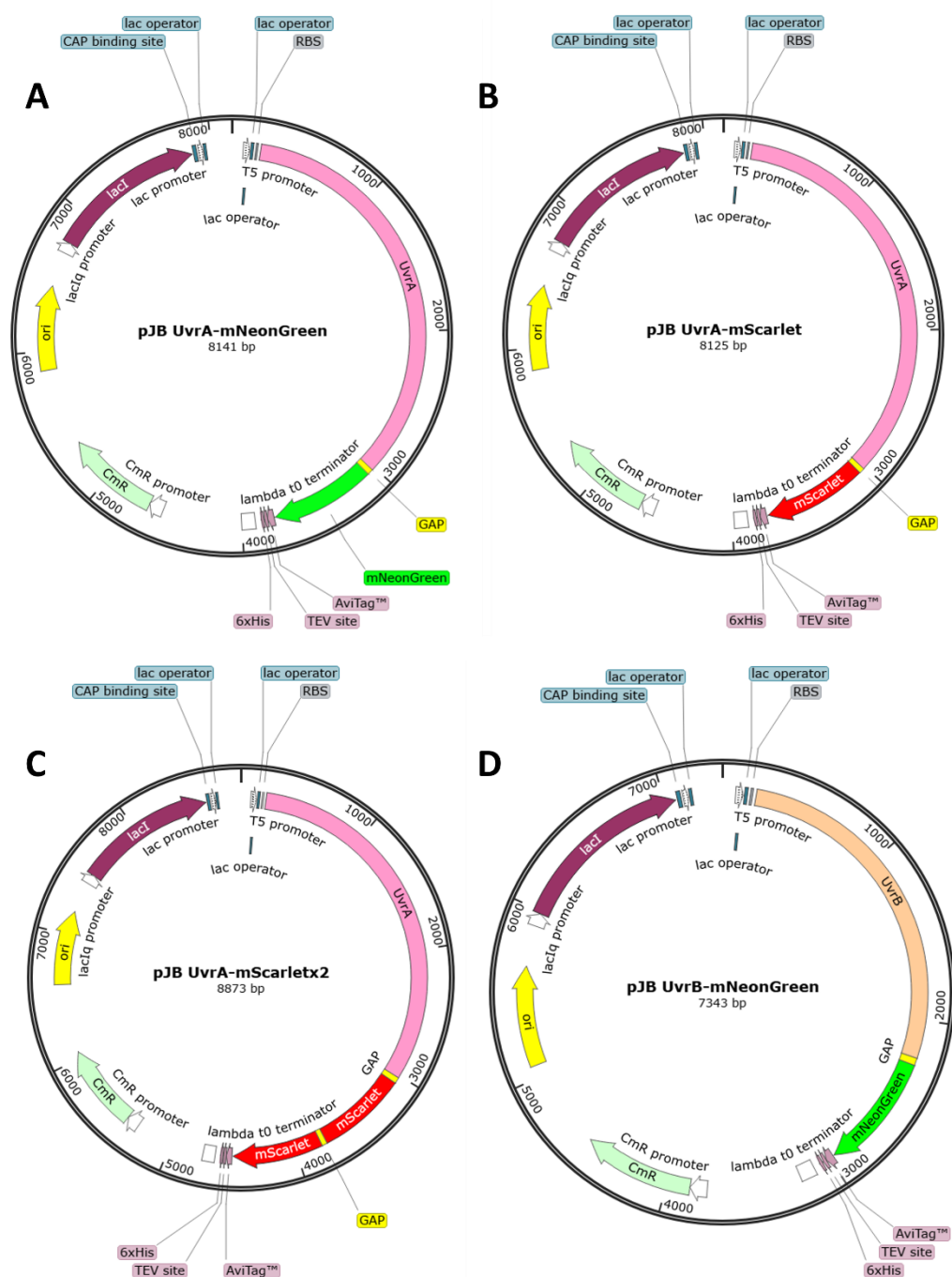


Figure 16: Plasmid maps of proteins used. A: Plasmid map of UvrA-mNeonGreen, B: UvrA-mScarlet, C: UvrA-mScarlet x2, and D: UvrB-mNeonGreen fusion proteins.

2.2 Protein purification

For protein purification, lysates are produced as previously described. Lysates are filtered through a 0.2 μm syringe filter and loaded onto a Proteus '1-step Batch'

Midi plus spin Columns (GEN-1SB08P) that were preloaded with cold Nickel-NTA resin. Samples are left to incubate with the resin for 3 hours in a cold room on a tube roller. After spinning the columns to get rid of unbound proteins, the column is washed and the protein is eluted with different concentrations of Imidazole (90, 130, 160 or 500 mM) by mixing resuspension buffer with high imidazole buffer (50 mM NaH₂PO₄, 300 mM NaCl, 500 mM imidazole). The elutions at 90, 130 and 160 mM are pooled together and the buffer is exchanged to the 2X UvrA storage buffer (100 mM Tris pH 8, 1 M KCl, 0.2 mM EDTA, 2 mM DTT) or 2X UvrB storage buffer (100 mM Tris pH 8, 200 mM KCl, 0.2 mM EDTA, 5 mM DTT) using Vivaspin® 20 (50 or 100 kDa molecular weight exclusion size, GE28-9323-62, or GE28-9323-63). This also allows for concentration of the protein to a volume of less than a millilitre which is subsequently mixed with glycerol 1:1 (V/V). The concentration of UvrA-mScarlet x2 is estimated by measuring absorbance at 569 nm (Extinction coefficient: 100,000 M⁻¹.cm⁻¹). The concentration of UvrB-mNeonGreen is estimated by measuring absorbance at 506 nm (Extinction coefficient: 116,000 M⁻¹.cm⁻¹). All the steps of the purifications from the expression of the protein to the elution steps are run in an SDS page gel shown in **Error! Reference source not found.A** for UvrA-mScarlet x2 and **Error! Reference source not found.B** for UvrB-mNeonGreen. The final purified proteins are shown in **Error! Reference source not found.C**. Since those proteins were used for single-molecule experiments at concentrations of in the order of nM, they do not require to be highly purified.

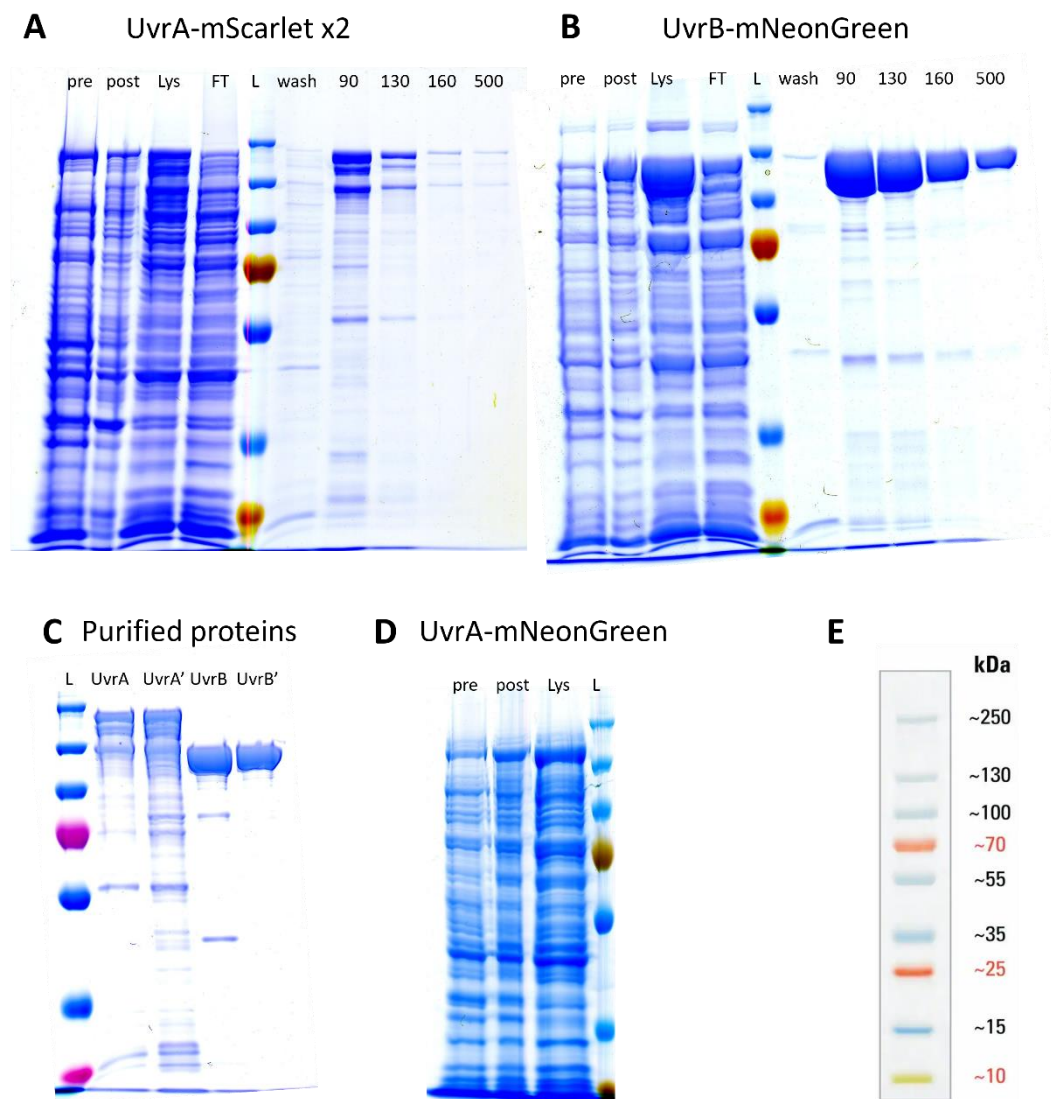


Figure 17: SDS page gel of UvrA-mNeonGreen purification. 10% Acrylamide gels. **A:** Batch purification of UvrA-mScarlet x2. Annotated are: pre (cells before induction), post (cells after induction) Lys (supernatant after lysis and spin down), (L: Pagaruler ladder (Fisher Scientific 11832124), FT (Unbounded to the column), wash (Wash step), 90,130,160 and 500 (Elutions at the corresponding concentration of imidazole in mM). Expected molecular weight for UvrA-mScarlet x2 is 161 kDa. **B:** Batch purification of UvrB-mNeonGreen with similar annotations as for UvrA-mScarlet x2. Expected molecular weight for UvrB-mNeonGreen is 105 kDa **C:** Purified proteins. Annotated are UvrA and UvrB which are proteins purified from a BL21 $\Delta uvrA \Delta uvrB$ background and UvrA' and UvrB' which are proteins purified from a wild-type background. **D:** Lysate production of UvrA-mNeonGreen. Expected molecular weight for UvrA-mNeonGreen is 135 kDa. **E:** Pagaruler ladder.

2.3 UV damage to DNA

40 μL of 20 ng per μL biotinylated Lambda DNA is deposited on parafilm and DNA damage is applied using a transilluminator (ANALYTIK JENA - CX-2000) which allows UV irradiation at 254 nm (which is within UVC range). 40 J/m^2 is applied to the DNA strands which are then aliquoted and kept frozen at $-20\text{ }^{\circ}\text{C}$. The number of CPD was calculated by applying the formula: $0.0221\text{ CPDs}/\text{kbp}/\text{J}\cdot\text{m}^2$ (198,199). Using this formula, the number of CPDs was estimated to be around 43 per DNA strand.

2.4 Data analysis

2.4.1 Kymographs

A kymograph is a 2D representation of a video. Kymographs were made in ImageJ (FIJI package) by tracing a straight line on the DNA strand. The resulting image shows each pixel along this line on the Y axis, and their progression in time is shown on the X axis. A fluorescent binder will appear as a bright line alongside the X-axis of a kymograph, with the length of the line representing how long the binder stays bound to the DNA.

2.4.2 Trackmate

The Trackmate plugin of the Fiji package of ImageJ was used on videos to extrapolate data for each binder on the DNA. Trackmate allows for the recognition of spots on an image. A few parameters were used to recognize fluorescent binders onto the DNA strand. First, the diameter of the binder was set to be around 400 nm with a quality threshold that varied depending on the background fluorescence of the video treated. Second, a LAP (Linear Assignment Problem) tracker was used, The LAP tracker allows the linking of binders from one frame to the next. The parameters used for the LAP tracker were a linking max distance of 144 nm (the equivalent of two pixels), a gap closing max distance of 144 nm and a gap closing max frame gap of 2. The data extrapolated from Trackmate includes

the coordinates in X and Y of the binders as well as a track ID that allows for the calculation of how long each of those binders stayed on the DNA strand. Coordinates were used to plot a 2D location map of binding events as shown in **Error! Reference source not found.** A line appears that shows the emplacement of the DNA strand. All events seen outside of this line were discarded as noise. Each binding event shorter or equal to 2 frames was also discarded. This allows for the calculation of the On-rate (also called the attachment rate constant or k_a), the Off-rate (also called the detachment rate constant or k_d) and the Dissociation constant (also called K_D).

2.4.3 Calculation of the On-rate

The On-rate is calculated by taking the number of binders per minute. It is expressed as the number of binders per minute per kbp throughout this thesis as shown in Equation 1. However, the rate that we observe " k_{obs} " varies from the theoretical On-rate " k_a "

$$k_{obs} = \frac{n}{t \times l}$$

Equation 1: On-rate calculation. Where n is the number of binders. t is the time during which the binders are observed in minutes. l is the length of the DNA in kbp.

2.4.4 Calculation of the Off-rate

The Off-rate was calculated by first plotting the distribution of binders per time spent on the DNA (example data shown in Figure 18). This fits to an exponential (**Error! Reference source not found.**). Out of this exponential fitting, the detachment rate constant can be extrapolated. The reciprocal of the detachment rate constant gives the lifetime (as shown in Equation 3).

$$f(t) = A \times e^{-k \times t}$$

Equation 2: Exponential fit. Exponential equation. A represents the amplitude of the exponential. k represents the rate of dissociation. t represents time in seconds. This equation is used to determine the detachment rate constant of a protein from the DNA.

$$\text{Dwell time} = \frac{1}{k}$$

Equation 3: Dwell time formula. This equation relates that the dwell time is one over the Off-rate (k) from Equation 2.

2.4.5 Comparison of the affinity of UvrA to the DNA strand calculations

To calculate the affinity of UvrA to the DNA strands, we need to assess the dissociation rate constant. This can be evaluated using Equation 4. However, we only have the value of the observed attachment rate constant k_{obs} . To get a more representative value for our data we incorporated Equation 5 which related the observe attachment rate constant with the attachment rate constant into Equation 4, resulting in Equation 6. Finally, to get the fold increase of the affinity variations, we divided the observed dissociation constant under one condition by the observed dissociation constant under another condition, resulting in a fold increase in affinity Equation 7.

$$K_D = \frac{k_d}{k_a}$$

Equation 4: Dissociation constant formula. Where K_D is the dissociation constant, k_d is the detachment-rate constant and k_a is the attachment rate constant.

$$k_{obs} = k_a \times [UvrA]$$

Equation 5: Relation between k_{obs} and k_a . Where $[UvrA]$ is the concentration of protein, here for UvrA but could be replaced by any protein studied.

$$K_D = \frac{k_d \times [UvrA]}{k_{obs}}$$

Equation 6: Adaptation of the dissociation constant. Where K_D is now the observed dissociation constant.

$$\text{Affinity variation} = \frac{K_{D1}}{K_{D2}}$$

Equation 7: Calculation of the variations in affinity of UvrA to the DNA strand. Where K_{D1} is the observed dissociation constant under one condition, and K_{D2} is the observed dissociation constant under another condition.

2.4.6 Calculation of the distance to the transition state

The On-rate and the Off-rate can be plotted against the forces applied to the DNA. This can be fitted to a Bell-fit (**Error! Reference source not found.**) which in turn allows for extrapolation of the distance to the transition state for the on-rate and the off-rate. The Bell equation is a modified Arrhenius/Eyring equation that allows to study how variations of forces affect a system.

$$k = k_0 \times e^{\frac{-d \times F}{k_B T}}$$

Equation 8: Modified Bell equation. Where k : rate of the reaction. k_0 : rate of the reaction at 0 forces. F : forces applied to the system. d : distance to the transition state. k_B : Boltzmann constant. T : temperature in Kelvin.

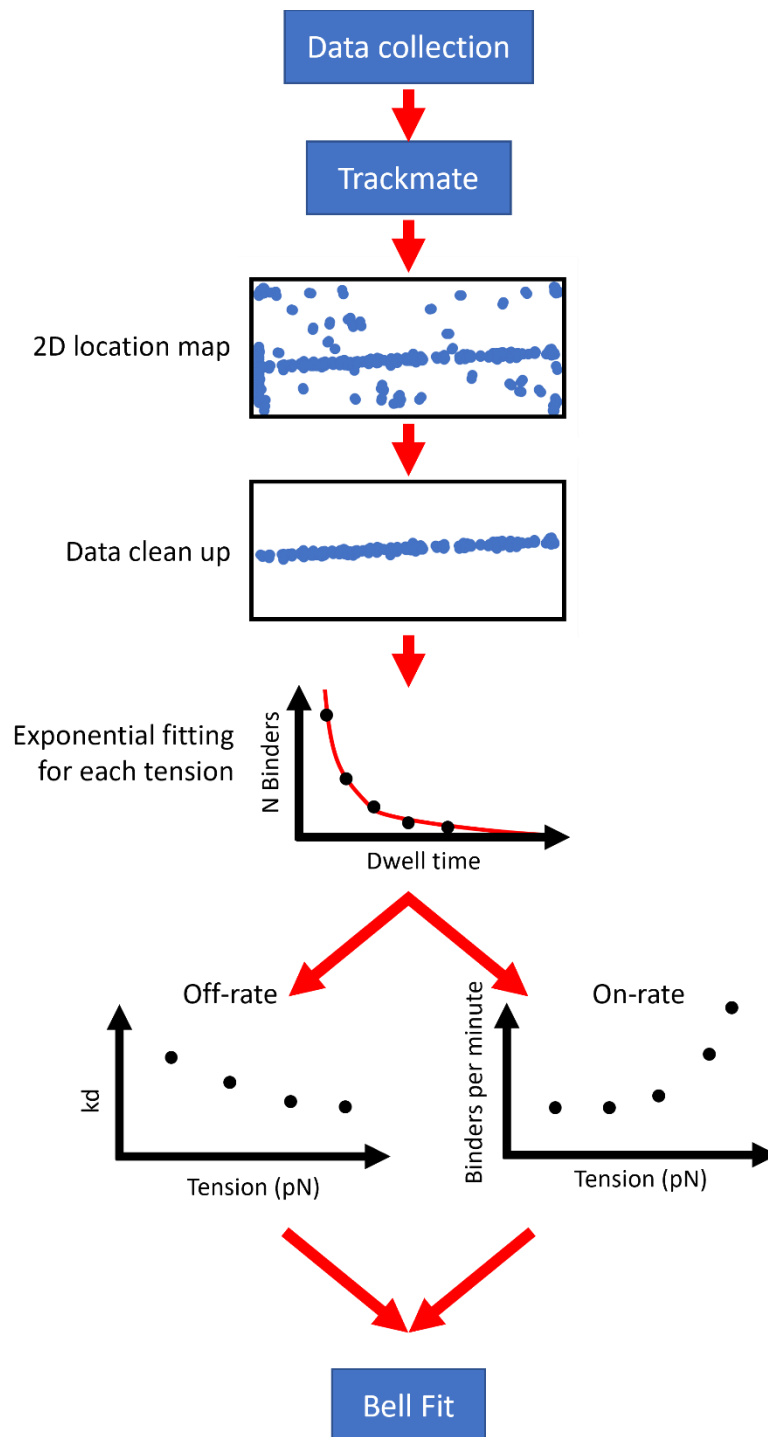


Figure 18: Typical data analysis pathway. Where data is extracted from videos using Trackmate. Such data include the x and y coordinates of each binder within the video, as well as how long each of them stays on the DNA strand. Each binding event can be plotted according to its X and Y coordinate. This is followed up by data cleanup in Excel where every “binder” not located

on the DNA is removed. Then the distribution of dwell times is plotted and fitted to an exponential giving the off-rate. Both the off-rate versus tension and the on-rate (binders per minute) versus tension can now be plotted and fitted to the Bell relationship (200,201). Examples of data and fits are shown in Figure 30 for lifetime extraction exponential fits and Figure 36 for bell fits.

Chapter III: Applying tensile forces to DNA affects prokaryotic NER *in vitro*

3.1 Introduction

3.1.1 The importance of forces within cells

In prokaryotic cells, DNA is subjected to many changes in its structure. Prokaryotic chromosomal DNA is heavily condensed to be able to fit within the volume of a prokaryotic cell. Such condensation is done by supercoiling the DNA (202). To divide, the totality of the DNA is duplicated and the two resulting chromosomes are segregated (203). Interestingly, DNA replication can be continuous in fast replicating bacteria where they begin replicating DNA before the previous replication is complete (204). DNA replication is performed by the replisome which is composed of at least 14 different proteins in *E coli* (205). This induces local changes in the structure of the DNA strand (206). Interestingly, it was shown that the UvrABC system might be involved in the processing of Okazaki fragments during the replication where the UvrABC system replaces DNA Polymerase I's function by acting as a backup system, however no further evidence was brought forward (207). Furthermore, during transcription, the presence of UV damage stalls RNA Polymerase which recruits MFD, a transcription-coupled repair factor. The interaction of RNA Polymerase with MFD induces a 90-degree bend of the DNA strand. In turn, RNA polymerase dissociates and MFD recruits UvrAB directly to the damage site (208). This is interesting because NER can recognize and process a multitude of lesion types and it has been suggested that NER recognizes local differences in the structure of the DNA proximal to the lesion more than the lesion itself (196). Such disturbances can be a change in either the structure or the flexibility of the DNA or both. It is important to note that supercoiling is altered during both transcription and replication which makes DNA a heavily structured and versatile molecule that undergoes numerous structural changes *in vivo* (209,210). How the UvrABC system interacts with those variations in structures is unknown. In this chapter, the structure of DNA strands is altered by applying stretching forces to the strands. The goal is to assess the effect of such structure

modifications on UvrA and UvrB binding and relate those to UV and fluorescein damage recognition.

3.1.2 Binding of proteins to DNA.

In undamaged cells there are around 20, 50 and 20 copies of UvrA, UvrB and UvrC respectively, going up to 200, 500 and 20 copies when the SOS response is triggered (211). However, a recent estimate showed an equal number of UvrA and UvrB proteins in *E. coli* of around 85 copies per cell (13). This was done by replacing the endogenous UvrA or UvrB genes by a functional C-terminal PA-mCherry fusion. In both cases, the quantity of DNA binding protein in the cell is way too low compared to the time each protein dwells on the DNA and the large quantity of DNA that need to be checked in between each division. This cannot be explained only through diffusion. Indeed it has previously been suggested that localisation of damage happens in a two-step manner where the protein binds to unspecific DNA with this first binding facilitating the scanning of other DNA regions, either in proximity from the initial binding through DNA sliding and intradomain hopping, or far, by intersegmental transfer and interdomain hopping (as illustrated in Figure 19) (212–214). Initial protein-to-DNA binding is hypothesised to occur through diffusion and charge-based interactions between DNA phosphate (-) and basic residues of the protein (+). While some damage repair proteins have been shown to scan DNA using a sliding mechanism (215–217), this is not the case for UvrA. A single molecule study showed that UvrA was capable of binding to DNA on its own but did not show any sliding. However, UvrA could jump from one DNA strand to the next going as far as a micrometre (15). Interestingly, it was shown that UvrA dimers were capable of binding to two different DNA molecules at the same time (218). The addition of UvrB to form UvrA₂B₂ complexes doesn't impact UvrA's attachment rate but shows complexes moving following a sliding movement, hinting at UvrB molecules switching the search mechanism to a 1D diffusional search (15). Furthermore, *in vivo* observation of UvrA's 3D diffusion is slower than modelled, hinting at transient interactions with DNA that are shorter than 15 ms

(13). This was confirmed using an *in vitro* assay using iSCAT microscopy with a time resolution of 40 ms that shows two modes of binding with a fast and a slow rate of release (219).

Interestingly, an *in vivo* experiment shows UvrA localised mostly within the nucleoid region, while UvrB doesn't have a localisation preference, making it difficult for UvrA₂B₂ complexes to be formed *in vivo* (13). This is also confirmed by their diffusion distributions being dissimilar *in vivo* (13). It was shown that UvrA can bind to undamaged DNA without UvrB, and UvrB don't associate with DNA in the absence of UvrA, further confirming that UvrB is recruited directly from the solution to the site of damage (13).

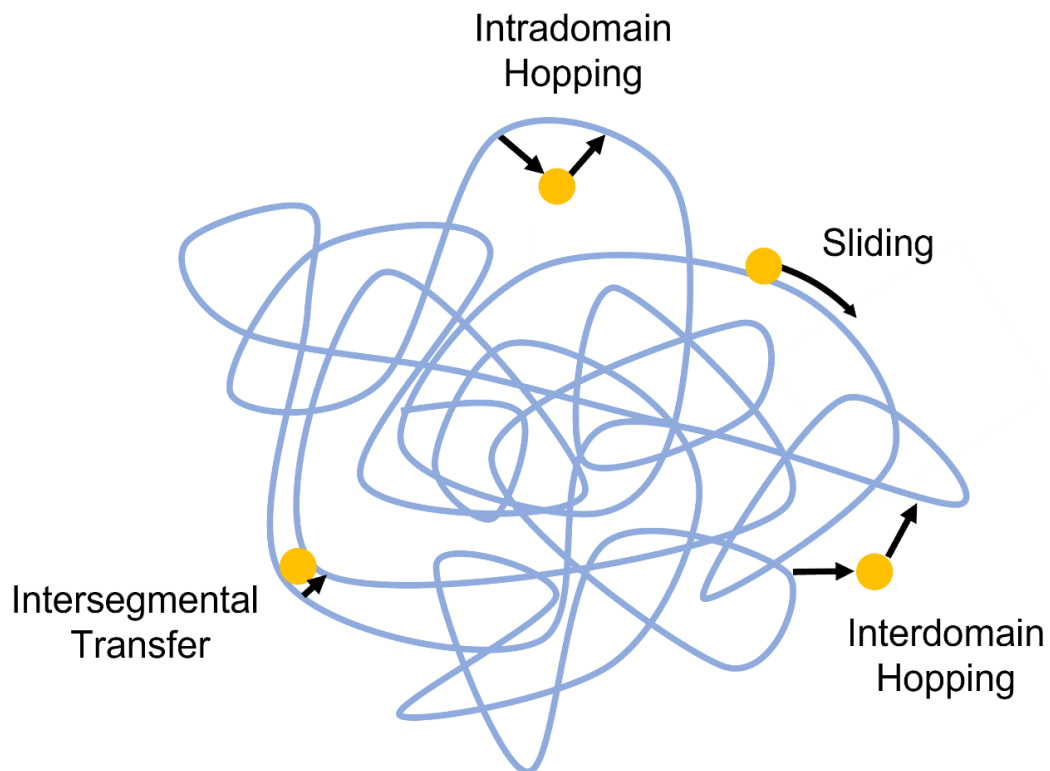


Figure 19: Different modes of DNA scanning by proteins. In blue is represented DNA within a cell. DNA binding proteins are represented in yellow. Arrows represent different modes of DNA scanning. Intersegmental transfer is the ability of the protein to transfer from one segment of DNA to another by simultaneously binding to both. Once DNA strands start to move apart from each other the protein will have a 50% chance of staying on its original segment or moving on to the next. It does require the protein to have several DNA binding domains or to work as a dimer or

more. Sliding is the ability of the protein to stay bound to the DNA strand and move in a one-dimensional manner following a random walk behaviour. Hopping is a quick dissociation of the protein, but the proximity of DNA allows for both intradomain and interdomain quick rebinding. Adapted from (214).

3.1.3 UvrA and UvrB kinetics in single molecule studies.

In vivo, the dwell time of static *E. coli* UvrA-mCherry on DNA is 3 s and 12 s for undamaged and damaged DNA respectively (13). Dwell time of static *E. coli* UvrB-mCherry on DNA is 11.8 s and 15.6 s for undamaged and damaged DNA respectively (13). Discrepancies of UvrA and UvrB dwell times in damaged DNA are consistent with UvrB removing UvrA and staying on the DNA longer to allow recruitment of UvrC (13). UvrA possesses two diffusion profiles where it is either bound to DNA or slowly diffusing (58 %; $0.31 \mu\text{m}^2.\text{s}^{-1}$) while UvrB possesses three diffusion profiles where it is either bound to DNA, slowly diffusing (24 %; $0.41 \mu\text{m}^2.\text{s}^{-1}$), or quickly diffusing (61 %; $1.24 \mu\text{m}^2.\text{s}^{-1}$) (13). Interestingly, the proportion of DNA-bound UvrA goes from 42 % to 75 % upon the addition of UV damage. Similarly, UvrB sees its DNA-bound population go from 15 % to 59 % upon the addition of UV damage, most of it being taken from the quickly diffusing proteins (13). *In vitro* experiments using OAF microscopy show that the lifetime of *E. coli* UvrA-mScarlet is 0.81 s and 2.43 s in the presence of undamaged and UV-damaged DNA respectively (48). *B. caldotenax* shows even longer lifetimes with a lifetime of 7 s for UvrA and 40 s for UvrAB (15). UvrA has also been shown to hop between close-by DNA strands, therefore performing a 3D search (15,48). However, despite all those lifetimes showing discrepancies, it is clear that UvrA is not capable of scanning the whole genome of *E. coli* in between each cell division (15). Interestingly, *in vitro* experiments with an iSCAT microscope have shown *E. coli* UvrA (labelled with a Qdot) binding to DNA with either a fast lifetime of 0.13 s or a slow lifetime of 0.7 s in undamaged DNA and 0.128 s and 0.77 s for damaged DNA when using fluorescein as damage (219). Fast lifetimes were predominant as they represented 90 % of binding events when using undamaged DNA and 78 % of binding events when using damaged DNA. Those fast lifetimes were observed for

the first time due to the very fast frame rate of the iSCAT technology and they render the scanning of the totality of *E. coli* genome every cell division mathematically possible (15,219,220).

3.1.4 Importance of single-molecule studies

Non-single-molecule studies have many purposes. However, their results are representative only if the population studied is homogeneous. However, individual protein might have different behaviours when observed individually. Heterogeneity of a population can come in two different ways. It can be a static heterogeneity, which relates to persistent differences in properties and behaviours of individual proteins within a population. Or it can be a dynamic heterogeneity, which relates to a variability in the properties and behaviours of individual proteins within a population over time. Bulk methods cannot detect those variations as they are averaged across the population (221). In this thesis, we use optical trapping to capture DNA strands and apply load to them. Other force-based approaches could have been used. The most common ones are magnetic trapping and atomic force microscopy. All have pros and cons and they all could have been used to answer some of our questions. The most convenient ones to answer our question was either optical trapping or magnetic trapping. They are both non-invasive technologies that would have allowed to capture DNA strands and apply forces to it. Optical trapping comes with a big disadvantage which is that it adds heat to the system. However, that heat is located where the lasers are but have little impact on the rest of the DNA strand (we used DNA strands that are around 17 μm long). One advantage of optical trapping over magnetic trapping is that it does have very good spatial resolution. Atomic force microscopy have been used extensively to study NER (222,223). However, it does have a very slow imaging speed. In this thesis we are looking at interactions that occurs at the sub-second speed (it was shown that UvrA can have a fast dwell time of around 140 ms (219)).

3.1.5 Project aim

NER can repair a wide variety of DNA lesions. However, NER only has one protein, UvrA, that is in charge of responding to damage. How one protein alone can recognize a plethora of lesions is puzzling. It has been suggested that UvrA was recognizing local disturbances on the DNA rather than the damages per se (196). This chapter aims to assess the effect of structural changes of the DNA strand on the binding of UvrA and UvrB and relating those to UV and fluorescein damage recognition. To do so, the binding profiles of UvrA and UvrB will be assessed while applying various loads to the DNA strand. In parallel, some DNA strands will be damaged by being irradiated by UVs or by incorporating fluorescein which act both as a localisation marker and as a DNA lesion recognized by NER. By comparing both the DNA binding behaviour of NER protein in presence of damaged and stretched DNA we will be able to assess how changes of DNA structure relate to damage.

3.2 Material and methods

3.2.1 The C-Trap system.

The bulk of this thesis was performed on a Widefield C-Trap® Optical Tweezers manufactured by Lumicks (Netherlands). This system is equipped with four optical traps with a force resolution of 0.1 pN and a distance resolution of 0.3 nm at 50 Hz. The optical traps are generated by a 1064 nm laser and allow for the trapping of small beads, as illustrated in Figure 20B (224). The microscope is equipped with a μ -flux system (in green in Figure 20A) which allows regulation of the flow within a chamber containing six channels (Figure 20D). This flow cell chamber contains 5 input channels and 1 output channel. Each input channel can be provided with a different buffer or sample. Typically channel one, two and three will contain beads, DNA, and buffer respectively while channel four and five will contain protein. Laminar flow ensures the different buffers or samples do not mix when the flow is turned on as illustrated by the different colours in Figure 20D. The C-Trap is equipped with multiple modes of image acquisition (widefield, fluorescence, total internal reflectance microscopy). For this thesis, the fluorescence camera was used extensively for image acquisition. This is facilitated by the C-Trap being equipped with three lasers with wavelengths of 488 nm, 532 nm, and 635 nm which allows for the imaging of several fluorescent proteins at the same time.

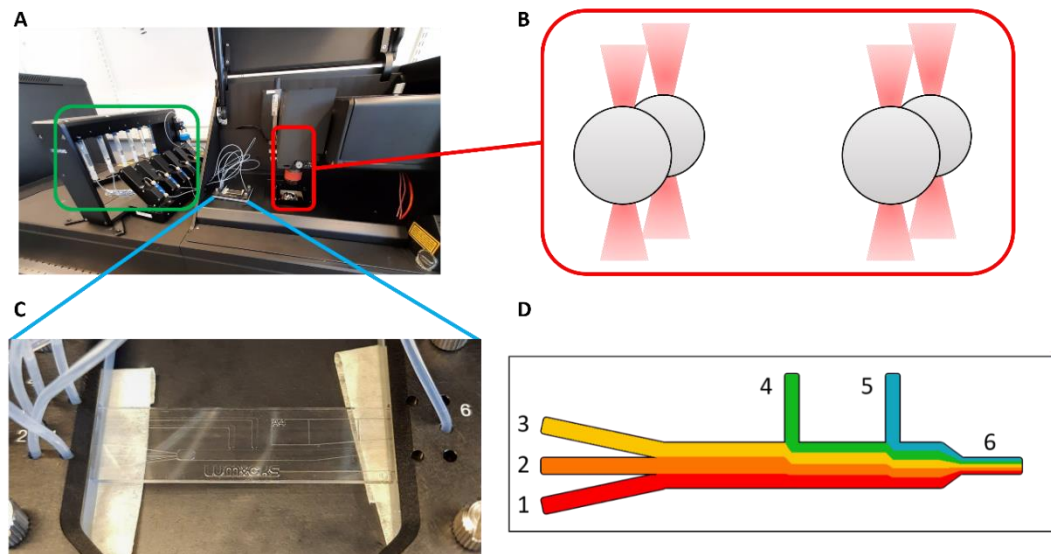


Figure 20: The C-Trap system **A:** Picture of the working station of the C-Trap. In red is presented the objective and the condenser that allows for imaging, optical trapping, and force measurement (in green is the u-Flux™ microfluidics system where different buffers/samples can be added to different syringes.). **B:** Illustration of four beads that have been captured by the four optical traps installed in the C-Trap. **C:** Close-up of the microfluidic cell chamber where the different input channels allow the creation of a **D:** laminar flow where the components of those different channels don't mix when the flow is on. Channels numbers are annotated.

3.2.2 Optical traps

Optical trapping, also called laser tweezers, is a technology that allows for the capture of small particles within the focus of a laser. An optical trap is obtained by focusing a gradient laser with an objective lens of high numerical aperture (224,225), producing an hourglass shape as represented in Figure 20B and Figure 21. As a result, the photon density will increase closer to the centre of the hourglass shape. This allows for the capture (or trapping) of dielectric particles. Dielectric particles are particles that do not allow the flow of electrical currents (insulators). It was shown very early on that optical traps were able to capture small particles from individual atoms to 10 μm polystyrene latex spheres, to bacteria or yeast cells, to organelles within a living protozoan (224,226–228). In this thesis, we capture exclusively polystyrene beads. A bead near the focus of the laser beam experiences two forces. First, photons hitting the bead are refracted

and reflected at the surface of the bead. This corresponds to a shift of momentum of photons. Newton's third law states that for every action, there is an equal and opposite reaction. As such, this shift of momentum of photons on the beads induces an equal and opposite momentum applied to the bead. This is the scattering force applied to the bead. Figure 21A illustrates the scattering forces applied to the bead when the bead is positioned in the center of the laser beam, where "A" are the incident rays and " F_A " are the resulting forces from the two optical paths drawn. Those forces are proportional to the light intensity. Since the photon density is higher in the centre part of the hourglass shape of the laser tweezers, a higher density of photons will hit the part of the bead that is closer to the centre of the trap (as represented in Figure 21B, which focuses on the effect of the gradient of photons present within the laser beam). As such, there is an offset in the amount of forces applied to the bead, leading to a net momentum acting on the bead that pushes the bead towards the denser part of the gradient, here toward the centre of the trap as represented by the green arrow in Figure 21B. This is the second force applied to the bead, called the gradient force. Altogether, the scattering force and the gradient force can efficiently trap beads (224).

The force and the displacement are measured by assessing how much the trapping laser is deflected by the bead. This is assessed by using a position sensitive detector that detects changes in scattered light intensity. The position sensitive detector converts the position of the particle into an electrical signal. The resulting voltage depends on the Brownian motion of the bead within the trap, as well as the response of the position sensitive detector to the incident light (229). Since the light beam has a gaussian profile, the optical trap functions as a spring. This means that the forces can be easily calculated following Equation 9 where the force depends on both the trap stiffness and the bead displacement.

The trap stiffness is calculated from the power spectrum (Figure 22). On this power spectrum is plotted the power spectral density P (V^2/Hz) over the frequency (Hz).

It is possible to fit the power spectrum to a Lorentzian model which allows to determine the corner frequency (frequency at which the power spectrum drops off), which in turn provides information on the trap stiffness(229).

$$F = K \times \Delta x$$

Equation 9: Force calculation. With F : Forces applied to the bead. K : trap stiffness. Δx : bead displacement.

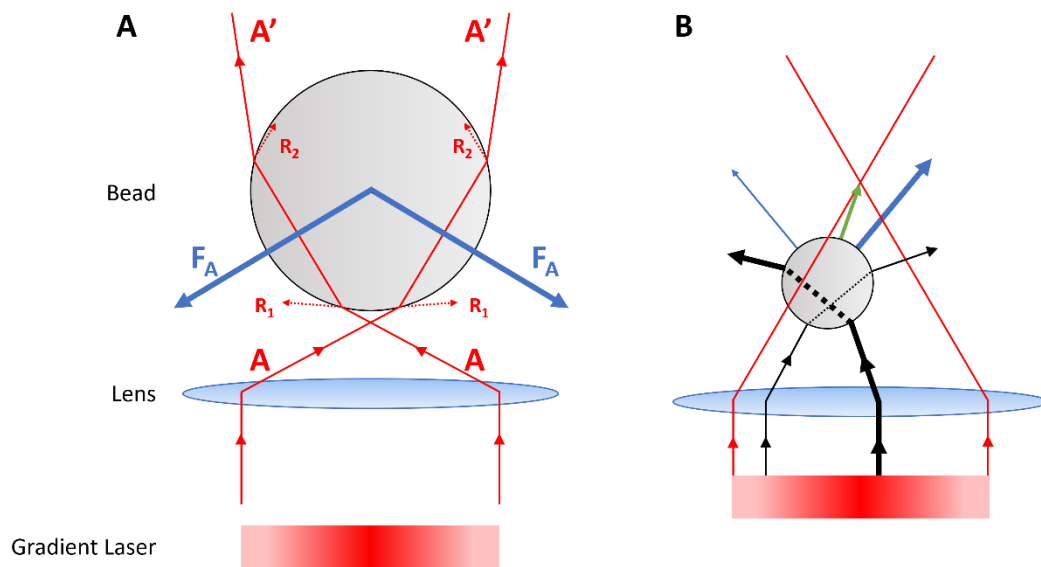


Figure 21: Schematics of an optical trap. **A:** When a gradient laser is focused with a high numerical aperture lens, it creates an optical trap that applies forces to dielectric particles. Here is represented a bead that is subjected to those forces. “A” represents the incoming rays. “A’” represents the refraction of the ray “A” through the bead. “R1” and “R2” represent the reflection of the ray “A” at the two points of contact with the bead. The refracted (mostly) and reflected (less so) rays are responsible for the momentum transfer from photons to the bead. This causes the bead to be pushed towards the beam propagation. A gradient force is also applied, which pushes the bead in the direction of the field gradient. With the intensity of the laser gradient being the greatest at the centre of the hourglass shape, the bead is pushed towards it. “ F_A ” represents the resulting forces of the combinations of both the scattering and the gradient forces. This is highlighted in **B:** where the bead is slightly offset from the centre of the laser beam. As a result, a higher density of photons hit the bead on the side closer to the centre of the laser beam. As the scattering force is proportional to the optical intensity (224), there is an offset of the momentum transfer, pushing the

beads toward its centre. This offset is represented here by the difference in size between the arrows representing the rays of light. In black are represented the incident rays of light and refractions. In blue are represented the resulting forces. In green is represented the net momentum acting on the bead. In red is represented the hourglass shape of the optical trap (Inspired by (224,230)).

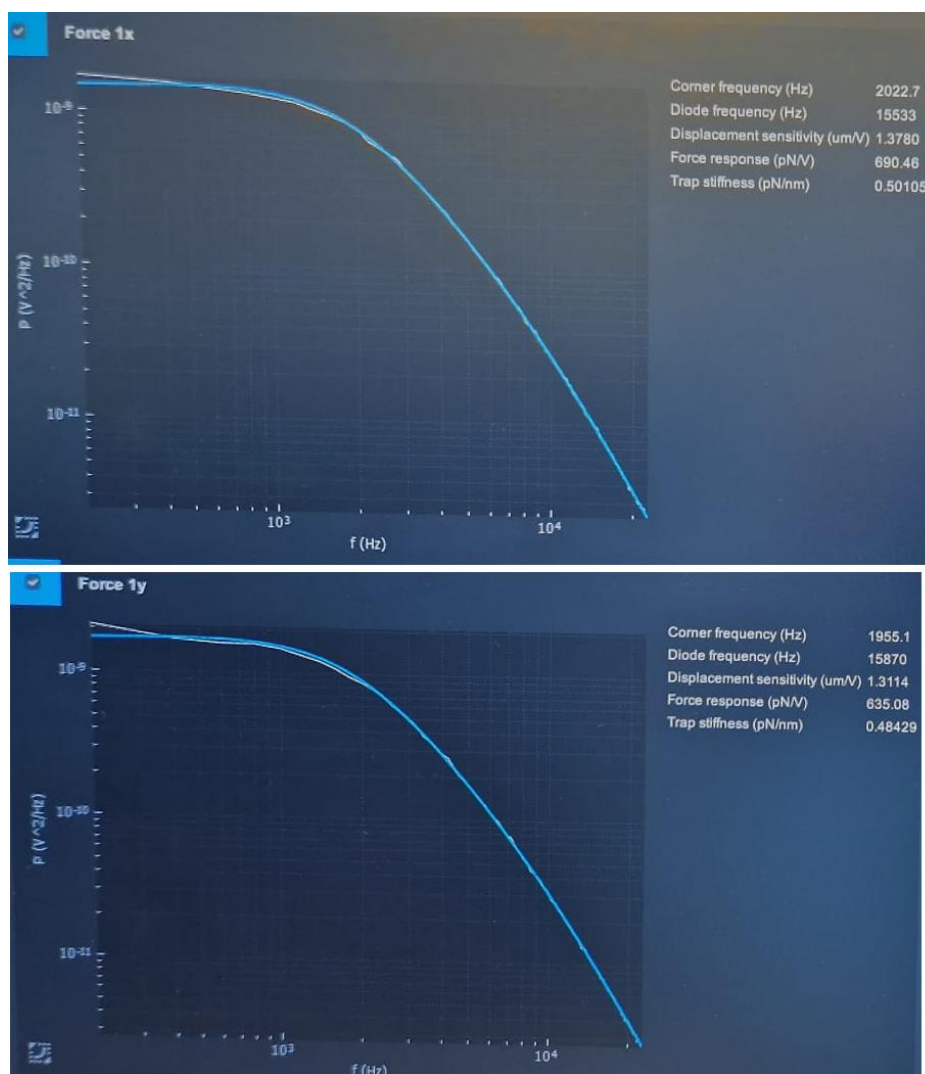


Figure 22: Example of calibration curve. This is the calibrations curves in the X and Y axis of a 4.7 μm bead.

3.2.3 Laser tweezers allow for the tethering of DNA strands.

Laser tweezers have been used extensively to study many molecular mechanisms. A few examples would be the folding and unfolding of proteins, DNA or RNA structures, the self-folding forces that nascent protein chains exert while exiting the exit tunnel of ribosomes, how protein stops stalling of RNA polymerase, the

accurate step size of molecular motor or even the stretching of chromatin (231–236). In this thesis, laser tweezers have been used to capture and stretch DNA strands. The DNA used originated from the *E. coli* bacteriophage lambda and is a linear double-stranded DNA strand of 48,502 base pairs. 4.8 μm streptavidin-coated polystyrene beads are captured then DNA is tethered in between those beads by moving the captured beads to a channel containing biotinylated Lambda DNA under flow. Thanks to the strong interaction between biotin and streptavidin, the DNA is bound to the beads as illustrated in Figure 23.

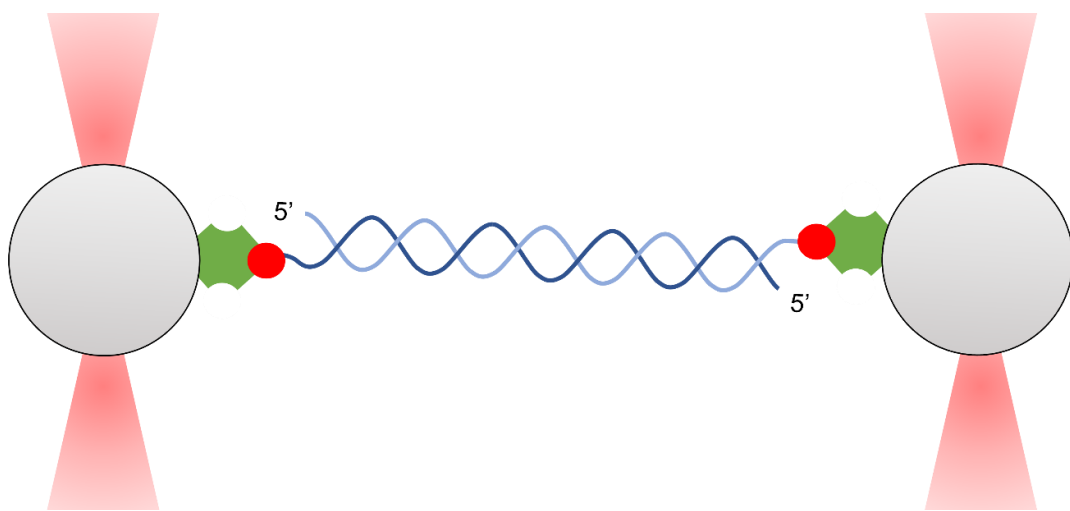


Figure 23: Schematic of a strand of biotinylated DNA tethered to streptavidin beads, captured by optical traps. 3' Biotinylated Lambda (in dark and light blue, red circle represents biotin) is bound to streptavidin-coated beads (in grey, green shape represents streptavidin). Each bead is captured within an optical trap (red gradient) resulting in a single double helix DNA strand tethered in between two beads.

Increasing the distance between the beads increases the forces applied to the DNA. When a DNA strand is stretched, it follows a worm like chain model (WLC), this means that if the DNA has to bend, it will spread the bending over large distances in opposition to bending sharply at a smaller number of locations (237,238). But as DNA reaches around 65 pN of tension, it will start to overstretch and deviate from the WLC model where very little increases in forces are required to increase DNA length (Figure 24). It overstretches and follows the worm like chain model for single-stranded DNA. This overstretching could be due to two

events. A torque motion within the dsDNA unfolds the two strands resulting in the formation of S-form DNA or the two strands of the DNA are directly disconnected from each other, resulting in an increasing portion of the DNA being single-stranded (239–241).

The WLC model is a model that encapsulate both the entropic and the enthalpic characteristics of many system and can be applied to double-stranded DNA. It considers the persistence length of the DNA (length at which, if bellow it, the DNA act like a rod, and if above it, the DNA behave like a three-dimensional random walk) and the contour length (total length of the DNA molecule). The DNA has a conformational entropy which is the entropy associated with the different conformations the DNA can adopt. If you pull the DNA into an extended chain, you would slowly diminish the number of possible conformations with a final unique possibility at maximum extension (237). The DNA is also subject to thermal fluctuations which contribute to its entropy. The DNA has enthalpic properties (measure of the total energy in a system) like the bending energy, which is the energy required to bend the DNA, as well as the elastic deformation, which is the property of the DNA to absorb energy when a force is applied resulting in a change in its shape. When the force is removed, the DNA returns to its original shape, hence the use of the word “elastic”. An extended WLC model exist that more accurately represents the behaviour of DNA, especially at high tension. This model incorporate the stretch modulus, which is the intrinsic stretch elasticity of the DNA backbone, as well as force dependant stretching to account for the fact that under heavy load, DNA stops behaving as a bendable rod and starts behaving as an extensible one (239).

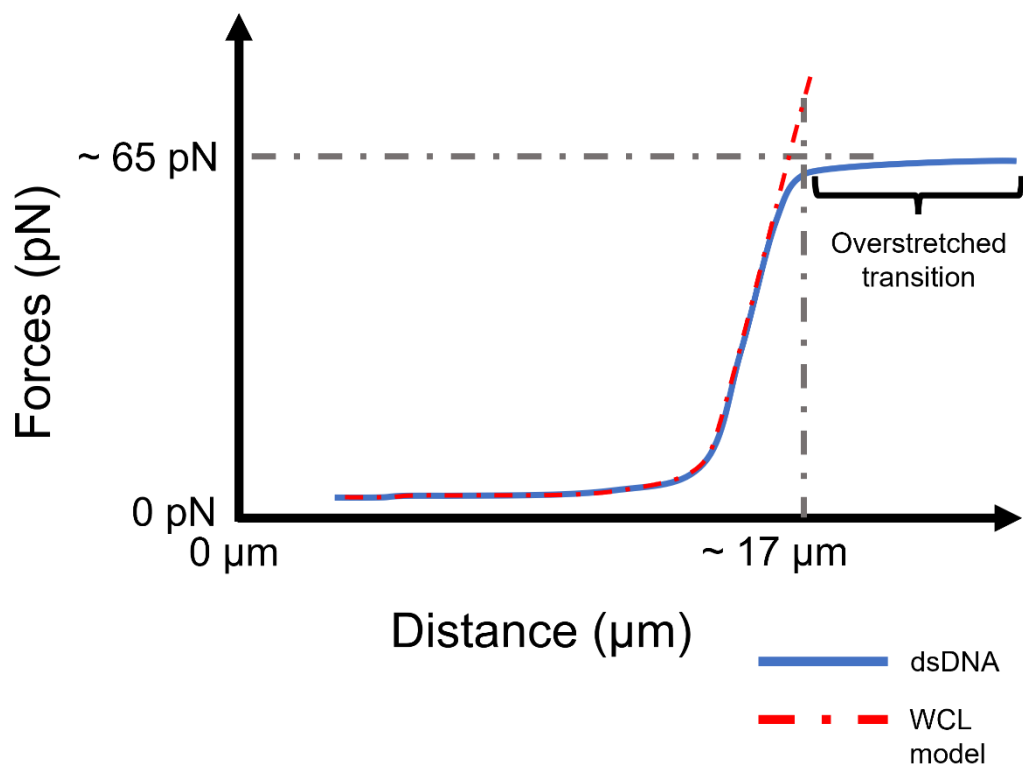


Figure 24: Representation of a Force Distance (FD) curve for dsDNA. When forces are applied to dsDNA, the DNA strand will at first follow a worm like chain model (represented in red dots here) where no forces will be required to increase the length of the dsDNA until it reaches its contour length. Then the forces required to increase the length of the dsDNA will increase until it reaches ~65 pN where the dsDNA will start to overstretch until forming S-form DNA or single-stranded DNA.

In this thesis, stretching of the DNA is used extensively. This implies that in some experiments the forces applied to the DNA vary. How variations of forces affect a system can be studied through a modified Arrhenius/Eyring equation also called the Bell equation shown in **Error! Reference source not found.** (201,242):

From this equation can be extrapolated the distance to the transition state. What the distance to the transition state means varies depending on the system studied and the rate used. In our case, the distance to the transition state is the distance required to observe a difference in either the on rate or the off rate of the protein binding to the DNA. In other words, how much the DNA must be stretched to facilitate or impede protein/DNA interaction, respectively. The free energy

landscape of UvrA binding with DNA can be represented in a simplistic way as shown in Figure 25 where collisional binding occurs resulting in UvrA-ATP molecules binding to the DNA (On-rate). This is followed by hydrolysis of ATP which helps UvrA to release from the DNA (Off-rate) (48). Unbinding of UvrA-ADP from the DNA is very quick and therefore not rate-limiting. Both the on-rate and the off-rate require different energies to reach the transition state.

If by applying different conditions to our system there is a reduction or an increase in the distance to the transition state for the on-rate, it means that the transition barrier to binding is altered, which means that there has been a change in the amount of energy required for the protein to cross upon binding to DNA. The same goes for a reduction or an increase in the distance to the transition state for the off-rate.

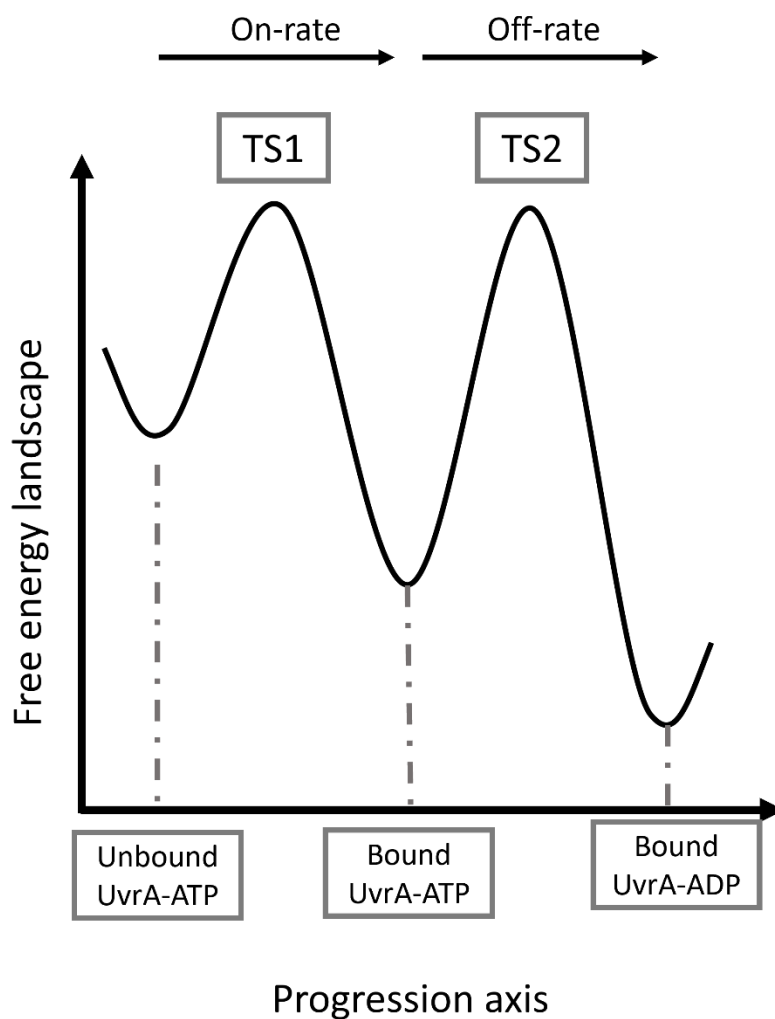


Figure 25: Simplified free energy landscape of UvrA binding to DNA. The binding of UvrA to DNA is a complex phenomenon. Its free energy landscape can be approximated as presented here in black where collisional binding occurs resulting in UvrA-ATP molecules binding to the DNA (On-rate). This is followed by hydrolysis of ATP which helps UvrA to release from the DNA (Off-rate) (48). Unbinding of UvrA-ADP from the DNA is very quick and therefore not rate-limiting. TS1 and TS2 are the two transition states that divide the free energy landscape. 3.2.4 Medial and lateral flow affects the DNA strand.

Throughout this thesis, flow is used sometimes to impact the binding of proteins. The different possibilities are shown in Figure 26 where at low tension and in the absence of flow the DNA strands stay straight in between the beads. However, when a flow is applied at an angle of 90° with the DNA, this will induce the DNA to adopt a curved confirmation as shown in Figure 26B. This curvature is not visible anymore as the tension increases (Figure 26C). This kind of flow angle will be subsequently called “Medial flow”. However, when a flow is applied in the same direction as the DNA strand, there aren’t any changes in the DNA strand curvature (Figure 26D). This will be referred to as “Lateral flow” for the rest of this thesis.

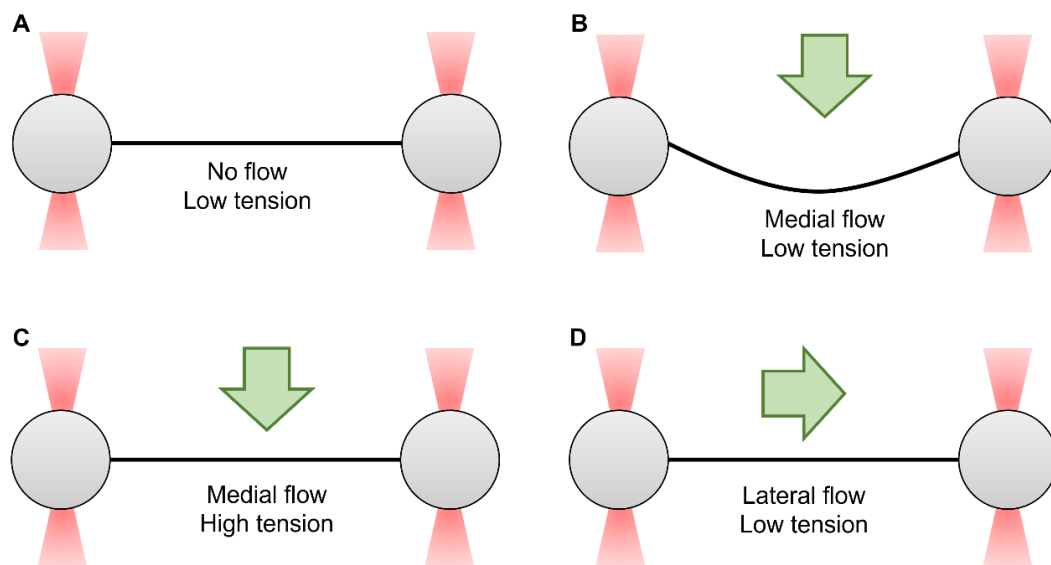


Figure 26: Difference between Lateral and Medial flow. *A: When no flow is applied to low-tension DNA strands, the DNA is straightened in between the beads that have captured it. B: However, when medial flow is applied, it induces the DNA strand to curve in the sense of the flow. C: The DNA strands appear straight again once higher tensions are applied. D: When lateral flow is applied, there are no differences in the DNA strand appearances.*

3.2.5 Widefield, Total Internal Reflection Fluorescence, and Oblique Angle Fluorescence microscopy

The C-Trap system can switch from Widefield epi-fluorescence mode to Total Internal Reflectance Fluorescence (TIRF), which allows for illumination only in the evanescent field (Figure 27). Widefield is ideal for imaging anywhere in the flow

cell height-wise, but it comes at the cost of increased background fluorescence where all the fluorescent proteins within the flow cell will be excited and participate, despite being out of focus, in the information received by the camera. This will dim the signal and can in extreme cases lead to loss of signal. This can be measure as the signal to noise ratio. Several factors participate in the signal to noise ratio. Those includes the intensity of the fluorescent signal emitted by our fluorescent protein, intrinsic noise from the detector, scattering light, illumination intensity, and exposure time. Raman scattering happens when a photon is scattered by a water molecule and gain or lose energy corresponding to the vibrational energy levels of the water molecule. This can participate in the background noise by producing a range of non-fluorescent wavelengths that overlap with the emission spectrum of the fluorophore. Altogether, reducing the illumination volume (laser power and exposure time) usually results in a slight reduction of the signal fluorescence while it also results in a great reduction of the background fluorescence. This often leads to an increase of the signal to noise ratio.

A built-in alternative to widefield is TIRF. This requires having the laser go at a specific angle which is reflected back through the objective. This will create an evanescent field at the surface of the flow cell which allows for excitation only at proximity to the surface (less than 100 nm). The Snell law (Equation 10) states the relationship between the angles of incidence and refraction when a light beam goes from one medium to another. When θ_2 is 90° , we call it the critical angle (Equation 11). When the angle of incidence exceeds the critical angle, total internal reflection occurs, which means that all light is reflected back into the objective, as represented in Figure 27. This creates the evanescent field which has a penetration depth within the second media which depends on the angle of

incidence the wavelength of the light in the first medium and the refractive indices
(Error! Reference source not found.Equation 12)(243).

$$n_1 \times \sin \theta_1 = n_2 \times \sin \theta_2$$

Equation 10: Snell's law. Where n_1 represents the refractive indice of the first media. n_2 represents the refractive indice of the the second media. ϑ_1 is the angle of incidence. ϑ_2 is the angle of refraction.

$$\theta_c = \sin^{-1} \left(\frac{n_2}{n_1} \right)$$

Equation 11: Critical angle. ϑ_c represents the critical angle which is the angle of incidence at which the angle of refraction ϑ_2 is equal to 90° .

$$d_p = \frac{\lambda}{4\pi \times \sqrt{n_1^2 \times \sin^2 \theta_1 - n_2^2}}$$

Equation 12: Evanescence depth (d_p) formula. Where λ is the wavelength of the light.

This is ideal for surface assays and prevents most of the background fluorescence. However, the beads used in this thesis are $4.8 \mu\text{m}$ in diameter, meaning that captured DNA can only be as close as $2.4 \mu\text{m}$ from the surface, far from the 100 nm range of the evanescence field. By tweaking the angle of the mirror that allows it to go from Widefield to TIRF, the system was put in Oblique Angle Fluorescence (OAF). This allows for the illumination of a partial portion of the flow cell, which is sufficient for imaging the DNA strand, but also greatly reduces background

fluorescence. The work presented in this thesis exclusively uses the microscope in the OAF configuration.

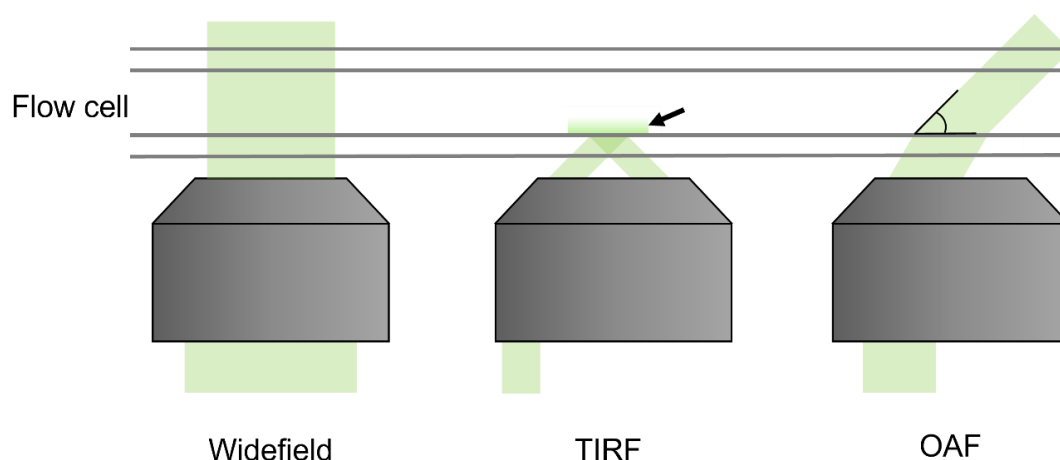


Figure 27: Difference between Widefield, TIRF and OAF microscopy. Images can be acquired through different optical paths by changing the angles of mirrors within the system. Represented here are the different optical pathways leading to different laser exposures. Widefield corresponds to a straight vertical path that goes through the entire flow cell. This leads to a lot of background fluorescence. If the laser comes in with a TIRF angle, it will lead to reflection of the laser ray but will create an evanescent field at the surface with a height of less than 100 nm (Black arrow). This is optimal for surface assay and greatly reduces background fluorescence. Finally, if you tune your optical path to be in OAF, only parts of the flow cell will be illuminated, leading to reduced background fluorescence. The work presented throughout this thesis used the OAF configuration of the optical path.

3.2.6 Lysate preparation

Lysate was prepared as described in chapter II. 3.2.7 Protein purification

Proteins were purified as described in Chapter II.

3.2.8 UV damage to DNA

DNA was damaged as described in Chapter II.

3.2.9 Nick translation

Nicking was performed on 1 µg of biotinylated Lambda DNA with 20 units of NtBspQI nicking enzyme. This was done in a total volume of 60 µL containing 6 µL of 10x NEB 3.1 buffer. The reaction was incubated at 37 °C for one hour. The enzyme was then inactivated at 80 °C for 20 minutes; then the reaction was gradually cooled to 4 °C. After cooling down, 0.8 µg of freshly nicked Lambda DNA was mixed with 40 µM of each dNTP at the exception of dTTP which was replaced with Fluorescein-12-dUTP (thermoscientific R0101), 10 units of DNA Polymerase I (thermoscientific EP0041), 10X Pol I reaction buffer up to a final volume of 60 µL. The reaction was incubated for 12 minutes at 37 °C. 25 µL of the reaction mix was supplemented with 8 mM ATP and 10 units of T4 DNA ligase in NEB buffer 2.1 overnight at 16 °C. This resulted in the incorporation of fluorescein to the DNA strand as shown in Figure 28.

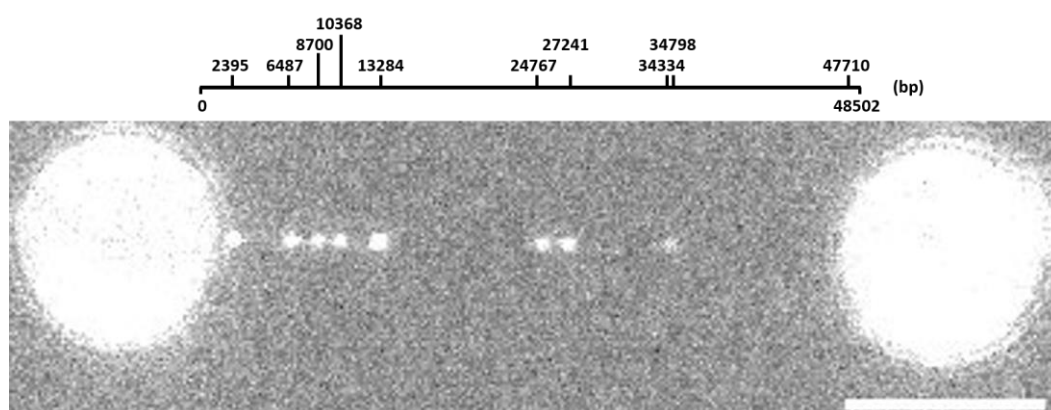


Figure 28: Nt.BspQI nick translation result and corresponding Lambda map. On the top is the map of Lambda's expected nick locations. On the bottom, each dot is fluorescein-dUTPs which have been incorporated through nick translation. Different quantity of dUTP is present resulting in different fluorescence intensity. (Scale bar: 5 µm)

3.2.10 General Data analysis

General Data analysis was performed as described in Chapter II.

3.3 Results

3.3.1 UvrA-mNeonGreen binds to tethered DNA

Biotinylated Lambda DNA was tethered to streptavidin-coated beads as previously described. Then the DNA strand was moved to a channel containing 5 nM UvrA-mNeonGreen (lysate) in solution within ABC buffer (50 mM Tris pH 7.5, 50 mM KCl, 10 mM MgCl₂) supplemented with 1 mM of ATP and 1 mM DTT. It is important to note that fusion proteins of NER proteins with fluorescent tags have been shown to not affect the function of the NER proteins both *in-vivo* and *in-vitro* (13,48,198). The 488 nm laser was turned ON at 30 % power while a video was recorded (exposure time: 200 ms with exposure synchronisation, framerate: 4.42 Hz) with great signal to noise. One frame of this video is shown in Figure 30A where bright spots are single binders of UvrA-mNeonGreen. The same video is represented as a kymograph in Figure 30B, highlighting that the proteins stay on DNA for a varied amount of time each.

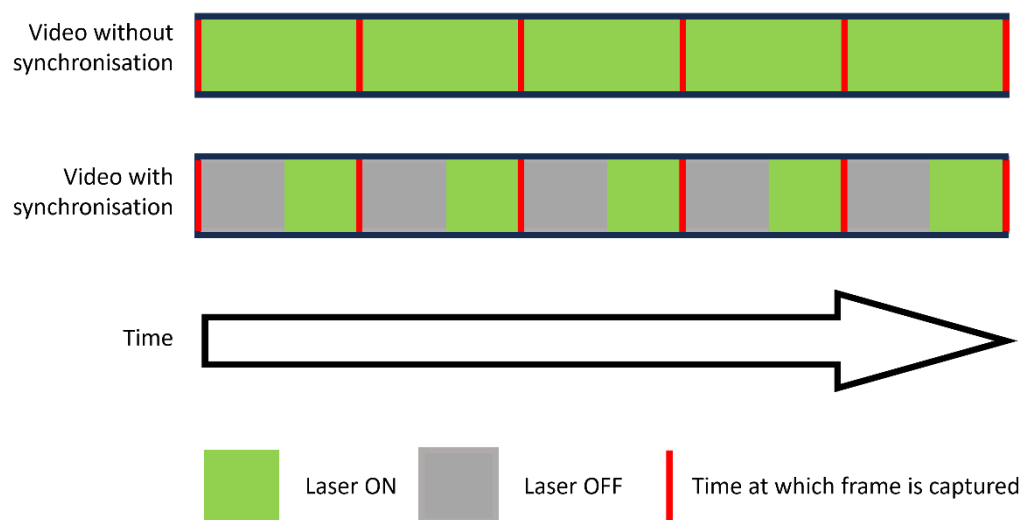
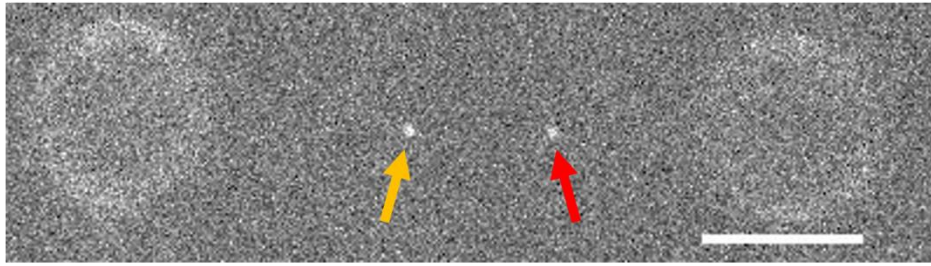
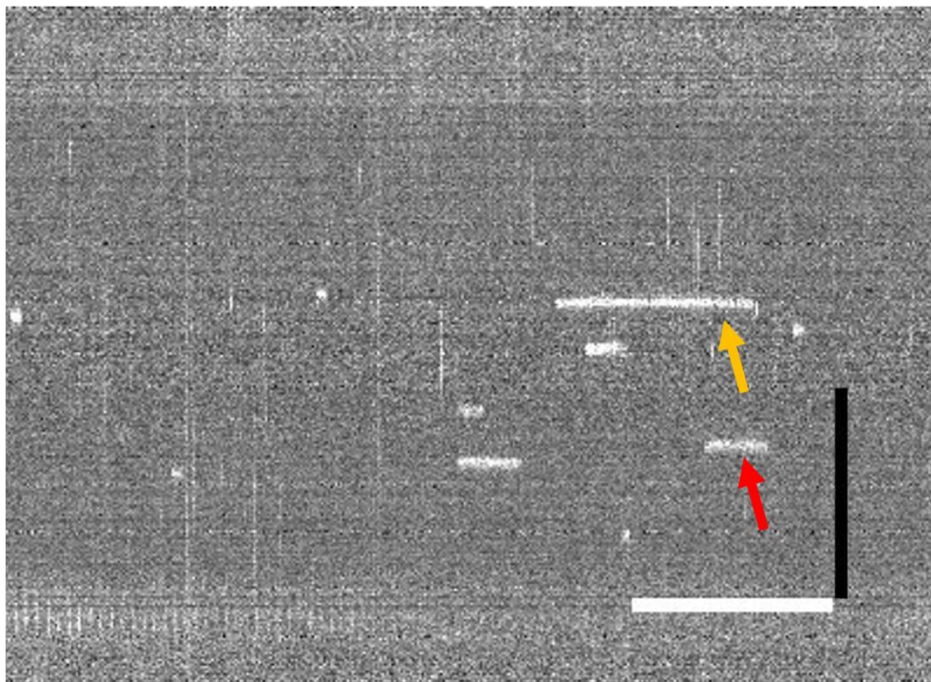


Figure 29: Exposure synchronisation: Allows to reduce the amount of light that hits a sample before capturing a frame. In red is represented the time at which the frame is captured. In green is the time during which the sample is under light exposure. If we turn on the exposure synchronisation, the sample will be exposed to light for a shorter amount of time before the frame is captured.

A**B**

Time

Figure 30: UvrA-mNeonGreen binds to tethered DNA. **A:** Picture extracted from a video where a tethered DNA strand was moved to a channel containing a final concentration of 5 nM of UvrA-mNeonGreen after the lysate was diluted with ABC buffer. Red and yellow arrows point to single UvrA-mNeonGreen binders (white scale bar = 5 μm). **B:** kymograph of the video shown in A where the same UvrA-mNeonGreen molecules are shown (red and yellow arrows) while evolving with time (White scale bar = 20 seconds; black scale bar = 5 μm). Beads are visible on the top and bottom of the image as a slightly lighter band.

3.3.2 UvrA binding is influenced by the flow

Now that it was shown that UvrA-mNeonGreen was capable of binding to the DNA strand, a few technical checks had to be done. First, it was necessary to check the effect of the flow to the binding of the protein to the DNA. This was needed as the system allows for imaging either with the flow turned on or turned off. A helpful finding was that the flow affects greatly the propensity of UvrA-mNeonGreen proteins bound to the DNA strand. To demonstrate that, DNA strands were tethered as previously described and put under 35 pN of tension with or without 0.1 Pa of lateral flow. The DNA strand was within a channel containing 5 nM of UvrA-mNeonGreen (originated from lysate) in ABC buffer supplemented with 100 mM DTT, 1 mM ATP and protease inhibitor to a final concentration of 0.07 mg per mL. Videos were recorded (100 ms exposure, 2 Hz) with 488 nm laser exposure (30% laser power). Lifetimes and attachment rate constants were calculated as previously described. As a result of the change of flow conditions, the number of binders per minute increases from 0.66 ± 0.18 binders per minute per kbp to 1.86 ± 0.44 binders per minute per kbp when using 0.1 Pa of lateral flow when compared to a strand observed under no flow, resulting in an increase of 2.8-fold (Figure 31F) (P-value: 0.02). While the lifetime goes from 2.40 ± 0.11 s to 2.76 ± 0.10 s (Figure 31E) (P-value: 0.004). As a result, there is a 3.5-fold increase of the affinity of UvrA to the DNA in presence of flow. (P-value: 0.11). Altogether this strongly suggests that the binding of UvrA-mNeonGreen is strongly affected by the addition of flow. However, the difference in binding behaviours is mostly seen for the attachment rate constant. A potential explanation is that underflow there are some movements of the DNA, making it more likely to get into contact with passing by UvrA. At the same time, UvrA movement is no longer limited by its diffusion constant, but is increased by the speed of the current within the flow. These were not investigated further and most experiments were carried out without flow. However, in some cases there was a need to increase the decoration of UvrA on the DNA strand. In those cases, flow was used.

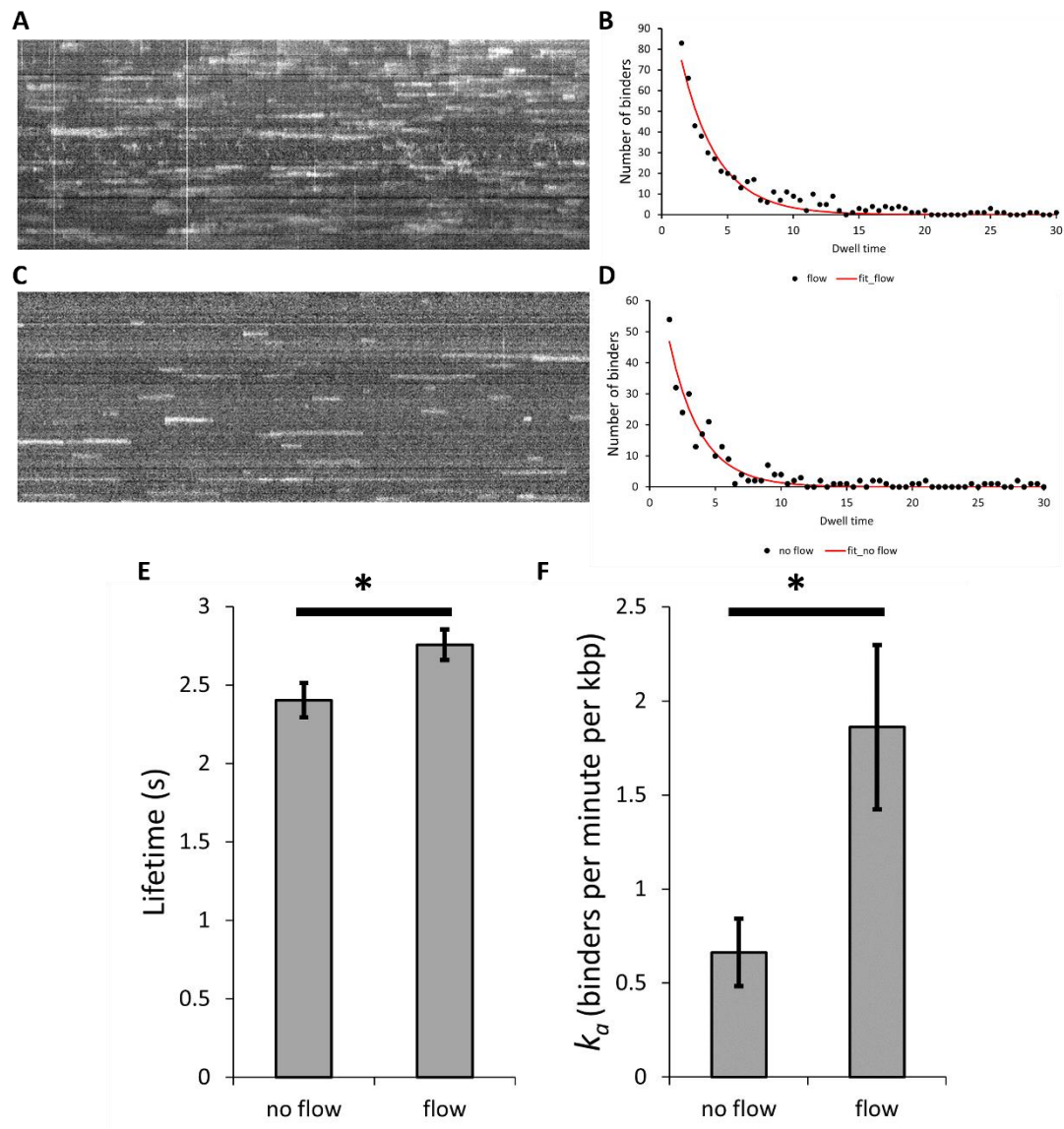


Figure 31: The presence of 0.1 Pa of flow greatly increases the binding of UvrA to the DNA strand. **A:** When strands that were under 35 pN of tension were put under 0.1 Pa of lateral flow, UvrA-mNeonGreen shows a high decoration of the DNA strand as seen in this kymograph. **B:** Gathering the dwell time of all binders onto the DNA allows for the plotting of the distribution of the number of binders per dwell time. This fits to an exponential from which the lifetime can be extrapolated (R^2 : 0.96). **C:** In the absence of flow, there is lower decoration of the DNA strand. **D:** Exponential fit is done similarly (R^2 : 0.94). **E:** The lifetime seems to be slightly affected with its lifetime going from 2.40 ± 0.11 s to 2.76 ± 0.10 s (R^2 : 0.94 and 0.96 for the fits of dwell time of UvrA-mNeonGreen in the absence and presence of flow respectively; P -value: 0.004). Error bars represent the error of the exponential fit. **F:** However, the average number of UvrA-mNeonGreen binding to the tethered DNA increases from 0.66 ± 0.18 binders per minute per kbp to 1.86 ± 0.44

binders per minute per kbp when compared with strands that were under no flow (n no flow: 5 strands, 781 binders; n flow: 3 strands, 1228 binders) (P-value: 0.02). The error bars represent the standard error of the mean. As a result, there is a 3.5 fold increase of the affinity of UvrA to the DNA in presence of flow.

3.3.3 UvrA-mNeonGreen binding is affected by time and protease inhibitor

As we use lysate and not purified protein, we were worried about the effect of potential proteases within the lysate. This is why we used a protease inhibitor mix. We wanted to check if the protease inhibitor mix was having an effect on the binding of UvrA-mNeonGreen to the DNA strand. We also observed in this experiment that UvrA-mNeonGreen binding to tethered DNA in a time-dependent manner. This was demonstrated by placing a tethered Lambda DNA strand within a channel containing 5 nM of UvrA-mNeonGreen lysate in ABC buffer supplemented with 1 mM of ATP and 1 mM of DTT under 0.1 Pa of lateral flow. The DNA strand was put under 50 pN of tension and left under those conditions for 2 minutes. Then a 488 nm laser was turned on with exposure synchronisation (30% power, 200 ms exposure). The tethered DNA was immediately put in the channel containing only ABC buffer and the video was recorded (4.3 Hz framerate) for 200 frames (roughly 46 seconds). This is followed by relaxation of the DNA strand and the same DNA strand was used until the connection between the beads was lost. A piece of code was written to avoid human variations when performing this experiment (Appendix 1).

To analyse the data, a kymograph along the DNA strand was extracted for each video using the FIJI package of ImageJ. Those kymographs were exported as text files and imported into Excel where the average fluorescence over time was calculated. This fits to an exponential and the amplitude was extrapolated. This amplitude was plotted against the time (Figure 32) at which the corresponding video was captured, relative to the time at which the protein mix was done.

As represented by squares in Figure 32, the binding of UvrA-mNeonGreen is time-dependent where binding is very limited for the first 150 minutes and then greatly increases. Interestingly, the addition of protease inhibitors (Pierce, Thermo

Scientific, reference A32963) has an impact on the time-dependent binding of UvrA-mNeonGreen. A protease inhibitor mix was added by crushing a tablet and diluting the obtained powder in ABC buffer at various concentrations. Notably, when protease inhibitor is added to a final concentration of 0.07 mg per mL, there is still that time dependency where binding is very limited for the first 70 minutes and then greatly increases (as represented by triangles in Figure 32). When the protease inhibitor concentration is increased to a total of 0.35 mg per mL, there is limited binding for the first 40 minutes, followed by a great increase in the decoration of the DNA strand (as represented by circles in Figure 32). When a large excess of protease inhibitor is added, to a final concentration of 7 mg per mL, there is very limited binding of UvrA-mNeonGreen to the DNA strand (data not shown). Altogether, this shows that there might be some proteases within the lysate. To balance this, protease inhibitor will be used in subsequent experiments.

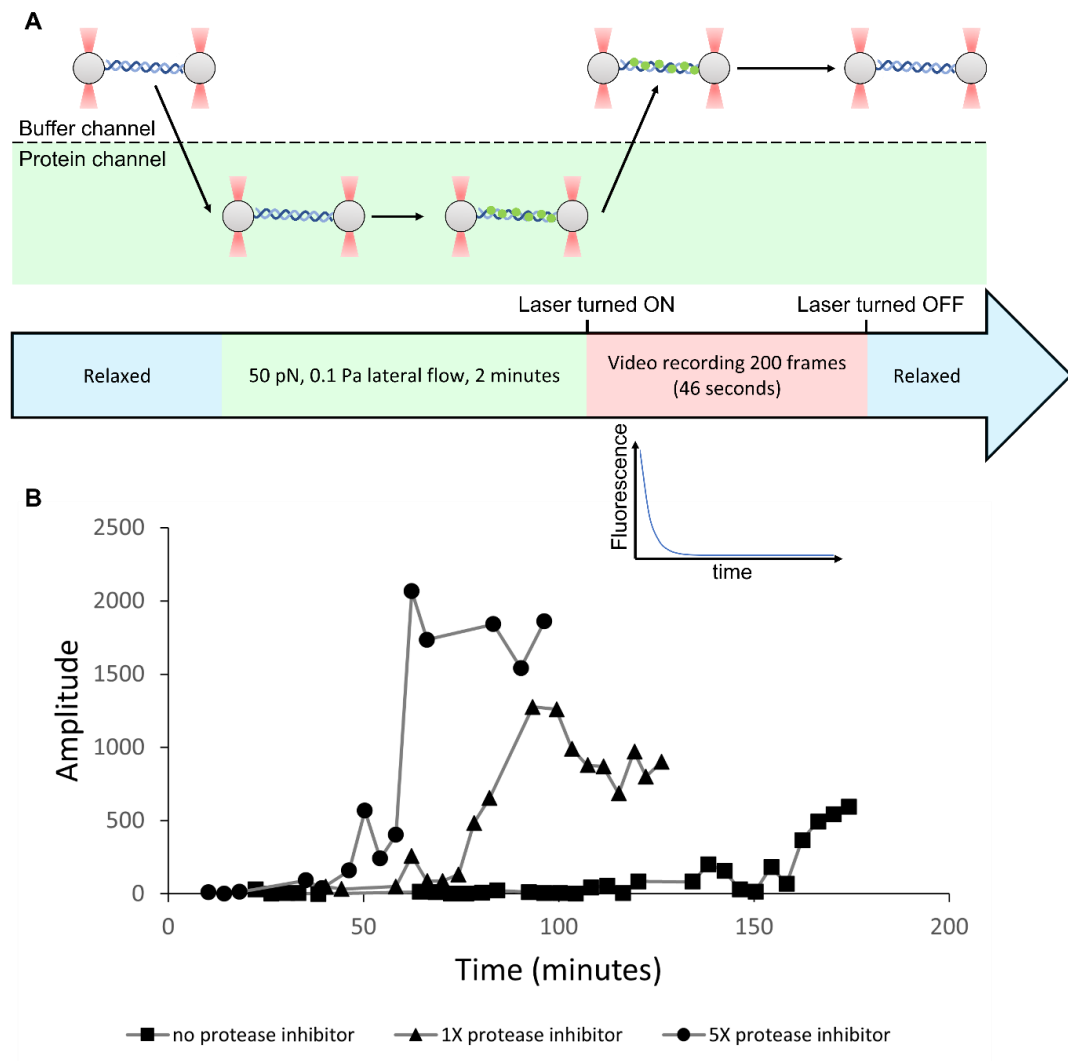


Figure 32: Impact of time and protease inhibitor on the binding of UvrA-mNeonGreen.

A: Workflow of the experiment where DNA tether is moved to a protein channel under 0.1 Pa of flow and 50 pN of tension for 2 minutes. Then a 488 nm laser is turned ON, and the strand is instantly moved to a protein-free channel. Video is recorded which allows quantifying the overall fluorescence of the DNA strand coated with UvrA-mNeonGreen. **B:** Amplitude of exponential fits over time where squares represent the amplitude of exponential fits in the absence of protease inhibitor; triangles represent the amplitude of exponential fits in the presence of 0.07 mg per mL of protease inhibitor and circles represent the amplitude of exponential fits in presence of 0.35 mg per mL of protease inhibitor.

3.3.4 Increases in tension show higher decoration of UvrA-mNeonGreen to the DNA strand.

The C-Trap allows to increase the tension applied to the DNA strand by separating the two beads connected to the DNA. Interestingly, increases of tension did affect the binding of UvrA-mNeonGreen. To illustrate this effect, DNA strands were captured as previously described. The tethered DNA was moved to a channel containing 5 nM of UvrA-mNeonGreen lysate within ABC buffer and was supplemented with 1 mM of ATP, 100 mM of DTT and protease inhibitor to a final concentration of 0.07 mg per mL. DNA strands were subjected to a distance alteration from 19.1 to 16.9 μm resulting in variations of tension between 50 and 8 pN while being under 0.1 Pa of medial flow, illustrated in Figure 33 . The oscillation was as follow: 10 seconds of rest, 6.35 seconds of decrease in distance at 0.26 μm per second followed by 10 second of rest and 6.35 seconds of increase in distance at 0.26 μm per second. Interestingly increases in tension of the DNA strand allow for higher decoration of UvrA-mNeonGreen to the DNA strand, as shown in Figure 33 . It should be mentioned that DNA strands were under medial flow when videos were recorded. This strongly suggests that the binding of UvrA is affected by the tension. A higher decoration of the DNA strand could be due to an increase in the number of binders per minute and/or an increase in the time each binder stays on the DNA. This will be investigated further in the subsequent sections.

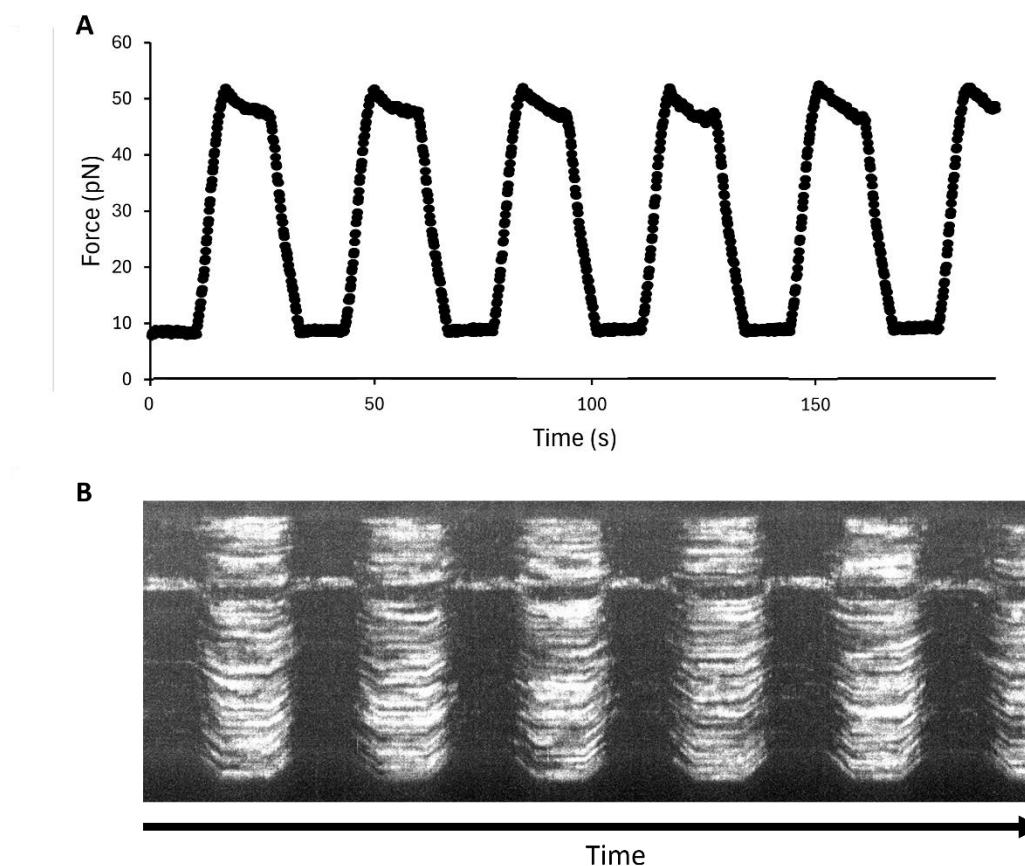


Figure 33: Kymograph of Increase of tension shows a higher decoration of UvrA-mNeonGreen to the DNA strand. A: Variation of forces applied to the DNA strand. **B:**

Kymograph of a DNA strand under variable tension while medial flow is on. The pattern of tension applied to the DNA strand is represented in blue where tension will be kept at 8 pN for 10 seconds, then the DNA is stretched until the tension reaches 50 pN and kept at 50 pN for 10 seconds until it is released back to 8 pN. The lighter part of the kymograph represents UvrA-mNeonGreen proteins bound to the DNA strand. As the tension increases, more proteins bind to the DNA. Once the tension decreases, the proteins leave the DNA strand.

3.3.5 Tensile force affects both the On-rate and the Off-rate of lysate UvrA-mNeonGreen in the presence or absence of UV damage to the DNA

To determine which of the On-rate or the Off-rate was being affected by the changes of tension, the experimental set-up had to be altered in a way that

allowed the gathering of quantitative data. To do so undamaged and UV-damaged DNA strands were tethered as previously described. UV-damaged DNA strands were produced by irradiating biotinylated Lambda with 40 J.m² of 254 nm UV and tethered similarly to undamaged DNA. UvrA-mNeonGreen in lysate is mixed in solution with ABC buffer to a concentration of 5 nM and supplemented with 1 mM of ATP, 100 mM of DTT and protease inhibitor to a final concentration of 0.07 mg per mL. A Python script (Appendix 2) made the same DNA strand go through successive tensions (10, 15, 25, 35, 45 pN) as shown in Figure 34A while recording UvrA-mNeonGreen binders on the DNA strand as shown in Figure 34B. The minimal and maximal values (10 and 45 pN) were chosen as being the “low” and “high” tensions. The reasoning for the 45 pN is to avoid stretching the DNA strand too close to its overstretched transition. With hindsight, the “low” tension should have been much lower (around 2.2 pN would have been more appropriate to compare with literature (244)).

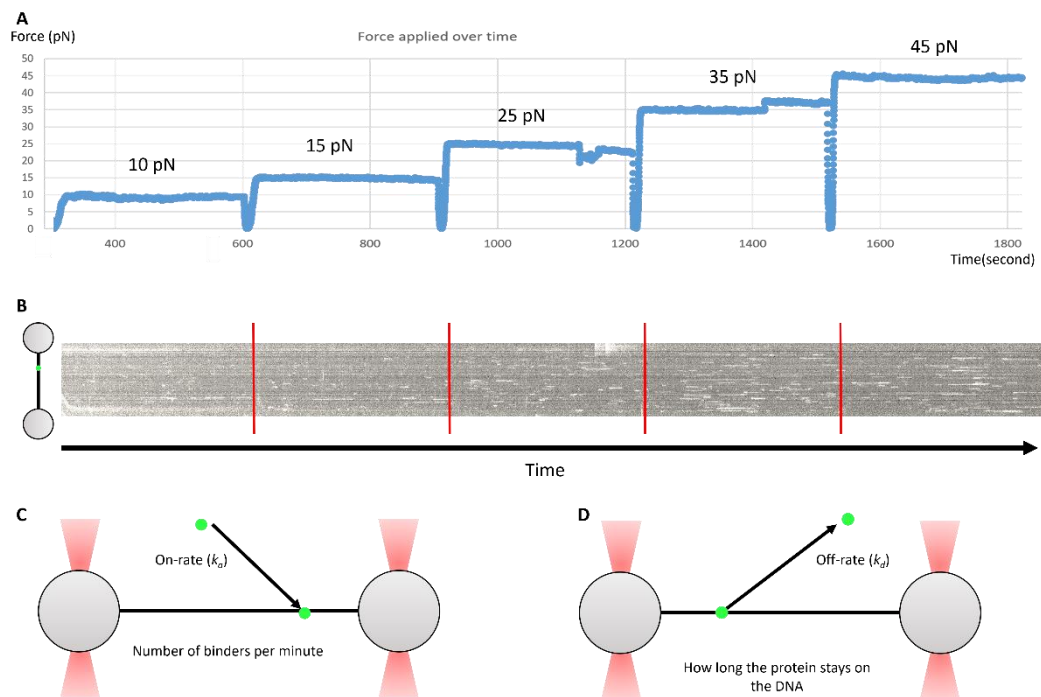


Figure 34: Experimental set-up for tension dependency study. **A:** Measure of the force applied to the DNA strand as the program is running where the tension is increased gradually from 10 to 15, 25, 35, and 45 pN over time. **B:** Resulting kymograph from the experiment in A, red lines

represent the time at which the different tensions are applied to the DNA. C: Visual representation of the on-rate which is the number of binders per minute. D: Visual representation of the off-rate which is the reciprocal of the attached lifetime.

Lifetime and attachment rate constants were calculated as previously described. An increase of DNA tension from 10 pN to 45 pN induces the lifetime of UvrA-mNeonGreen to go from 1.43 ± 0.04 s to 2.28 ± 0.08 s in the absence of damage (P-value: <0.0001) and from 1.07 ± 0.02 s to 3.28 ± 0.10 s in the presence of UV damage (P-value: <0.0001) as shown in Figure 35A and Figure 35B. Similarly, the number of binders per minute per kbp increases by 135 % (P-value: 0.04) and 94 % (P-value: 0.01) in the absence and presence of UV damage as shown in Figure 35C and D. With both lifetimes and the attachment rate constant increasing when the tension applied to the DNA goes from 10 pN to 45 pN, naturally there is a 3.8 fold increase of the affinity of UvrA-mNeonGreen to undamaged DNA and 6 fold for UV-damaged DNA (P-values: 0.03 and 0.0006 respectively).

Plotting of the attachment rate constant, the detachment rate constant, and the dissociation constant against the force applied to the DNA is possible. Such plots allow for Bell fitting from which the distance to the transition state is extrapolated as shown in Figure 36. The distance to the transition state is 0.05 nm and 0.16 nm for the detachment rate constant of undamaged and damaged DNA strands respectively (Figure 36A and B). The distance to the transition state of the attachment rate constant is -0.10 nm and -0.06 nm for undamaged and damaged DNA strands respectively (Figure 36C and D). The distance to the transition state is an indication of how much the DNA must be stretched to affect the binding of the protein. It is calculated for both the attachment rate constant (how much the DNA must be stretched to facilitate the binding of the protein to the DNA), and for the detachment rate constant (how much the DNA must be stretched to increase the lifetime of the protein to the DNA).

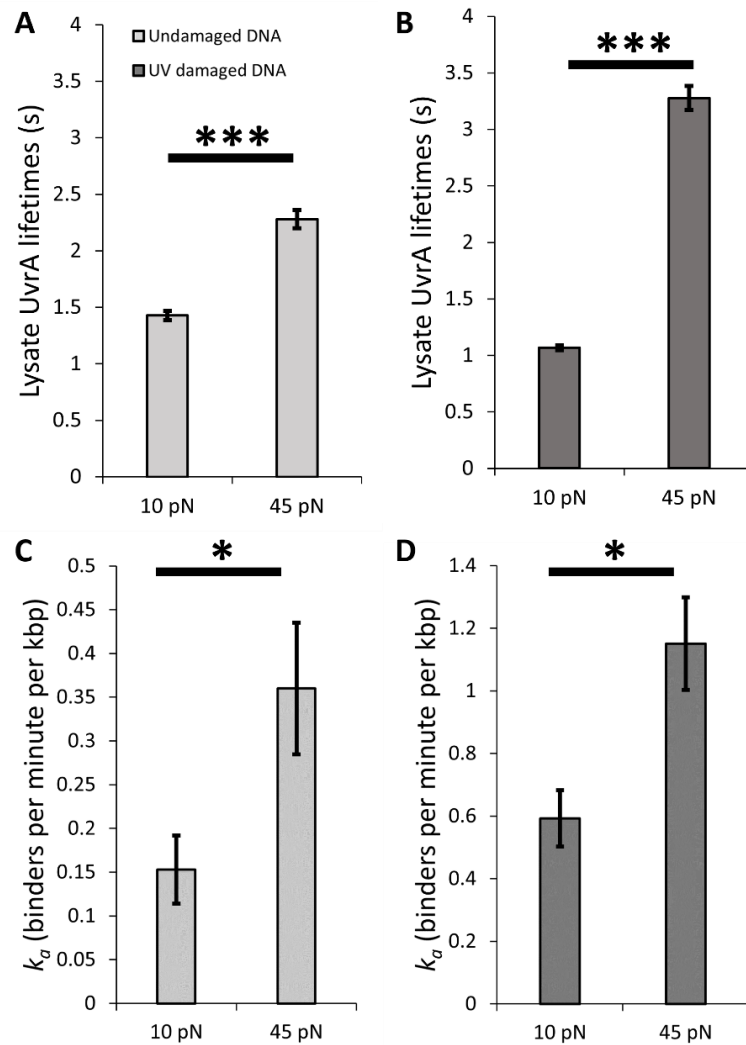


Figure 35: UvrA-mNeonGreen lifetime is affected by both tension and UV damage. Light grey represents undamaged DNA and dark grey represents UV-damaged DNA. **A:** Lysate UvrA-mNeonGreen lifetime increases from 1.43 ± 0.04 s to 2.28 ± 0.08 s when tension is increased from 10 pN to 45 pN (n binders: 170 and 422 respectively; n strands: 5 for both; R^2 : 0.97 and 0.96 respectively; P -value: <0.0001). **B:** Similarly, in the presence of UV damage, the lifetime increases from 1.07 ± 0.02 s to 3.28 ± 0.10 s when the tension is increased from 10 pN to 45 pN (n binders: 660 and 1352 respectively; n strands: 5 for both; R^2 : 0.99 and 0.98 respectively; P -value: <0.0001). P -values between undamaged and UV-damaged strands are also <0.0001 . Error bars represent the errors of the exponential fit. **C:** The binding of UvrA to the tethered DNA strand increases from 0.15 ± 0.04 binders per minute per kbp to 0.36 ± 0.08 binders per minute per kbp when going from 10 pN to 45 pN of tension in the presence of undamaged DNA, which accounts for an increase of 135 % (P -value: 0.04) and from **D:** 0.59 ± 0.09 binders per minute per kbp to 1.15 ± 0.15 binders per minute per kbp in the presence of UV-damaged DNA (P -value: 0.01) which results in an increase of

94%. Error bars for the lifetime represent the error of the exponential fit. Error bars for the attachment rate constant represent the standard error of the mean.

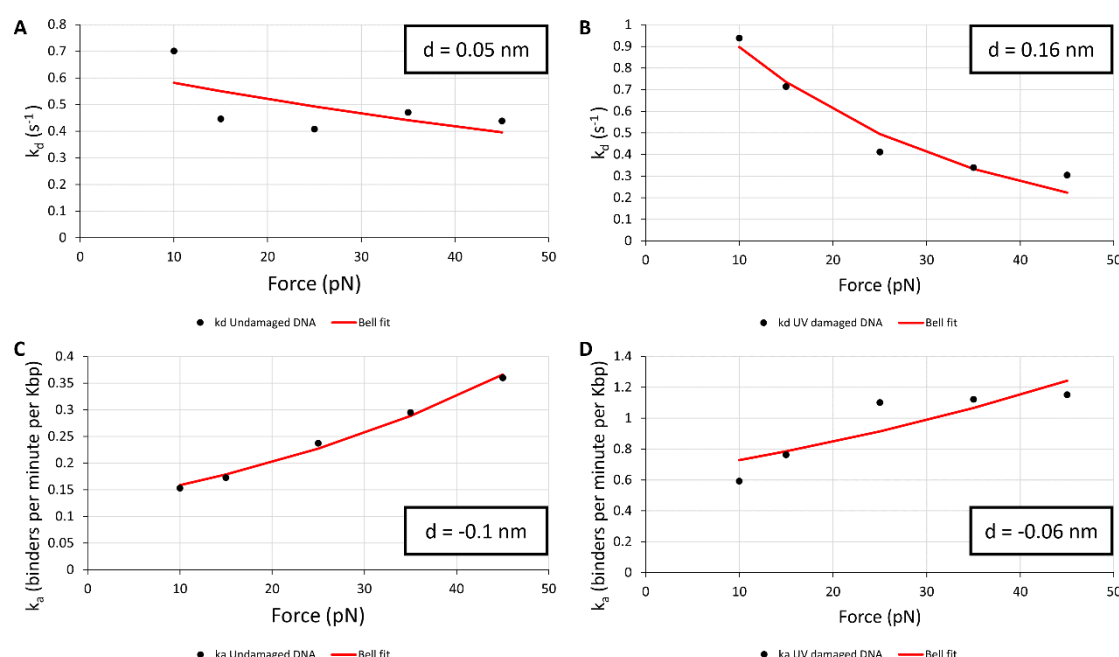


Figure 36: Bell-fits of k_d , k_a and K_D of the binding of UvrA-mNeonGreen to undamaged and UV-damaged DNA under various forces. **A:** The Bell-fit of the detachment rate constant of lysate UvrA-mNeonGreen highlights a distance to the transition state of 0.05 nm when using undamaged DNA as a substrate and **B:** a distance to the transition state of 0.16 nm when using UV-damaged DNA as a substrate. **C:** Similarly, the Bell-fit of the attachment rate of lysate UvrA-mNeonGreen highlights a distance to the transition state of -0.10 nm when using undamaged DNA as a substrate and **D:** a distance to the transition state of -0.06 nm when using UV-damaged DNA as a substrate.

3.3.6 UvrA-mNeonGreen's binding is affected by fluorescein-damaged DNA.

Fluorescein on DNA has been extensively described as a lesion that is recognised and repaired by NER (59,245). Fluorescein was incorporated into biotinylated Lambda using nick translation. It allows for nicking the DNA at specific places which in turn allows for priming of DNA polymerase I to the DNA. Synthesis of DNA at the location of the nicks permits incorporation of Fluorescein by only providing ATP, GTP, CTP and Fluorescein-12-dUTP (And not providing dTTP), as shown in Figure 28. Fluorescein-Biotinylated-Lambda was tethered in-between beads as described

for undamaged DNA and put under 10 pN of tension. A snapshot of the location of the fluorescein alongside the DNA strand was captured (488 nm, 30% power) in a buffer channel which allows for mapping of the damage sites as shown in Figure 28. Fluorescein is a fluorophore that photobleaches very quickly, once photobleached, the DNA strand was cautiously moved to a channel containing 5 nM of UvrA (lysate) within ABC buffer, supplemented with 1 mM of ATP, 1 mM of DTT and 0.07 mg per mL of protease inhibitor mix. The two traps were kept at the same distance from each other to make sure that the localisation of the photobleached fluorescein stays put. This was necessary as both fluorescein and mNeonGreen are excited by the 488 nm laser and result in similar fluorescent spots. Then a 488 nm laser is turned on and a video is recorded (200 ms exposure, 2 Hz, exposure synchronisation ON, 30% laser power). The videos containing UvrA-mNeonGreen are also analysed with Trackmate as shown previously (**Error! Reference source not found.**). Individual binder proximity to lesion sites was evaluated. Binders within 72 nm of the localisation of a lesion were grouped together (named proximal to the lesion) while the ones that weren't within that window were put in another group (named distal to the lesion). This was also done for other distances with an increment of 72 nm for a total of six distances to the lesion. The lifetime (Figure 37A) and attachment rate constant (Figure 37B) were calculated for binders proximal and distal to the lesion for each of those six distances. Since the attachment rate constant is expressed in binder per second per kbp, it considers the difference in DNA size. Interestingly, both the attachment rate constant and the lifetime proximal to the lesion are greater than those distal to the lesion at all the distances evaluated.

To choose a distance to the lesion that is representative of how UvrA behaves near a lesion site, several aspects must be considered. First, the number of lesion sites per DNA strand was variable, from three to six. Some of those lesion sites were relatively close with the smallest distance observed being between two lesion sites being 556 nm. This means that any distances above 278 nm will induce biases in the analysis. Second, the DNA strands were moved in between the acquisition of

the lesion site localisation and the imaging of UvrA-binding. This could induce some small displacement of the damage sites, which in turn could cause a bias in the data analysis if the distance to the lesion site chosen for the analysis is too small. As such, the distance to the lesion site can only be 144 or 216 nm to be both large enough to ensure small displacements do not affect the analysis and small enough to differentiate distances from different lesions that are close to each other. The distance chosen to be representative of the behaviour of UvrA-mNeonGreen binding at proximity to the lesion is 144 nm as it is the one that shows the highest difference for both the lifetime (Figure 37C) and the attachment rate constant (Figure 37D). As such, there is an increase in the lifetime of UvrA-mNeonGreen from 1.19 ± 0.03 s when the binding occurs distal to the lesion, to 1.62 ± 0.06 s when the binding occurs proximal to the lesion site (P-value: <0.0001) (Figure 37C). The number of UvrA-mNeonGreen binders increases from 0.27 ± 0.05 binders per minute per kbp proximal to lesions to 0.37 ± 0.10 binders per minute per kbp distal to the lesion (Figure 37D). However, this variation is not statistically significant (P-value: 0.41). As a result, there is an increase of the affinity of UvrA-mNeonGreen to the DNA of 1.8-fold when proximal to the lesion (P-value: 0.09). It is important to note that we are not looking at colocalization between UvrA-mNeonGreen and one fluorescein molecule, but rather at the difference of binding of UvrA-mNeonGreen at proximity to the lesion. This is exacerbated by the presence of a multitude of fluorescein tags at every lesion site. This is why we didn't take into account the diffraction limit uncertainty in this study.

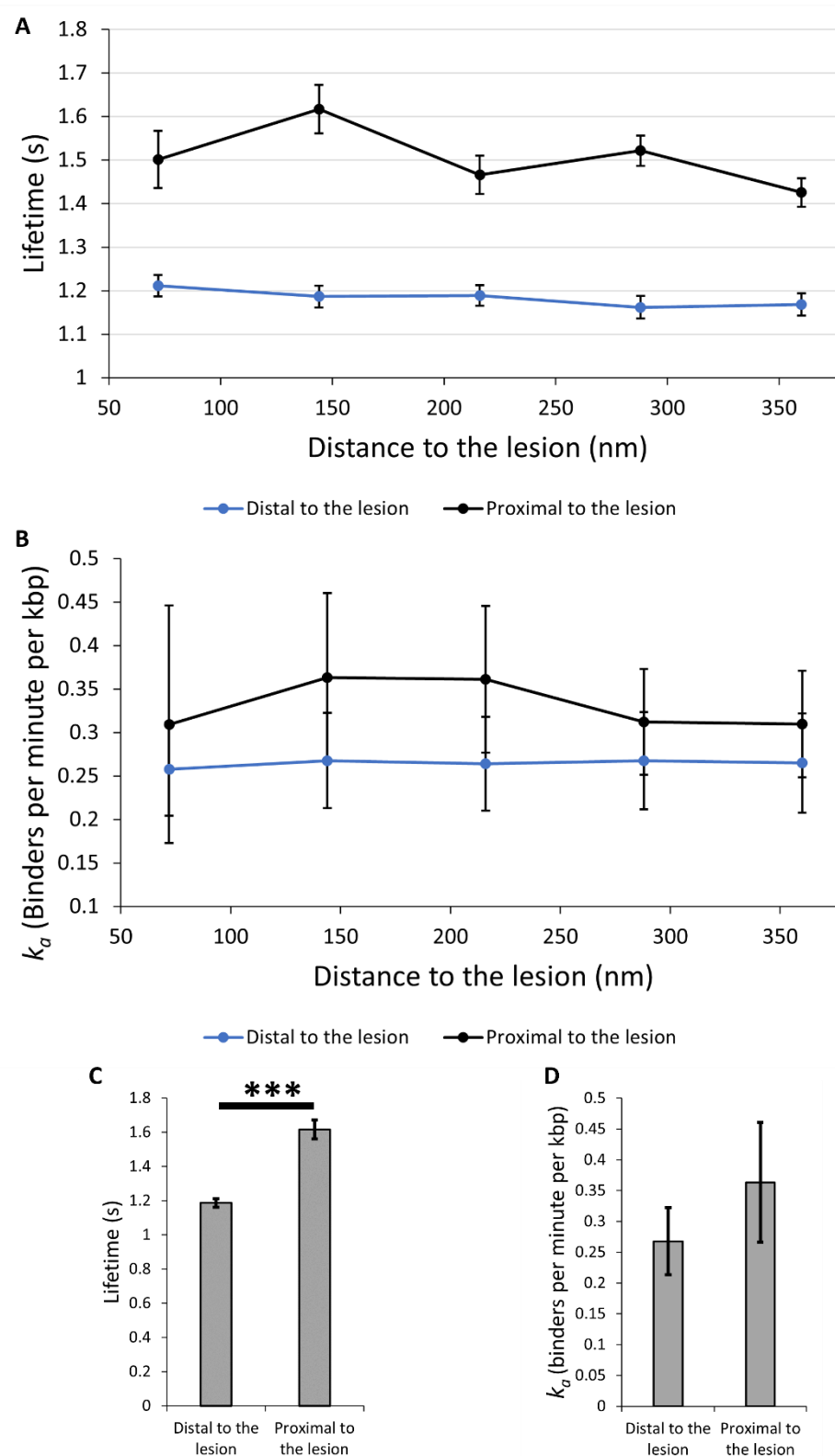


Figure 37: Fluorescein affects the lifetime of UvrA-mNeonGreen but not its on-rate.

Using fluorescein-labelled DNA as a template for UvrA-mNeonGreen binding allows for localisation

of UvrA's binding with DNA damage lesion sites. The lifetime and the attachment rate constant of UvrA were assessed depending on the distance of each individual binder relative to the lesion. Data analysis was performed with a distance incrementally increasing by 72 nm (72 nm being the width of a pixel on the C-Trap) from 72 nm to 360 nm (one to five pixels). The **A:** lifetime and **B:** attachment rate constant are plotted against the distance to the lesion. **C:** Notably, there is a significant difference in the off-rate with lifetimes reaching 1.62 ± 0.06 seconds within 144 nm to the lesion and 1.19 ± 0.03 seconds outside of this 144 nm windows (R^2 : 0.98 and 0.99 respectively; n binders: 206 and 1646 respectively, n strands: 7; P -value: <0.0001). **D:** Binders proximal to the lesion (within 144 nm of damage sites) show no statistically significant differences in their attachment rate constant compared to binders distal from the lesion (k_a proximal to the lesion: 0.36 ± 0.10 binders per minute per kbp; k_a distal from lesion: 0.27 ± 0.05 binders per minute per kbp; P -value: 0.41). Error bars for the lifetime represent the errors of the exponential fit. Error bars for the attachment rate constant represent the standard error of the mean.

3.3.7 Effect of Tension and UV Damage on UvrB's Recruitment by UvrA.

As changes in tension affect the binding of UvrA to the DNA, it raises questions on how it affects the binding of the next protein involved in NER: UvrB. To assess this, 5 nM of purified UvrA-mScarlet was used with 10 nM of lysate UvrB-mNeonGreen in ABC buffer supplemented with 1 mM ATP, 100 mM DTT and 0.07 mg per mL of protease inhibitor mix. Undamaged or UV-damaged DNA strands were tethered as previously described. However, data collection was only performed at 10 pN or 45 pN of tension. Videos were recorded (200 ms exposure time, exposure synchronisation ON, 2 Hz) under the excitation of a 488 nm and a 532 nm laser (both at 30% power). Data was analysed as previously described to get the on-rate and off-rate of both UvrA-mScarlet and UvrB-mNeonGreen (**Error! Reference source not found.**) allowing us to relate the quantity of UvrB to UvrA. Under those conditions, UvrA-mScarlet shows an increase in its lifetime from 0.42 ± 0.01 s to 0.78 ± 0.01 s as the tension of the DNA is increased from 10 pN to 45 pN when using undamaged DNA as the substrate (Figure 39A; P -value: <0.0001). High tension also increases the attachment rate constant of UvrA-mScarlet by 382 % (Figure 39C; P -value: 0.008). However, using UV-damaged DNA as substrate shows a lifetime for UvrA-mScarlet of 0.63 ± 0.01 s at low tension and 0.72 ± 0.01 s at high tension (Figure 39B; P -value: 0.001), with an increase of the attachment rate

constant not statistically significant (Figure 39D; P-value: 0.51). With both lifetimes and the attachment rate constant increasing when the tension applied to the DNA goes from 10 pN to 45 pN, naturally the affinity of UvrA-mScarlet increases by 9.1 fold while using undamaged DNA and by 1.7 fold while using UV-damaged DNA (P-values: 0.0007 and 0.38 respectively).

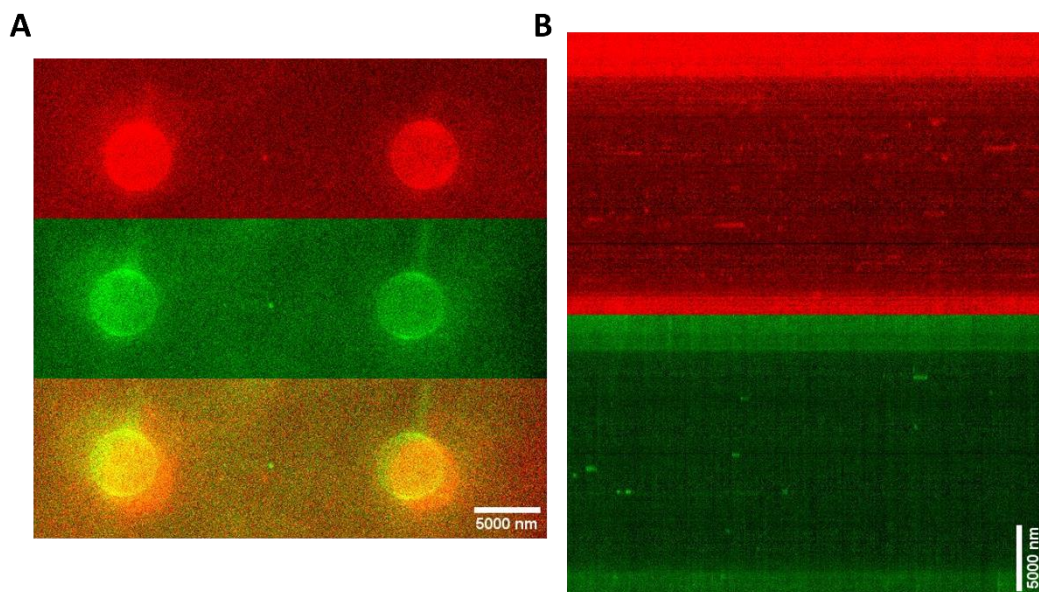


Figure 38: Example of experimental data. A: In red is UvrA-mScarlet. In green is UvrB-mNeonGreen. B: Kymograph of both UvrA-mScarlet and UvrB-mNeonGreen.

The lifetime of UvrB-mNeonGreen was not calculable at low tension due to the small number of binding events (n binders: 7 and 19 for undamaged and damaged DNA respectively; n strands: 2 and 2 respectively). The lifetime of UvrB-mNeonGreen at high tension was 1.38 ± 0.06 s and 1.56 ± 0.07 s when using undamaged and UV-damaged DNA strands as substrate respectively (Figure 40A) (P-value: 0.02). However, UvrB's attachment rate constant increases in a non-statistically significant way (P-value: 0.09) from 0.05 ± 0.02 binders per minute per kbp when using undamaged DNA as substrate to 0.12 ± 0.05 binders per minute per kbp when using UV damaged DNA as substrate. As a result, UvrB's affinity for the DNA strand increases by 2.8 folds (P-value: 0.2). However, the attachment rate constant, and therefore the dissociation constant of UvrB comes

with a bias as UvrB's recruitment to the DNA is dependent on UvrA. To take that into consideration, the ratio of the number of UvrB binders to the number of UvrA binders was assessed (Figure 41). As such, when undamaged DNA is used as the substrate, there is a $4 \pm 4 \%$ to $17 \pm 6 \%$ of UvrB per UvrA increase between 10 pN and 45 pN, but this difference is not statistically significant (P-value: 0.12). However, when using UV-damaged DNA, the ratio of UvrB per UvrA goes from $6 \pm 3 \%$ to $34 \pm 7 \%$ with statistical significance (P-value: 0.02). Since only two tensions were tested here, it is not possible to fit the data gathered to Bell-fits.

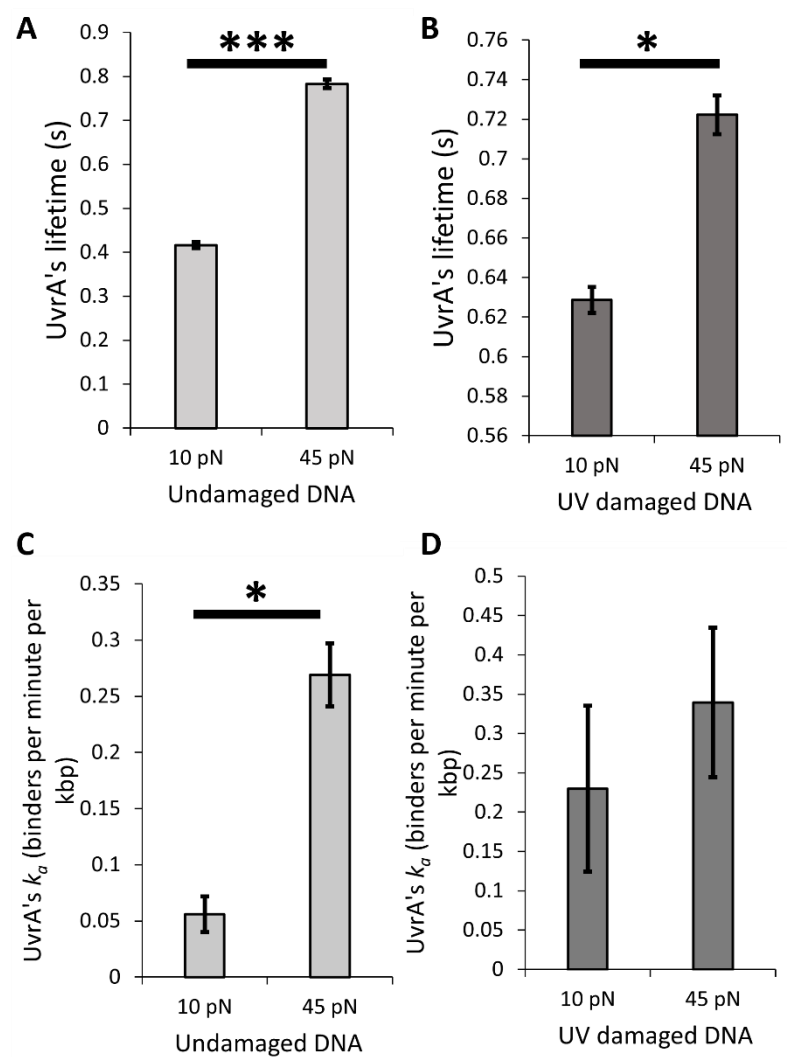


Figure 39: UvrA's kinetic in the presence of UvrB. When 5 nM of purified UvrA-mScarlet is in presence of 10 nM of lysate UvrB-mNeonGreen, **A:** UvrA's lifetime increases from 0.42 ± 0.01 s to

0.78 ± 0.01 s when the tension increases from 10 pN to 45 pN using undamaged DNA (n binders: 156 and 1196 respectively; n strands: 2 and 4 respectively, R^2 : 0.99 and 0.99 both; P -value: <0.0001) **B**: while it increases from 0.63 ± 0.01 s to 0.72 ± 0.01 s when using UV-damaged DNA (n binders: 443 and 1026 respectively; n strands: 2 and 3 respectively, R^2 : 0.99 and 0.99 both; P -value: 0.0011). P -values between undamaged and UV-damaged DNA are <0.005 . **C**: The binding of UvrA to the tethered DNA strand increases from 0.06 ± 0.02 binders per minute per kbp to 0.27 ± 0.03 binders per minute per kbp when going from 10 pN to 45 pN of tension in the presence of undamaged DNA, which accounts for an increase of 382 % (P -value: 0.008). **D**: However, no statistically significant difference was found when using a UV-damaged DNA strand as a substrate (k_a 10 pN: 0.23 ± 0.1 binders per minute per kbp; k_a 45 pN: 0.34 ± 0.10 binders per minute per kbp; P -value: 0.51). Error bars for the lifetime represent the errors of the exponential fit. Error bars for the attachment rate constant represent the standard error of the mean.

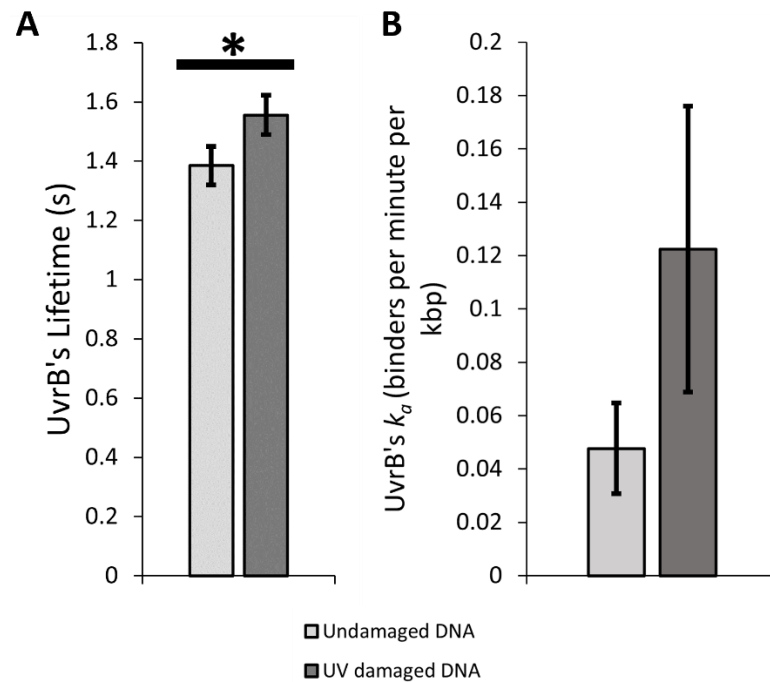


Figure 40: Kinetics of Lysate UvrB-mNeonGreen at 45 pN in the absence or presence of UV damage. The kinetic of UvrB was assessed when 10 nM of Lysate UvrB-mNeonGreen was in the presence of 5 nM of purified UvrA-mScarlet. There were few numbers of UvrB binders at low tension (10 pN) (n binders: 7 and 19 for undamaged and damaged DNA respectively; n strands: 2 and 2 respectively). Therefore, the lifetime, attachment rate constant and dissociation constant were assessed only at high tension (45 pN). **A**: As such, UvrB lifetimes at 45 pN are 1.38 ± 0.06 s and 1.56 ± 0.07 s for undamaged and damaged DNA respectively (n binders: 229 and 326

respectively; n strands: 4 and 3 respectively; R^2 : 0.97 and 0.98 respectively; P -value: 0.02). **B:** UvrB's attachment rate constant goes from 0.05 ± 0.02 binders per minute per kbp when using undamaged DNA as substrate to 0.12 ± 0.05 binders per minute per kbp when using UV-damaged DNA as substrate. However, this difference is not significant (P -value: 0.09). Error bars for the lifetime represent the errors of the exponential fit. Error bars for the attachment rate constant represent the standard error of the mean.

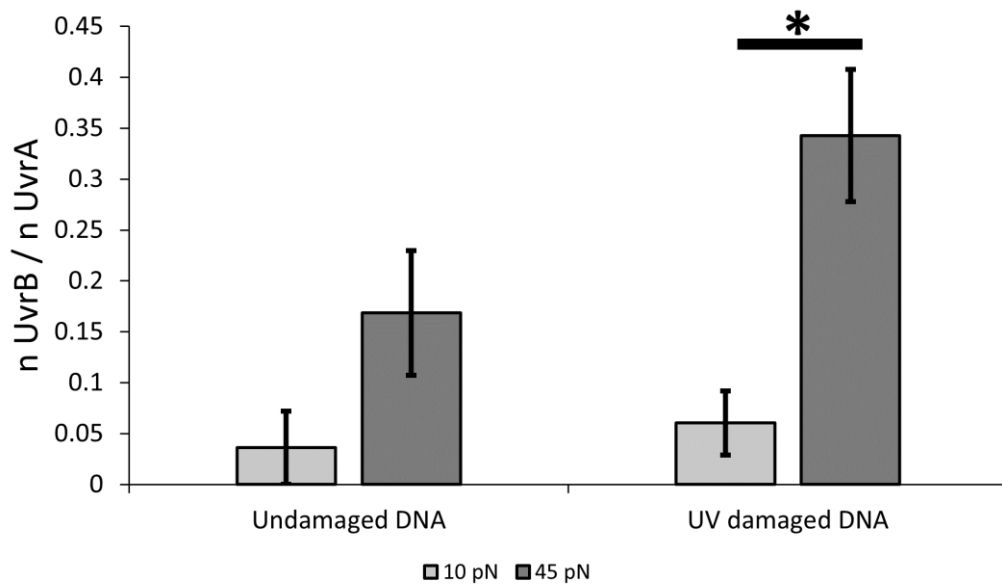


Figure 41: Recruitment of UvrB by UvrA depending on tension.

As UvrB is usually recruited to the DNA by UvrA, and UvrA is already tension dependent, it was necessary to assess the evolution of the number of UvrB relative to the tension while taking into account the evolution of UvrA. As such, the proportion of UvrB per UvrA increases from $4 \pm 4\%$ to $17 \pm 6\%$ when going from 10 to 45 pN using undamaged DNA but the difference is not significant (P -value: 0.12). However, when using UV-damaged DNA, the proportion of UvrB per UvrA increases from $6 \pm 3\%$ to $34 \pm 7\%$ (P -value: 0.02). There are no significant differences between undamaged and damaged DNA (P -value: 0.33 for low tension and P -value: 0.06 for high tension). Error bars represent the standard error of the mean.

3.3.8 A high concentration of purified UvrA-mScarlet x2 shows little difference in behaviours upon UV damage and tension changes

We wanted to assess if the use of purified protein showed different results than the use of protein within the lysate. However, we stumbled upon few difficulties that will be explained here. 25 nM of purified UvrA-mScarlet x2 was used in ABC buffer supplemented with 1 mM ATP, 100 mM DTT and 0.07 mg/mL of protease inhibitor mix. Other larger protein fusions have been previously used, such as UvrA-mNeonGreen x3, without showing any difference in NER function *in-vivo* (Alexandra Moores, unpublished data). Data collection and analysis were done as previously described. Purified UvrA-mScarlet x2 didn't seem to bind at 5 nM, hence why the protein concentration was increased. Notably several proteins were tested including UvrA-mNeonGreen and UvrA-mScarlet. However, UvrA-mScarlet x2 is the one that showed the most useable qualities. The high concentration of the protein resulted in videos with a lower signal-to-noise ratio. Undamaged or UV-damaged DNA strands were tethered as previously described and put under specific DNA tension (10 pN, 20 pN, 30 pN, 40 pN, and 50 pN. Each tension was done with a newly captured DNA strand. The laser was turned on (488 nm at 30 % laser power) and videos were recorded (100 ms exposure time, exposure synchronisation ON, 2 Hz, 1200 frames). Under those conditions, the lifetime of UvrA-mScarlet x2 is very similar going from 0.67 ± 0.003 s to 0.65 ± 0.01 s for low and high tension, using undamaged DNA as substrate (P-value: 0.02). However, when using damaged DNA, the lifetime goes from 0.69 ± 0.004 s to 0.91 ± 0.01 s (Figure 42A; P-value: <0.0001). Despite the data showing significance, Figure 43 hints that the lifetime at 50 pN is an outlier and therefore not real. There are no statistical differences between low and high tension for the attachment rate constant of UvrA-mScarlet x2 (Figure 42B; P-value for untreated DNA strands: 0.56; P-value for DNA damaged DNA strand: 0.85). In turn, it results in no differences in the affinity of UvrA-mScarlet x2 to the DNA strand (P-value: 0.6 for both of them). It is notable to mention that due to the high noise-to-signal ratio, gathering data for this experiment was challenging. It required pooling data

from different days to have enough binding events to proceed with the data analysis. With the time dependency of the binding of UvrA, it renders the attachment rate unusable so this result must be taken with caution. Furthermore, Bell fitting of the off-rate of UvrA-mScarlet x2 seems to be unaffected by the tension as shown in Figure 42B with distances to the transition state of 0 nm and of 0.02 nm when using undamaged and UV-damaged DNA as substrate.

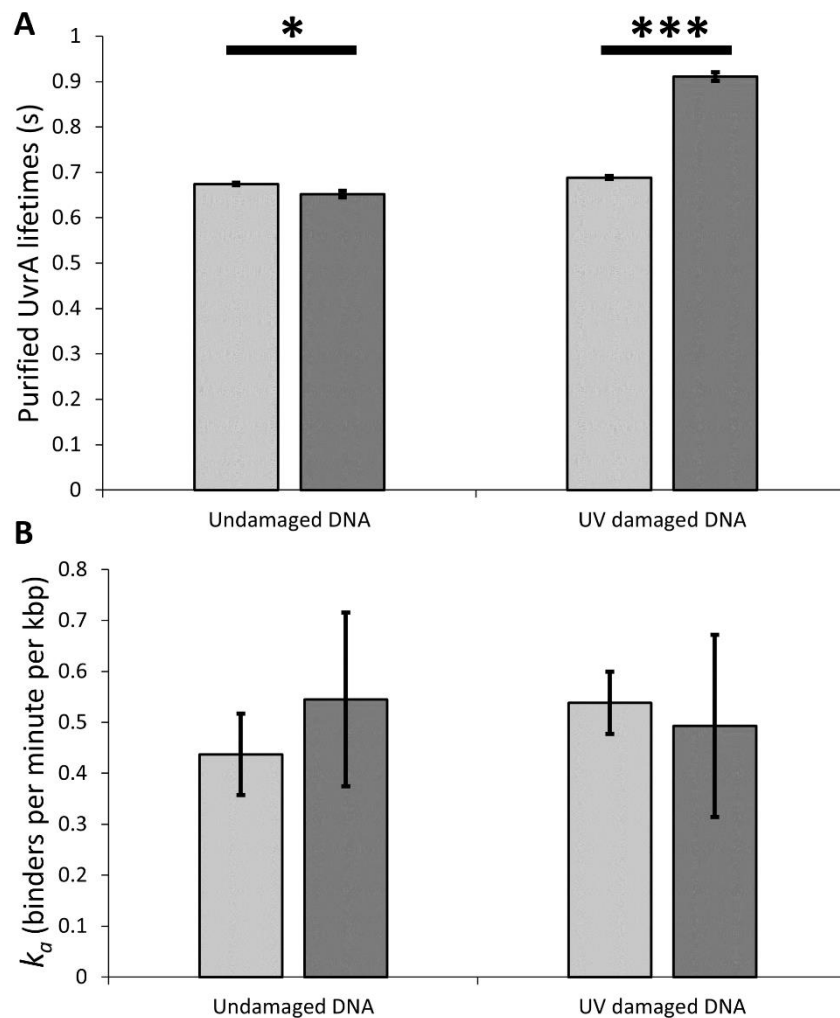


Figure 42: A high concentration of purified UvrA shows an unclear effect of tension and UV damage on UvrA's binding. A: Purified UvrA-mScarlet x2 was used at a concentration of 25 nM and showed similar lifetimes when undamaged DNA was used with lifetimes of 0.67 ± 0.003 s and 0.65 ± 0.01 s at 10 pN and 50 pN respectively (n binders: 763 and 463 respectively; n strands: 3 and 2 respectively; R^2 : 0.99 and 0.99 respectively; P -value: 0.02). When using UV-damaged DNA

there is an increase of the lifetime from 0.69 ± 0.004 s to 0.91 ± 0.01 s respectively (n binders: 939 and 313 respectively; n strands: 3 and 3 respectively; R^2 : 0.99 and 0.99 respectively; P -value: <0.0001). **B:** The number of UvrA binders per minute per kbp doesn't show differences between low and high tension, with the attachment rate constant going from 0.43 ± 0.08 binders per minute per kbp at 10 pN to 0.55 ± 0.17 binders per minute per kbp at 50 pN when using undamaged DNA. Similarly, when using UV-damaged DNA, the attachment rate constant goes from 0.54 ± 0.06 binders per minute per kbp at 10 pN to 0.49 ± 0.18 binders per minute per kbp at 50 pN (P -value for untreated DNA strands: 0.56; P -value for UV-damaged DNA strand: 0.85) nor between undamaged and UV-damaged DNA (P -value 10 pN: 0.37; P -value 50 pN: 0.87). Error bars for the lifetime represent the errors of the exponential fit. Error bars for the attachment rate constant represent the standard error of the mean.

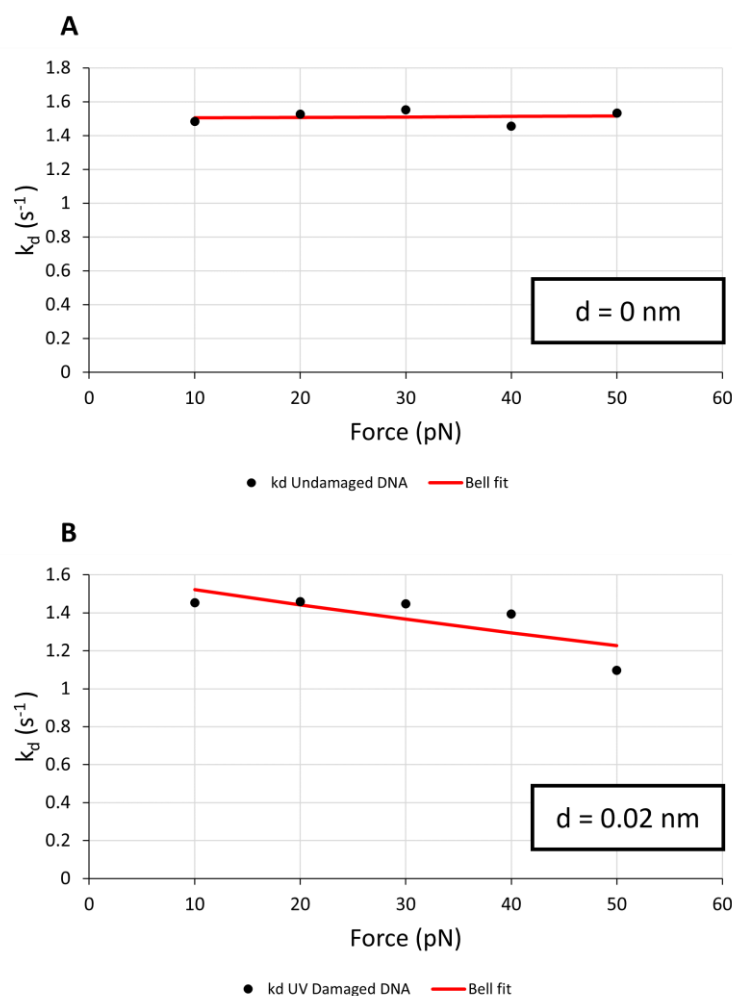


Figure 43: Effect of tension and UV damage to UvrA-mScarlet x2's dwell time on DNA.

A: Bell-fit of the detachment rate constant of UvrA-mScarlet x2 show a distance to the transition state of 0 nm when using undamaged DNA as substrate and of **B:** 0.02 nm when using UV-damaged DNA as substrate. However, the data point at 50 pN seems to be an outsider as it is clearly standing out, with no curvature in the previous data points. This suggest that the distance to the transition state calculated is probably wrong. Data for this experiment were pooled from two different days of experiments rendering Bell-fits of attachment rate constants, and therefore dissociation constants, impossible.

3.3.9 Purified UvrB-mNeonGreen behaviour with undamaged and UV-damaged DNA substrates under various DNA tensions.

Even though the binding profile of purified UvrA-mScarlet x2 is different to the one of UvrA-mNeonGreen within lysate, we wanted to assess the recruitment of UvrB-

mNeonGreen to the system depending on differences in load. Although having differences in the binding of UvrA is a nuisance to the data collected here, there is still value in the data collected for UvrB. To assess the recruitment of purified UvrB to the DNA, 25 nM of purified UvrA-mScarlet x2 was used in combination with 50 nM of purified UvrB-mNeonGreen in ABC buffer supplemented with 1 mM ATP, 100 mM DTT, and 0.07 mg per mL of protease inhibitor mix. UV-damaged and undamaged DNA strands were tethered as previously described and put under specific tensions (10, 20, 30, 40 and 50 pN). Undamaged or UV-damaged DNA strands were captured and then moved to the protein-containing channel. Once in the protein channel, the DNA strands were put under specific tensions (10, 20, 30, 40 or 50 pN), laser turned on (488 nm and 532 nm, both at 30% laser power) and videos recorded (100 ms exposure time, exposure synchronisation ON, 2 Hz, 1200 frames). The Off-rate of UvrA and UvrB was assessed as previously described. The On-rate of both UvrA and UvrB had to be adapted due to the high and variable background noise. UvrA and UvrB binders per minute had to be normalised with the background fluorescence. In each of the videos, a box of 68x120 pixels in frame one was snapped and the intensity of the fluorescence on that frame was averaged. Then the number of protein binding per minute was divided by that background fluorescence and multiplied by the lowest measured background fluorescence of that day. This was necessary to be able to solve the Bell-fit equations. Otherwise, the values were too small, and Excel was unable to process the fitting.

First, the kinetics of UvrA-mScarlet x2 were assessed. As such, UvrA's lifetime is 0.54 ± 0.01 s and 0.61 ± 0.01 s between low and high tension when using undamaged DNA as a substrate (P-value: <0.008) and 0.60 ± 0.01 s and 0.53 ± 0.01 s when using UV-damaged DNA as a substrate (Figure 44A; P-value: 0.0008). The attachment rate constant of UvrA-mScarlet x2 didn't show any statistical differences between low and high tension as well as between undamaged and UV-damaged DNA (Figure 44B). As a result, the affinity of UvrA-mScarlet x2 shows no

differences between all conditions (P-value: 0.8 in the absence of damage and P-value: 0.49 in the presence of UV-damage).

UvrB-mNeonGreen's lifetime at low tension wasn't calculated due to the too-low number of binders (n binders: 14 for both undamaged and UV-damaged DNA). However, UvrB-mNeonGreen lifetime at high tension had enough binders to properly estimate the lifetime and resulted in a lifetime of 1.03 ± 0.05 s and 1.19 ± 0.03 s when using undamaged and UV-damaged DNA respectively (Figure 45A; P-value: 0.014). Furthermore, UvrB-mNeonGreen's attachment rate constant shows an increase of 458 % in the number of binders per minute per kbp when increasing the tension from 10 pN to 50 pN using undamaged DNA as substrate (Figure 45B; P-value: 0.07). A similar increase of 680 % is also seen when using UV-damaged DNA as substrate (Figure 45B; P-value: 0.04). With the attachment rate constant of UvrA-mScarlet x2 staying similar between low and high tension, the ratio of UvrB per UvrA is increasing as the tension goes from low to high forces. This increase is shown in Figure 45C where the number of UvrB per UvrA goes from 2 ± 0.9 % to 15 ± 1.5 % when using undamaged DNA as substrate (P-value: 0.03) and from 2 ± 0.5 % to 31 ± 2.8 % when using UV-damaged DNA as substrate (P-value: 0.04).

Interestingly Bell fitting of the detachment rate constant of UvrB has shown a distance to the transition state of 0.01 nm for both undamaged and UV-damaged DNA substrates (Figure 46A and B). This is because there is little tension-dependent variation in the lifetime. It is important to note that the lifetime at low tensions fluctuates a lot due to the small number of binders. More interestingly, Bell fitting of the attachment rate constant of UvrB-mNeonGreen shows a distance to the transition state of -0.20 nm and -0.21 nm when using undamaged and UV-damaged DNA as substrate (Figure 46C and D). Bell fitting of the ratio of UvrB per UvrA shows a very similar distance to the transition state of -0.34 nm and -0.35 nm when using undamaged and UV-damaged DNA as substrate (Figure 47A and B).

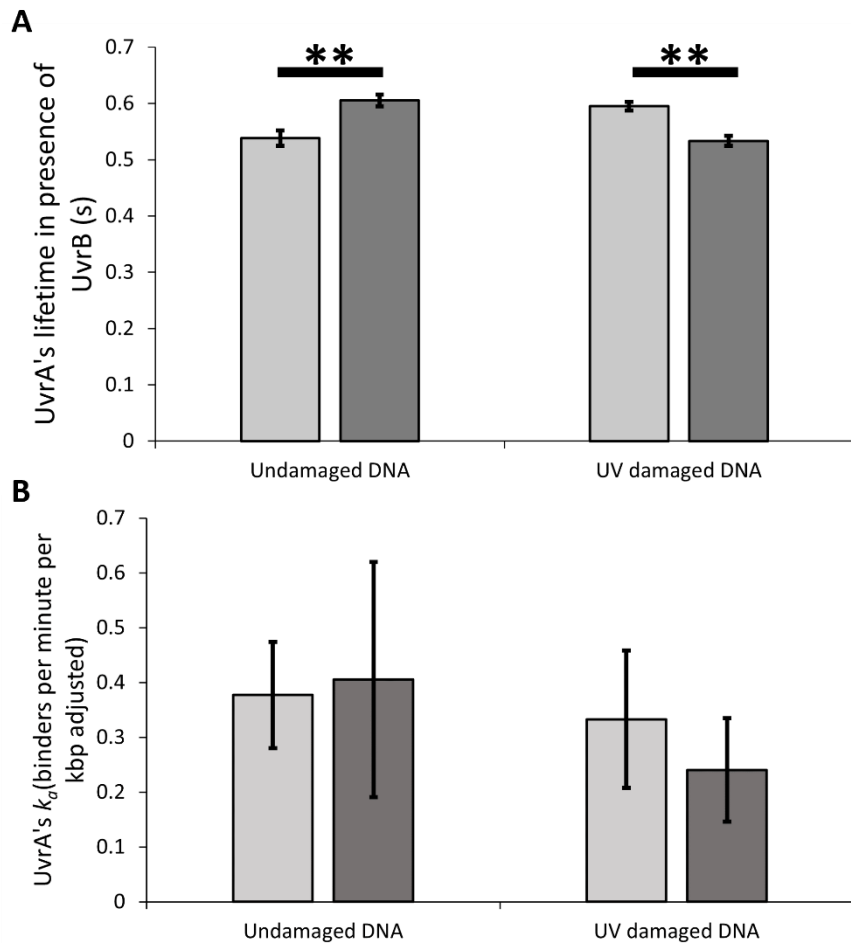


Figure 44: Purified UvrA's kinetics in the presence of purified UvrB. When 25 nM of purified UvrA-mScarlet x2 is in the presence of 50 nM of lysate UvrB-mNeonGreen, **A:** the lifetime of 25 nM UvrA-mScarlet x2 is not affected by the increase of tension from 10 pN (0.54 ± 0.01 s) to 50 pN (0.61 ± 0.01 s) for undamaged DNA (n binders: 567 and 876 respectively; n strands: 2 and 3 respectively; R^2 : 0.99 for both; P -value: 0.008) nor for increases of tension from 10 pN (0.60 ± 0.01 s) to 50 pN (0.53 ± 0.01 s; P -value: 0.0008) for UV-damaged DNA (n binders: 1197 and 608 respectively; n strands: 3 for both; R^2 : 0.99 for both). **B:** Similarly, UvrA's attachment rate isn't affected by the increase in tension nor the presence of UV damage. The attachment rate goes from 0.38 ± 0.10 binders per minute per kbp (adjusted) to 0.41 ± 0.21 binders per minute per kbp (adjusted) when the tension increases from 10 pN to 50 pN while using undamaged DNA as substrate. When UV-damaged DNA is used, the attachment rate goes from 0.33 ± 1.13 binders per minute per kbp (adjusted) to 0.24 ± 0.09 binders per minute per kbp (adjusted). Error bars for the lifetime represent the errors of the exponential fit. Error bars for the attachment rate constant represent the standard error of the mean.

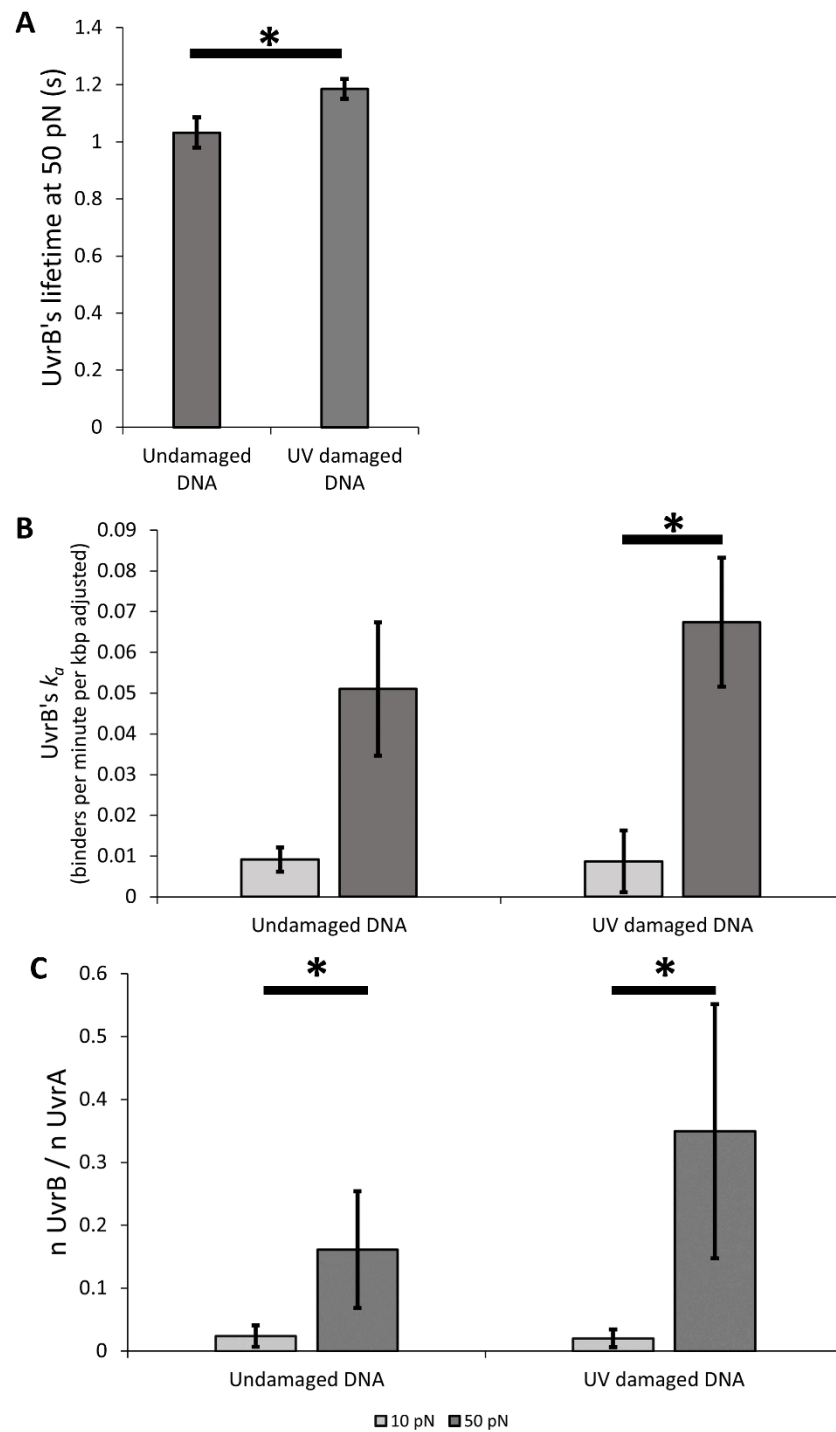


Figure 45: Kinetics of purified UvrB-mNeonGreen. **A:** The lifetime of 50 nM of UvrB-mNeonGreen at 50 pN shows a slight difference between undamaged DNA (1.03 ± 0.05 s) and UV-damaged DNA (1.19 ± 0.03 s) (n binders: 128 and 186 respectively, R^2 : 0.96 and 0.99 respectively; P -value: 0.01). However, the number of UvrB binders at 10 pN was too small to properly estimate the lifetime resulting in poor exponential fits (n binders: 14 for both; R^2 : 0.81 and 0.86). **B:** The

binding of UvrB binders per minute per kbp increases from 0.01 ± 0.003 binders per minute per kbp to 0.05 ± 0.02 binders per minute per kbp when the tension goes from 10 pN to 50 pN using undamaged DNA (*P*-value: 0.07), resulting in an increase of 458 %. A similar increase is observed when using UV-damaged DNA where the number of UvrB binders per minute per kbp increases from 0.01 ± 0.01 binders per minute per kbp to 0.08 ± 0.02 binders per minute per kbp, resulting in an increase of 680 % (*P*-value: 0.04). **C:** The proportion of UvrB to UvrA increases from 2 ± 0.9 % to 15 ± 1.5 % when using undamaged DNA (*P*-value: 0.03) and from 2 ± 0.5 % to 31 ± 2.8 % when using UV-damaged DNA (*P*-value: 0.04). Error bars for the lifetime represent the errors of the exponential fit. Error bars for the attachment rate constant represent the standard error of the mean.

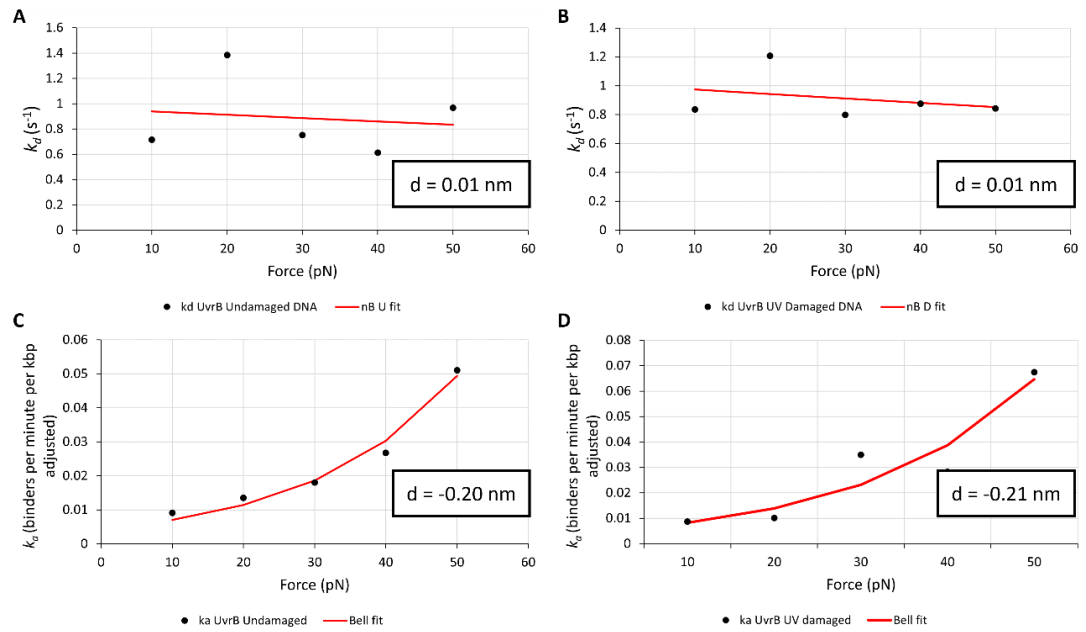


Figure 46: Effect of Tension and UV on UvrB-mNeongreen's binding to DNA. **A:** Bell fitting of the detachment rate constant of UvrB-mNeonGreen shows a distance to the transition state of 0.01 nm when using both undamaged or **B:** UV-damaged DNA as substrate. **C:** Bell fitting of the k_a of UvrB shows a distance to the transition state of -0.20 nm when using undamaged DNA and of **D:** -0.21 nm when using UV-damaged DNA as substrate.

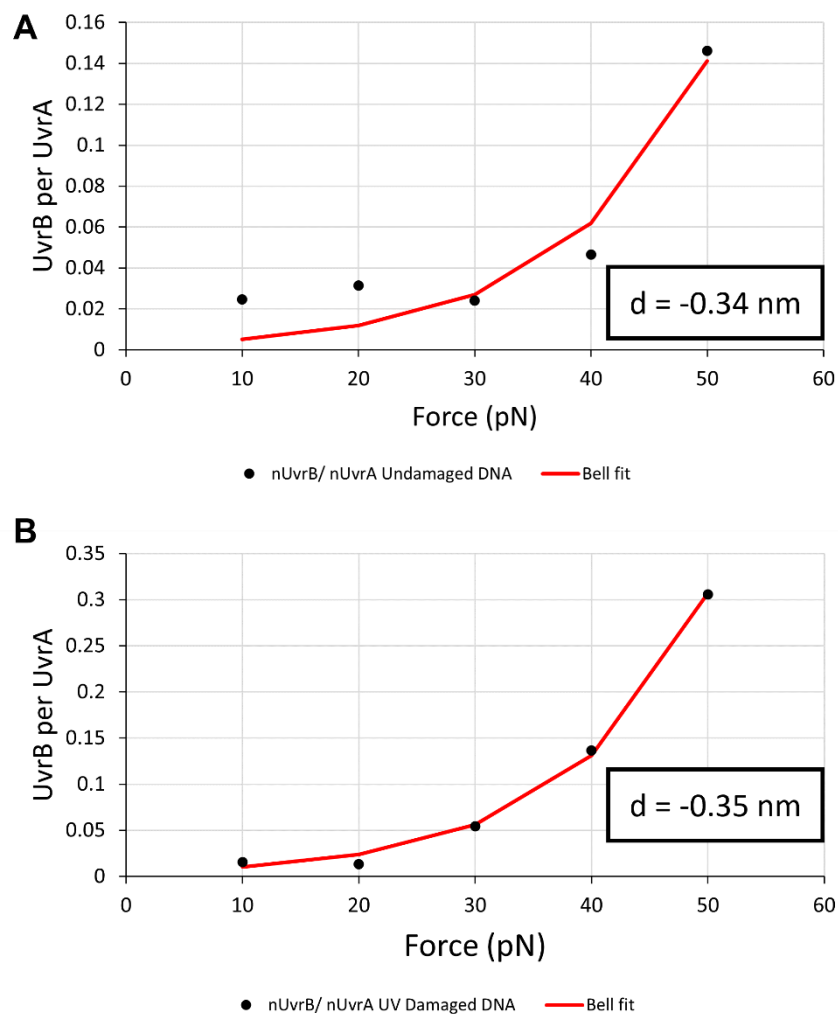


Figure 47: Effect of tension and UV damage on the recruitment of UvrB by UvrA.

A: Bell fitting of the ratio of UvrB-mNeonGreen per UvrA-mScarlet x2 shows a distance to the transition state of -0.34 nm when using undamaged DNA and of **B:** -0.35 nm when using UV-damaged DNA as substrate.

3.4 Discussion

How NER recognizes a plethora of DNA damage types while having only a few proteins involved is puzzling. It has been proposed that NER recognizes distortions in DNA such as changes in structure and/or changes in flexibility (196). However, no solid evidence has been put forward. The work presented in this chapter shows several UvrA constructs in the presence or absence of various sources of DNA damage and/or changes in tension to bring forward evidence on a mechanism of action.

3.4.1 UvrA binding is influenced by DNA tension, UV damage and Fluorescein lesions.

3.4.1.1 UvrA's binding is influenced by DNA tension.

Change of DNA tension from low (10 pN) to high (45 pN) increases UvrA's on-rate by 135 % (P-value: 0.04) and lifetime from 1.43 ± 0.04 s to 2.28 ± 0.08 s (P-value: <0.0001) when using 5 nM of purified UvrA-mNeonGreen (Figure 35). When 5 nM of purified UvrA-mScarlet is used in combination with 10 nM of lysate UvrB-mNeonGreen, there is also an increase of the on-rate of UvrA-mScarlet by 382 % (P-value: 0.008) and of the lifetime from 0.42 ± 0.01 s to 0.78 ± 0.01 s (P-value: <0.0001) (Figure 39). This shows a clear effect of the increase in tension of the DNA strand on UvrA's binding ability to DNA. This is in accordance with the changes in decorations observed under flow in . Interestingly, this shows a difference between the two constructs (UvrA-mNeonGreen and UvrA-mScarlet), but both shows a significant increase of both lifetime and attachment rate constant in the presence of tension. However, using a high concentration (25 nM) of purified UvrA-mScarlet x2 shows no differences in either the on-rate or the lifetime when going from low (10 pN) to high (50 pN) DNA tension (Figure 42). There are also no differences in between low and high DNA tension when UvrA-mScarlet x2 is in the presence of a high concentration (50 nM) of purified UvrB-mNeonGreen (Figure 44). This change of behaviour of UvrA at high concentration could either be due to the increase of concentration of the protein which increases its ability to bind to

the DNA, indeed UvrA is a dimer with a dimerization constant of 10 nM (50), which is higher than what was used in our low concentration experiments (5 nM) and much lower than what was used in our high concentration experiments (25 nM). It could also be due to the different constructs that were used. Indeed, the data that shows an effect of the tension on the binding ability of UvrA is the shorter ones (UvrA-mNeonGreen or UvrA-mScarlet) while the one that doesn't show an effect is a longer construct (UvrA-mScarlet x2).

3.4.1.2 UvrA's binding in the presence of UV damage shows conflicting results.

The effect of UV damage on the binding of UvrA shows conflicting results throughout this thesis. The effect of UV on the lifetime of 5 nM of UvrA-mNeonGreen from the lysate is unclear as it seems to have reduced the lifetime from 1.43 ± 0.04 s to 1.07 ± 0.02 s for low tension (10 pN; P-value: <0.0001) and increased the lifetime from 2.28 ± 0.08 s to 3.28 ± 0.10 s for high tension (45 pN; P-value: <0.0001) (Figure 35). When 5 nM of purified UvrA-mScarlet is used with 10 nM of lysate UvrB mNeonGreen, the lifetime increases at low tension (10 pN; P-value: <0.002 from 0.42 ± 0.01 s to 0.63 ± 0.01 s but slightly decreases from 0.78 ± 0.01 s to 0.72 ± 0.01 s at high tension (45 pN; P-value: 0.0004) (Figure 39). Finally, high concentrations of purified UvrA-mScarlet x2 alone or in combination with a high concentration of purified UvrB-mNeonGreen show very little difference in lifetime in-between undamaged and UV-damaged strands despite being statistically significant (Figure 42 and Figure 44).

It is not possible to compare the on-rate between undamaged and UV-damaged DNA when using 5 nM of lysate UvrA-mNeonGreen alone or 5 nM of purified UvrA-mScarlet with 10 nM of lysate UvrB-mNeonGreen because those experiments were performed on different days and UvrA's on-rate varies too much from one day to the next. However, it is still possible to assess the increase in the attachment rate constant between low- and high-tension conditions on different days, thereby allowing a comparison between undamaged and UV-damaged DNA. As such the attachment rate of 5 nM lysate UvrA-mNeonGreen shows a significant

increase of 135 % (P-value: 0.04) in the absence of DNA damage and 94 % (P-value: 0.01) in the presence of UV damage (Figure 35). This difference of 41 % might be due to UvrA-mNeonGreen binding more easily at low tension because of the presence of UV damage. Similarly, the attachment rate of 5 nM of purified UvrA-mNeonGreen in the presence of 10 nM of lysate UvrB-mNeonGreen shows an increase of 382 % (P-value: 0.008) in between low and high tension of undamaged DNA and 26 % (P-value: 0.51) in-between low and high tension of UV-damaged DNA (Figure 39). The lack of significance might also indicate higher recruitment of UvrA to the DNA at low tension because of the presence of UV lesion sites.

It has previously been shown that UV damage induces UvrA to increase the lifetime of UvrA (48). However, in that study 1000 J/m² was used on tightropes while 40 J/m² was used here. This is a 25-fold difference in irradiation which corresponds to an increase in the number of expected CPDs from 43 to 1,072 per DNA strand. Therefore, the lack of consistent results in the lifetime might be due to noise pollution of UvrA binding to undamaged DNA. However, irradiation of DNA strands at 1000 J/m² resulted in DNA strands that disconnected from the beads very easily, rendering experiments difficult. This is why a lower dose of irradiation was used.

3.4.1.3 UvrA's binding in the presence of Fluorescein shows an effect on the off-rate but not on the attachment rate.

UV damage occurs randomly across the DNA strand. However, using nick translation allowed for the incorporation of lesions at specific places on the DNA strand. Fluorescein was the perfect candidate as it is a substrate of NER and is fluorescent which allows for precise localisation of the lesions onto the DNA strand. This allows for a comparison of UvrA's DNA binding for both damaged and undamaged DNA within the same strand. Binders within 144 nm of the lesions show a longer lifetime compared to those outside of this 144 nm range from lesions (lifetime proximal to the lesion: 1.62 ± 0.06 s; lifetime distal from the lesion: 1.19 ± 0.03 s; P-value: <0.0001) (Figure 37C). However, there is no statistical

differences between the attachment rate constant of UvrA-mNeonGreen proximal and distal from the lesion (P-value: 0.41). Fluorescein is a well-known target of NER. We have shown earlier that the distortion to the DNA strand produced by increasing the tension resulted in an increase in the lifetime and attachment rate constant of UvrA. However, fluorescein lesions induced only an increase in the lifetime. This could be due to the structural differences between DNA that is stretched in one direction, and the unique distortion caused by the presence of fluorescein on the DNA strand.

3.4.1.4 Bell fitting of UvrA-mNeonGreen's binding.

Measuring both the attachment rate, the off-rate, and the equilibrium dissociation constant of UvrA-mNeonGreen binding at different tensions allows for Bell fitting and therefore for extrapolation of the distance to the transition state. The distance to the transition state when using undamaged DNA as the substrate is 0.05 nm, -0.10 nm and 0.19 nm for the off-rate, the attachment rate, and the equilibrium dissociation constant respectively of UvrA-mNeonGreen. In the presence of UV damage, those go to 0.16 nm, -0.06 nm, and 0.32 nm (Figure 36).

The work presented here shows that both the off-rate and the attachment rate are affected by UV damage as the distance to the transition state for the off-rate increases and the distance to the transition state for the attachment rate decreases as illustrated in the free energy landscape in Figure 48. It was shown that UvrA binds best to damaged DNA but is capable of binding to undamaged DNA (12). Interestingly, it is not the protein that is subjected to the tension here but the DNA. When forces are applied to the DNA, it changes the structure of the DNA progressively as the tension increases. Our hypothesis is that it would reach a theoretical optimal fit for the protein.

The distance to the transition state is a measure of how the rate constant responds to load. A higher distance to the transition states for the on-rate or the off-rate means that more work needs to be done on the molecule to get over the transition barrier. In our case, UvrA's binding to DNA is assessed by applying forces

to the DNA and not to the protein itself. This means that we are assessing the effect of the load applied on the substrate of UvrA on UvrA's ability to bind to it. However, UvrA has a complex binding behaviour. Simply, collisional binding allows binding of UvrA-ATP to the DNA strand, which relates to the attachment rate constant (illustrated in Figure 48). This is followed by hydrolysis of ATP which leads the protein to unbind to the DNA (relating to the detachment rate constant) (48). As load changes the structure of the DNA, we are assessing how much change is required for the protein to optimally bind to DNA, which could be how much change is required for the DNA to be recognized as damage.

In our case, the presence of UV damage alters the energy landscape by getting the unbound UvrA-ATP state closer to the first transition state and the UvrA-ATP bound state further from the second transition states (as illustrated in Figure 48). By tilting of the axis of the free energy landscape, it relates to alteration of the different energy barriers (Figure 48).

Bell fitting of the dissociation constant gives the change in the equilibrium position of the UvrA's molecule due to the application of load on the DNA (200). As such it is the combined effect of load of the on-rate and the off-rate.

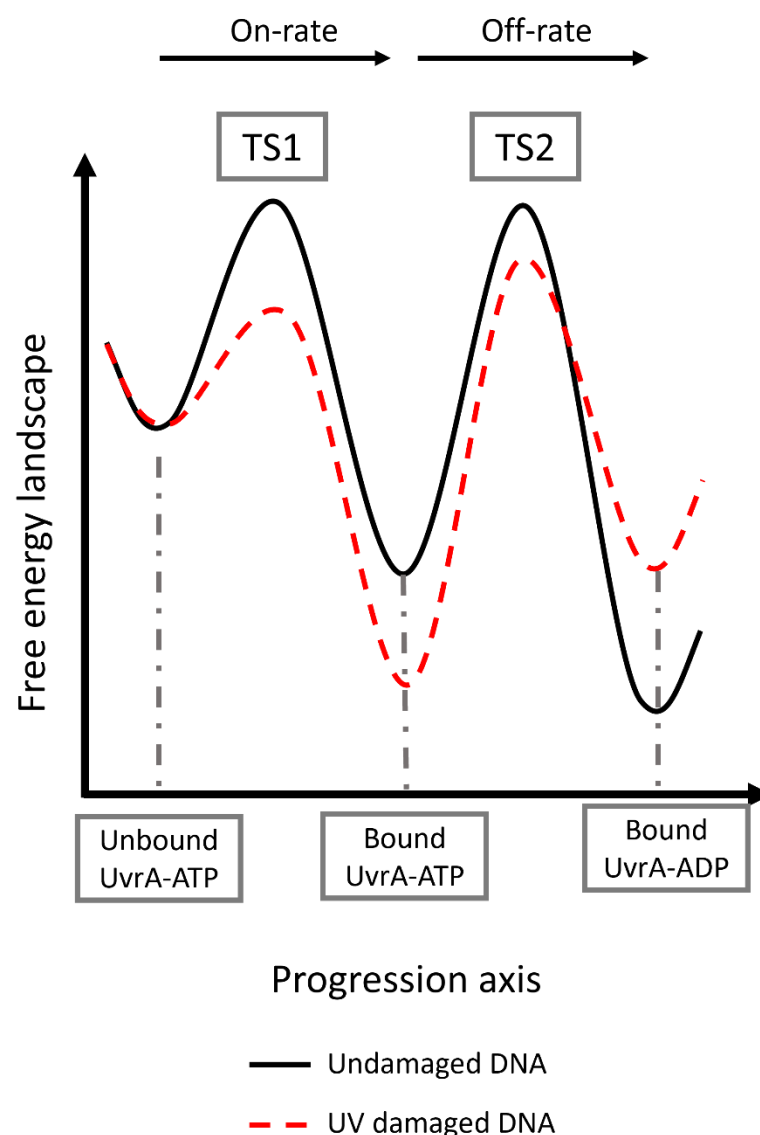


Figure 48: Free energy landscape of UvrA-mNeonGreen lysate when using undamaged or UV-damaged DNA as substrate. The binding of UvrA to DNA is a complex phenomenon. Its free energy landscape can be approximated as presented here in black where collisional binding occurs resulting in UvrA-ATP molecules binding to the DNA (On-rate). This is followed by hydrolysis of ATP which helps UvrA to release from the DNA (Off-rate) (48). Unbinding of UvrA-ADP from the DNA is very quick and therefore not rate-limiting. However, upon the addition of UV-damage (in red here), the corresponding free energy landscape shows some differences. Since the distance to the transition state for the attachment rate constant is lower than for undamaged DNA, it results in a tilting in the y-axis of the energy barrier of the first transition state (TS1). Similarly, the distance to the transition state for the detachment rate constant is higher in the presence of UV-damage, resulting in a tilting in the y-axis of the energy barrier of the second transition state (TS2). Overall,

upon the addition of UV damage, the protein binds faster to the DNA and stays on the DNA for a longer amount of time.

DNA extension has been described as following a worm-like chain model (237,238). This means that as tension is applied to the DNA, small changes in structure will occur at many places on the DNA instead of acutely at a smaller number of locations. It was suggested that DNA structural perturbations induced by the DNA-damaging agents could be recognized by repair enzymes (196). We hypothesize that the change in structure that happens when the DNA is stretched resembles the changes that occur in DNA lesions that are recognized by UvrA and therefore allows UvrA to bind to the DNA. It is also possible that the DNA might be transiently opening into single-stranded DNA pockets as the DNA is stretched. It was shown that UvrA has a greater affinity for single-stranded DNA than double-stranded DNA (246). However, this still could be indicative of what is happening with damage where slight changes of structures would resemble single-stranded DNA and therefore increase binding of UvrA to the site.

UvrA recognizes a plethora of damage which alters the DNA in a plethora of ways. Despite our experiments providing proof that DNA topology is simulating DNA damage enough for UvrA to recognize it, the distances to the transition state give just an approximation of what is the minimum DNA structure alteration to be recognized as damage when the DNA is stretched linearly. As such the DNA only needs to stretch an Ångström to affect the attachment rate and of half an Ångström to affect the off-rate of UvrA's binding to the DNA. UvrA has a footprint of 33 bp (247). With 3.4 Å per base pair, a modification in length at the resolution of an Ångström relates to a change of 0.9 % and 0.5 % of UvrA's total footprint for the attachment rate and the off-rate respectively. And we propose that is sufficient to be recognized as damage. Interestingly, a change of 0.5 % and 1.4 % is necessary for the recruitment of UvrA on UV-damaged DNA strands for both the attachment rate and the off-rate respectively. Those numbers were expected to be smaller than the ones for undamaged DNA. However, numerous UvrAs do bind to the undamaged part of the DNA strand, reducing the signal to noise.

Furthermore, the localised distortions of the UV damage might interact with UvrA differently than the lateral stretching.

3.4.2 UvrB's binding is influenced by DNA tension and UV damage.

UvrB has been used here under two different conditions. Either at low concentration (5 nM purified UvrA-mScarlet with 10 nM of lysate UvrB-mNeonGreen) or at high concentration (25 nM purified UvrA-mScarlet with 50 nM purified UvrB-mNeonGreen). At low tension (10 pN) for both of those conditions, when using either undamaged or UV-damaged DNA as substrate, the number of UvrB-mNeonGreen binders was too low to properly estimate its lifetime. At high tension (45 pN and 50 pN), the lifetime of UvrB at low concentration is 1.38 ± 0.06 s when using undamaged DNA as the substrate to 1.56 ± 0.07 s when using UV-damaged DNA as the substrate (Figure 40A; P-value: 0.02). This increase was also seen when using a high concentration of UvrB where the lifetime went from 1.03 ± 0.05 s to 1.19 ± 0.03 s (Figure 45A; P-value: 0.014). However, those lifetimes are much shorter than the one observed in literature with a UvrB lifetime of 12 s and 16 s for undamaged and damaged DNA respectively *in vivo*, and a UvrAB lifetime of 40 s for undamaged DNA *in vitro* (13,15). This might suggest that UvrB is not recruited to the damage properly.

UvrB can either be recruited to DNA by UvrA or bind as an already formed UvrA₂B or UvrA₂B₂ complex (15,17,18). It seems clear that UvrB binding was influenced by the tension as the number of UvrB binders increased greatly with increases in tension. However, a big bias is UvrA's recruitment to the DNA strand being already affected by the tension. Therefore, to assess the effect of the tension on the recruitment of UvrB, it is necessary to look at the evolution of the ratio UvrB to UvrA as the tension increases. UvrB has been used in two conditions. First, 5 nM of purified UvrA-mScarlet was used with 10 nM of lysate UvrB-mNeonGreen (That lysate was produced in BL21 $\Delta uvrA \Delta uvrB$, therefore, no wild-type versions of UvrA and UvrB were present within the lysate). In those conditions, the ratio of UvrB to UvrA goes from 4 ± 4 % to 17 ± 6 % (P-value: 0.12) when using undamaged DNA as

substrate. The ratio of UvrB to UvrA goes from $6 \pm 3 \%$ to $34 \pm 7 \%$ (P-value: 0.02) when going from low- to high-tension; using UV-damaged DNA as substrate (Figure 41). Similar increases in the ratio of UvrB to UvrA are seen when using 25 nM of purified UvrA-mScarlet x2 with 50 nM of purified UvrB-mNeonGreen. Indeed, under those conditions, the ratio of UvrB to UvrA goes from $2 \pm 0.9 \%$ to $15 \pm 1.5 \%$ (P-value: 0.03) when using undamaged DNA and from $2 \pm 0.5 \%$ to $31 \pm 2.8 \%$ (P-value: 0.04) when using UV-damaged DNA (Figure 45B). Interestingly, there are extremely similar values for both the low-concentration experiment using lysate UvrB and the high-concentration experiment using purified UvrB. This might suggest that the recruitment of UvrB to the DNA strand is indeed affected by the tension. Furthermore, the lack of differences between the use of purified proteins and lysate validates the use of lysate. The low number of UvrB binders (n=23) at low tension when using a low concentration of UvrB is probably responsible for the non-significance of the increase in the UvrB to UvrA ratio in the undamaged DNA strand. It also suggests that this recruitment might be affected by the presence of UV damage. Overall, it seems like the increase in tension might help UvrB's recruitment by UvrA to UV damage sites. However, the difference in high tension from $17 \pm 6 \%$ to $34 \pm 7 \%$ at low concentration and from $15 \pm 1.5 \%$ to $31 \pm 2.8 \%$ at high concentration when using UV-damaged DNA as substrate is not statistically significant. It is important to note that those experiments had some major variations between them. Indeed, the low-concentration experiment was performed with lysate UvrB-mNeonGreen and purified UvrA-mScarlet while the high concentration was done with purified UvrB-mNeonGreen and purified UvrA-mScarlet x2. Another variation is that the "high tension" was done at 45 pN for the low-concentration experiment while it was done at 50 pN for the high-concentration experiment. Altogether, it is important to approach those results with a critical eye. Further repeats need to be done to further assess UvrB's binding to DNA strands with both UV damage and tension changes. Bell fitting of the ratio of UvrB to UvrA shows a distance to the transition state of 0.34 nm and 0.35 nm for undamaged and UV-damaged DNA respectively. UvrB's footprint

being 20 bp (248), those accounts for a decrease of 5 % and 5.1 % of the number of base pairs that UvrB is covering when bound to DNA which accounts for the size of a full base pair. The addition of load seems to be sufficient for UvrA to recruit UvrB. However, as mentioned earlier UvrB dwell time on the DNA is much lower than expected and could indicate that despite being recruited to the lesion, UvrB doesn't process the lesion correctly.

3.4.3 Kinetics discrepancies with literature.

UvrA kinetics have shown a lot of variability within this thesis. However, it has also shown a lot of variabilities in literature. Most studies have been performed with thermostable versions of the protein (15,244,249,250). Furthermore, the attachment rate constant has not been the main focus of those studies which preferred to focus on the detachment rate constant. This is because of the experimental design of some of those studies that shows huge variabilities in attachment rate constant. However, those studies also have disparities in the values for their lifetime of NER proteins. For example, in vivo study of *E. coli* proteins shows a lifetime of UvrA of 3 s with undamaged DNA and 12 s with damaged DNA (13). This is much different to our lifetime values described in this thesis which range from 0.42 s to 1.43 s when under no tension and no DNA damage, depending of the experiments, and from 0.78 s to 3.28 s when under tension and/or in presence of damage. Similarly, UvrB binding to the DNA strand shows huge discrepancy with literature with lifetimes being around 1.38 s to 1.56 s while it was shown in vivo to be 11.8 s in absence of damage and 15.6 s in presence of damage (13). Those discrepancies could be explained by the fact that in single molecule experiments, each slight variations of the experimental design can have huge impact on the outcome of the experiment. However, consistency between experiments, and performing experiments in parallel on the same days allows for results to be comparable with each other's.

3.5 Conclusion

NER can recognize and process a plethora of DNA lesions. Lesions induce DNA distortions that change the structure and/or the flexibility of the DNA locally, and it has been suggested that it is those changes that are recognised by NER instead of the lesion itself (196). However, those claims have not been backed up. This chapter put forward evidence that DNA changes of structures are indeed sufficient to affect the recruitment of both UvrA and UvrB. It could be a universal mechanism on how other DNA damage repair proteins recognize damage.

3.5.1 Future work

Further work is needed to properly assess the effect of tension on UvrB binding to DNA. Indeed, the number of binders at low tension was too small to properly assess its lifetime.

UvrA is a protein that has a complex behaviour. Much of UvrA's complex behaviour is due to the presence of proximal and distal ATPase cassettes that have an important role in damage recognition. It would be interesting to see how mutants of either or both ATPase cassettes would behave under various tensions. Such mutants have been used extensively to try to decipher UvrA's binding behaviour (47).

Furthermore, it would be great to assess if UvrC, the subsequent protein involved in NER, is also affected by changes in tension. UvrC is the protein that cleaves the DNA both upstream and downstream of the lesion.

3.5.2 Future optimisations

The work presented here offers opportunities for improvement. Repeats of experiments while addressing these areas would increase the quality of the data acquired.

Firstly, most of the videos were captured at a rate of 2 Hz but the C-Trap is well capable of going faster. Increasing the frame rate would allow to increase in the

precision of the lifetime measurement, especially since the lifetime of some binders was at their lowest around 0.42 s. It was also shown that UvrA has a fast binding behaviour that we could not see at all using this framerate of 2 Hz (219). However, increasing the framerate also induces an increase in the photobleaching, hence why it wasn't done here. A solution would be to also diminish the laser power and/or the exposure time. This could alter the signal-to-noise ratio and that could have been a problem due to our experiment showing great variability in the background fluorescence depending on the concentration of the protein used and the flow applied.

Secondly, most experiments were performed using a protease inhibitor mix as it was shown to help UvrA's binding to DNA as shown in Figure 32. However, it will be shown in Chapter IV that Aprotinin, one of the components of the protease inhibitor mix is an inhibitor of NER by increasing UvrA's ability to bind to DNA and its lifetime (Figure 53, Figure 54C, Figure 55). Even though Aprotinin is in small quantities in the protease inhibitor mix, it did introduce a bias.

Thirdly, UV damage to DNA might have been too light to assess its effect on UvrA's binding to DNA. Indeed, UvrA does bind to undamaged DNA and 40 J.m² of irradiation with 254 nm UV might have been not enough to distinguish between UvrA binding to undamaged DNA and UvrA binding to UV-damaged DNA. Previous experiments were done with UV-damaged DNA tighropes that were damaged by being irradiated with 1000 J.m² of 254 nm UV(48). However, a large proportion of those strands were breaking prematurely when trying to tether them to the C-Trap, hence the use of a lower dose of UV. Furthermore, 40 J.m² was previously used by another laboratory when studying a eukaryotic NER protein (251).

Fourthly, binding events analysed at low tension are already at a significant amount of DNA tension. Indeed, much NER data has been gathered using DNA tighropes instead of DNA tethers. It was shown that such tighropes were at a tension of 2.2 pN (244), much lower than our 10 pN "low tension" measurement.

Chapter IV: Understanding the mechanism of antimicrobial action: the effect of NER inhibitors on UvrA's DNA binding ability

4.1 Introduction

Cancer is one of the greatest challenges of modern medicine and is the second most common cause of death worldwide (252). Cancer treatments usually target fast-growing cells, which is ideal for hindering cancer growth. A classic cancer medicine is cisplatin, a compound that is used to treat different types of cancers like sarcomas, lung cancer, ovarian cancer, testis cancer, bone cancer, etc (253,254). Cisplatin inhibits cell division by crosslinking purine bases on the DNA, therefore interfering with DNA replication/repair mechanisms leading to apoptosis (254). This was first shown in *E. coli* where cell segmentation was inhibited leading to growth up to 300 times longer than normal (255). One of the big risks of cisplatin chemotherapy is suppression of neutrophil number, leading to severe neutropenia (256), which is highly detrimental to the immune system (257,258). A direct link between the duration and severity of circulating white blood cells and the risks of infections has been demonstrated (259). This is not anecdotal. Despite causes of death for cancerous patients differ depending on the type of cancer, patient age, follow-up time, etc., infection is one of the leading causes of noncancer deaths after heart disease (260–262). This is partially due to treatments causing physical barrier damage (261,263). For example, it was shown that cisplatin treatment causes mucositis by reducing the quantity of mucin, a component of mucus that is known to play an important role in physiological defence (264). Furthermore, chemotherapy causes the thinning of the epithelium by disrupting the basal cells and inducing apoptosis, therefore rendering this physical barrier less effective at preventing infections (265,266).

Another danger is the rise of antibiotic-resistant bacterial strains that make for tough challenges in patient survivability (262,267). Indeed, 25,000 patients die every year in Europe only from multidrug-resistant bacterial infections (87). There is a growing concern that antimicrobial resistance would become such a threat that the world would effectively return to a pre-penicillin state where infections

would get deadlier (88). The search for new antimicrobials is, therefore, a necessity but is hindered by the extreme costs of developing new drugs, the high risk of failure, and the speed at which antimicrobial resistance can be acquired by bacteria (268–270).

To tackle antimicrobial resistance, we have proposed NER as a potential candidate for an adjuvant antibiotic for cancerous patients (91,271,272). The reasoning is that cisplatin-like compounds damage DNA, and said damage is repaired by NER in both the patient and hazardous bacteria. By inhibiting prokaryotic NER, the bacteria's ability to thrive when its DNA is damaged is hindered. However, NER is not essential for bacteria when there is no damage to the DNA. It is important to note that NER has a similar method of action for prokaryotes and eukaryotes, but the proteins are not conserved (273). This means that inhibition of prokaryotic NER does not affect the patient's cells.

4.1.1 Project aim

This chapter studies how specific NER inhibitors affect the characteristic binding of UvrA to undamaged DNA. The compounds used here originated from different studies and experiments were performed in close collaboration with other members of the lab. Notably, Lorenzo Bernacchia and Arya Gupta gathered relevant data upstream and downstream of my implication in this project. This work resulted in several publications (91,271,272). The use of the C-Trap was essential as it allowed to give single molecule level intelligence of the molecular mechanism behind the simple functional inhibition of NER that was observed *in vivo*. Using an OAF microscope would have resulted in lifetime data but would have lacked the on-rate data (which is more difficult to gather because of the variability in on-rate between flow cells). Furthermore, the C-Trap allows for use of the same DNA strand in both untreated and treated conditions by simply moving the DNA strand from one chamber to another. Overall, other methods could have provided interesting insights, but the C-Trap was an easy and simple way to gather much data in a time efficient manner.

4.1.2 Compounds background: ATBC

Prior to this study, ATBC (structure shown in Figure 49) was the only described inhibitor of the prokaryotic UvrABC NER system after a screening of 38000 small chemical compounds on *Mycobacterium smegmatis* (274). It was then further confirmed as an inhibitor of UvrA's function and shown to inhibit the growth of bacteria in the presence of DNA-damaging agents (271). The localisation of ATBC's binding to UvrA was checked using *in silico* docking and shown to be in the same cavities as ATP, suggesting an effect on UvrA's ATPase capabilities. It was confirmed to be affecting UvrA's ability to hydrolyse ATP as shown in Figure 50 (data gathered and analysed by Lorenzo Bernacchia).

4.1.3 Compounds background: L-Thyroxine, Dienestrol and Aprotinin

To find new NER inhibitors, a screen of more than 2700 FDA (Food and Drug Administration) approved compounds was performed which highlighted L-Thyroxine, Dienestrol and Aprotinin among others as compounds of high interest (structures shown in Figure 49) (272). The three compounds show a great reduction in the ATPase activity of UvrA as shown in Figure 50.

L-Thyroxine (for levothyroxine) is a synthetic isomer of Thyroxine (T4) that is both biochemically and physiologically identical (275). It is commonly used as a substitution for the naturally produced human thyroid hormone in the treatment of subclinical hypothyroidism which is linked to cardiovascular diseases (276).

Dienestrol is a synthetic non-steroidal oestrogen. It is used to treat atrophic vaginitis (thinning of the vaginal epithelium) and kraurosis vulvae (lesions of the vulvae that can occur post-menopause) (277,278). Interestingly it was shown to affect the genitals and fertility of the male offspring of treated gestating female rats (279).

Aprotinin is an FDA-withdrawn drug. It is a serine protease inhibitor that was used to reduce the risk of blood loss and the need for blood transfusion during surgeries (280,281). It is only used now for research after it was shown to increase the risk

of complications (282). Out of the different compounds tested in this work, it is the only one that is a small protein and therefore the biggest compound overall with a molecular weight of 6.5 kDa.

4.1.4 Compounds background: Bemcentinib

An *in-silico* approach was used to virtually dock more than 100,000 compounds to UvrA's ATPase cassettes, highlighting a high number of potential inhibitors (91). As the structure of *E. coli*'s UvrA has not been solved, the structure used in this study was generated by AlphaFold (283,284), and shows high similarity to the known thermophilic UvrA structures. The first 50 hits with the highest binding energy were assessed individually and of those hits, Bemcentinib was chosen for further study. It was shown that Bemcentinib significantly decreased UvrA's ability to hydrolyse ATP as shown in Figure 50 (structure shown in Figure 49) (271). In a medical setting, Bemcentinib is an AXL receptor tyrosine kinase inhibitor that is under investigation in several phase II trials in both cancer and COVID-19 studies (285,286). AXL is a high-value target as it plays a central part in tumour cell growth, metastasis, drug resistance, etc. (287).

4.1.5 Structures of Compounds

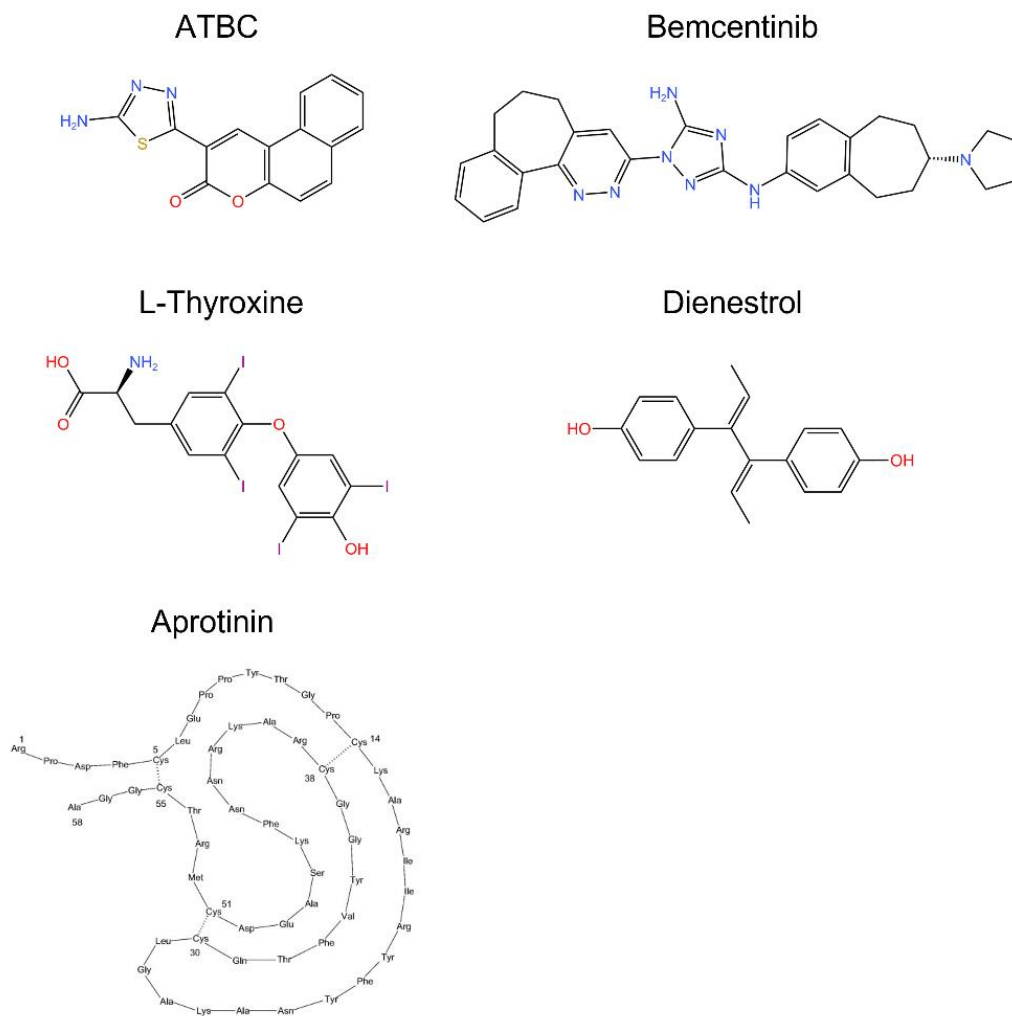


Figure 49: Chemical structure of ATBC, Bemcentinib, L-Thyroxine, Dienestrol and secondary structure of the Aprotinin peptide. PubChem CID: 399112 (ATBC), 46215462

(Bemcentinib), 5819 (L-Thyroxine), 667476 (Dienestrol). CAS: 9087-70-1 (Aprotinin). Chemical structures were drawn using the KingDraw software. Aprotinin's drawing was adapted from Fisher Scientific.

4.1.6 Effect of various compounds on the ATPase activity of UvrA

Proper hydrolysis of ATP by UvrA was previously shown to affect DNA binding (48,219). ATPase assays were performed by Lorenzo Bernacchia to assess the effect of those compounds on the ATPase capabilities of UvrA. As shown in Figure 50, all compounds show statistically significant inhibition of the ATPase

capabilities of UvrA with the exception of aprotinin when used at 20 μ M. When used at 50 μ M, aprotinin's effect becomes significant (data not shown). The reduction in ATP hydrolysis leads us to inquire how this decrease relates to UvrA's binding abilities.

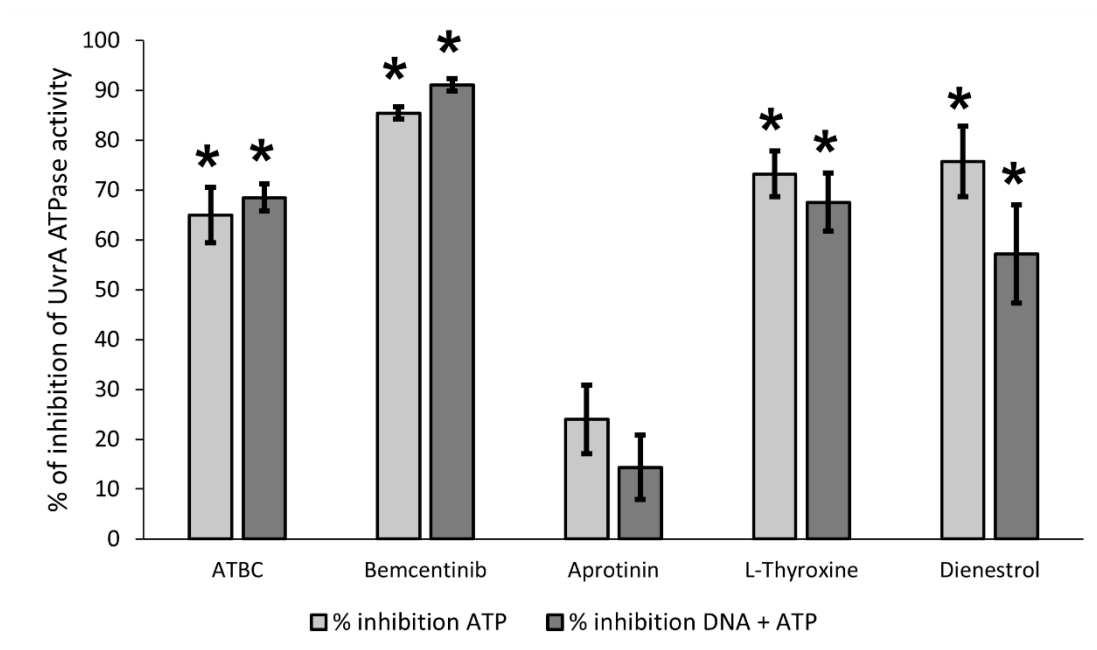


Figure 50: UvrA shows a reduction in ATPase activity when in the presence of various compounds. Data for this figure was gathered and analysed by Lorenzo Bernacchia and used in various publications (91,271,272). ATBC was used at a concentration of 50 μ M while Bemcentinib, Aprotinin, L-Thyroxine and Dienestrol were used at a concentration of 20 μ M. Asterisks mark significance: P -value < 0.05. n = 3 independent replicates for Bemcentinib, Aprotinin, L-Thyroxine, Dienestrol and UvrA without compounds. For the ATBC to no ATBC comparison, n = 6 for ATBC and n = 19 for UvrA without ATBC. The error bars represent the standard error of the mean.

4.2 Material and Methods

4.2.1 Origin and purity of compounds

ATBC was sourced from Green Pharma, Ambinter with a purity $\geq 90\%$. Bemcentinib, L-Thyroxine, and Aprotinin were sourced from MedChemExpress with a purity $\geq 98\%$. Dienestrol was sourced from Merck with a purity $\geq 95\%$.

4.2.2 Lysis preparation

UvrA-mNeonGreen lysate was prepared as described in Chapter II.

4.2.3 DNA tethering

DNA tethering was performed as described in Chapter III.

4.2.4 Video capture parameters

Videos were taken under the illumination of a 488 nm laser at 30% power with exposure synchronisation. Data from the ATBC experiment was exposed for 200 ms with a framerate of 4.3 Hz while data for all the other experiments were exposed for 100 ms with a framerate of 2 Hz.

4.2.5 Workflow for picture generation of the effect of compounds on UvrA-mNeonGreen binding to DNA.

A variety of methods have been used to estimate the effect of compounds on UvrA-mNeonGreen binding abilities. The methods vary per compound and are shown in Figure 51. These methods allowed for the realisation of a “black and white” picture shown in Figure 53. In all cases, the tethered DNA was subjected to 50 pN of force. UvrA-mNeonGreen lysate was diluted to a concentration of 5 nM in ABC buffer supplemented with 1 mM of ATP and 0.07 mg per mL of protease inhibitors as well as 1 mM of DTT for ATBC and Aprotinin and 5 mM of DTT for L-Thyroxine, Dienestrol and Bemcentinib. The same mixture was prepared and split into two parts. One part was treated with the tested compound, while the other received an equivalent volume of DMSO (except for the Aprotinin experiment as Aprotinin is dissolved in water). DMSO at high concentration (50 %) is capable of

denaturing the DNA (288) and is capable of altering the double stranded structure of the DNA at a concentration as little as 5 %. This is why the concentration of DMSO was kept below 5 % in those experiments with a concentration of 1 % for ATBC; 2 % and 0.8 % when L-Thyroxine was at 50 and 20 μ M respectively; 0.5 % and 0.2 % when Dienestrol was at 50 and 20 μ M respectively; and 2.5 % and 1 % when Bemcentinib was at 50 and 20 μ M respectively. There was no noticeable difference with samples that were not treated with DMSO (data not shown). It is important to note that for those experiments, both the treated and the untreated sample are in the presence of the same quantity of DMSO.

UvrA's binding in the presence of 50 μ M of ATBC has been imaged after putting the DNA strand under lateral flow at 0.1 Pa for 2 minutes. Then the lateral flow was stopped, and lasers and camera were turned on. The third frame was used to generate the pictures. Imaging of the effect of 50 μ M of Bemcentinib was done in similar ways but under a medial flow at 0.3 Pa for 5 minutes instead. To assess the effect of 50 μ M of Aprotinin, 20 μ M of L-Thyroxine or 20 μ M of Dienestrol a slightly different method was used where 0.3 Pa of medial flow was applied for Aprotinin while no flow was applied for L-Thyroxine and Dienestrol. Videos were recorded for 600 frames for Aprotinin and 1200 frames for L-Thyroxine and Dienestrol. They were post-processed by z-stack (standard deviation) using the Fiji package of ImageJ resulting in the pictures presented in Figure 53.

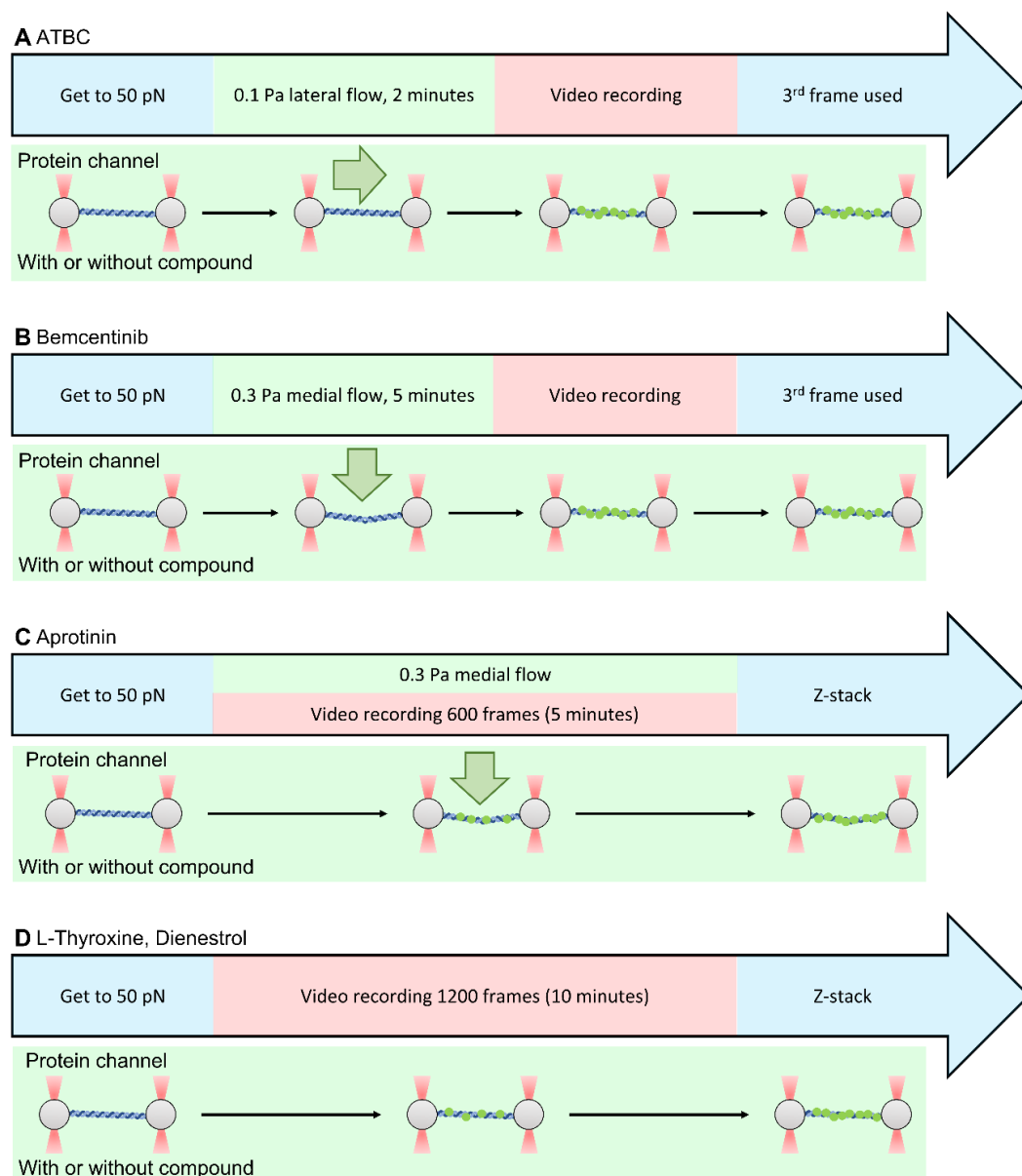


Figure 51: Breakdown of the workflows used to generate pictures of the effect of compounds on UvrA-mNeonGreen binding to DNA. **A:** Workflow for picture generation of the effect of ATBC on UvrA-mNeonGreen binding to DNA. Tethered DNA is put under 50 pN of tension and 0.1 Pa of lateral flow for 2 minutes in the presence or absence of 50 μ M of ATBC. Then the flow is stopped, and the laser and camera are turned ON. The third frame was used to generate the pictures. **B:** Workflow for picture generation of the effect of Bemcentinib on UvrA-mNeonGreen binding to DNA. Tethered DNA is put under 50 pN of tension and 0.3 medial flow for 5 minutes in the presence or absence of 50 μ M of Bemcentinib. Flow is then stopped, and the laser and camera are turned ON. The third frame was used to generate the pictures. **C:** Workflow for picture generation of the effect of Aprotinin on UvrA-mNeonGreen binding to DNA. Tethered DNA is put

under 50 pN of tension and 0.3 Pa of medial flow in the presence or absence of 50 μ M of Aprotinin. Videos are recorded for 600 frames (2 Hz, 100 ms exposure time) while the flow is still ON. Z-stacks (standard deviation) of the video were used to generate the picture. D: Workflow for picture generation of the effect of L-Thyroxine or Dienestrol on UvrA-mNeonGreen binding to DNA. Tethered DNA is put under 50 pN of tension in the presence or absence of 20 μ M of L-Thyroxine or 20 μ M of Dienestrol. Videos are recorded for 1200 frames (2 Hz, 100 ms exposure time). Z-stack (standard deviation) of the video was used to generate the picture.

4.2.6 Workflow for quantification of the effect of ATBC on UvrA-mNeonGreen binding

Using the C-Trap, DNA strands were put under 50 pN of tension in a microfluidic channel containing 5 nM of UvrA-mNeonGreen in ABC buffer supplemented with 1mM ATP, 1mM DTT and 0.07 mg/mL protease inhibitor mix, with or without 50 μ M of ATBC. 50 pN was used because we have shown previously that high tensions increase the decoration of the DNA strand with UvrA. Once at 50pN of tension the tension feedback was stopped, and medial flow was turned on in the channel at 0.2 bar of pressure for 2 minutes. Then the flow was stopped, and the 488 nm laser was turned on (30% power), followed by the recording of the video for 200 frames at 4.3 Hz with 200 ms exposure and with exposure synchronisation. This was then repeated until the DNA snapped. Kymographs were generated using the Fiji package, allowing manual counting of the number of binders per video. A summary of the workflow is presented in Figure 52A.

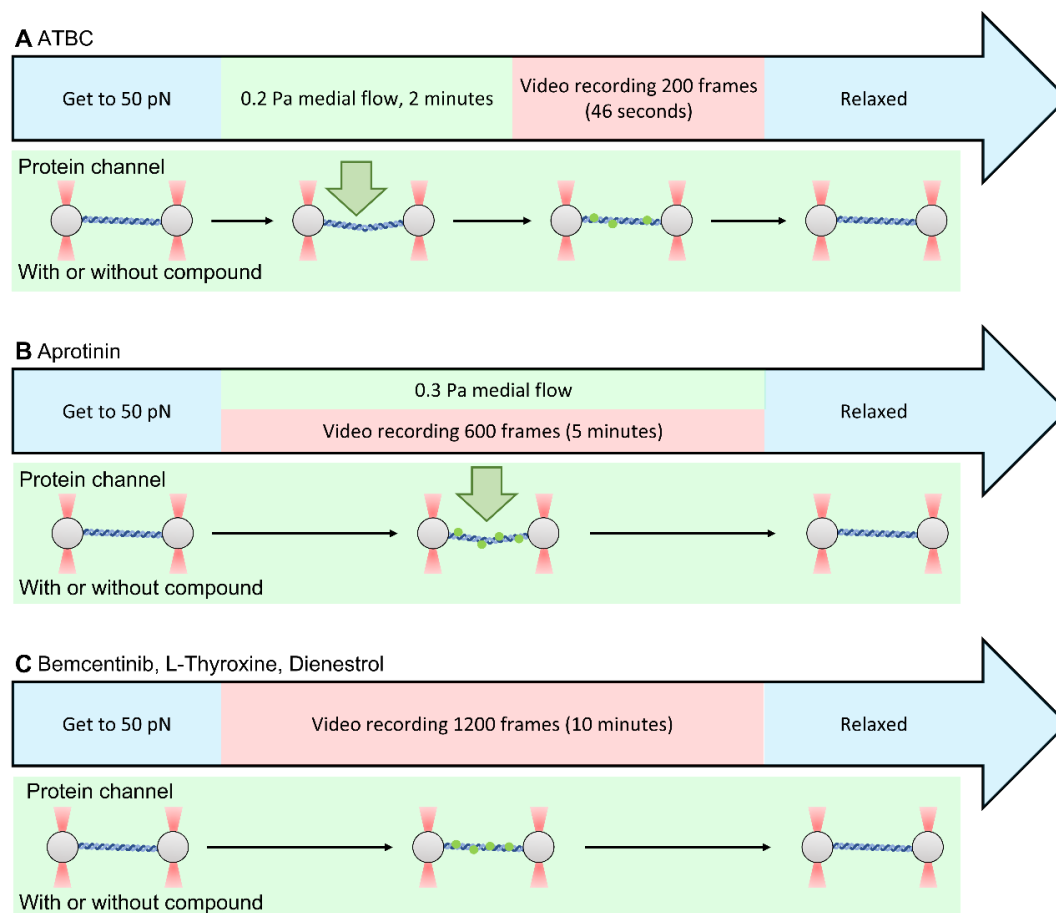


Figure 52: Workflow for quantification of the effect of compounds on UvrA-mNeonGreen binding. **A:** Workflow of data collection in the presence or absence of 50 μM of ATBC. Tethered DNA is put under 50 pN of tension and subjected to 0.2 Pa of medial flow for 2 minutes, then a laser is turned ON and video is recorded for 200 frames at 4.3 Hz with 200 ms of exposure time. The same strands were used several times and, when possible, in both treated and untreated conditions. **B:** Workflow of data collection in the presence or absence of 50 μM of Aprotinin. Tethered DNA is put under 50 pN of tension. Videos are recorded while the strands are under 0.3 Pa of medial flow, for 600 frames at 2 Hz, with 100 ms of exposure time. The same strands were used in both treated and untreated conditions when possible. **C:** Workflow of data collection in the presence or absence of 20 μM of Bemcentinib, L-Thyroxine and Dienestrol. DNA tethers are put under 50 pN of tension and videos are recorded for 1200 frames at 2 Hz with 100 ms of exposure time. The same DNA strand was used in both the untreated and the treated conditions, in this order or the other way around.

4.2.7 Workflow for quantification of the effect of Aprotinin on UvrA-mNeonGreen binding

Using the C-Trap, individual strands of DNA were put under 50 pN of forces in a microfluidic channel containing 5 nM UvrA-mNeonGreen in ABC buffer supplemented with 1 mM ATP, 1 mM DTT and 0.07 mg per mL protease inhibitor mix, with or without 50 μ M of Aprotinin. Tension feedback was turned off and 0.3 Pa of medial flow was applied to the DNA strand for the duration of the video. Videos were recorded for 600 frames at 2 Hz with 100 ms exposure and exposure synchronisation turned on using a 488 nm laser at 30 % power. Using the Trackmate plugin of ImageJ, the number of binders per strand was assessed, allowing the calculation of the number of binders per minute per kbp. Those were averaged for the strands in the presence or absence of Aprotinin respectively. A summary of the workflow is presented in Figure 52B.

4.2.8 Workflow for quantification of the effect of Bemcentinib, L-Thyroxine and Dienestrol on UvrA-mNeonGreen binding

Using the C-Trap, tethered DNA strands were moved into a microfluidic channel containing 5 nM of UvrA-mNeonGreen in ABC buffer supplemented with 1 mM ATP, 5 mM DTT and 0.07 mg per mL of protease inhibitor mix in the presence or absence of 20 μ M of compound (Bemcentinib, L-Thyroxine or Dienestrol). 50 pN of tension was then applied to the tethered DNA strand, then the tension feedback was turned off. Videos were recorded for 1200 frames at 2 Hz with 100 ms exposure and exposure synchronisation using a 488 nm laser. Thanks to the ability of the C-Trap to maintain different channels with different contents, the same DNA strand was used in both conditions with and without the compound. The tethered DNA strand was passed from the untreated channel to the treated channel, or vice versa. The overall data were processed and analysed as previously described for Aprotinin. A summary of the workflow is presented in Figure 52C. The data presented in Figure 56 originated from the same experiments but all the

strands were discriminated between those who had been in contact with the compound first and those who hadn't.

4.3 Results

4.3.1 Snapshot of the effect of various NER inhibitors on UvrA's binding to undamaged DNA

As shown in Figure 50, various NER inhibitors affect the ATPase activity of UvrA (271). As UvrA's ability to recognize lesions is ATP-dependent, it was necessary to assess the effect of those inhibitors on UvrA's ability to bind to DNA. This was done using the C-Trap. Those inhibitors are ATBC, Bemcentinib, Aprotinin, L-Thyroxine, and Dienestrol.

The effect of those inhibitors on the binding of UvrA-mNeonGreen in lysate were assessed in several steps with slight variations in protocols between compounds. First, the overall effect of the compound on the binding was determined by the capture of snapshots presented in Figure 53. This allows for a crude assessment of the effect of a compound on the overall decoration of the DNA strand by UvrA. To do so, 5 nM of lysate UvrA-mNeonGreen was mixed within ABC buffer supplemented with 1 mM of ATP and protease inhibitor as previously described and with 1 mM of DTT for ATBC and Aprotinin and 5 mM of DTT for Bemcentinib, L-Thyroxine, and Dienestrol. The same mixture was prepared and halved with one half receiving 50 μ M for ATBC, Bemcentinib, and Aprotinin and 20 μ M for L-Thyroxine and Dienestrol. The other half received the equivalent volume in either DMSO or water when appropriate. It is important to note that the pictures presented in Figure 53 were issued from different protocols on the C-Trap and those are described in detail in Figure 51. As such, ATBC's and Bemcentinib's pictures are the third frames of one video while Aprotinin's, L-Thyroxine's and Dienestrol's pictures are a z-stack of a full video.

As a result, the untreated strand shows a complete coating of the DNA with UvrA-mNeonGreen, while the treated one shows only occasional binders when under treatment with ATBC, Bemcentinib, L-Thyroxine, or Dienestrol. However,

Aprotinin shows a great increase in the decoration of the DNA strand by UvrA-mNeonGreen, as illustrated in Figure 53.

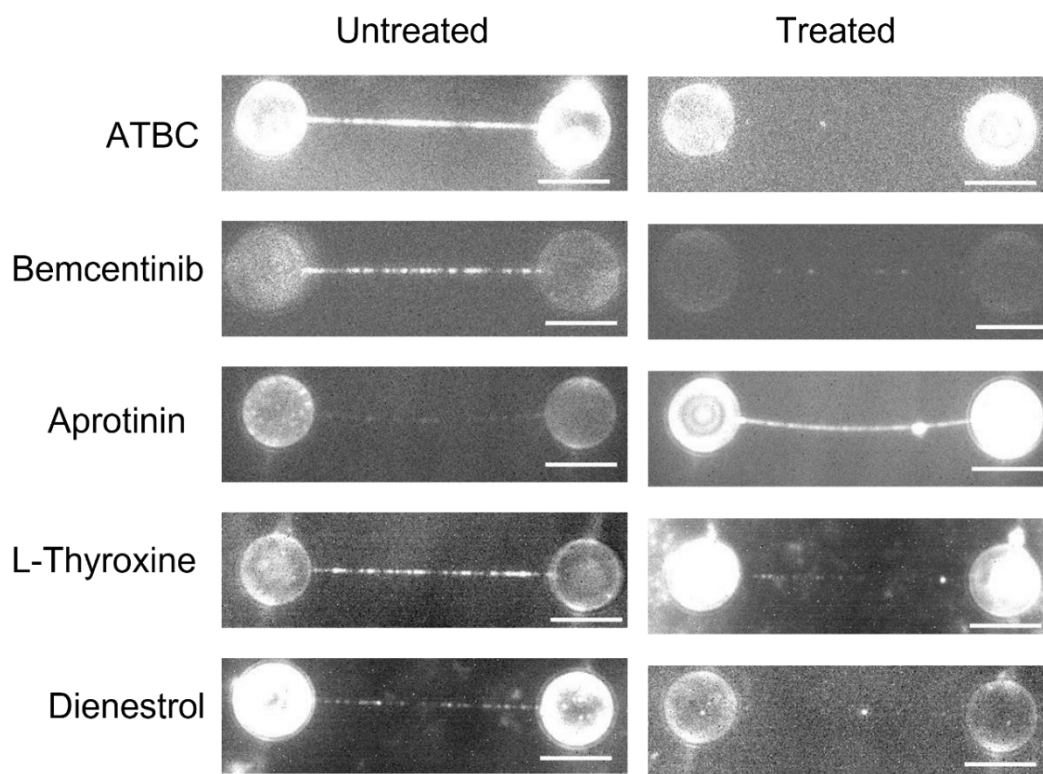


Figure 53: Compounds affect the binding of UvrA-mNeonGreen to the DNA. Scale bars = 5 μ m. The addition of 50 μ M of ATBC (n strands untreated = 2, n strands treated = 3) or 50 μ M of Bemcentinib (n strands untreated = 3, n strands treated = 3), 20 μ M of L-Thyroxine (n strands untreated = 6, n strands treated = 6) or 20 μ M of Dienestrol (n strands untreated = 6, n strands treated = 6) greatly diminished the decoration of UvrA-mNeonGreen to the DNA. However, the addition of 50 μ M of Aprotinin (n strands untreated = 3, n strands treated = 4) increases the decoration of UvrA-mNeonGreen to the DNA.

4.3.2 Kinetics of UvrA while in the presence or absence of NER inhibitors

As discussed earlier, differences in the decoration of the DNA strand can mean either a change in the attachment rate constant and/or in the detachment rate constant (Figure 34C and D). High decoration of DNA strands renders quantification of the on-rate and the off-rate difficult. To calculate the kinetics of UvrA-mNeonGreen under the effect of the different compounds, the workflow

was adapted as presented in Figure 52. Data acquisition for Bemcentinib, L-Thyroxine, and Dienestrol were done by applying 50 pN of tension on the DNA strand under no flow, Then, videos were recorded for 10 minutes. The same strand of DNA was used twice, once in the presence of the compound, and once in the absence of the compound, and the order of which was varied. The addition of flow was done to increase the number of binders as illustrated in Figure 31. Data acquisition for Aprotinin was performed similarly with two variations: acquisition under 0.3 Pa of medial flow (flow perpendicular from the DNA strand), and videos were recorded for 5 minutes. Finally, data acquisition for ATBC was very different because ATBC is prone to precipitation. DNA strands were put under 50 pN of tension under a 0.2 medial flow (perpendicular to the DNA strand). Then the flow was stopped and the videos were recorded for 46 seconds. Trackmate was used to extract data from the videos as previously described. The attachment rate constant, the detachment rate constant, and the dissociation constant were calculated as previously described.

4.3.2.1 ATBC reduces the number of binders of UvrA to tethered DNA.

Under those new conditions, UvrA-mNeonGreen shows a ~7-fold reduction of the number of binders per minute per kbp when comparing untreated samples with ATBC-treated samples, as shown in Figure 54A. This confirms that the change in UvrA's ATPase ability translates to a change in UvrA's binding ability. The effect of ATBC on the lifetime of UvrA was not assessed as the number of binders was too low (n binders: 64 for untreated, 5 for treated).

4.3.2.2 Bemcentinib decreases both the attachment rate and the lifetime of UvrA on tethered DNA.

Bemcentinib however shows a reduction of around 11-fold in the number of binders per minute per kbp when comparing treated samples with untreated ones, as shown in Figure 54B (P-value: 0.0006). Furthermore, this decrease in the attachment rate of UvrA is accompanied by a decrease of the lifetime that goes from 2.18 ± 0.1 s to 1.37 ± 0.11 s when in the absence or presence of 20 μ M of

Bemcentinib (Figure 55) (P-value: <0.0001). As a result, the affinity of UvrA to the DNA is decreased approximately 17-fold (P-value: 0.03) in the presence of Bemcentinib.

4.3.2.3 Aprotinin increases both the attachment rate and the lifetime of UvrA on tethered DNA.

UvrA shows a different behaviour when in the presence of Aprotinin. Indeed, the attachment rate constant increases by around 12-fold when UvrA-mNeonGreen is in the presence of Aprotinin, as shown in Figure 54C (P-value: 0.0007). The lifetime is also affected with and goes from 2.34 ± 0.11 s to 2.96 ± 0.04 s respectively (Figure 55) (P-value: 0.0008). As a result, the affinity of UvrA to the DNA is increased by approximately 15-fold when in the presence of Aprotinin (P-value: 0.003). Interestingly, the DNA strand was more prone to break in the presence of Aprotinin.

4.3.2.4 L-Thyroxine decreases the attachment rate of UvrA on tethered DNA.

Quantification of the number of binders per minute per kbp showed a decrease of around 16-fold in the presence of L-Thyroxine as shown in Figure 54D (P-value: 1.34×10^{-7}). The lifetime of UvrA is not affected much by the treatment of L-Thyroxine. Indeed, the lifetime of UvrA-mNeonGreen binding to DNA goes from 2.30 ± 0.04 s to 2.17 ± 0.12 s for untreated and treated respectively (Figure 55) (P-value: 0.03). As a result, the affinity of UvrA to the DNA strand is decreased by approximately 17-fold (P-value: 0.0006).

4.3.2.5 Dienestrol decreases the attachment rate of UvrA on tethered DNA.

The attachment rate constant of UvrA in the presence of Dienestrol shows a decrease of around 2.5-fold when compared with untreated samples, as shown in Figure 54E (P-value: 0.04). However, the lifetime of UvrA-mNeonGreen doesn't show a difference between treated and untreated samples with a lifetime going from 2.25 ± 0.13 s to 2.4 ± 0.28 s for untreated and treated respectively (Figure 55) (P-value: 0.26). Furthermore, the affinity of UvrA to the DNA strand is decreased by approximately 2-fold (P-value: 0.02).

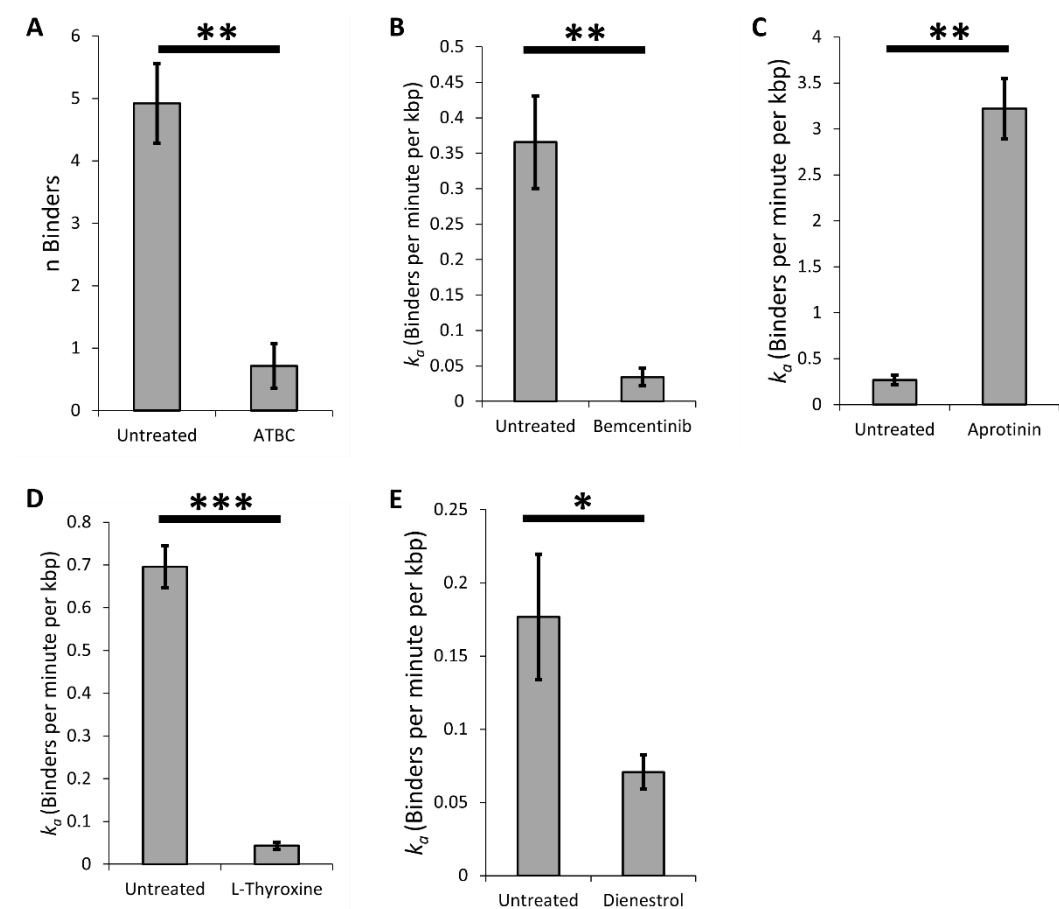


Figure 54: UvrA-mNeonGreen's attachment rate to DNA is greatly reduced in the presence of ATBC, Bemcentinib, L-Thyroxine and Dienestrol, but not in the presence of Aprotinin where the binding is increased. **A:** The addition of 50 μM of ATBC greatly reduces the number of UvrA-mNeonGreen binding to the DNA strand by 6.89-fold (n untreated: 13 videos, 3 strands, 64 binders; n treated: 7 videos, 5 strands, 5 binders) (P -value: 0.00022). **B:** The addition of 20 μM of Bemcentinib greatly reduce the number of protein binding to the DNA strand by 10.67-fold from 0.37 ± 0.07 binders per minute per kbp to 0.03 ± 0.01 binders per minute per kbp (n untreated: 6 strands, 824 binders; n treated: 6 strands, 99 binders) (P -value: 0.0006). **C:** The addition of 50 μM of Aprotinin greatly increases the number of UvrA-mNeonGreen to the DNA strand by 11.97-fold from 0.27 ± 0.05 binders per minute per kbp to 3.22 ± 0.33 binders per minute per kbp (n untreated: 3 strands, 194 binders; n treated: 4 strands, 1503 binders) (P -value: 0.0007). **D:** The addition of 20 μM of L-Thyroxine greatly diminished the number of UvrA-mNeonGreen binders on the DNA strand by 16.07-fold from 0.70 ± 0.05 binders per minute per kbp to 0.04 ± 0.008 binders per minute per kbp (n untreated: 6 strands, 2025 binders; n treated: 6 strands, 126 binders) (P -value: $1.34\text{E-}07$). **E:** The addition of 20 μM of Dienestrol greatly decreases the number of binders of UvrA-mNeonGreen to the DNA strand by 2.5-fold from 0.18 ± 0.04 binders per minute

per kbp to 0.07 ± 0.01 binders per minute per kbp (n untreated: 6 strands, 513 binders; n treated: 6 strands, 206 binders) (P -value: 0.04). The error bars represent the standard error of the mean.

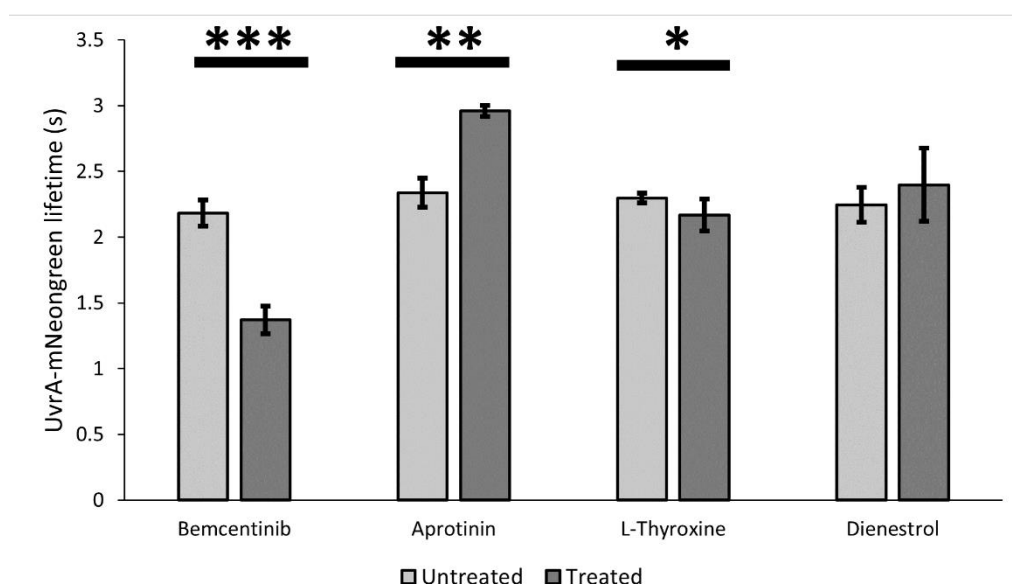


Figure 55: Bemcentinib and Aprotinin affect greatly the lifetime of UvrA-mNeonGreen.

The lifetime of UvrA-mNeonGreen goes from 2.18 ± 0.1 s to 1.37 ± 0.11 s in the absence and presence of 20 μ M of Bemcentinib ($n = 824$ and 99 binders respectively; R^2 : 0.98 and 0.94 respectively; P -value: <0.0001) and from 2.34 ± 0.11 s to 2.96 ± 0.04 s in absence and presence of 50 μ M of Aprotinin ($n = 194$ and 1503 binders respectively; R^2 : 0.95 and 0.99 respectively; P -value: 0.0008). The lifetime of L-Thyroxine and Dienestrol doesn't appear to be affected much. Indeed, the lifetime goes from 2.30 ± 0.04 s to 2.17 ± 0.12 s in the absence and presence of 20 μ M of L-Thyroxine ($n = 2025$ and 126 binders respectively; R^2 : 0.99 and 0.96 respectively; P -value: 0.03) and from 2.25 ± 0.13 s to 2.40 ± 0.28 s in absence and presence of 20 μ M of Dienestrol ($n = 513$ and 206 binders respectively; R^2 : 0.95 and 0.84 respectively; P -value: 0.26). Error bars represent the errors of the exponential fits.

4.3.3 Differences in the data depending on the order of compound exposition.

As previously shown, the various compounds affect the kinetics of UvrA's binding to DNA. In this dataset, videos were recorded within the untreated channel first then the same strand of DNA was used again in the treated channel, or vice-versa. This was rendered possible by the C-Trap which allows to have different work conditions within the same flow cell. Interestingly, this dataset shows

discrepancies between the data of the DNA strands going from an untreated to a treated channel compared with the data of the DNA strands going from a treated to an untreated channel. Those discrepancies affected Bemcentinib, L-Thyroxine, and Dienestrol. It couldn't be verified on the ATBC data because of the very different experimental design and the low number of binders. It also couldn't be verified on the Aprotinin data as the DNA strands seemed to be more likely to break in the presence of Aprotinin. Because we are dividing the original dataset into smaller portions, only effects on the attachment rate constant will be evaluated here.

4.3.6.1 The first use of a DNA strand has a higher attachment rate constant than the second use of a DNA strand.

There are two possible origins for the untreated data. Either the DNA strand was put first in the untreated channel, or the DNA strand was put first in the treated channel and then moved to the untreated channel. The data shows that the use of a DNA strand first in the untreated channel shows a higher attachment rate constant than when a DNA strand was used in the treated channel first. As such, UvrA within the untreated channel shows a reduction in its attachment rate constant of 16 % after being put in presence of Bemcentinib (Statistically not significant, P-value: 0.68), of 26 % after being put in the presence of L-Thyroxine (P-value: 0.007), and of 66 % after being put in the presence of Dienestrol (P-value: 0.01) when compared with DNA that were put directly in the untreated channel (Figure 56).

Similarly, there are two possible origins for the treated data. Either the DNA strand was put first in the treated channel, or the DNA strand was put first in the untreated channel and then moved to the treated channel. Here too, the data shows that the use of a DNA strand first in the treated channel shows a higher attachment rate constant than when a DNA strand was used in the untreated channel first. As such, UvrA within the treated channel shows a reduction in its attachment rate constant of 76 % when treated with Bemcentinib (however not

statistically significant with a P-value of 0.23), of 46 % when treated with L-Thyroxine (not statistically significant, P-value: 0.1), and 51 % when treated with Dienestrol (P-value: 0.01) (Figure 56).

Altogether, this data indicates that the first use of a DNA strand always has a higher attachment rate constant when in the same treatment condition. It can be partially explained by the fact that the channels were not refreshed, and the flow was kept turned off. This could indicate overall photobleaching of the flow cell or diffusion of the channels into channel 3 (containing only ABC buffer). It was expected that the decrease in the attachment rate constant would be of similar amplitude for the different compounds as experiments were performed similarly with the same concentration of UvrA.

4.3.6.2 The first exposure of the DNA strand shows the impact of the compound on the binding.

Now that we know that there is an experimental bias, it is possible to re-assess the effect of the various compounds by looking only at the first time a DNA strand is used. This newly formed dataset is formed of the untreated data that was gathered in the untreated channel first and the treated data that was gathered in the treated channel first. This dataset is illustrated by the green bar in Figure 56.

There is a reduction of the attachment rate constant of UvrA to the DNA of 97 %, 93 %, and 64 % for Bemcentinib, L-Thyroxine, and Dienestrol respectively (P-value: 0.0006 for Bemcentinib; P-value: <0.0001 for L-Thyroxine, and P-value: 0.004 for Dienestrol). This excludes the experimental bias and clearly shows that the compounds inhibit the ability of UvrA to bind to DNA.

4.3.6.3 Binding of compounds to the DNA strand.

All the compounds used were shown to affect the ATPase activity of UvrA in the presence and absence of DNA. However, the data presented in Figure 56 highlight a potential other mode of action of Dienestrol.

This other potential mode of action is highlighted by comparing two datasets. First, when looking only at the untreated conditions, there is a reduction in the attachment rate constant when the DNA strand is put in contact with the compound beforehand. This reduction is of 16 % for Bemcentinib (P-value: 0.68), 26 % for L-Thyroxine (P-value: 0.007); and 66% for Dienestrol (P-value: 0.01). This shows a great reduction in the attachment rate constant for Dienestrol (Figure 56).

The potential second mode of action is also seen when looking at the effect of compounds when the DNA strand is put first in the channel containing the compound, then in the untreated channel (blue bar in Figure 56). As such, UvrA shows a reduction in its attachment rate constant of 76 % when in the presence of Bemcentinib (P-value: 0.051), of 90 % when in the presence of L-Thyroxine (P-value: 0.0002), and an increase of 5 % in the attachment rate constant when in presence of Dienestrol (not statistically significant, P-value: 0.90) (Figure 56).

Altogether, this data suggests that Dienestrol has an effect that is carried over from one channel to the next. Most likely Dienestrol binds tightly to the DNA and prevents UvrA's binding. It was however previously shown that Dienestrol reduces the ATPase activity of UvrA even without DNA (Figure 50; (272)). This confirms that Dienestrol has at least two modes of inhibition.

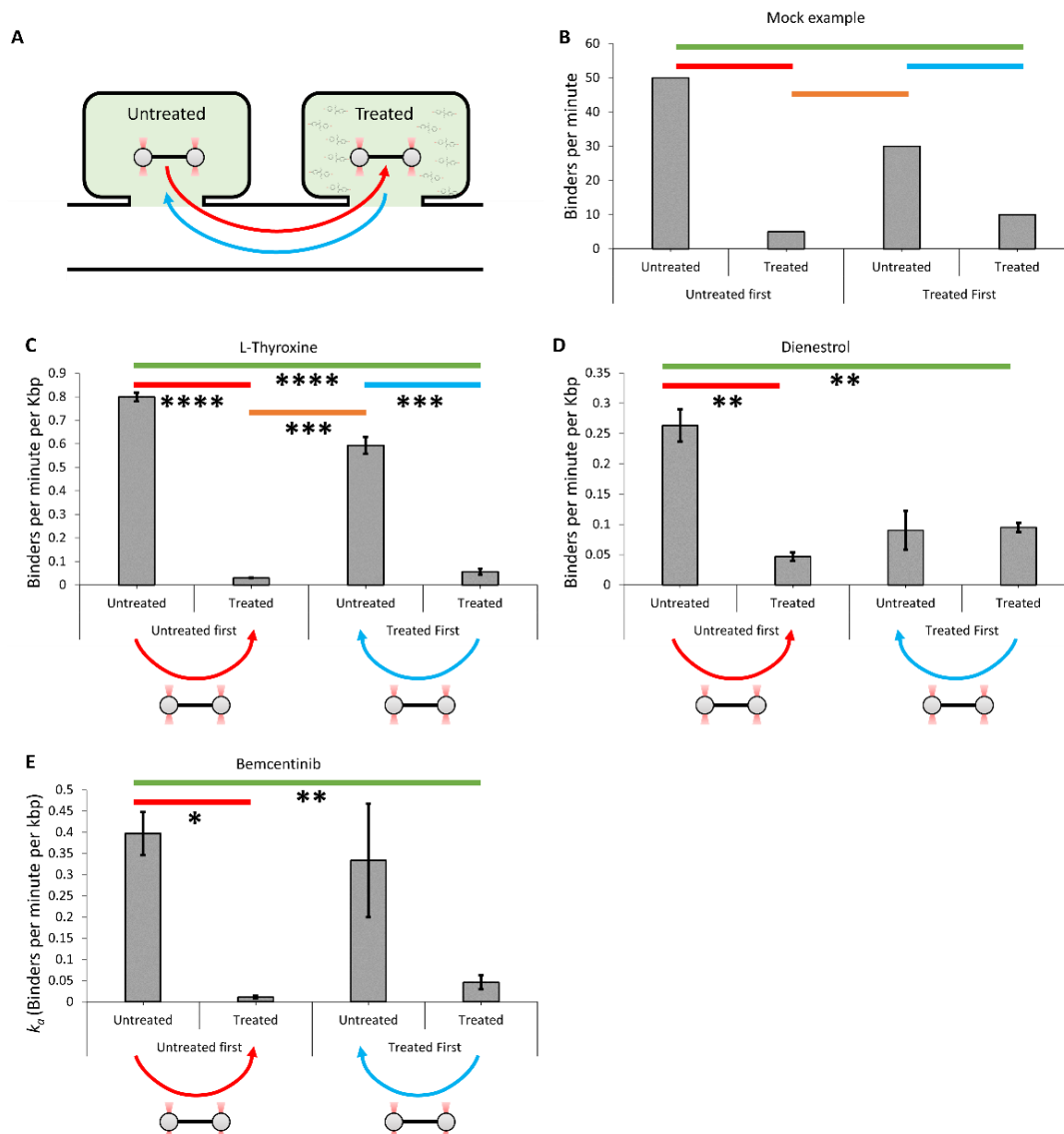


Figure 56: Experimental set-up highlights potential carryover of compound on the DNA strand. **A:** Schematics of the experimental setup. One strand of DNA is tethered and put under 50 pN of tension. Data is acquired first in a microfluidic channel lacking the compound and then in a different channel containing the compound (Shown with the red arrow), or vice versa (shown with the blue arrow). No flow is applied once the DNA is tethered. **B:** Mock example of the data representation in this figure. The red line regroups data from the same strands of DNA in both untreated and treated conditions, but that have been in untreated conditions first. The blue line regroups the same strands of DNA in both untreated and treated conditions, but that has been in treated conditions first. The green line regroups data from different strands on their first exposure to UvrA-mNeonGreen, either in untreated conditions or in treated conditions. The orange line regroups data from different strands on their second exposure to UvrA-mNeonGreen, either in untreated conditions after having been exposed to treated conditions, or in treated conditions after

having been exposed to untreated conditions. **C:** When the DNA strand is put in contact with L-Thyroxine in any order, there is a great reduction in UvrA-mNeongreen's number of binders per minute. **D:** However, when a DNA strand is put in contact with Dienestrol there is a great reduction of the number of binders per minute when the same strand of DNA is used in the untreated channel first (red bar). This reduction disappears when a strand of DNA is used in the treated channel first (blue bar). Furthermore, the on-rate in the untreated channel is significantly lower when the strand is used after being in contact with Dienestrol (*P*-value: 0.01). Altogether, this seems to advocate for a different mechanism of action where Dienestrol is carried over on the DNA strand from the treated channel to the untreated channel. **E:** Treatment with Bemcentinib shows similar results to treatment with Dienestrol with one major difference. There is no significant difference between the untreated strands conditions (*P*-value: 0.68). This seems to indicate that the carried-over effect of Dienestrol is not present for Bemcentinib. The attachment rate constant, *N* binders, and *P*-values are shown in table 1.

L-Thyroxine	k_a Untreated	k_a Treated	N binders Untreated	N binders Treated	p-value	Fold decrease
Same strand, Untreated first	0.80 ± 0.02	0.03 ± 0.001	1162	44	2.01E-06	26.4 %
Same strand, Treated first	0.59 ± 0.04	0.06 ± 0.01	863	82	0.000152	10.5 %
First exposure to UvrA-mNeongreen	0.80 ± 0.02	0.06 ± 0.01	1162	82	4.99E-06	14.2 %
Second exposure to UvrA-mNeongreen	0.59 ± 0.04	0.03 ± 0.001	863	44	0.0001	19.6 %

Dienestrol	k_a Untreated	k_a Treated	N binders Untreated	N binders Treated	p-value	Fold decrease
Same strand, Untreated first	0.26 ± 0.03	0.05 ± 0.01	383	68	0.001372	5.6 %
Same strand, Treated first	0.09 ± 0.03	0.09 ± 0.01	130	138	0.896609	0.9 %
First exposure to UvrA-mNeongreen	0.26 ± 0.03	0.09 ± 0.01	383	138	0.003538	2.8 %
Second exposure to UvrA-mNeongreen	0.09 ± 0.03	0.05 ± 0.01	130	68	0.256979	1.9 %

Bemcentinib	k_a Untreated	k_a Treated	N binders Untreated	N binders Treated	p-value	Fold decrease
Same strand, Untreated first	0.39 ± 0.05	0.01 ± 0.003	578	10	0.01	97 %
Same strand, Treated first	0.33 ± 0.13	0.05 ± 0.02	246	89	0.051	86 %
First exposure to UvrA-mNeongreen	0.39 ± 0.05	0.05 ± 0.02	578	89	0.0006	88 %
Second exposure to UvrA-mNeongreen	0.33 ± 0.13	0.01 ± 0.003	246	10	0.16	97 %

Table 1: Associated values from Figure 54. Associated values, errors, and *P*-values. Colour code is respected between the bar charts of Figure 54 and the table. In bold are represented *P*-value that is above the 0.05 level of significance. Error bars represent the standard error of the mean. *N* strands for Bemcentinib are 3 for the untreated data in the untreated first dataset; 2 for

the treated data in the untreated first dataset; 3 for the untreated data in the treated first dataset; and 4 for the treated data in the treated first dataset. N strands for each condition are 3 for L-Thyroxine and Dienestrol.

4.4 Discussion

4.4.1 ATBC is inhibiting UvrA-mNeongreen's ability to bind to DNA.

ATBC was the first and only prokaryotic NER inhibitor discovered prior to this work (274). We show here that its ability to inhibit UvrA's ATPase activity (Figure 50) does translate into a decrease in the attachment rate of UvrA-mNeonGreen onto tethered DNA (Figure 54A). However, due to the small number of binders, it was not possible to assess if ATBC acts on the lifetime of UvrA-mNeonGreen. It was however shown to inhibit bacterial growth in the presence of DNA-damaging agent 4NQO or UV damage (271) demonstrating great potential as a new anti-microbial. However, ATBC's propensity to precipitate highlights the fact that it needs chemical modifications to increase solubility before even being considered as a potential therapeutic agent (271,274).

4.4.2 L-Thyroxine, Dienestrol and Aprotinin affect UvrA-mNeongreen's ability to bind to DNA.

L-Thyroxine, Dienestrol and Aprotinin were discovered in a recent *in vivo* screening and have all been shown to inhibit UvrA's ATPase activity. We show here that the reduction of ATPase activity (Figure 50) does relate to a decrease in the attachment rate of UvrA-mNeonGreen for both L-Thyroxine and Dienestrol (Figure 54D and E). Both of those compounds were found to bind within or in the proximity of the ATPase cassettes of UvrA through in-silico docking (272). However, neither L-Thyroxine nor Dienestrol seems to affect the lifetime of UvrA-mNeonGreen onto DNA (Figure 55). Furthermore, Dienestrol appears to bind to DNA, hindering UvrA's ability to bind to the DNA (Figure 56D). This suggests that Dienestrol might have several modes of inhibition against UvrA. One is to reduce UvrA's ATPase capacities and the other is to bind to the DNA, both resulting in a reduction of UvrA's ability to bind to the DNA.

Despite inducing a reduction in UvrA's ATPase activity, Aprotinin did show an increase in both the attachment rate (Figure 54C) and the lifetime (Figure 55) of

UvrA-mNeonGreen to the DNA strand. Both of those resulted in an increase of the affinity of UvrA to the DNA strand of approximately 15-fold of the (P-value: <0.0001). It was however shown to inhibit the growth of an MG1655 $\Delta toI/C$ strain when in the presence of cisplatin (personal communication, Lorenzo Bernacchia). Furthermore, incision assays show curved DNA bands when NER is used in the presence of aprotinin (data not shown). We hypothesise that Aprotinin promotes the binding of UvrA to DNA in a non-damage-specific manner, therefore diminishing the quantity of UvrA in the cell available to be recruited at DNA lesions. A notable fact is that most experiments done for this thesis were done using a protease inhibitor (Pierce Protease inhibitor tablets, A32963, Thermofisher) that contains AEBSF, bestatin, E-64, leupeptin, pepstatin A and finally Aprotinin. Aprotinin concentration in the protease mix is between 10 and 800 nM before dilutions. We did show that increasing the concentration of the protease inhibitor mix does increase UvrA's binding to DNA in Chapter III. However, this is very far from the 50 μ M concentration used in this chapter. The clear impact of using the protease inhibitor mix is still not certain.

4.4.3 Bemcentinib

ATBC, L-Thyroxine and Dienestrol were all shown to bind in the proximity of the ATPase pockets using *in-silico* docking. By doing an in-silico docking screening aimed at those ATPase pockets, we were able to find a plethora of potential inhibitors for UvrA within days (91). One of them, Bemcentinib was tested and showed ATPase activity reduction (Figure 50). We have shown here that the reduction in ATPase activity did relate to a reduction of the attachment rate (Figure 54B) and of the lifetime (Figure 55) of UvrA-mNeonGreen onto tethered DNA decreasing by approximately 17-fold the affinity of UvrA to the DNA strand (P-value: <0.0001). This compound was later shown efficient in reducing the growth of EC958 when used in combination with cisplatin (91). EC958 is a clinically relevant *E. coli* strain as it is a multi-resistant strain that infects urinary tracts (289).

Altogether this highlights the potential of Bemcentinib as a prospective antimicrobial.

4.5 Conclusion

Altogether this work highlights single molecule change in behaviours in the binding of UvrA-mNeonGreen to tethered DNA when in the presence of various compounds, further confirming their activity as inhibitors of UvrA. It also indicates that there is a strong link between the ATPase of UvrA and its ability to bind DNA, making the search for inhibitors based on ATPase a relevant approach for the future. Those compounds have further been shown to be able to alter growth in different bacterial strains with the most impactful being Bemcentinib's ability to reduce growth in a multidrug-resistant *E. coli* strain. It is a great proof of concept and highlights the potential of NER as a target for the development of antimicrobials.

4.5.1 Future work

The effect of Bemcentinib on inhibiting NER shows great promise. Indeed, we show in this thesis that Bemcentinib is capable of inhibiting UvrA's ability to bind to DNA. The work done here was done in collaboration with Lorenzo Bernacchia who also showed that treatment with sub-MIC quantities of Bemcentinib was sufficient to reduce growth when combined with sub-MIC quantities of cisplatin in a multidrug-resistant *E. coli* strain (EC958) (91). This is a great proof of concept of the use of NER as a target for combinational therapy. It is notable to note that *E. coli* is responsible for only around 15 % of bacterial infections in cancer patients (290). Further work is needed to assess how other common bacterial strains react to this kind of combinational treatment. It is also important to note that bacterial infection represents only a portion of infections with viral and fungal infections being very common in cancerous patients (263). However, given the similarities of these NER systems to those in Humans it is not possible to ensure low off-target effects.

Chemical variations of the compounds studied here could be made to both increase their efficiency in inhibiting NER and increase their usability in patients. This is particularly true for ATBC which is poorly soluble. The solubility of a

compound can be increased by various means, a good example is the introduction of hydrophilic groups into the compound (291).

Only a few newly found UvrA inhibitors have been tested on the C-Trap. However, many promising inhibitors found during the various screenings could be tested. Some of the potential inhibitors that have been highlighted with the virtual screening show very tight theoretical binding with the ATPase cassettes of UvrA. Those compounds have the potential to be the strongest inhibitors yet as only Bemcentinib from the virtual screening was tested. Furthermore, random chemical variations could be virtually added to each of our main compounds and screened, which could lead to optimisation of the binding of the compounds to their binding pocket within UvrA's molecule (292).

A few intercalating compounds have been shown to have a NER inhibitor effect such as Pirarubicin (272). However, using such compounds was difficult as they greatly altered the structure of the DNA with distortion of the Force/Distance curve. This renders comparisons between untreated and treated samples difficult. Only a qualitative assessment of the effect of the different compounds on the DNA itself was performed. Pirarubicin showed a massive difference in the structure of the DNA. Such changes were not observed for neither L-Thyroxine, Dienestrol, ATBC, Bemcentinib, nor Aprotinin. However, a more quantitative approach could highlight the binding of the different compounds to the DNA. This would particularly be interesting to assess if Dienestrol alters the structure of the DNA.

Aprotinin has a unique effect on UvrA and should be investigated further. It is the only inhibitor found that seems to increase the number of binders to DNA. Its mechanism of inhibition at the cellular level might be that aprotinin increases the affinity of UvrA for undamaged DNA as well as UvrA's lifetime onto undamaged DNA, therefore diminishing UvrA's ability to find lesions on the DNA. It is interesting to note that incision assays show a decrease in incisions when NER was in the presence of Aprotinin (Lorenzo Bernacchia, unpublished data). Therefore, Aprotinin doesn't seem to increase UvrA's ability to recruit the rest of the NER

machinery. This suggests that although binding is enhanced, discrimination of damage is probably not affected.

Altogether, the C-Trap is an excellent choice to assess the effect of a few compounds of high-interest thanks to its ability to have both untreated and treated samples within the same flow cell. However, collecting data was complex and required several hours to gather sufficient data. Furthermore, the flow cell had to be cleaned between testing of different compounds which is a process that could take 1-2 hours. The latter inconvenience can be tackled by using different flow cells within the same day, but cleaning the flow cells requires being connected to the u-flux system. Disconnections of the flow cell can also introduce bubbles within the system which can be troublesome to get rid of. This means the C-Trap is not the best tool for high throughput screening, however as a medium-throughput mechanism testing system it is ideal.

Chapter V: Stalling of ribosomes on specific codons

5.1 Introduction

5.1.1 Project aim

This chapter is focused on trying to get a better understanding of the translation process, particularly on the tRNA-ribosome interface during the elongation. The first aim of the project is to set a technique allowing the observation of ribosomes at a single molecule scale. Several steps to reach that point are required. First, the ribosomes need to be stalled at a specific codon. This would allow us to study specific codons-anticodons interactions. Second, said stalled ribosomes need to be visualized. Finally, the interaction of near-cognate aa-tRNA in combination with EF-Tu interactions needs to be assessed. Fluorescently labelling ribosomes and tRNAs would allow to study such interactions using single-molecule microscopy. During this project, we made significant progress on the first two steps while laying out the ground for the third.

5.1.2 Principle

Using an *in vitro* approach where transcribing then translating a DNA template that contains a luciferase gene as a marker should allow for stalling of ribosomes. Indeed, such transcription/translation kits allow for great control over translation reactions. If the luciferase is correctly translated, there should be great luciferase activity while if the ribosomes are indeed stalled, luciferase shouldn't be expressed and therefore, no luciferase activity should be observed, as illustrated in Figure 57. The main idea to stall the ribosomes at a specific codon is to use an amino-acid mix lacking the corresponding amino acid, therefore forcing the ribosomes to dwell on that precise codon. A luciferase gene fused to a HIS tag was chosen as it allows for both the stalling luciferase assay through the DNA coding for the luciferase and for linking to the surface of a flow cell. The expression of the luciferase was initially done in the TnT® Coupled Reticulocyte Lysate Systems (L4600) by Promega but was later moved to the PURExpress E6840s recombinant kit by NEB. The reasons for this change will be discussed in detail within this chapter.

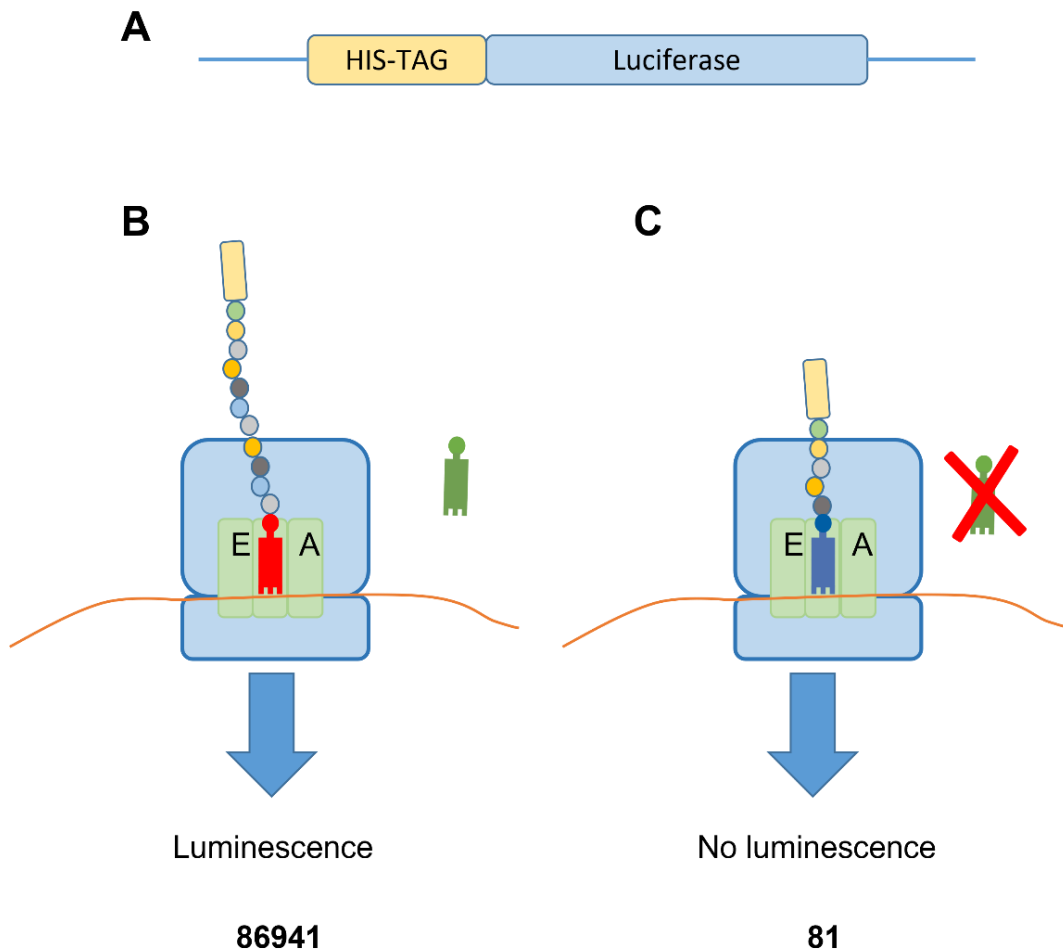


Figure 57: Principle of ribosome stalling. *A: schematic of the luciferase gene used. B: When a transcription/translation kit is used in the presence of all amino acids, the protein will be expressed, which is quantifiable by luciferase assay. Luminescence is expressed in arbitrary unit C: When a transcription/translation kit is used with an amino-acid mix lacking one amino acid, the ribosome won't be able to decode the corresponding codon, which is expected to stall the ribosome on that codon. As a result, the protein won't be expressed, and the sample won't show any luminescence activity in a luciferase assay.*

To link stalled ribosomes to the surface of a microfluidic chamber, a succession of elements was used as shown in Figure 58. First, a mixture of biotin-mPEG and regular mPEG would be used to cover the totality of the surface of the flow cell chamber. Playing on the concentrations of biotin-mPEG and regular mPEG would play a role in how much ribosomes would be bound to the surface of the flow cell

as the linking of the ribosomes will happen through this biotin. To this would be added streptavidin which binds very strongly to biotin. A biotinylated-anti-HIS antibody would be used to link this streptavidin to the nascent protein chain of the luciferase gene as its sequence starts with a HIS-tag. As the ribosome is in principle stalled, the nascent protein chain should be linked through its tRNA to the P-site of the ribosome. So, with this system, ribosomes should be able to directly bind to the surface. Interestingly, a non-stalled ribosome would express the protein and dissociate from it, therefore the non-stalled ribosomes shouldn't be bound to the surface through this system. The next step is to visualize the ribosomes on the surface. To do so a combination of primary and secondary antibody that specially recognize the ribosomes and are linked to a Qdot can be used. There is also the need for a fluorescently labelled near-cognate aa-tRNA bound to EF-Tu to study the near-cognate tRNA/ribosome interaction.

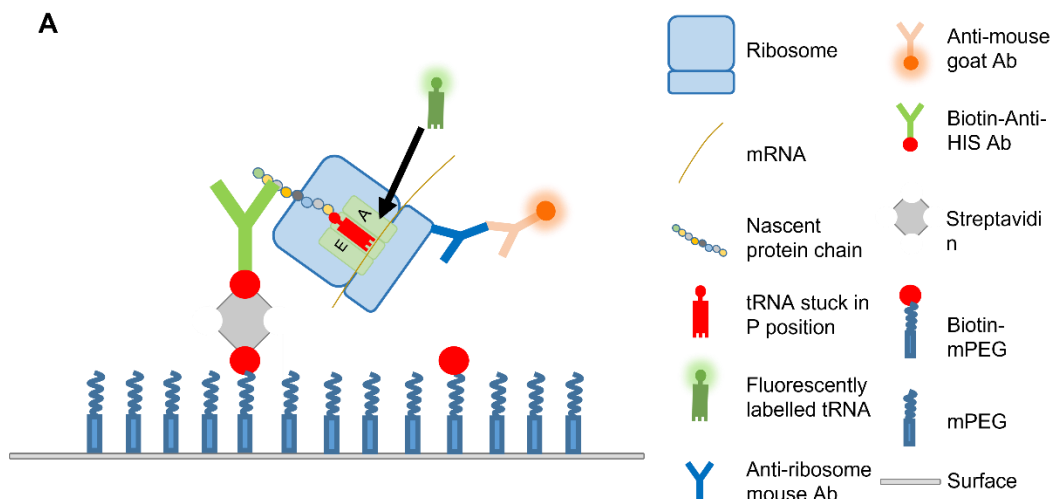


Figure 58: Schematic of a single molecule experimental set-up: where a mixture of mPEG and biotinylated mPEG is spread across the glass surface of a flow cell chamber. Adding streptavidin allows connecting the biotinylated-mPEG with a biotinylated-Anti-HIS antibody which recognizes the nascent protein chain and therefore the newly expressed HIS-tag. The nascent protein chain is sticking out of the ribosome enough for the HIS tag to be recognized by the antibody. Since the ribosome has been pre-emptively stalled, the nascent protein chain is bound to a tRNA stuck in the P site of the ribosome. The dwell time of the tRNA to the ribosome can be assessed if using a fluorescently labelled tRNA. To visualize where the ribosomes are located within the flow cell surface, a primary anti-ribosome mouse antibody is used in combination with a secondary anti-mouse goat antibody bound to a 655 Qdot.

5.2 Materials and Methods

5.2.1 TnT® Coupled Reticulocyte Lysate Systems typical reaction

TnT® Coupled Reticulocyte Lysate Systems (Promega L4610) is an *in vitro* transcription/translation coupled system that allows for the expression of proteins by adding template DNA. This kit uses components extracted from rabbits and as such possesses the eukaryotic machinery for transcription and translation and therefore eukaryotic ribosomes (293,294). A typical reaction contains 12 µL of TNT Rabbit reticulocyte lysate, 1 µL of TNT reaction buffer and 0.5 µL of TNT RNA polymerase T7 (all the above are regrouped under “TNT mix” in the following tables). This is complemented with 0.25 µL of 1 mM amino acid mix lacking leucine and 0.25 µL of 1 mM amino acid mix lacking Methionine. This allows all amino acids to be present in the reaction. Finally, a DNA template is added to start the reaction. Water is added until the reaction reaches a volume of 25 µL. The components are thawed and added in the same order as described above. The reaction is incubated at 30°C for 90 minutes and stopped by placing tubes on ice.

5.2.2 PURExpress typical reactions

PURExpress (NEB E6840S) is an *in vitro* transcription/translation coupled system as well. It has two main differences with the TNT-coupled Reticulocyte Lysate System. Firstly, it is a prokaryote system and as such possesses the prokaryotic transcription and translation machinery. Secondly, it is a recombinantly produced system which means that components were individually purified and then put back together. This has for effect that the precise concentration of each of its components is known and easily manipulable (295,296). A typical PURExpress reaction contains 7.5 µL of E6840S mix, which is composed of Solution A (containing buffer systems and small molecules) as well as solution B (containing all the proteins and ribosomes) and tRNA mix. 1.25 µL of amino acids are added to a final concentration of 0.3 mM. The DNA template is added and finally, water is added to a volume of up to 12.5 µL. The reaction is incubated for 2 hours at 37°C and stopped by placing tubes on ice.

5.2.3 Amino-Acid mix preparation

Amino-acid mix was made in two different ways. At first, amino acids were dissolved individually at a concentration of 1 M in 5 M KOH. Amino-acid mix was then assembled in milliQ water to a final concentration of 3 mM. Then, to minimise amino acid mix KOH concentration, the amino-acid mix was produced by dissolving most amino acids in Milli-Q water altogether, apart from aspartic acid, glutamic acid, tyrosine, and tryptophan, which were dissolved in 1M KOH and added last to the mix. In both cases, the amino-acid mixes were assembled without the amino acid of interest, then split in half and one of the amino-acid mixes received the lacking amino-acid, resulting in a complete amino-acid mix and an amino-acid mix lacking one amino-acid.

5.2.4 One-glo™ luciferase assay

Luciferase activity was evaluated using the ONE-Glo™ Luciferase assay system (E6110 Promega). This system uses a luciferin analogue that is more stable than luciferin and allows the production of light when in the presence of Luciferase (Figure 59) (297).

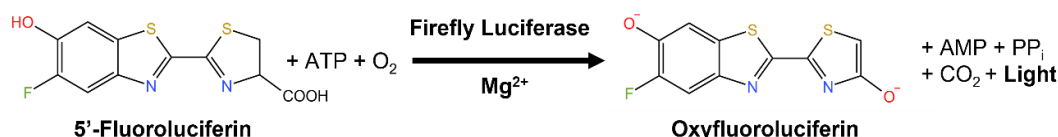


Figure 59: Luciferase reaction. Luciferase catalyses the oxidation of 5'-Fluoroluciferin into Oxyfluoroluciferin. This produces light by converting the chemical energy of luciferin oxidation through an electron transition. Adapted from Promega's ONE-Glo™ Luciferase Assay System protocol sheet.

Reagents are thawed at room temperature before use. Samples from the TNT rabbit reticulocyte kit (25 µL) were mixed with 25 µL of the ONE-Glo reagent. Samples from the PURExpress kit (12.5 µL) were diluted with 25 µL of water and 12.5 µL of the ONE-Glo reagent. In both cases, the reaction is mixed within a 1.5 mL Eppendorf tube and deposited in a 96-well plate. This allows reading of the luminescence emitted using a FLUOstar Omega microplate reader.

5.2.5 Gibson assembly of pls7

The DHFR gene from the DHFR plasmid provided with the PURExpress kit as an expression control was replaced with a HIS-luciferase gene. It was done by using a Gibson assembly master mix (NEB E2611S). Insert and vector fragments were amplified by PCR using Q5® High-Fidelity 2X Master Mix (NEB M0492). Forward primer for the insert fragment: 5' **TTAACTTTAAGAAGGAGATATACAT** atgggacaccatcaccatc 3', reverse primer for the insert fragment: 5' **CTCCTGCAGGTTAACCTTACTCGAG** ttactttccgccttcttgcc 3', forward primer for the vector fragment: 5' **CTCGAGTAAGGTTAACCTGCAGGAG** 3', reverse primer for the vector fragment: 5' **CATatgtatatctccttcttaagttaacaaaattatttct** 3'. The PCR product was run on a 1% agarose gel and the DNA bands of the appropriate size were cut off. DNA was extracted from the gel using the QIAquick® gel extraction kit (QIAGEN 28706X4). 5 µL of the Gibson assembly mix was mixed with 2 µL of purified vector DNA (18.8 fmol) and 3.2 µL of purified insert DNA (37.7 fmol).

5.2.6 Colony PCR

A PCR master mix was assembled with 12.5 µL of Taq 2X Master Mix (#MO270S, NEB) with 1.25 µL of T7 forward primer (TAATACGACTCACTATAGGG), 1.25 µL of T7 reverse primer (CTAGTTATTGCTCAGCGG) and 9 µL of water per colony that had to undergo PCR reaction. Each colony was picked, streaked on a backup plate, and put within 24 µL of the PCR master mix. The following PCR programme was used to amplify the DNA: 30 seconds of denaturation at 95 °C, 60 seconds of primer annealing at 45 °C and 130 seconds of extension time at 68 °C. This is preceded by 30 seconds of initial denaturation at 95 °C and followed by a final extension time of 5 minutes at 72 °C. The results of that colony PCR are shown in Figure 60. The 7th colony was chosen, and its plasmid was purified and sent for sequencing.

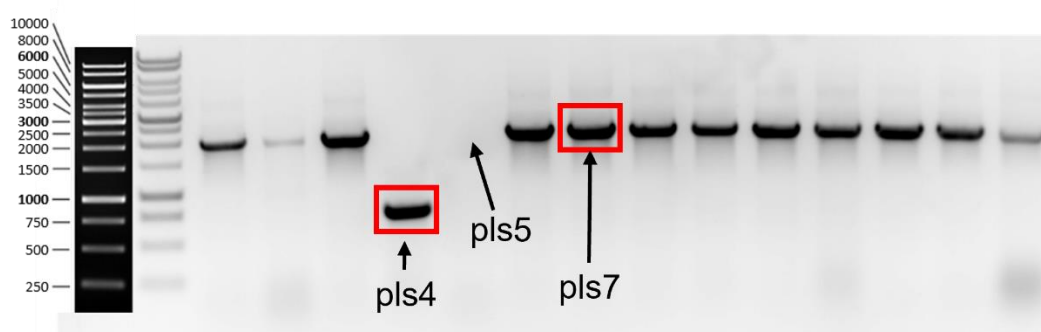


Figure 60: Colony PCR of Gibson reaction. 1% agarose gel. Most plasmids showed the expected fragment size post-Gibson and colony PCR of 1921 bp. Colony 7 was chosen and led to the purification of its plasmid which will be called *pls7* for the rest of the thesis. The 5th colony don't show any amplification and the 4th colony shows the amplification of a fragment that corresponds to the expected size for amplification from the DHFR plasmid at 697 bp.

5.2.7 Single-molecule glass slide and coverslip treatment

For single-molecule experiments that include the assembly of homemade flow-cell chambers, both glass slides and coverslips must be cleaned before assembly. They were first treated with acetone overnight on a shaker, followed by a 0.5 M HCl wash for 1 hour. Then they were washed in ethanol for 1 hour and dried with nitrogen. Then they were put in a 2% (3-Aminopropyl)triethoxysilane in acetone for 10 minutes, washed with water and dried with nitrogen. In between each of those steps, the coverslips and slides were washed with Milli-Q water. The slides and coverslips are plasma cleaned (Harrick PDC-32-2) and are ready to be assembled.

5.2.8 Flow cell chamber assembly

Flow chambers are assembled as shown in Figure 61. Glass slides are pre-drilled. Both glass slide and coverslip are cleaned before assembly as described above. To assemble the flow cells, tubes are inserted in the glass slide holes and maintained in position using UV glue (Nordland Optical Adhesive 68). One of the extremities of the tubes is widened using a hot air flux, allowing for easier placement of the tubes and UV glue. A UV lamp is used to solidify the glue. Then, the gasket is positioned on top of the glass slide. The gasket is made of double-sided adhesive

which then allows the addition of the coverslip on top. The back of a scalpel is used to apply pressure on the gasket to make sure that no leak will occur once flow is applied to the flow cell chamber. The surface that is imaged is the inner side of the coverslip.

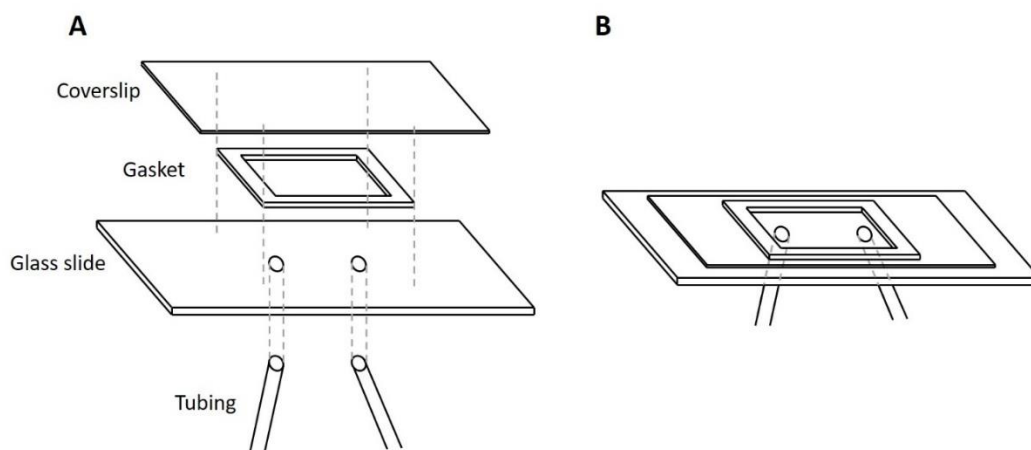


Figure 61: Flow chamber construction. **A:** Layout of the different elements of the flow chamber. Dimensions of the glass slide are 26x76 mm with a thickness of 1.0-1.2 mm (Thermo-scientific 12332098). Dimensions of the Coverslip are 24x40 mm with a thickness of 0.16-0.19 mm. Dimensions of the gasket are 20x30 mm for the outer layer and 10x20mm for the chamber. Tubing dimensions are 1.15 mm internal diameter and 0.2 mm wall (Gradko international, GE-0115-020). **B:** Flow chamber assembled.

5.2.9 Flow cell chamber passivation

Flow cell chambers were passivated by incubating overnight with 0.1 mg/mL biotin-mPEG + 25 mg/mL mPEG in 250 mM NaHCO₃. Then the flow chamber was treated with 2.5 % tween20 in water for 20 minutes, followed by treatment with 10 µM of BSA for 30 minutes followed by hybridized oligos. The purpose of the oligos were to cover any spots where the ribosomes could bind non-specifically to the flow cell chamber. Using the oligos resulted in better passivation (data not shown). Finally flow chamber was washed with 200 µL of Milli-Q water. Washes with 200 µL of Milli-Q water were performed in between each step. The hybridized oligos were made using complementary 40 nucleotides long oligos (A:

AGTTCTTCTCCTTTGGACATGTTTTT-GGCGTCTTCGGATC B:
GATCCGAAGACGCCAAAAACATGTCCAAAGGAGAAGAACT). 100 µL of each oligo were mixed with 200 µL of annealing buffer (10 mM tris, 50 mM NaCl, 1 mM EDTA) then placed on a heating block at 95°C for 5 minutes and left to slowly cool down.

5.2.10 Single-molecule sample preparation

1 µL of either the PURExpress reaction mix that has been used to stall ribosomes or the PURExpress reaction mix that has been used to produce luciferase are mixed with 1 µL of ribosome antibody (22B12B2, targeting 30S ribosomal protein S3) and 1 µL of ribosome antibody (193E11E5B11, targeting 30S ribosomal protein S13) as well as 3 µL of anti-mouse antibody that is fluorescently labelled with Qdot 605. 2.5 µL of this reaction is diluted in 100 µL of Polymix buffer (50 mM Tris-OAc (pH 7.5), 100 mM KCl, 5 mM NH₄OAc, 0.5 mM Ca(OAc)₂, 5 mM Mg(OAc)₂, 6 mM 2-mercaptoethanol, 5 mM putrescine and 1 mM spermidine) to a final concentration of roughly 5 nM for the ribosomes and 7.5 nM for the Qdot.

5.2.11 Single-molecule experimental setup

Using an Aladdin SyringeONE Programmable Syringe Pump (World precision instruments, AL-1000), samples are flowed in then retraction of the flow removes the samples. This allows for the flow cell chamber to be filled with the sample for around 25 seconds. Once the sample is retracted, the surface of the flow chamber is imaged.

5.3 Results

5.3.1 APCT2 allows expression of functional luciferase using a TNT rabbit reticulocyte coupled system

To study the interaction of various near-cognate tRNA with a specific codon, ribosomes must be stalled at that specific codon. Here is shown work that focuses on stalling the ribosomes at a specific codon. The DNA used (and therefore the mRNA associated) codes for a luciferase. A luciferase assay is performed to assess if the translation goes through, and therefore if the stalling is happening.

An *in vitro* transcription/translation coupled system is used so that the expression of the luciferase gene can be assessed quickly. In addition, the content of the kit can be used directly within a flow-cell chamber without further steps. The gene used is luciferase as luciferase expression is very easy and quick to assess through a luciferase assay. First, the ability of the TNT rabbit reticulocyte kit to express active luciferase protein from the HIS-luciferase construct was assessed. The TNT rabbit reticulocyte kit comes with amino-acid mixes that are lacking one amino acid each, either leucine, methionine, or cysteine. Using a combination of two amino acid mixes ensures that all amino acids are present within the reaction. A simple reaction in the presence or absence of the plasmid APCT2, containing the luciferase gene, showed great luciferase activity (43064 AU) when the DNA template was present, compared to the negative control (1400 AU). This shows that the DNA template is capable of expressing active luciferase (Table 2). It is notable to mention that the luminescence recorded for the negative control is way higher than it should be. Because those two samples were put in two adjacent wells on 96 well plates, it resulted in light pollution coming from the positive control. A typical value for a negative control should be around 100 AU.

Components	Control (-)	Control (+)
TNT mix	14	14
AA mix -Leu 1mM	0.25	0.25
AA mix -Met 1mM	0.25	0.25
pAPCT2	0	1
Water	To 25 μ L	To 25 μ L
Luminescence	1400	43064

Table 2: TNT Rabbit Reticulocyte coupled system luciferase expression control. *In the presence of DNA coding for luciferase, there is luminescence while in the absence of DNA there is little luminescence, confirming both the potency of the expression kit to express protein from DNA and that the DNA constructs contain the genetic information necessary for luciferase expression. Luciferase activity is assessed with a luciferase assay.*

5.3.2 Removing one amino acid doesn't prevent the expression of luciferase

A similar experiment was done to try to stall the ribosomes, with a reaction mix lacking one amino acid. Without that amino acid, the ribosome should not be able to process the mRNA and should get stalled at the corresponding codon. However, luciferase was expressed even though the reaction lacked leucine (Table 3). It could be due to contamination of amino acids somewhere in the kit or the DNA. Notably, the luminescence of the no DNA control is way lower than the one seen previously (Table 2, Table 3) this was because of light pollution in between adjacent wells within the plate. This time samples were separated by two empty wells.

Components	Control (-)	Control (+)	Sample
TNT mix	14	14	28
AA mix -Leu 1mM	0.25	0.25	1
AA mix -Met 1mM	0.25	0.25	0
pAPCT2	0	1	2
Water	To 25µL	To 25µL	To 50µL
Luminescence	96	62595	58909

Table 3: Removing one amino acid doesn't prevent the expression of luciferase. *The sample lacks leucine in the mixture while both controls have a complete amino acid mix. In the absence of DNA, there is no luminescence. In the presence of DNA, there is luminescence both when using the complete amino acid mix and when using the depleted one. Luciferase activity is assessed with a luciferase assay.*

5.3.3 Using different amino acid mixes or different DNA doesn't prevent the expression of luciferase in the absence of one amino acid

Different combinations of DNA and amino-acid mixes were tried to check if there was amino acid contamination in the amino-acid mix or the DNA. Table 4 and Table 5 show results using two different plasmid preparations while using two different amino acid mixes lacking leucine or cysteine. It was expected that some of those combinations would not be able to express luciferase. However, all those conditions show luciferase expression similar to the positive control, as shown in Table 4 and Table 5. This shifted the hypothesis from contamination in the DNA or the amino-acid mixture to the contamination of another part of the kit. The kit comes with 4 aliquots of lysate, and only one was used in those previous experiments. The different aliquots had to be tested to see if the contamination of amino acids was coming from the first aliquot.

Components	Control (-)	Control (+)	Without Leu	Without Cys
TNT mix	14	14	14	14
AA mix -Leu 1mM	0.25	0.25	0.5	0
AA mix -Met 1mM	0.25	0.25	0	0
AA mix -Cys 1mM	0	0	0	0.5
pAPCT2	0	1	1	1
Water	To 25µL	To 25µL	To 25µL	To 25µL
Luminescence	135	5005	7583	8346

Table 4: The use of a different amino acid mix doesn't change the outcome of luciferase expression. Negative and positive controls were made as previously described. The samples without leucine or cysteine show similar luciferase expression to the positive control. Luciferase activity is assessed with a luciferase assay.

Components	Control (-)	Control (+)	Without Leu	Without Cys
TNT mix	14	14	14	14
AA mix -Leu 1mM	0.25	0.25	0.5	0
AA mix -Met 1mM	0.25	0.25	0	0
AA mix -Cys 1mM	0	0	0	0.5
pAPCT2v2	0	1	1	1
Water	To 25µL	To 25µL	To 25µL	To 25µL
Luminescence	135	7942	14764	10714

Table 5: Use of a different plasmid miniprep with different amino acid mix doesn't change the expression of luciferase. Using a newly miniprep plasmid shows similar results as in Table 4 where the lack of an amino acid doesn't lead to a defect in luciferase expression. Luciferase activity is assessed with a luciferase assay.

5.3.4 Amino-acid contamination is present in all the lysate aliquots

Previous experiments were done using the aliquot Lysate 1, so are both the negative and positive controls shown in Table 6. Both lysates 2 and 3 show expression of luciferase in the absence of an amino acid mix. This suggests that the lysates contain endogenous amino acids in sufficient quantity to have a great expression of luciferase.

Components	Control (-)	Control (+)	Lysate 2	Lysate 3
TNT mix	14	14	14	14
AA mix -Leu 1mM	0.25	0.25	0	0
AA mix -Met 1mM	0.25	0.25	0	0
pAPCT2	0	1	1	1
Water	To 25µL	To 25µL	To 25µL	To 25µL
Luminescence	91	16250	15015	17438

Table 6: The different lysates don't affect luciferase expression in the absence of amino acids. This suggests that there is already an excess of endogenous amino acids within the lysates.

Luciferase activity is assessed with a luciferase assay.

5.3.5 Exhausting the amount of amino acids doesn't show an increase in luciferase expression when complemented with said amino acid

To deal with the endogenous amino acids within the TNT kit, an exhaustion experiment was conducted with the aim of exhausting one amino acid in the solution. To do so, the reaction was done using an amino-acid mix lacking leucine and the reaction was allowed to proceed for 90 minutes, then leucine was added, and the reaction was allowed to pursue for a further 90 minutes. As shown in Table 7, there is almost no difference in-between pre- and post-exhaust luminescence, suggesting that the endogenous amino acids are present in quantity greater than what can be exhausted in 90 minutes. The level of luciferase expression in between a reaction with or without added amino acids shows similar expression levels, further hinting that the endogenous amino-acid content is too great to deal with and highlighting the need for a different approach.

Components	Control (-) no AA	Control (-) no AA	Control (+) all AA	Without Leu	+ Leu
TNT mix	14	14	14	42	
AA mix -Leu 1mM	0	0	0.5	3	
AA mix -Cys 1mM	0	0	0.5	0	+1µL
pAPCT2	0	1	1	3	
Water	To 25µL	To 25µL	To 25µL	To 75µL	
Luminescence	204	147379	125504	618866	579174

Table 7: The exhaust experiment doesn't show differences in luciferase expression. Both controls in the presence of DNA with and without amino acids show similar levels of luciferase expression. Furthermore, if a reaction mix containing all amino-acids but leucine is incubated for 90

minutes, and then leucine is supplemented and the reaction runs for 90 minutes more, there is no increase in luciferase expression in-between before and after the addition of leucine. Both of those observation highlights the need to use a different approach. Luciferase activity is assessed with a luciferase assay.

5.3.6 APCT2 doesn't allow the expression of functional luciferase when using the PURExpress kit

As the TnT® Coupled Reticulocyte Lysate Systems proved itself unusable for stalling ribosomes, the PURExpress recombinated kit (NEB E6840s) was used instead. They both are transcription/translation *in vitro* coupled systems, but the TnT® Coupled Reticulocyte Lysate Systems is acquired by lysing of cells while the PURExpress kit is acquired by purifying all the necessary elements for transcription and translation and assembling them together. The version of the kit that was used has both the amino acids and tRNA not already pre-mixed with the rest of the kits, which allows us to have better control of reaction contents. One big difference is also that the TnT® Coupled Reticulocyte Lysate Systems is a eukaryotic system (rabbit) while the PURExpress kit is a prokaryotic system (*E. coli*), which means that the ribosomes and other translation elements within them are different. The gene coding for the luciferase that was being used beforehand (APCT2) was moved by Gibson into the DHFR control plasmid provided by the PURExpress kit. This newly built construct will be called pls7 and will be used for all subsequent reactions.

To check that our newly built DNA construct could express luciferase, two reactions were performed. One with a homemade amino-acid mix containing all 20 amino acids required for translation, the other with the exact same mix but lacking leucine. Unexpectedly, none of them showed luminescence when tested with a luciferase assay, suggesting that luciferase wasn't expressed, as shown in Table 8. This needed further controls to assess which part of the reaction mix was troubling the proper expression of luciferase.

Components	Control (-)	Control (+)	AA mix - Leu
E6840S mix	7.5	7.5	7.5
AA mix -Leu	0	0	1.25
AA mix complete	0	1.25	0
DNA template	1	1	1
Water	To 12.5µL	To 12.5µL	To 12.5µL
Luminescence	95	78	88

Table 8: The PURExpress kit doesn't express luciferase. Despite the addition of a DNA template and amino-acid mix, there was no expression of luciferase, suggesting that there is an issue with at least one of the reaction components. Here the only elements that are not from the kit are the miniprep DNA and the amino-acid mix. Luciferase activity is assessed with a luciferase assay.

5.3.7 The PURExpress kit doesn't allow expression of luciferase using the pls7 construct but does allow expression of the DHFR control plasmid

To check if the kit could use our homemade amino-acid mix to express the protein, an expression assay using the provided DHFR plasmid with the homemade or provided amino-acid mix was performed. It shows that expression of DHFR is only occurring when using the kit's amino-acid mix as shown in Figure 62. In parallel with the DHFR expression, a luciferase assay was performed using the pls7 plasmid and the kit's amino-acid mix, showing that expression of luciferase doesn't happen when using the pls7 plasmid as shown in Table 9. Both of those highlight issues in both the DNA template and the homemade amino-acid mix preparation. Issues within the DNA template could be due to several problems. Despite having been sequenced, there could be a mutation within the sequence of the luciferase gene. There could also be issues in the way that the plasmid was purified including RNase contamination.

Components	Control (-)	A	B	C
E6840S mix	0	7.5	7.5	7.5
AA mix kit	0	1.25	1.25	0
AA mix homemade	0	0	0	1.25
DNA template (1μL)	0	Pls7	DHFR	DHFR
Water	25			
Luminescence	84	93	NA	NA

Table 9: Pls7 doesn't show luciferase expression in the presence of the kit's amino-acid mix. Despite using the kit's amino-acid mix, there is no expression of luciferase when using minipreped pls7. This seems to suggest that there is an issue within the minipreped plasmid. Shown in this table are preparations B and C for Figure 62. Luciferase activity is assessed with a luciferase assay.

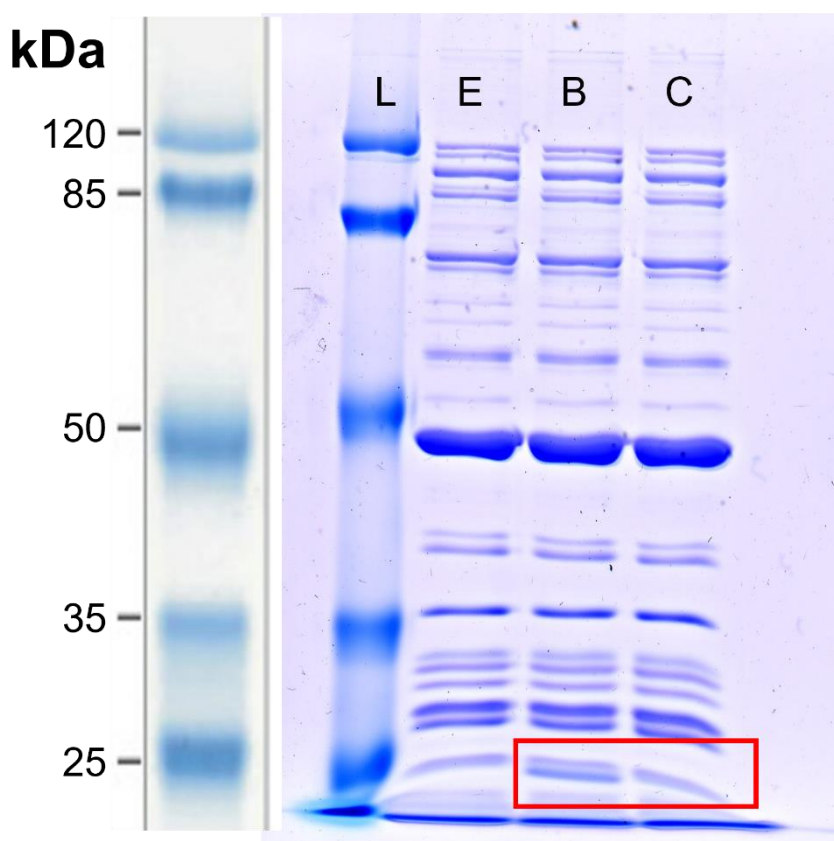


Figure 62: Expression control of DHFR. 10 % SDS Page gel. **L:** Molecular weight marker (Pierce 26612) **E:** PURExpress reaction without DNA template. **B:** PURExpress reaction with control DHFR plasmid and using the kit's amino acid mix, showing expression of DHFR at the estimated size molecular weight size of 18 kDa (within the red square). **C:** PURExpress reaction with control DHFR

plasmid and using homemade amino acid mix showing no expression of DHFR. This highlights an issue within the amino acid mix.

5.3.8 Pls7 plasmid does allow expression of luciferase when using the TNT rabbit reticulocyte kit

First, the pls7 plasmid capacity of expressing luciferase was assessed using the TNT rabbit reticulocyte kit using a standard reaction. As shown in Table 10, there is luminescence, and therefore luciferase expression, when using either the APCT2 plasmid or the pls7 plasmid. This means that at least the luciferase sequence was still coding for an active luciferase and that the issue lies somewhere else.

Components	APCT2	pls7
TNT mix	14	14
AA mix -Leu 1mM	0.25	0.25
AA mix -Met 1mM	0.25	0.25
DNA template	1	1
Water	To 25µL	To 25µL
Luminescence	450499	251348

Table 10: TNT rabbit reticulocyte luciferase activity check. Both the APCT2 and the pls7 DNA constructs are sufficient to express active luciferase when using the TNT rabbit reticulocyte kit. Luciferase activity is assessed with a luciferase assay.

5.3.9 RNase contamination in miniprep samples prevents the expression of protein

It was proven that the newly constructed pls7 plasmid could express luciferase when used within the TNT rabbit reticulocyte kit. It leaves the hypothesis that the issue could be coming from the way that the plasmid was prepared. Therefore, the DHFR control plasmid was transformed into a DH5 cell and purified by miniprep. Both the miniprep and the control plasmid were used within the PURExpress kit as previously described and as shown in Figure 63A. Expression of DHFR was only seen using the provided DHFR plasmid while the newly prepped plasmid didn't allow for expression as shown in Figure 63B. This suggests that there might

be RNase co-purified with the DNA during the miniprep (RNase A is present within one of the miniprep buffers). This also suggests that the PURExpress kit is more sensitive than the TNT rabbit reticulocyte one because the latter could express luciferase while using the miniprep luciferase plasmid. To tackle this issue, 10 U of murine RNase inhibitor was added to the reaction as described in Figure 64A. The addition of the RNase inhibitor did allow the expression of DHFR even when using our own plasmid, confirming that the DNA issue was RNase contamination as shown in Figure 64B.

A

Components	1	2
E6840S mix	7.5	7.5
Kit AA mix	1.25	1.25
DNA construct	Kit DHFR	Miniprepped DHFR
Water	To 12.5 μ L	To 12.5 μ L

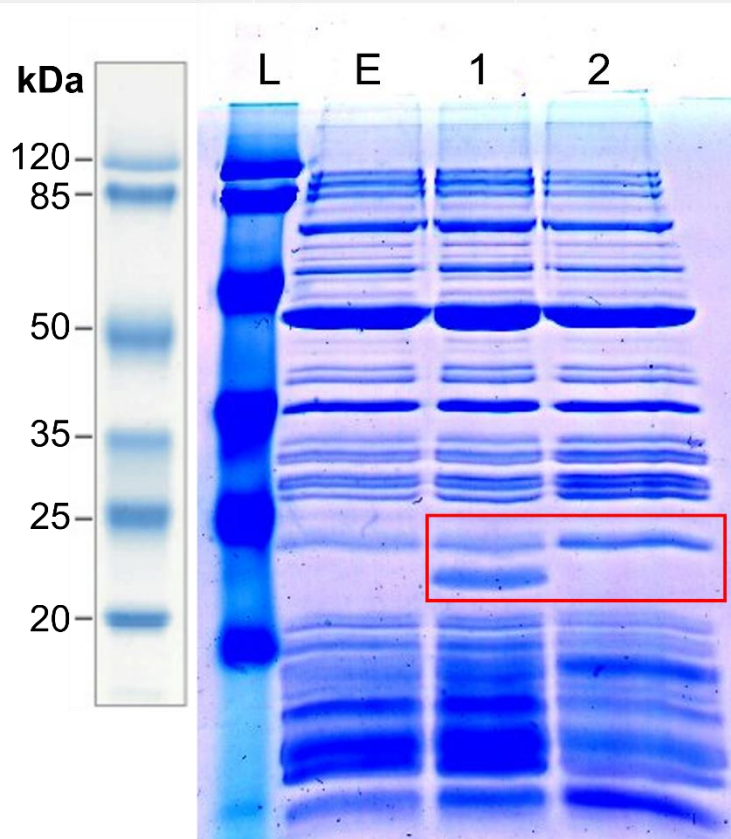
B

Figure 63: Miniprepped pDNA doesn't allow for the expression of DHFR within the PURExpress kit. **A:** Table of the different reaction mixes. **B:** 15% SDS Page gel. L: Molecular weight marker (Pierce 26612) E: PURExpress reaction without DNA template. 1: PURExpress reaction using the kit's DHFR plasmid. 2: PURExpress reaction using miniprepped DHFR plasmid. Expression of DHFR only occurs when using the provided DHFR control plasmid.

A

Components	1	2	3
E6840S mix	7.5	7.5	7.5
DNA construct	Miniprepped DHFR	Kit DHFR	Miniprepped DHFR
Water	To 12.5 μ L	To 12.5 μ L	To 12.5 μ L
RNAse I			10 U
Water	To 12.5 μ L	To 12.5 μ L	To 12.5 μ L

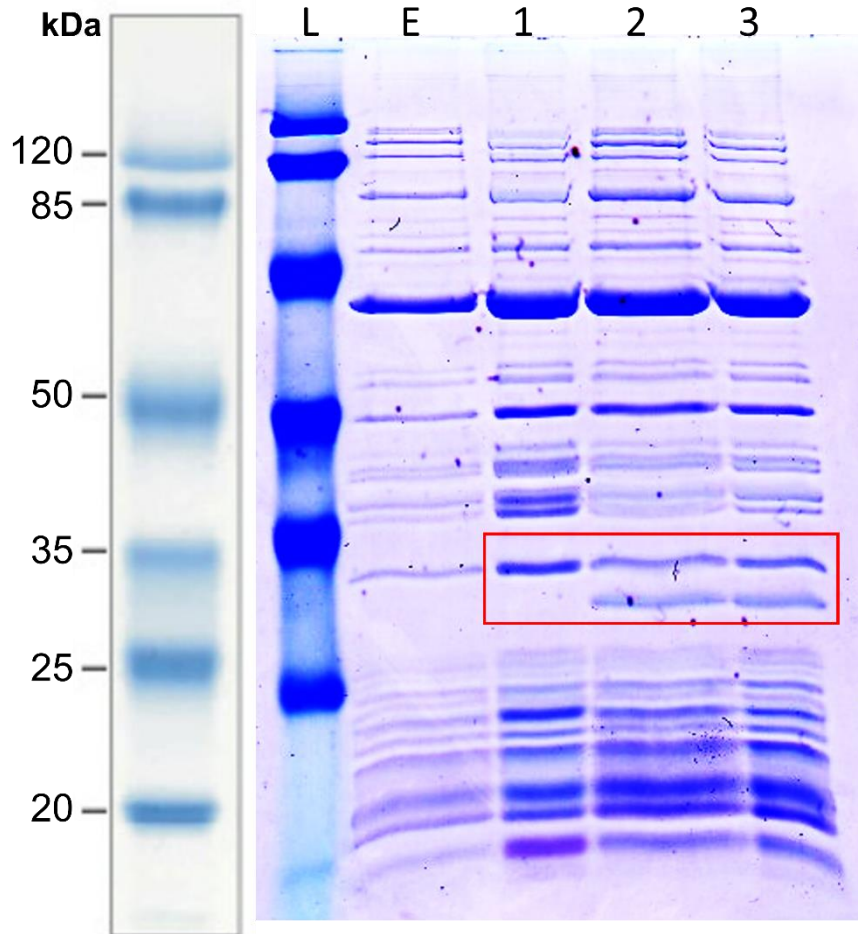
B

Figure 64: The addition of RNAse Inhibitor allows for miniprepped DHFR expression within the PURExpress kit. **A:** Table of the different reaction mixes. **B:** 15% SDS Page gel. L: Molecular weight marker (Pierce 26612) E: PURExpress reaction with no template DNA. 1: PURExpress reaction with miniprepped DHFR plasmid 2: PURExpress reaction with kit's DHFR plasmid. 3: PURExpress reaction with miniprepped DHFR plasmid supplemented with 10 U of RNAse I inhibitor. Expression of DHFR only occurs when using the provided DHFR plasmid or with the addition of RNAse inhibitor.

5.3.10 Stalling of ribosomes is possible when using an amino-acid mix with a minimized amount of KOH in the absence of one amino acid.

Now that the DNA issue was resolved, there is still an issue with the use of homemade amino-acid mixes. First, it was shown that the PURExpress kit was able to express active luciferase using the kit's amino-acid mix as shown in Table 11 column A. Then, it was shown that our amino-acid mix couldn't express luciferase as shown in Table 11, column B. The homemade amino-acid mix was made by dissolving each amino acid at a concentration of 1 M in 5 M of KOH and then pooling together to a final reaction concentration of 0.3 mM. To remedy this issue, the new amino-acid mix was made by dissolving all amino acids together directly in water except for leucine which was added last, and aspartic acid, glutamic acid, tyrosine, and tryptophan which were dissolved in 1 M KOH and added to the amino-acid mix. This was necessary due to their poor solubility. Using this new amino acid mix resulted in the expression of luciferase as shown in Table 11 column C, proving that the excess of KOH was the reason why the expression wasn't occurring. Using the exact same homemade amino-acid mix but lacking leucine, the expression of luciferase was prevented as shown in Table 11 column D, suggesting that the ribosomes might be stalled onto the mRNA. Another explanation would be that the lack of that amino acid is sufficient to stop translation and that the ribosome detaches from the mRNA or that the sub-units dissociate.

Components	A	B	C	D
E6840S mix	7.5	7.5	7.5	7.5
Kit AA mix	1.25			
Homemade AA mix		1.25		
Minimized KOH AA mix			1.25	
Minimized KOH AA mix without Leucine				1.25
pls7 (DNA)	1	1	1	1
RNAse Inhibitor	10 U	10 U	10 U	10 U
Water	To 12.5 μ L	To 12.5 μ L	To 12.5 μ L	To 12.5 μ L
Luminescence	111342	96	92120	81

Table 11: The use of a minimized KOH amino-acid mix lacking leucine allows for stalling of ribosomes within the PURExpress kit. A succession of experiments where each column shows important conclusions. Column A: minipreped pls7 allows for the expression of luciferase when supplemented with RNAse inhibitor. Column B: This expression of luciferase is hindered when using a homemade amino-acid mix. Column C: Reducing the amount of KOH within the final amino-acid mix results in the PURExpress kit being able to express luciferase once again. Column D: Finally, by using the exact same amino-acid mix, but lacking leucine, the expression of luciferase was completely stopped. This seems to suggest that the ribosomes are stalled. Luminescence is assessed with a luciferase assay.

5.3.11 Stalled ribosomes seem to bind to the surface

Now that stalled ribosomes have been produced, single-molecule confirmation of the stalling is necessary. To do so flow cell chambers were passivated and prepared as described in Figure 58. In short, the flow cell chamber surface was coated with a mixture of mPEG and biotinylated mPEG. Streptavidin bridges the biotinylated mPEG with biotinylated anti-HIS antibody which in turn recognizes the HIS tag of the nascent protein chain sticking out of the ribosome. Since the ribosomes are stalled, this connects the ribosomes to the surface. To visualize the ribosomes, anti-ribosomes mouse antibodies were coupled with a fluorescently labelled anti-mouse goat antibody. All of this allows for the visualisation of ribosomes at the surface of flow cell chambers. Despite efforts to passivate the flow cell chamber, there was a high number of binders (297) when the antibodies

and the Qdot alone were flown in (Figure 65A). There is also a higher number of binders (435) when the PURExpress reaction mix containing ribosomes that are not stalled (Figure 65B) is added. Finally, there is another increase in the number of binders (859) when the PURExpress reaction mix containing stalled ribosomes (Figure 65C) is used. This seems to suggest that despite the passivation being insufficient, there is indeed stalling of ribosomes and that the defect in luciferase expression is caused by the stalling.

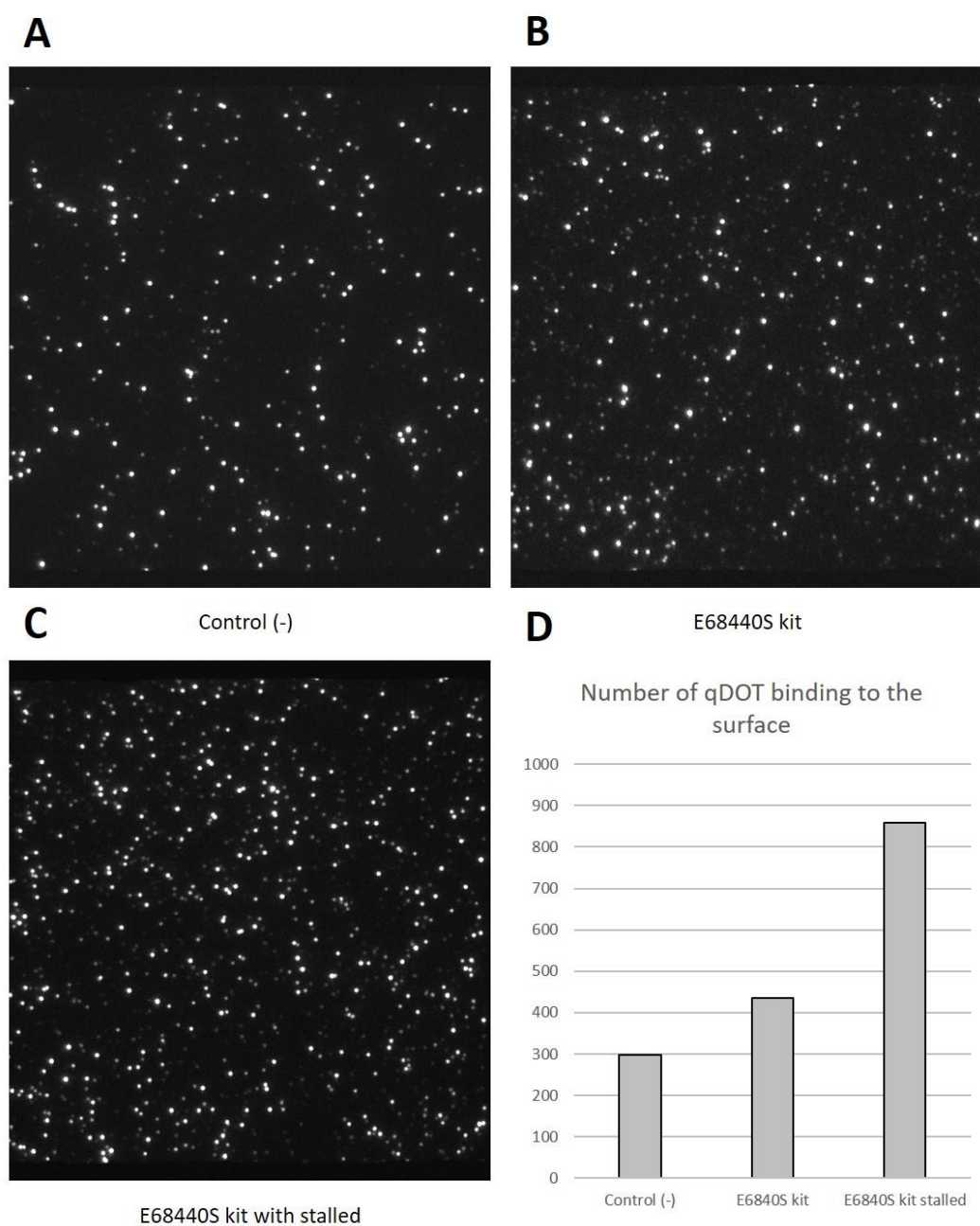


Figure 65: Flow cell surface passivation. A, B and C are pictures of three different flow chamber surfaces that have been passivated with mPEG/biotin-mPEG overnight, followed by 2.5 % tween20 treatment for 20 minutes, BSA for 30 minutes and oligos for 1h, then the addition of streptavidin, biotinylated anti-HIS antibody. **A:** Anti-ribosome mouse antibody with anti-mouse goat Qdot 605 without the addition of ribosomes are flown in the flow cell chamber. The presence of surface binders indicates that the passivation is still insufficient. **B:** Anti-ribosome mouse antibody with anti-mouse goat Qdot 605 with ribosomes (PURExpress reaction mix with complete amino-acid mix) are flown in the flow cell chamber. **C:** Anti-ribosome mouse antibody with anti-

*mouse goat Qdot 605 with stalled ribosomes (PURExpress reaction mix with incomplete amino-acid mix) are flown in the flow cell chamber. **D:** Number of binders on the flow cell after the flow was retracted. The great increase of binders in the presence of stalled ribosomes confirms that the ribosomes are stalled.*

5.4 Discussion

Although the idea of stalling the ribosomes by providing all amino acids excluding one is simple, it turned out to be difficult and troubleshooting was lengthy. This is due to several factors. Both the rabbit reticulocyte kit and the E6840s kit are expensive. Troubleshooting using those kits had to be done cautiously to avoid waste. Furthermore, the presence of endogenous amino acids within the rabbit reticulocyte kit, and the sensitivity to KOH of the E6840s kit greatly hindered the troubleshooting. Despite those obstacles, we managed to successfully stall ribosomes as shown in Table 11.

Visualisation of the stalled ribosomes using single-molecule was also challenging with the presence of a sizeable amount of non-specific binding. Indeed, the Qdot used for visualisation was binding to the flow-cell surface despite having no ribosome present. It is non-specific as the Qdot is bound to an anti-mouse antibody that targets a secondary anti-ribosome mouse antibody and therefore should bind to the surface only in the presence of ribosomes. Furthermore, the ribosome was only supposed to bind to the surface if they were stalled with a nascent protein chain containing an HIS tag. However, we see an increase in the number of Qdot bound to the surface when using non-stalled ribosomes. Altogether, this result is mitigated and requires further optimisations before assessing ribosome/tRNA interactions.

It is important to note that stalling of ribosomes can happen due to a wide variety of reasons ranging from the effect of antibiotics (298,299), to the effect of aberrant mRNAs (300), nascent protein chain interacting with the ribosome (301), or use of specific codons (302). As such a wide variety of techniques are used to stall and study the ribosomes, both *in-vivo*, *in-vitro*, and using single-molecule. However, those are not always relevant to study the elongation. The technique that we put forward here should allow us to have the freedom to change the codon of interest easily by either cloning a different codon at the same location or by changing the content of the amino acid mix if possible. Other laboratories have

used similar single-molecule surface-based assays, but to study different aspects of translation (303–305).

5.5 Conclusion

By being able to visualize stalled ribosomes on a flow cell surface we achieved two things. First, we confirmed that the ribosomes were indeed stalled and that the defect in luciferase expression wasn't due to other factors. Secondly, this will allow for further study of elongation events at a single molecule scale where fluorescently labelled aa-tRNA dwell time will be assessed depending on the codon and anticodon sequences. This will bring knowledge on specific near-cognate dwell times that are still to this date poorly understood. However, this was only partially successful as we didn't add tRNAs to the equation so we were not able to visualize ribosome/tRNA interactions. Further work is required to assess the biological question of interest to us which is to which extent different near-cognates affect the ribosome speed.

Chapter VI: Discussion

6.1 Mechanism of action of UvrA and UvrB recognition of DNA damage

Achievements:

- Showed for the first time that NER protein shows different binding behaviours depending on DNA load, proving that it is changes in DNA structure changes that are recognized as damage instead of the damage itself.
- Incorporated DNA damage at known locations on the DNA (Fluorescein) and correlated them with preferential UvrA binding to the DNA strand, which allowed for comparison with the load dependency.

NER can recognize a plethora of damages ranging from CPDs to cisplatin adducts and peptides covalently bound to the DNA(19,44,211). How NER is able to treat such a wide range of lesions is puzzling. It was speculated that instead of recognizing the lesions per se, NER was recognizing alterations of DNA structures and/or DNA flexibility locally at the perimeter of the lesions(196). However, this theory wasn't proved until now. Indeed, the work presented in Chapter III of this thesis highlights that changes in DNA structure are sufficient to be recognized as damaged by NER. The DNA structure was changed by pulling both ends of the DNA strand, hence stretching the DNA(306). Interestingly, different types of damage affect NER in different ways. Both the attachment rate and the lifetime of UvrA seem to be increased by distortions induced by DNA stretching when compared to unstretched DNA, while fluorescein shows only an increase in UvrA's lifetime. But UV damage had conflicted results on UvrA's recruitment to the DNA strand. UvrB however shows an increase in the recruitment of UvrB by UvrA to the DNA strand. How tension affects the lifetime of UvrB wasn't assessed. However, UV damage seems to increase the lifetime of UvrB on the DNA strand.

Altogether this indicates that DNA distortions due to changes in tension are sufficient to be recognized as damage by NER. However, different types of lesions affect the attachment rate and the off-rate of NER components in different ways.

It can be explained by the distortion caused by DNA damages will be unique for each lesion type and each distortion will interact uniquely with NER.

Although we proved here that UvrA was indeed recognizing changes in DNA structures instead of the lesion per se, many questions remain unanswered. First more data needs to be gathered for UvrB as the number of binders at low tension was too low. Second, the binding of UvrA to the DNA strand is a very complex phenomenon, due to the presence of two proximal and two distal ATPase cassettes per UvrA dimers. Mutants of each, or both of those ATPase cassettes have been used extensively in literature to try to decipher UvrA's binding behaviour (47). It would be interesting to see how such mutants behave under various loads.

6.2 Effect of various inhibitors on UvrA's binding to DNA

Achievements:

- Successfully assessed the effectiveness of newly found NER inhibitors on altering the binding behaviour of UvrA. Such inhibitors could have some medical applications to reduce the risk of infection-related death in cancer patients.

Antimicrobial resistance has been declared by the World Health Organisation as one of the biggest public health threats facing humanity (88,269). There is an urgent need for new antimicrobials. Works done here in Chapter IV were performed in collaboration with other members of the laboratory to put forward NER as a potential target for new antimicrobials (91,271,272,307). NER is a mechanistically conserved process between eukaryotic and prokaryotic cells, but they use different proteins (19). This means that inhibitors of prokaryotic NER cells shouldn't affect eukaryotic NER cells. This could be taken advantage of by bombarding patients with DNA-damaging agents that are repaired by NER while treating the patients with a prokaryotic NER inhibitor. DNA damaging agents are however dangerous for DNA integrity. However, a very common cancer treatment is Cisplatin, which attacks quickly dividing cells by crosslinking to the DNA. Cisplatin adducts are repairable by the NER pathway. By inhibiting prokaryotic NER, we ensure that the cisplatin adducts that are forming within bacterial cells are not repaired, therefore interfering with cell fitness. Targeting DNA damage repair pathways to affect the growth or the survivability of bacterial cells is not a new idea (92–95,308). However, until now only one inhibitor of prokaryotic NER was discovered (274). Both an *in vivo* and an *in vitro* screening took place in the lab which highlighted numerous compounds as potential inhibitors. Some of the most promising compounds were tested in this thesis. We decided to assess the effect of those compounds on UvrA's ability to bind as the first inhibitor described, ATBC, was suspected to act on UvrA. This compound is very insoluble and aggregates








easily and rapidly, making it difficult to work with. Due to the very low number of UvrA binders when treated with ATBC, the lifetime of UvrA's binding to DNA wasn't calculated. However, the four other inhibitors could be categorised by their effects as shown in Table 12. Bemcentinib reduces both the attachment rate and the lifetime of UvrA on the DNA. Aprotinin increases both the attachment rate and the lifetime of UvrA on the DNA. Finally, both L-Thyroxine and Dienestrol reduce the attachment rate of UvrA on the DNA but don't influence the lifetime.

Aprotinin increases the decoration of UvrA to the undamaged strand. It was also shown that aprotinin inhibits NER in an incision assay. It is possible that the increase of affinity of Aprotinin-treated UvrA to undamaged DNA causes unspecific over-loading of UvrA to undamaged regions of the DNA and therefore proteins are less likely to find DNA lesions.

Interestingly, Dienestrol seems to have several modes of action when inhibiting UvrA. Firstly, it was shown that Dienestrol affects UvrA's ability to hydrolyse ATP as shown in Figure 50. This reduction in ATPase activity does relate to a reduction in the attachment rate of UvrA. However, we also noticed that Dienestrol is very likely to be able to bind to DNA on his own and prevent UvrA to DNA binding this way as well.

Overall, those newly discovered NER inhibitors show great promises as potential adjuvants for cancer patients to reduce prokaryotic infections. This is exacerbated by the increase in antibacterial resistance and the fact that DNA damage repair is a crucial factor in the development of resistances (96). However, some clinical data is required to push those claims further.

Table 12: Effect of compounds on UvrA's ability to bind to DNA.

Compound	Origin	Effect on On-rate	Effect on lifetime
ATBC	Literature		NA
Bemcentinib	<i>In silico</i> screen		
Aprotinin	<i>In vivo</i> screen		
L-Thyroxine	<i>In vivo</i> screen		∅
Dienestrol	<i>In vivo</i> screen		∅

6.3 Ribosome stalling

Achievements:

- Successfully stalled ribosomes at a specific codon. This technic could be used to assess the dwell times of different combinations of near-cognates tRNAs/codons.

Ribosomes are involved in the translation of mRNA to proteins and are a very common target for antimicrobials. Chapter V presents work that was performed in anticipation of experiments that would help elucidate an understudied part of the translation. The translation is divided into three major steps: initiation, elongation, and termination. During the elongation phase, cognate aa-tRNA will decode the codon and give its amino acid to the nascent protein chain. However, when near-cognate tRNA are presented to the codon, they will stall the ribosome for a set amount of time before being discarded. How much time will the near-cognate aa-tRNA stay in the ribosome? It has been resolved for a few codons to tRNA interactions (173,174,309). But to which extent the dwell time varies between all the different combinations of codons and tRNAs is unknown. In this thesis, we put the groundwork that would allow us to assess those dwell times using single-molecule microscopy. Our proposed methods allow for ribosome stalling at any codons onto the mRNA. From there. Future work aims at deciphering the dwell time of many of those combinations. This will allow to feed data in models which can be used to help optimize protein production, amongst others, as well as providing a better understanding of how regulated some translational events are (109,181).

Appendix

7.1 Appendix 1: Code for Impact of time and protease inhibitor on the binding of UvrA-mNeonGreen

```
import bluelake as bl
from bluelake import trap1, trap2, stage, fluidics, microstage,
nanostage, timeline, pause, reset_force, force_feedback, trap2
#Input
tension_target=40                #tension wanted in pN
date="XXXXXXXX"                 #date of the experiment
nstrand="1"                     #which strand are we using
Number_frame=200                #number of frames to take video
N=5                             #number of repeats per strand
#Commonly used parameters
Rest_distance=12.5              #distance for rest
recover_distance=7.5            #distance for recovery
time_in_protein=120             #time the strand is left
in the protein channel
force_feedback.set_device("1")   #don't touch this
force_feedback.set_detector("Trap 2") #don't touch this
break_distance = 25              #distance at which we
estimate the strand to be broken
M=N+1
hi_press=0.1 #set the pressure applied to create the flow
count=1
distance = bl.timeline["Distance"]["Distance 1"]
def goto_distance(target):
    """Move trap 1 until it reaches the `target` distance from
trap 2"""
    distance = bl.timeline["Distance"]["Distance 1"]
    dx = distance.latest_value - target

    while abs(dx) > 0.2: # um
        if dx <= 0:
            bl.mirror1.move_by(dx=+0.1)
        else:
            bl.mirror1.move_by(dx=-0.1)
        dx = distance.latest_value - target

def setpressure(pres):
    curpres=fluidics.pressure
    if curpres<pres:
        while fluidics.pressure < pres:
            fluidics.increase_pressure()
            pause(0.1)
    else:
        while fluidics.pressure > pres:
            fluidics.decrease_pressure()
            pause(0.1)

setpressure(hi_press)
fluidics.open(1,2,3,6)          #open channels 1, 2, 3, and 6
while count<M and abs(distance.latest_value)<break_distance:
    setpressure(hi_press)
    fluidics.open(1, 2, 3, 6)
    print(tension_target)
    force_feedback.set_target(tension_target)
#set up the force target
```

```

    tension_export = str(tension_target)+"_strand_" + str(nstrand)
+ "_" + str(count)      #get name for export file
    Name_export = "D:\\\" + date + "\\\" + date + "_" +
tension_export + ".tiff"      #get name for export file
    print(Name_export)
    fluidics.open(1, 2, 3, 6)      #open channels 1, 2, 3, and 6
    bl.excitation_lasers.blue=0    #makes sure the laser is off
    force_feedback.set_enabled(False)    #makes sure that the
forces are not activated to go to the wanted tension
    print("Repetition_"+str(count+1))
    goto_distance(Rest_distance)    #put the beads at
their "rest" distance where the DNA is going to be under minimal
forces
    pause(10)
    print("beads at " + str(Rest_distance) + "um")
    print("move to protein channel")
    microstage.move_to("protein",speed=0.1) #move the DNA strand
to the protein channel
    pause(20)
    print("moved to protein channel")
    reset_force()                  #get the forces to 0
    print("force reset")
    pause(5)                       #wait 5 seconds
    force_feedback.set_enabled(True) #turn on the force feedback
    print("forces applied")
    pause(time_in_protein)          #stay in the protein
channel for a set amount of time (here 2 minutes)
    print("paused in protein")
    bl.excitation_lasers.blue = 30  #turn on laser at 30 %
power
    pause(3)                        #wait 3 seconds
    print("pause finished")
    microstage.move_to("buffer")    #go to the buffer channel
    print("moved to buffer channel")
    pause(1)                        #wait 1 second
    bl.widefield.start_recording(Name_export,
frames=Number_frame).wait()        #starts recording video
    print("recording_"+str(count+1))
    force_feedback.set_enabled(False) #stop adjusting beads to
stay exactly at the set force
    fluidics.stop_flow()            #stop flow in channels 1,
2, 3, and 6
    goto_distance(recover_distance) #reduce distance until it
reaches the recovering distance as set
    pause(10)                       #wait 10 seconds
    count+=1                         #repeats until count = M
(as set)
    print("done")
    force_feedback.set_enabled(False) #turn off the force
feedback
    bl.excitation_lasers.blue=0      #turn off the laser

```

7.2 Appendix 2: Code for the tension dependency of UvrA-mNeongreen

```
import bluelake as bl
from bluelake import trap1, trap2, stage, fluidics, microstage,
nanostage, timeline, pause, reset_force, force_feedback, trap2
#Input
date="XXXXXXXX" #today's date
#Commonly used parameters
tension_target=10 #tension in pN
force_feedback.set_device("1") #don't touch this
force_feedback.set_detector("Trap 2") #don't touch this
distance = bl.timeline["Distance"]["Distance 1"]
def goto_distance(target):
    """Move trap 1 until it reaches the `target` distance from
    trap 2"""
    distance = bl.timeline["Distance"]["Distance 1"]
    dx = distance.latest_value - target

    while abs(dx) > 0.2: #um
        if dx <= 0:
            bl.mirror1.move_by(dx=+0.1)
        else:
            bl.mirror1.move_by(dx=-0.1)
        dx = distance.latest_value - target

def setpressure(pres):
    curpres=fluidics.pressure
    if curpres<pres:
        while fluidics.pressure < pres:
            fluidics.increase_pressure()
            pause(0.1)
    else:
        while fluidics.pressure > pres:
            fluidics.decrease_pressure()
            pause(0.1)

force_feedback.set_target(tension_target) #force target
tension_export = "all_tension_strand_8" #get name for export file
Name_export = "D:\\\" + date + "\\\" + date + \"_\" + tension_export +
\".tiff\" # get name for export file
print(Name_export)
bl.excitation_lasers.blue = 0 #turn off the laser
goto_distance(12.5) #put the beads to a certain
distance to each others
microstage.move_to("protein",speed=0.5) #makes sure all videos are
taken at the same location
pause(3) #wait 3 seconds
reset_force() #get the forces to 0
goto_distance(12.5) #put the beads to a certain
distance to each others
reset_force() #get the forces to 0
pause(1) #wait 1 second
print("start recording")
bl.widefield.start_recording(Name_export, frames=3660) #start
recording video for set amount of frames
bl.excitation_lasers.blue = 30 #turn on laser power

print("5pN")
```



```

tension_target=5
force_feedback.set_target(tension_target) # force target
force_feedback.enabled = True # Turn on the force feedback
pause(30)
force_feedback.enabled = False # Turn off the force feedback
pause(270)
goto_distance(12.5)
reset_force()
print("10pN")
tension_target=10
force_feedback.set_target(tension_target) # force target
force_feedback.enabled = True # Turn on the force feedback
pause(30)
force_feedback.enabled = False # Turn off the force feedback
pause(270)
goto_distance(12.5)
reset_force()
print("15pN")
tension_target=15
force_feedback.set_target(tension_target) # force target
force_feedback.enabled = True # Turn on the force feedback
pause(30)
force_feedback.enabled = False # Turn off the force feedback
pause(270)
goto_distance(12.5)
reset_force()
print("25pN")
tension_target=25
force_feedback.set_target(tension_target) # force target
force_feedback.enabled = True # Turn on the force feedback
pause(30)
force_feedback.enabled = False # Turn off the force feedback
pause(270)
goto_distance(12.5)
reset_force()
print("35pN")
tension_target=35
force_feedback.set_target(tension_target) # force target
force_feedback.enabled = True # Turn on the force feedback
pause(30)
force_feedback.enabled = False # Turn off the force feedback
pause(270)
goto_distance(12.5)
reset_force()
print("45pN")
tension_target=45
force_feedback.set_target(tension_target) # force target
force_feedback.enabled = True # Turn on the force feedback
pause(30)
force_feedback.enabled = False # Turn off the force feedback
pause(270)
goto_distance(12.5)
reset_force()
bl.excitation_lasers.blue = 0 # Turn off laser power

```

References

1. Mullenders LHF. Solar UV damage to cellular DNA: from mechanisms to biological effects. *Photochem Photobiol Sci*. 2018 Dec 5;17(12):1842–52.
2. Chen CZ, Sutherland JC. Gel electrophoresis method for quantitation of gamma ray induced single- and double-strand breaks in DNA irradiated in vitro. *Electrophoresis*. 1989 May-Jun;10(5–6):318–26.
3. Taylor W, Camilleri E, Craft DL, Korza G, Granados MR, Peterson J, et al. DNA Damage Kills Bacterial Spores and Cells Exposed to 222-Nanometer UV Radiation. *Appl Environ Microbiol* [Internet]. 2020 Apr 1;86(8). Available from: <http://dx.doi.org/10.1128/AEM.03039-19>
4. Cortez D. Replication-Coupled DNA Repair. *Mol Cell*. 2019 Jun 6;74(5):866–76.
5. Borges HL, Linden R, Wang JYJ. DNA damage-induced cell death: lessons from the central nervous system. *Cell Res*. 2008 Jan;18(1):17–26.
6. Kerem BS, Zielenski J, Markiewicz D, Bozon D, Gazit E, Yahav J, et al. Identification of mutations in regions corresponding to the two putative nucleotide (ATP)-binding folds of the cystic fibrosis gene. *Proc Natl Acad Sci U S A*. 1990 Nov;87(21):8447–51.
7. Cystic Fibrosis Foundation [Internet]. Cystic Fibrosis Foundation. Available from: <https://www.cff.org/>
8. De Boeck K. Cystic fibrosis in the year 2020: A disease with a new face. *Acta Paediatr*. 2020 May;109(5):893–9.
9. Black JO. Xeroderma Pigmentosum. *Head Neck Pathol*. 2016 Jun;10(2):139–44.
10. Harris K, Pritchard JK. Rapid evolution of the human mutation spectrum. *Elife* [Internet]. 2017 Apr 25;6. Available from: <http://dx.doi.org/10.7554/eLife.24284>
11. Hershberg R. Mutation--The Engine of Evolution: Studying Mutation and Its Role in the Evolution of Bacteria. *Cold Spring Harb Perspect Biol*. 2015 Sep 1;7(9):a018077.
12. Van Houten B, Gamper H, Sancar A, Hearst JE. DNase I footprint of ABC excinuclease. *J Biol Chem*. 1987 Sep 25;262(27):13180–7.

13. Stracy M, Jaciuk M, Uphoff S, Kapanidis AN, Nowotny M, Sherratt DJ, et al. Single-molecule imaging of UvrA and UvrB recruitment to DNA lesions in living *Escherichia coli*. *Nat Commun*. 2016 Aug 26;7(1):1–9.
14. Mazur SJ, Grossman L. Dimerization of *Escherichia coli* UvrA and its binding to undamaged and ultraviolet light damaged DNA. *Biochemistry*. 1991 May 7;30(18):4432–43.
15. Kad NM, Wang H, Kennedy GG, Warshaw DM, Van Houten B. Collaborative dynamic DNA scanning by nucleotide excision repair proteins investigated by single- molecule imaging of quantum-dot-labeled proteins. *Mol Cell*. 2010 Mar 12;37(5):702–13.
16. Orren DK, Sancar A. The (A)BC excinuclease of *Escherichia coli* has only the UvrB and UvrC subunits in the incision complex. *Proc Natl Acad Sci U S A*. 1989 Jul;86(14):5237–41.
17. Verhoeven EEA, Wyman C, Moolenaar GF, Goosen N. The presence of two UvrB subunits in the UvrAB complex ensures damage detection in both DNA strands. *EMBO J*. 2002 Aug 1;21(15):4196–205.
18. Orren DK, Sancar A. Formation and enzymatic properties of the UvrB.DNA complex. *J Biol Chem*. 1990 Sep 15;265(26):15796–803.
19. Truglio JJ, Croteau DL, Van Houten B, Kisker C. Prokaryotic nucleotide excision repair: the UvrABC system. *Chem Rev*. 2006 Feb;106(2):233–52.
20. Sancar A, Rupp WD. A novel repair enzyme: UVRABC excision nuclease of *Escherichia coli* cuts a DNA strand on both sides of the damaged region. *Cell*. 1983 May;33(1):249–60.
21. Husain I, Van Houten B, Thomas DC, Abdel-Monem M, Sancar A. Effect of DNA polymerase I and DNA helicase II on the turnover rate of UvrABC excision nuclease. *Proc Natl Acad Sci U S A*. 1985 Oct;82(20):6774–8.
22. Caron PR, Kushner SR, Grossman L. Involvement of helicase II (*uvrD* gene product) and DNA polymerase I in excision mediated by the *uvrABC* protein complex. *Proc Natl Acad Sci U S A*. 1985 Aug;82(15):4925–9.
23. Van Houten B, Croteau DL, DellaVecchia MJ, Wang H, Kisker C. “Close-fitting sleeves”: DNA damage recognition by the UvrABC nuclease system. *Mutat Res*. 2005 Sep 4;577(1–2):92–117.
24. Lee S-J, Sung R-J, Verdine GL. Mechanism of DNA Lesion Homing and Recognition by the Uvr Nucleotide Excision Repair System. *Research*. 2019 Aug 28;2019:5641746.

25. de Gruijl FR, Forbes PD. UV-induced skin cancer in a hairless mouse model. *Bioessays*. 1995 Jul;17(7):651–60.
26. Chandrasekhar D, Van Houten B. In vivo formation and repair of cyclobutane pyrimidine dimers and 6-4 photoproducts measured at the gene and nucleotide level in *Escherichia coli*. *Mutat Res*. 2000 May 30;450(1–2):19–40.
27. Khan AQ, Travers JB, Kemp MG. Roles of UVA radiation and DNA damage responses in melanoma pathogenesis. *Environ Mol Mutagen*. 2018 Jun;59(5):438–60.
28. Dianov G, Bischoff C, Piotrowski J, Bohr VA. Repair pathways for processing of 8-oxoguanine in DNA by mammalian cell extracts. *J Biol Chem*. 1998 Dec 11;273(50):33811–6.
29. Crul M, van Waardenburg RCAM, Beijnen JH, Schellens JHM. DNA-based drug interactions of cisplatin. *Cancer Treat Rev*. 2002 Dec;28(6):291–303.
30. Liu S, Wang Y. Mass spectrometry for the assessment of the occurrence and biological consequences of DNA adducts. *Chem Soc Rev*. 2015 Nov 7;44(21):7829–54.
31. Jaciuk M, Nowak E, Skowronek K, Tańska A, Nowotny M. Structure of UvrA nucleotide excision repair protein in complex with modified DNA. *Nat Struct Mol Biol*. 2011 Feb;18(2):191–7.
32. Juan-Carlos P-DM, Perla-Lidia P-P, Stephanie-Talia M-M, Mónica-Griselda A-M, Luz-María T-E. ABC transporter superfamily. An updated overview, relevance in cancer multidrug resistance and perspectives with personalized medicine. *Mol Biol Rep*. 2021 Feb;48(2):1883–901.
33. Braibant M, Gilot P, Content J. The ATP binding cassette (ABC) transport systems of *Mycobacterium tuberculosis*. *FEMS Microbiol Rev*. 2000 Oct;24(4):449–67.
34. Doolittle RF, Johnson MS, Husain I, van Houten B, Thomas DC, Sancar A. Domainal evolution of a prokaryotic DNA repair protein and its relationship to active-transport proteins. *Nature*. 1986 Oct 1;323:451–3.
35. Linton KJ. Structure and function of ABC transporters. *Physiology* . 2007 Apr;22:122–30.
36. Pakotiprapha D, Inuzuka Y, Bowman BR, Moolenaar GF, Goosen N, Jeruzalmi D, et al. Crystal structure of *Bacillus stearothermophilus* UvrA provides insight into ATP-modulated dimerization, UvrB interaction, and DNA binding. *Mol Cell*. 2008 Jan 18;29(1):122–33.

37. Pakotiprapha D, Samuels M, Shen K, Hu JH, Jeruzalmi D. Structure and mechanism of the UvrA-UvrB DNA damage sensor. *Nat Struct Mol Biol.* 2012 Feb 5;19(3):291–8.
38. Hopfner K-P, Tainer JA. Rad50/SMC proteins and ABC transporters: unifying concepts from high-resolution structures. *Curr Opin Struct Biol.* 2003 Apr;13(2):249–55.
39. Pakotiprapha D, Liu Y, Verdine GL, Jeruzalmi D. A structural model for the damage-sensing complex in bacterial nucleotide excision repair. *J Biol Chem.* 2009 May 8;284(19):12837–44.
40. Timmins J, Gordon E, Caria S, Leonard G, Acajjaoui S, Kuo M-S, et al. Structural and mutational analyses of *Deinococcus radiodurans* UvrA2 provide insight into DNA binding and damage recognition by UvrAs. *Structure.* 2009 Apr 15;17(4):547–58.
41. Croteau DL, DellaVecchia MJ, Perera L, Van Houten B. Cooperative damage recognition by UvrA and UvrB: identification of UvrA residues that mediate DNA binding. *DNA Repair .* 2008 Mar 1;7(3):392–404.
42. Croteau DL, DellaVecchia MJ, Wang H, Bienstock RJ, Melton MA, Van Houten B. The C-terminal zinc finger of UvrA does not bind DNA directly but regulates damage-specific DNA binding. *J Biol Chem.* 2006 Sep 8;281(36):26370–81.
43. Wagner K, Moolenaar GF, Goosen N. Role of the insertion domain and the zinc-finger motif of *Escherichia coli* UvrA in damage recognition and ATP hydrolysis. *DNA Repair .* 2011 May 5;10(5):483–96.
44. Kisker C, Kuper J, Van Houten B. Prokaryotic nucleotide excision repair. *Cold Spring Harb Perspect Biol.* 2013 Mar 1;5(3):a012591.
45. Kraithong T, Channgam K, Itsathitphaisarn O, Tiensuwan M, Jeruzalmi D, Pakotiprapha D. Movement of the β -hairpin in the third zinc-binding module of UvrA is required for DNA damage recognition. *DNA Repair .* 2017 Mar;51:60–9.
46. Myles GM, Sancar A. Isolation and characterization of functional domains of UvrA. *Biochemistry.* 1991 Apr 23;30(16):3834–40.
47. Case BC, Hartley S, Osuga M, Jeruzalmi D, Hingorani MM. The ATPase mechanism of UvrA2 reveals the distinct roles of proximal and distal ATPase sites in nucleotide excision repair. *Nucleic Acids Res.* 2019 May 7;47(8):4136–52.

48. Barnett JT, Kad NM. Understanding the coupling between DNA damage detection and UvrA's ATPase using bulk and single molecule kinetics. *FASEB J*. 2019 Jan;33(1):763–9.
49. Oh EY, Claassen L, Thiagalingam S, Mazur S, Grossman L. ATPase activity of the UvrA and UvrAB protein complexes of the *Escherichia coli* UvrABC endonuclease. *Nucleic Acids Res*. 1989 Jun 12;17(11):4145–59.
50. Myles GM, Hearst JE, Sancar A. Site-specific mutagenesis of conserved residues within Walker A and B sequences of *Escherichia coli* UvrA protein. *Biochemistry*. 1991 Apr 23;30(16):3824–34.
51. Kraithong T, Sucharitakul J, Buranachai C, Jeruzalmi D, Chaiyen P, Pakotiprapha D. Real-time investigation of the roles of ATP hydrolysis by UvrA and UvrB during DNA damage recognition in nucleotide excision repair. *DNA Repair*. 2021 Jan;97:103024.
52. Oh EY, Grossman L. Characterization of the helicase activity of the *Escherichia coli* UvrAB protein complex. *J Biol Chem*. 1989 Jan 15;264(2):1336–43.
53. Theis K, Chen PJ, Skorvaga M, Van Houten B, Kisker C. Crystal structure of UvrB, a DNA helicase adapted for nucleotide excision repair. *EMBO J*. 1999 Dec 15;18(24):6899–907.
54. Selby CP, Sancar A. Molecular mechanism of transcription-repair coupling. *Science*. 1993 Apr 2;260(5104):53–8.
55. Seeley TW, Grossman L. The role of *Escherichia coli* UvrB in nucleotide excision repair. *J Biol Chem*. 1990 May 5;265(13):7158–65.
56. Wang H, DellaVecchia MJ, Skorvaga M, Croteau DL, Erie DA, Van Houten B. UvrB Domain 4, an Autoinhibitory Gate for Regulation of DNA Binding and ATPase Activity*. *J Biol Chem*. 2006 Jun 2;281(22):15227–37.
57. Malta E, Moolenaar GF, Goosen N. Base Flipping in Nucleotide Excision Repair*. *J Biol Chem*. 2006 Jan 27;281(4):2184–94.
58. Moolenaar GF, Höglund L, Goosen N. Clue to damage recognition by UvrB: residues in the beta-hairpin structure prevent binding to non-damaged DNA. *EMBO J*. 2001 Nov 1;20(21):6140–9.
59. Skorvaga M, Theis K, Mandavilli BS, Kisker C, Van Houten B. The beta -hairpin motif of UvrB is essential for DNA binding, damage processing, and UvrC-mediated incisions. *J Biol Chem*. 2002 Jan 11;277(2):1553–9.
60. Jaciuk M, Swuec P, Gaur V, Kasprzak JM, Renault L, Dobrychłop M, et al. A combined structural and biochemical approach reveals translocation and

stalling of UvrB on the DNA lesion as a mechanism of damage verification in bacterial nucleotide excision repair. *DNA Repair* . 2020 Jan;85:102746.

61. Moolenaar GF, Franken KL, Dijkstra DM, Thomas-Oates JE, Visse R, van de Putte P, et al. The C-terminal region of the UvrB protein of *Escherichia coli* contains an important determinant for UvrC binding to the preincision complex but not the catalytic site for 3'-incision. *J Biol Chem*. 1995 Dec 22;270(51):30508–15.
62. Seck A, De Bonis S, Stelter M, Ökvist M, Senarisoy M, Hayek MR, et al. Structural and functional insights into the activation of the dual incision activity of UvrC, a key player in bacterial NER. *Nucleic Acids Res*. 2023 Mar 3;gkad108.
63. Minko IG, Zou Y, Lloyd RS. Incision of DNA-protein crosslinks by UvrABC nuclease suggests a potential repair pathway involving nucleotide excision repair. *Proc Natl Acad Sci U S A*. 2002 Feb 19;99(4):1905–9.
64. Sharma R, Lewis S, Wlodarski MW. DNA Repair Syndromes and Cancer: Insights Into Genetics and Phenotype Patterns. *Front Pediatr*. 2020 Oct 23;8:570084.
65. Caradonna SJ, Cheng YC. DNA glycosylases. *Mol Cell Biochem*. 1982 Jul 7;46(1):49–63.
66. Krokan HE, Bjørås M. Base excision repair. *Cold Spring Harb Perspect Biol*. 2013 Apr 1;5(4):a012583.
67. Boiteux S, Coste F, Castaing B. Repair of 8-oxo-7,8-dihydroguanine in prokaryotic and eukaryotic cells: Properties and biological roles of the Fpg and OGG1 DNA N-glycosylases. *Free Radic Biol Med*. 2017 Jun;107:179–201.
68. Friedberg EC, Walker GC, Siede W, Wood RD. *DNA Repair and Mutagenesis*. American Society for Microbiology Press; 2005. 1118 p.
69. Joseph N, Duppatla V, Rao DN. Prokaryotic DNA mismatch repair. *Prog Nucleic Acid Res Mol Biol*. 2006;81:1–49.
70. Su SS, Modrich P. *Escherichia coli* mutS-encoded protein binds to mismatched DNA base pairs. *Proc Natl Acad Sci U S A*. 1986 Jul;83(14):5057–61.
71. Modrich P. Mechanisms and biological effects of mismatch repair. *Annu Rev Genet*. 1991;25:229–53.
72. Fishel R. Mismatch repair. *J Biol Chem*. 2015 Oct 30;290(44):26395–403.

73. Dabert P, Ehrlich SD, Gruss A. Chi sequence protects against RecBCD degradation of DNA in vivo. *Proc Natl Acad Sci U S A*. 1992 Dec 15;89(24):12073–7.
74. Anderson DG, Kowalczykowski SC. The translocating RecBCD enzyme stimulates recombination by directing RecA protein onto ssDNA in a chi-regulated manner. *Cell*. 1997 Jul 11;90(1):77–86.
75. Ragunathan K, Liu C, Ha T. RecA filament sliding on DNA facilitates homology search. *Elife*. 2012 Dec 13;1:e00067.
76. Forget AL, Kowalczykowski SC. Single-molecule imaging of DNA pairing by RecA reveals a three-dimensional homology search. *Nature*. 2012 Feb 8;482(7385):423–7.
77. Kowalczykowski, Dixon, Eggleston, Lauder, Rehrauer. Biochemistry of homologous recombination in *Escherichia coli*. *Microbiol Rev* [Internet]. 1994; Available from: <https://www.ncbi.nlm.nih.gov/pmc/articles/PMC372975/>
78. Cox MM, Lehman IR. recA protein of *Escherichia coli* promotes branch migration, a kinetically distinct phase of DNA strand exchange. *Proc Natl Acad Sci U S A*. 1981 Jun;78(6):3433–7.
79. Kowalczykowski SC. An Overview of the Molecular Mechanisms of Recombinational DNA Repair. *Cold Spring Harb Perspect Biol* [Internet]. 2015 Nov 2;7(11). Available from: <http://dx.doi.org/10.1101/cshperspect.a016410>
80. Bell JC, Kowalczykowski SC. Mechanics and Single-Molecule Interrogation of DNA Recombination. *Annu Rev Biochem*. 2016 Jun 2;85:193–226.
81. Gest H. The discovery of microorganisms by Robert Hooke and Antoni Van Leeuwenhoek, fellows of the Royal Society. *Notes Rec R Soc Lond*. 2004 May;58(2):187–201.
82. Hooke R. *Micrographia : or, Some physiological descriptions of minute bodies made by magnifying glasses: With observations and inquiries thereupon*. Martyn J, Allestry J, editors. London: Printed by Jo. Martyn, and Ja. Allestry, Printers to the Royal Society, and are to be sold at their Shop at the Bell, in S. Paul's Church-yard; 1665. 18 p. l., 246, [10] p. XXXVIII pl. (partly fold.).
83. Fleming A. On the Antibacterial Action of Cultures of a *Penicillium*, with Special Reference to their Use in the Isolation of *B. influenzae*. *Br J Exp Pathol*. 1929 Jun;10(3):226.
84. Browning CH, McKenzie I. THE TREATMENT OF SYPHILIS BY SALVARSAN. *Br Med J*. 1911 Sep 23;2(2647):654–5.

85. Dicker D, Nguyen G, Abate D, Abate KH, Abay SM, Abbafati C, et al. Global, regional, and national age-sex-specific mortality and life expectancy, 1950–2017: a systematic analysis for the Global Burden of Disease Study 2017. *Lancet*. 2018 Nov 10;392(10159):1684–735.
86. Spink WW, Ferris V. PENICILLIN-RESISTANT STAPHYLOCOCCI: MECHANISMS INVOLVED IN THE DEVELOPMENT OF RESISTANCE. *J Clin Invest*. 1947 May;26(3):379–93.
87. Aminov RI. A brief history of the antibiotic era: lessons learned and challenges for the future. *Front Microbiol*. 2010 Dec 8;1:134.
88. World Health Organisation. Antimicrobial resistance: global report on surveillance. World Health Organization. World Health Organization [Internet]. 2014; Available from: https://apps.who.int/iris/bitstream/handle/10665/112642/9789241564748_eng.pdf?sequence=1&isAllowed=y
89. Naylor NR, Atun R, Zhu N, Kulasabanathan K, Silva S, Chatterjee A, et al. Estimating the burden of antimicrobial resistance: a systematic literature review. *Antimicrob Resist Infect Control*. 2018 Apr 25;7:58.
90. Tenover FC. Mechanisms of antimicrobial resistance in bacteria. *Am J Infect Control*. 2006 Jun;34(5 Suppl 1):S3-10; discussion S64-73.
91. Bernacchia L, Paris A, Gupta A, Charman R, McGreig J, Kad NM. R428 as a novel NER inhibitor for multidrug resistant infections in cancer patients. waiting for submission [Internet]. 2023; Available from: Bernacchia, Lorenzo; Paris, Antoine; Gupta, Arya; Charman, Robert; McGreig, Jake; Kad, Neil M
92. Ledger Elizabeth V. K., Lau Katie, Tate Edward W., Edwards Andrew M. XerC Is Required for the Repair of Antibiotic- and Immune-Mediated DNA Damage in *Staphylococcus aureus*. *Antimicrob Agents Chemother*. 2023 Feb 21;67(3):e01206-22.
93. Memar MY, Yekani M, Celenza G, Poortahmasebi V, Naghili B, Bellio P, et al. The central role of the SOS DNA repair system in antibiotics resistance: A new target for a new infectious treatment strategy. *Life Sci*. 2020 Dec 1;262:118562.
94. Lim CSQ, Ha KP, Clarke RS, Gavin L-A, Cook DT, Hutton JA, et al. Identification of a potent small-molecule inhibitor of bacterial DNA repair that potentiates quinolone antibiotic activity in methicillin-resistant *Staphylococcus aureus*. *Bioorg Med Chem*. 2019 Oct 15;27(20):114962.

95. Bradbury JD, Hodgkinson T, Thomas AM, Tanwar O, La Monica G, Rogga VV, et al. Development of an inhibitor of the mutagenic SOS response that suppresses the evolution of quinolone antibiotic resistance. *Chem Sci*. 2024 Jun 26;15(25):9620–9.
96. Carvajal-Garcia J, Samadpour AN, Viera AJH, Merrikh H. Oxidative stress drives mutagenesis through transcription-coupled repair in bacteria. *Proceedings of the National Academy of Sciences*. 2023;120(27):e2300761120.
97. Lin J, Zhou D, Steitz TA, Polikanov YS, Gagnon MG. Ribosome-Targeting Antibiotics: Modes of Action, Mechanisms of Resistance, and Implications for Drug Design. *Annu Rev Biochem*. 2018 Jun 20;87:451–78.
98. Wilson DN. Ribosome-targeting antibiotics and mechanisms of bacterial resistance. *Nat Rev Microbiol*. 2014 Jan;12(1):35–48.
99. Pioletti M, Schlünzen F, Harms J, Zarivach R, Glühmann M, Avila H, et al. Crystal structures of complexes of the small ribosomal subunit with tetracycline, edeine and IF3. *EMBO J*. 2001 Apr 17;20(8):1829–39.
100. Mohan S, Donohue JP, Noller HF. Molecular mechanics of 30S subunit head rotation. *Proc Natl Acad Sci U S A*. 2014 Sep 16;111(37):13325–30.
101. Abrahams JP, van Raaij MJ, Ott G, Kraal B, Bosch L. Kirromycin drastically reduces the affinity of Escherichia coli elongation factor Tu for aminoacyl-tRNA. *Biochemistry*. 1991 Jul 9;30(27):6705–10.
102. Casadesús J, Sánchez-Romero MA. DNA Methylation in Prokaryotes. *Adv Exp Med Biol*. 2022;1389:21–43.
103. Zhang Y, Sun Z, Jia J, Du T, Zhang N, Tang Y, et al. Overview of Histone Modification. *Adv Exp Med Biol*. 2021;1283:1–16.
104. Lawrence M, Daujat S, Schneider R. Lateral Thinking: How Histone Modifications Regulate Gene Expression. *Trends Genet*. 2016 Jan;32(1):42–56.
105. Laalami S, Putzer H. mRNA degradation and maturation in prokaryotes: the global players. *Biomol Concepts*. 2011 Dec 1;2(6):491–506.
106. Casamassimi A, Ciccodicola A. Transcriptional Regulation: Molecules, Involved Mechanisms, and Misregulation. *Int J Mol Sci [Internet]*. 2019 Mar 14;20(6). Available from: <http://dx.doi.org/10.3390/ijms20061281>
107. Kozak M. Regulation of translation via mRNA structure in prokaryotes and eukaryotes. *Gene*. 2005 Nov 21;361:13–37.

108. Tarrant D, von der Haar T. Synonymous codons, ribosome speed, and eukaryotic gene expression regulation. *Cell Mol Life Sci.* 2014 Nov;71(21):4195–206.
109. von der Haar T. Mathematical and Computational Modelling of Ribosomal Movement and Protein Synthesis: an overview. *Comput Struct Biotechnol J.* 2012 Feb 20;1:e201204002.
110. Tuite MF, von der Haar T. Transfer RNA in Decoding and the Wobble Hypothesis. *Elsevier Oceanogr Ser* [Internet]. 2016; Available from: <https://kar.kent.ac.uk/58877>
111. Xie J, de Souza Alves V, von der Haar T, O’Keefe L, Lenchine RV, Jensen KB, et al. Regulation of the Elongation Phase of Protein Synthesis Enhances Translation Accuracy and Modulates Lifespan. *Curr Biol.* 2019 Mar 4;29(5):737-749.e5.
112. Stark H, Mueller F, Orlova EV, Schatz M, Dube P, Erdemir T, et al. The 70S Escherichia coli ribosome at 23 Å resolution: fitting the ribosomal RNA. *Structure.* 1995 Aug 15;3(8):815–21.
113. Palade GE. A small particulate component of the cytoplasm. *J Biophys Biochem Cytol.* 1955 Jan;1(1):59–68.
114. Bremer H, Dennis PP. Modulation of Chemical Composition and Other Parameters of the Cell at Different Exponential Growth Rates. *EcoSal Plus* [Internet]. 2008 Sep;3(1). Available from: <http://dx.doi.org/10.1128/ecosal.5.2.3>
115. Liu Q, Fredrick K. Intersubunit Bridges of the Bacterial Ribosome. *J Mol Biol.* 2016 May 22;428(10 Pt B):2146–64.
116. Dao Duc K, Batra SS, Bhattacharya N, Cate JHD, Song YS. Differences in the path to exit the ribosome across the three domains of life. *Nucleic Acids Res.* 2019 May 7;47(8):4198–210.
117. Fischer N, Neumann P, Konevega AL, Bock LV, Ficner R, Rodnina MV, et al. Structure of the E. coli ribosome-EF-Tu complex at <3 Å resolution by Cs-corrected cryo-EM. *Nature.* 2015 Apr 23;520(7548):567–70.
118. Ban N, Nissen P, Hansen J, Moore PB, Steitz TA. The complete atomic structure of the large ribosomal subunit at 2.4 Å resolution. *Science.* 2000 Aug 11;289(5481):905–20.
119. Yonath A, Leonard KR, Wittmann HG. A Tunnel in the Large Ribosomal Subunit Revealed by Three-Dimensional Image Reconstruction. *Science.* 1987;236(4803):813–6.

120. Malkin LI, Rich A. Partial resistance of nascent polypeptide chains to proteolytic digestion due to ribosomal shielding. *J Mol Biol.* 1967 Jun 14;26(2):329–46.
121. Zhang J, Pan X, Yan K, Sun S, Gao N, Sui S-F. Mechanisms of ribosome stalling by SecM at multiple elongation steps. *Elife* [Internet]. 2015 Dec 14;4. Available from: <http://dx.doi.org/10.7554/eLife.09684>
122. Huter P, Arenz S, Bock LV, Graf M, Frister JO, Heuer A, et al. Structural Basis for Polyproline-Mediated Ribosome Stalling and Rescue by the Translation Elongation Factor EF-P. *Mol Cell.* 2017 Nov 2;68(3):515–527.e6.
123. Doerfel LK, Wohlgemuth I, Kothe C, Peske F, Urlaub H, Rodnina MV. EF-P is essential for rapid synthesis of proteins containing consecutive proline residues. *Science.* 2013 Jan 4;339(6115):85–8.
124. Cramer F, Erdmann VA, von der Haar F, Schlimme E. Structure and reactivity of tRNA. *J Cell Physiol.* 1969 Oct;74(2):Suppl 1:163+.
125. Madison JT. Primary structure of RNA. *Annu Rev Biochem.* 1968;37:131–48.
126. Nissen P, Kjeldgaard M, Thirup S, Polekhina G, Reshetnikova L, Clark BF, et al. Crystal structure of the ternary complex of Phe-tRNA^{Phe}, EF-Tu, and a GTP analog. *Science.* 1995 Dec 1;270(5241):1464–72.
127. Dong H, Nilsson L, Kurland CG. Co-variation of tRNA abundance and codon usage in *Escherichia coli* at different growth rates. *J Mol Biol.* 1996 Aug 2;260(5):649–63.
128. Ibba M, Soll D. Aminoacyl-tRNA synthesis. *Annu Rev Biochem.* 2000;69:617–50.
129. Giegé R, Sissler M, Florentz C. Universal rules and idiosyncratic features in tRNA identity. *Nucleic Acids Res.* 1998 Nov 15;26(22):5017–35.
130. Jakubowski H. Negative correlation between the abundance of *Escherichia coli* aminoacyl-tRNA families and their affinities for elongation factor Tu-GTP. *J Theor Biol.* 1988 Aug 8;133(3):363–70.
131. Nissen P, Thirup S, Kjeldgaard M, Nyborg J. The crystal structure of Cys-tRNA^{Cys}-EF-Tu-GDPNP reveals general and specific features in the ternary complex and in tRNA. *Structure.* 1999 Feb 15;7(2):143–56.
132. Schrader JM, Chapman SJ, Uhlenbeck OC. Understanding the sequence specificity of tRNA binding to elongation factor Tu using tRNA mutagenesis. *J Mol Biol.* 2009 Mar 13;386(5):1255–64.

133. Grosjean H, de Crécy-Lagard V, Marck C. Deciphering synonymous codons in the three domains of life: co-evolution with specific tRNA modification enzymes. *FEBS Lett.* 2010 Jan 21;584(2):252–64.
134. Lorenz C, Lünse CE, Mörl M. tRNA Modifications: Impact on Structure and Thermal Adaptation. *Biomolecules* [Internet]. 2017 Apr 4;7(2). Available from: <http://dx.doi.org/10.3390/biom7020035>
135. de Crécy-Lagard V, Jaroch M. Functions of Bacterial tRNA Modifications: From Ubiquity to Diversity. *Trends Microbiol.* 2021 Jan;29(1):41–53.
136. Magee R, Rigoutsos I. On the expanding roles of tRNA fragments in modulating cell behavior. *Nucleic Acids Res.* 2020 Sep 25;48(17):9433–48.
137. Lee SR, Collins K. Starvation-induced cleavage of the tRNA anticodon loop in *Tetrahymena thermophila*. *J Biol Chem.* 2005 Dec 30;280(52):42744–9.
138. Rudland PS, Dube SK. Specific interaction of an initiator tRNA fragment with 30 s ribosomal subunits. *J Mol Biol.* 1969 Jul 28;43(2):273–80.
139. Schaffer AE, Eggens VRC, Caglayan AO, Reuter MS, Scott E, Coufal NG, et al. CLP1 founder mutation links tRNA splicing and maturation to cerebellar development and neurodegeneration. *Cell.* 2014 Apr 24;157(3):651–63.
140. Ivanov P, Emara MM, Villen J, Gygi SP, Anderson P. Angiogenin-induced tRNA fragments inhibit translation initiation. *Mol Cell.* 2011 Aug 19;43(4):613–23.
141. Han L, Lai H, Yang Y, Hu J, Li Z, Ma B, et al. A 5'-tRNA half, tRNA-Gly promotes cell proliferation and migration via binding to RBM17 and inducing alternative splicing in papillary thyroid cancer. *J Exp Clin Cancer Res.* 2021 Jul 5;40(1):222.
142. Chang B, Halgamuge S, Tang S-L. Analysis of SD sequences in completed microbial genomes: non-SD-led genes are as common as SD-led genes. *Gene.* 2006 May 24;373:90–9.
143. Shine J, Dalgarno L. Determinant of cistron specificity in bacterial ribosomes. *Nature.* 1975 Mar 6;254(5495):34–8.
144. Milón P, Maracci C, Filonava L, Gualerzi CO, Rodnina MV. Real-time assembly landscape of bacterial 30S translation initiation complex. *Nat Struct Mol Biol.* 2012 May 6;19(6):609–15.
145. Studer SM, Joseph S. Unfolding of mRNA secondary structure by the bacterial translation initiation complex. *Mol Cell.* 2006 Apr 7;22(1):105–15.

146. Loveland AB, Demo G, Grigorieff N, Korostelev AA. Ensemble cryo-EM elucidates the mechanism of translation fidelity. *Nature*. 2017 Jun 1;546(7656):113–7.
147. Maracci C, Peske F, Dannies E, Pohl C, Rodnina MV. Ribosome-induced tuning of GTP hydrolysis by a translational GTPase. *Proceedings of the National Academy of Sciences*. 2014;111(40):14418–23.
148. Ogle JM, Brodersen DE, Clemons WM Jr, Tarry MJ, Carter AP, Ramakrishnan V. Recognition of cognate transfer RNA by the 30S ribosomal subunit. *Science*. 2001 May 4;292(5518):897–902.
149. Sievers A, Beringer M, Rodnina MV, Wolfenden R. The ribosome as an entropy trap. *Proceedings of the National Academy of Sciences*. 2004;101(21):7897–901.
150. Sharma PK, Xiang Y, Kato M, Warshel A. What are the roles of substrate-assisted catalysis and proximity effects in peptide bond formation by the ribosome? *Biochemistry*. 2005 Aug 30;44(34):11307–14.
151. Wallin G, Åqvist J. The transition state for peptide bond formation reveals the ribosome as a water trap. *Proceedings of the National Academy of Sciences*. 2010;107(5):1888–93.
152. Moazed D, Noller HF. Intermediate states in the movement of transfer RNA in the ribosome. *Nature*. 1989 Nov 9;342(6246):142–8.
153. Blanchard SC, Kim HD, Gonzalez RL Jr, Puglisi JD, Chu S. tRNA dynamics on the ribosome during translation. *Proc Natl Acad Sci U S A*. 2004 Aug 31;101(35):12893–8.
154. Rodnina MV, Wintermeyer W. The ribosome as a molecular machine: the mechanism of tRNA-mRNA movement in translocation. *Biochem Soc Trans*. 2011 Apr;39(2):658–62.
155. Chen C, Stevens B, Kaur J, Smilansky Z, Cooperman BS, Goldman YE. Allosteric vs. spontaneous exit-site (E-site) tRNA dissociation early in protein synthesis. *Proc Natl Acad Sci U S A*. 2011 Oct 11;108(41):16980–5.
156. Tsai C-J, Sauna ZE, Kimchi-Sarfaty C, Ambudkar SV, Gottesman MM, Nussinov R. Synonymous mutations and ribosome stalling can lead to altered folding pathways and distinct minima. *J Mol Biol*. 2008 Nov 7;383(2):281–91.
157. Zhang G, Hubalewska M, Ignatova Z. Transient ribosomal attenuation coordinates protein synthesis and co-translational folding. *Nat Struct Mol Biol*. 2009 Mar;16(3):274–80.

158. Siller E, DeZwaan DC, Anderson JF, Freeman BC, Barral JM. Slowing bacterial translation speed enhances eukaryotic protein folding efficiency. *J Mol Biol.* 2010 Mar 12;396(5):1310–8.
159. Rodnina MV. Translation in Prokaryotes. *Cold Spring Harb Perspect Biol* [Internet]. 2018 Sep 4;10(9). Available from: <http://dx.doi.org/10.1101/cshperspect.a032664>
160. Korostelev A, Zhu J, Asahara H, Noller HF. Recognition of the amber UAG stop codon by release factor RF1. *EMBO J.* 2010 Aug 4;29(15):2577–85.
161. Laurberg M, Asahara H, Korostelev A, Zhu J, Trakhanov S, Noller HF. Structural basis for translation termination on the 70S ribosome. *Nature.* 2008 Aug 14;454(7206):852–7.
162. Korostelev A, Asahara H, Lancaster L, Laurberg M, Hirschi A, Zhu J, et al. Crystal structure of a translation termination complex formed with release factor RF2. *Proceedings of the National Academy of Sciences.* 2008;105(50):19684–9.
163. Weixlbaumer A, Jin H, Neubauer C, Voorhees RM, Petry S, Kelley AC, et al. Insights into translational termination from the structure of RF2 bound to the ribosome. *Science.* 2008 Nov 7;322(5903):953–6.
164. Jin H, Kelley AC, Loakes D, Ramakrishnan V. Structure of the 70S ribosome bound to release factor 2 and a substrate analog provides insights into catalysis of peptide release. *Proceedings of the National Academy of Sciences.* 2010;107(19):8593–8.
165. Zavialov AV, Buckingham RH, Ehrenberg M. A posttermination ribosomal complex is the guanine nucleotide exchange factor for peptide release factor RF3. *Cell.* 2001 Oct 5;107(1):115–24.
166. Gao N, Zavialov AV, Li W, Sengupta J, Valle M, Gursky RP, et al. Mechanism for the disassembly of the posttermination complex inferred from cryo-EM studies. *Mol Cell.* 2005 Jun 10;18(6):663–74.
167. Hirokawa G, Demeshkina N, Iwakura N, Kaji H, Kaji A. The ribosome-recycling step: consensus or controversy? *Trends Biochem Sci.* 2006 Mar;31(3):143–9.
168. Watson JD, Crick FH. The structure of DNA. *Cold Spring Harb Symp Quant Biol.* 1953;18:123–31.
169. Crick FH. Codon--anticodon pairing: the wobble hypothesis. *J Mol Biol.* 1966 Aug;19(2):548–55.

170. Curran JF. Decoding with the A:I wobble pair is inefficient. *Nucleic Acids Res.* 1995 Feb 25;23(4):683–8.
171. Lagerkvist U. “Two out of three”: an alternative method for codon reading. *Proc Natl Acad Sci U S A.* 1978 Apr;75(4):1759–62.
172. Kothe U, Rodnina MV. Codon reading by tRNA^{Ala} with modified uridine in the wobble position. *Mol Cell.* 2007 Jan 12;25(1):167–74.
173. Plant EP, Nguyen P, Russ JR, Pittman YR, Nguyen T, Quesinberry JT, et al. Differentiating between near- and non-cognate codons in *Saccharomyces cerevisiae*. *PLoS One.* 2007 Jun 13;2(6):e517.
174. Gromadski KB, Rodnina MV. Kinetic determinants of high-fidelity tRNA discrimination on the ribosome. *Mol Cell.* 2004 Jan 30;13(2):191–200.
175. Zhang H, Lyu Z, Fan Y, Evans CR, Barber KW, Banerjee K, et al. Metabolic stress promotes stop-codon readthrough and phenotypic heterogeneity. *Proc Natl Acad Sci U S A.* 2020 Sep 8;117(36):22167–72.
176. Jeon WY, Yoon BH, Ko BS, Shim WY, Kim JH. Xylitol production is increased by expression of codon-optimized *Neurospora crassa* xylose reductase gene in *Candida tropicalis*. *Bioprocess Biosyst Eng.* 2012 Jan;35(1–2):191–8.
177. Ramezani A, Mahmoudi Maymand E, Yazdanpanah-Samani M, Hosseini A, Toghraie FS, Ghaderi A. Improving Pertuzumab production by gene optimization and proper signal peptide selection. *Protein Expr Purif.* 2017 Jul;135:24–32.
178. Daniell H, Ruiz G, Denes B, Sandberg L, Langridge W. Optimization of codon composition and regulatory elements for expression of human insulin like growth factor-1 in transgenic chloroplasts and evaluation of structural identity and function. *BMC Biotechnol.* 2009 Apr 3;9:33.
179. Zhai Z, Nuylert A, Isobe K, Asano Y. Effects of codon optimization and glycosylation on the high-level production of hydroxynitrile lyase from *Chamberlinius hualienensis* in *Pichia pastoris*. *J Ind Microbiol Biotechnol.* 2019 Jul;46(7):887–98.
180. Meyer-Schuman R, Antonellis A. Emerging mechanisms of aminoacyl-tRNA synthetase mutations in recessive and dominant human disease. *Hum Mol Genet.* 2017 Oct 1;26(R2):R114–27.
181. Knight JRP, Garland G, Pöyry T, Mead E, Vlahov N, Sfakianos A, et al. Control of translation elongation in health and disease. *Dis Model Mech* [Internet]. 2020 Mar 26;13(3). Available from: <http://dx.doi.org/10.1242/dmm.043208>

182. Beckelman BC, Yang W, Kasica NP, Zimmermann HR, Zhou X, Keene CD, et al. Genetic reduction of eEF2 kinase alleviates pathophysiology in Alzheimer's disease model mice. *J Clin Invest*. 2019 Feb 1;129(2):820–33.
183. Jan A, Jansonius B, Delaidelli A, Bhansali F, An YA, Ferreira N, et al. Activity of translation regulator eukaryotic elongation factor-2 kinase is increased in Parkinson disease brain and its inhibition reduces alpha synuclein toxicity. *Acta Neuropathol Commun*. 2018 Jul 2;6(1):54.
184. Faller WJ, Jackson TJ, Knight JR, Ridgway RA, Jamieson T, Karim SA, et al. mTORC1-mediated translational elongation limits intestinal tumour initiation and growth. *Nature*. 2015 Jan 22;517(7535):497–500.
185. Loveridge CJ, Slater S, Campbell KJ, Nam NA, Knight J, Ahmad I, et al. BRF1 accelerates prostate tumourigenesis and perturbs immune infiltration. *Oncogene*. 2020 Feb;39(8):1797–806.
186. Zhou M, Guo J, Cha J, Chae M, Chen S, Barral JM, et al. Non-optimal codon usage affects expression, structure and function of clock protein FRQ. *Nature*. 2013 Mar 7;495(7439):111–5.
187. Chan CTY, Pang YLJ, Deng W, Babu IR, Dyavaiah M, Begley TJ, et al. Reprogramming of tRNA modifications controls the oxidative stress response by codon-biased translation of proteins. *Nat Commun*. 2012 Jul 3;3:937.
188. Varenne S, Buc J, Lloubes R, Lazdunski C. Translation is a non-uniform process. Effect of tRNA availability on the rate of elongation of nascent polypeptide chains. *J Mol Biol*. 1984 Dec 15;180(3):549–76.
189. Fluitt A, Pienaar E, Viljoen H. Ribosome kinetics and aa-tRNA competition determine rate and fidelity of peptide synthesis. *Comput Biol Chem*. 2007 Oct;31(5–6):335–46.
190. Wahab SZ, Rowley KO, Holmes WM. Effects of tRNA(1Leu) overproduction in *Escherichia coli*. *Mol Microbiol*. 1993 Jan;7(2):253–63.
191. Lu J, Deutsch C. Electrostatics in the ribosomal tunnel modulate chain elongation rates. *J Mol Biol*. 2008 Dec 5;384(1):73–86.
192. Charneski CA, Hurst LD. Positively charged residues are the major determinants of ribosomal velocity. *PLoS Biol*. 2013 Mar 12;11(3):e1001508.
193. Zur H, Tuller T. Strong association between mRNA folding strength and protein abundance in *S. cerevisiae*. *EMBO Rep*. 2012 Mar 1;13(3):272–7.
194. von Heijne G, Nilsson L, Blomberg C. Translation and messenger RNA secondary structure. *J Theor Biol*. 1977 Oct 7;68(3):321–9.

195. Vasquez KM, Christensen J, Li L, Finch RA, Glazer PM. Human XPA and RPA DNA repair proteins participate in specific recognition of triplex-induced helical distortions. *Proc Natl Acad Sci U S A*. 2002 Apr 30;99(9):5848–53.
196. Pearlman DA, Holbrook SR, Pirkle DH, Kim SH. Molecular models for DNA damaged by photoreaction. *Science*. 1985 Mar 15;227(4692):1304–8.
197. Lee Y-C, Cai Y, Mu H, Broyde S, Amin S, Chen X, et al. The relationships between XPC binding to conformationally diverse DNA adducts and their excision by the human NER system: is there a correlation? *DNA Repair* . 2014 Jul;19:55–63.
198. Barnett J. Combining single molecule and bulk phase approaches to investigate damage detection by nucleotide excision repair proteins [PhD of Biochemistry]. 2019.
199. Douki T, Perdiz D, Gróf P, Kuluncsics Z, Moustacchi E, Cadet J, et al. Oxidation of guanine in cellular DNA by solar UV radiation: biological role. *Photochem Photobiol*. 1999 Aug;70(2):184–90.
200. Kad NM, Trybus KM, Warshaw DM. Load and Pi control flux through the branched kinetic cycle of myosin V. *J Biol Chem*. 2008 Jun 20;283(25):17477–84.
201. Bell GI. Models for the specific adhesion of cells to cells. *Science*. 1978 May 12;200(4342):618–27.
202. Dorman CJ, Dorman MJ. DNA supercoiling is a fundamental regulatory principle in the control of bacterial gene expression. *Biophys Rev*. 2016 Nov;8(Suppl 1):89–100.
203. Gogou C, Japaridze A, Dekker C. Mechanisms for Chromosome Segregation in Bacteria. *Front Microbiol*. 2021 Jun 16;12:685687.
204. Alberts B, Johnson A, Lewis J, Raff M, Roberts K, Walter P. The Initiation and Completion of DNA Replication in Chromosomes. Garland Science; 2002.
205. Kornberg A, Baker TA. DNA Replication. W.H. Freeman; 1992. 931 p.
206. Lewis JS, Jergic S, Dixon NE. The E. coli DNA Replication Fork. *Enzymes*. 2016 May 13;39:31–88.
207. Moolenaar GF, Moorman C, Goosen N. Role of the Escherichia coli nucleotide excision repair proteins in DNA replication. *J Bacteriol*. 2000 Oct;182(20):5706–14.

208. Selby CP. Mfd Protein and Transcription-Repair Coupling in *Escherichia coli*. *Photochem Photobiol*. 2017 Jan;93(1):280–95.
209. Brochu J, Breton É-V, Drolet M. Supercoiling, R-loops, Replication and the Functions of Bacterial Type 1A Topoisomerases. *Genes* [Internet]. 2020 Feb 27;11(3). Available from: <http://dx.doi.org/10.3390/genes11030249>
210. Dorman CJ. DNA supercoiling and transcription in bacteria: a two-way street. *BMC Mol Cell Biol*. 2019 Jul 18;20(1):26.
211. Kad NM, Van Houten B. Dynamics of lesion processing by bacterial nucleotide excision repair proteins. *Prog Mol Biol Transl Sci*. 2012;110:1–24.
212. Berg OG, Winter RB, von Hippel PH. How do genome-regulatory proteins locate their DNA target sites? *Trends Biochem Sci*. 1982 Feb 1;7(2):52–5.
213. Berg OG, Winter RB, von Hippel PH. Diffusion-driven mechanisms of protein translocation on nucleic acids. 1. Models and theory. *Biochemistry*. 1981 Nov 24;20(24):6929–48.
214. von Hippel PH, Berg OG. Facilitated target location in biological systems. *J Biol Chem*. 1989 Jan 15;264(2):675–8.
215. Tafvizi A, Huang F, Fersht AR, Mirny LA, van Oijen AM. A single-molecule characterization of p53 search on DNA. *Proc Natl Acad Sci U S A*. 2011 Jan 11;108(2):563–8.
216. Gorman J, Chowdhury A, Surtees JA, Shimada J, Reichman DR, Alani E, et al. Dynamic basis for one-dimensional DNA scanning by the mismatch repair complex Msh2-Msh6. *Mol Cell*. 2007 Nov 9;28(3):359–70.
217. Ahmadi A, Rosnes I, Blicher P, Diekmann R, Schüttelpelz M, Glette K, et al. Breaking the speed limit with multimode fast scanning of DNA by Endonuclease V. *Nat Commun*. 2018 Dec 19;9(1):5381.
218. Wagner K, Moolenaar G, van Noort J, Goosen N. Single-molecule analysis reveals two separate DNA-binding domains in the *Escherichia coli* UvrA dimer. *Nucleic Acids Res*. 2009 Apr;37(6):1962–72.
219. Charman RJ, Kad NM. Single molecule iSCAT imaging reveals a fast, energy efficient search mode for the DNA repair protein UvrA. *Nanoscale* [Internet]. 2022 Mar 21; Available from: <http://dx.doi.org/10.1039/d1nr06913f>
220. Charman RJ. Developing high-speed scatterometry tools to detect early events during Nucleotide Excision Repair [Internet] [phd]. University of Kent; 2022 [cited 2023 Jan 10]. Available from: <https://kar.kent.ac.uk/97932/>

221. Sunney Xie X, Trautman JK. OPTICAL STUDIES OF SINGLE MOLECULES AT ROOM TEMPERATURE. *Annu Rev Phys Chem.* 1998 Oct 1;49(Volume 49, 1998):441–80.
222. Beckwitt EC, Kong M, Van Houten B. Studying protein-DNA interactions using atomic force microscopy. *Semin Cell Dev Biol.* 2018 Jan;73:220–30.
223. Wirth N, Gross J, Roth HM, Buechner CN, Kisker C, Tessmer I. Conservation and Divergence in Nucleotide Excision Repair Lesion Recognition. *J Biol Chem.* 2016 Sep 2;291(36):18932–46.
224. Ashkin A, Dziedzic JM, Bjorkholm JE, Chu S. Observation of a single-beam gradient force optical trap for dielectric particles. *Opt Lett.* 1986 May 1;11(5):288.
225. Neuman KC, Block SM. Optical trapping. *Rev Sci Instrum.* 2004 Sep;75(9):2787–809.
226. Chu S, Bjorkholm JE, Ashkin A, Cable A. Experimental observation of optically trapped atoms. *Phys Rev Lett.* 1986 Jul 21;57(3):314–7.
227. Ashkin A, Dziedzic JM, Yamane T. Optical trapping and manipulation of single cells using infrared laser beams. *Nature.* 1987;330(6150):769–71.
228. Ashkin A, Dziedzic JM. Optical trapping and manipulation of viruses and bacteria. *Science.* 1987 Mar 20;235(4795):1517–20.
229. 10. Force Calibration — lumicks.pylake [Internet]. [cited 2024 Jul 12]. Available from: https://lumicks-pylake.readthedocs.io/en/stable/tutorial/force_calibration.html
230. Lumicks [Internet]. Available from: <https://lumicks.com/knowledge/what-are-optical-tweezers/#:~:text=In%20a%20typical%20optical%20tweezers,a%20small%20object%20in%20place.>
231. Pope LH, Bennink ML, Greve J. Optical tweezers stretching of chromatin. *J Muscle Res Cell Motil.* 2002;23(5–6):397–407.
232. Cecconi C, Shank EA, Bustamante C, Marqusee S. Direct observation of the three-state folding of a single protein molecule. *Science.* 2005 Sep 23;309(5743):2057–60.
233. Ye S, Chen Z, Zhang X, Li F, Guo L, Hou X-M, et al. Proximal Single-Stranded RNA Destabilizes Human Telomerase RNA G-Quadruplex and Induces Its Distinct Conformers. *J Phys Chem Lett.* 2021 Apr 8;12(13):3361–6.

234. Goldman DH, Kaiser CM, Milin A, Righini M, Tinoco I Jr, Bustamante C. Ribosome. Mechanical force releases nascent chain-mediated ribosome arrest in vitro and in vivo. *Science*. 2015 Apr 24;348(6233):457–60.
235. Le TT, Yang Y, Tan C, Suhanovsky MM, Fulbright RM Jr, Inman JT, et al. Mfd Dynamically Regulates Transcription via a Release and Catch-Up Mechanism. *Cell*. 2018 Jan 11;172(1–2):344–357.e15.
236. Rief M, Rock RS, Mehta AD, Mooseker MS, Cheney RE, Spudich JA. Myosin-V stepping kinetics: a molecular model for processivity. *Proc Natl Acad Sci U S A*. 2000 Aug 15;97(17):9482–6.
237. Bustamante C, Bryant Z, Smith SB. Ten years of tension: single-molecule DNA mechanics. *Nature*. 2003 Jan 23;421(6921):423–7.
238. Kratky O, Porod G. Röntgenuntersuchung gelöster fadenmoleküle. *Recl Trav Chim Pays Bas*. 1949;68(12):1106–22.
239. Smith SB, Cui Y, Bustamante C. Overstretching B-DNA: the elastic response of individual double-stranded and single-stranded DNA molecules. *Science*. 1996 Feb 9;271(5250):795–9.
240. Cluzel P, Lebrun A, Heller C, Lavery R, Viovy JL, Chatenay D, et al. DNA: an extensible molecule. *Science*. 1996 Feb 9;271(5250):792–4.
241. Williams MC, Rouzina I, Bloomfield VA. Thermodynamics of DNA interactions from single molecule stretching experiments. *Acc Chem Res*. 2002 Mar;35(3):159–66.
242. Kad NM, Patlak JB, Fagnant PM, Trybus KM, Warshaw DM. Mutation of a conserved glycine in the SH1-SH2 helix affects the load-dependent kinetics of myosin. *Biophys J*. 2007 Mar 1;92(5):1623–31.
243. Liu J, Li Q, Li M, Gao S, Liu C, Zou L, et al. Elliptical mirror-based TIRF microscopy with shadowless illumination and adjustable penetration depth. *Opt Lett*. 2017 Jul 1;42(13):2587–90.
244. Simons M, Pollard MR, Hughes CD, Ward AD, Van Houten B, Towrie M, et al. Directly interrogating single quantum dot labelled UvrA2 molecules on DNA tightropes using an optically trapped nanoprobe. *Sci Rep*. 2015 Dec 22;5:18486.
245. Truglio JJ, Croteau DL, Skorvaga M, DellaVecchia MJ, Theis K, Mandavilli BS, et al. Interactions between UvrA and UvrB: the role of UvrB's domain 2 in nucleotide excision repair. *EMBO J*. 2004 Jul 7;23(13):2498–509.

246. Seeberg E, Steinum AL. Purification and properties of the uvrA protein from *Escherichia coli*. *Proc Natl Acad Sci U S A*. 1982 Feb;79(4):988–92.
247. Van Houten B. Nucleotide excision repair in *Escherichia coli*. *Microbiol Rev*. 1990 Mar;54(1):18–51.
248. Delagoutte E, Bertrand-Burggraf E, Dunand J, Fuchs RP. Sequence-dependent modulation of nucleotide excision repair: the efficiency of the incision reaction is inversely correlated with the stability of the pre-incision UvrB-DNA complex. *J Mol Biol*. 1997 Mar 7;266(4):703–10.
249. Springall L, Hughes CD, Simons M, Azinas S, Van Houten B, Kad NM. Recruitment of UvrBC complexes to UV-induced damage in the absence of UvrA increases cell survival. *Nucleic Acids Res*. 2018 Feb 16;46(3):1256–65.
250. Van Houten B, Kad N. Investigation of bacterial nucleotide excision repair using single-molecule techniques. *DNA Repair*. 2014 Aug;20:41–8.
251. Schaich MA, Schnable BL, Kumar N, Roginskaya V, Jakielski RC, Urban R, et al. Single-molecule analysis of DNA-binding proteins from nuclear extracts (SMADNE). *Nucleic Acids Res*. 2023 Apr 24;51(7):e39.
252. IHME. Global Burden of Disease [Internet]. our world in data. 2019. Available from: <https://ourworldindata.org/causes-of-death#what-do-people-die-from>
253. Ghosh S. Cisplatin: The first metal based anticancer drug. *Bioorg Chem*. 2019 Jul;88:102925.
254. Dasari S, Tchounwou PB. Cisplatin in cancer therapy: molecular mechanisms of action. *Eur J Pharmacol*. 2014 Oct 5;740:364–78.
255. Rosenberg B, Vancamp L, Krigas T. INHIBITION OF CELL DIVISION IN *ESCHERICHIA COLI* BY ELECTROLYSIS PRODUCTS FROM A PLATINUM ELECTRODE. *Nature*. 1965 Feb 13;205:698–9.
256. Crawford J, Dale DC, Lyman GH. Chemotherapy-induced neutropenia: risks, consequences, and new directions for its management. *Cancer*. 2004 Jan 15;100(2):228–37.
257. Pérez-Herrero E, Fernández-Medarde A. Advanced targeted therapies in cancer: Drug nanocarriers, the future of chemotherapy. *Eur J Pharm Biopharm*. 2015 Jun;93:52–79.
258. Chabner BA, Roberts TG Jr. Timeline: Chemotherapy and the war on cancer. *Nat Rev Cancer*. 2005 Jan;5(1):65–72.

259. Bodey GP, Buckley M, Sathe YS, Freireich EJ. Quantitative relationships between circulating leukocytes and infection in patients with acute leukemia. *Ann Intern Med.* 1966 Feb;64(2):328–40.
260. Zaorsky NG, Churilla TM, Egleston BL, Fisher SG, Ridge JA, Horwitz EM, et al. Causes of death among cancer patients. *Ann Oncol.* 2017 Feb 1;28(2):400–7.
261. Rolston KVI. Infections in Cancer Patients with Solid Tumors: A Review. *Infect Dis Ther.* 2017 Mar;6(1):69–83.
262. Nanayakkara AK, Boucher HW, Fowler VG Jr, Jezek A, Outtersson K, Greenberg DE. Antibiotic resistance in the patient with cancer: Escalating challenges and paths forward. *CA Cancer J Clin.* 2021 Nov;71(6):488–504.
263. Zembower TR. Epidemiology of infections in cancer patients. *Cancer Treat Res.* 2014;161:43–89.
264. Yamamoto H, Ishihara K, Takeda Y, Koizumi W, Ichikawa T. Changes in the mucus barrier during cisplatin-induced intestinal mucositis in rats. *Biomed Res Int.* 2013 Dec 23;2013:276186.
265. Tamaki T, Naomoto Y, Kimura S, Kawashima R, Shirakawa Y, Shigemitsu K, et al. Apoptosis in normal tissues induced by anti-cancer drugs. *J Int Med Res.* 2003 Jan-Feb;31(1):6–16.
266. Rahnama M, Madej-Czerwinka B, Jastrzębska-Jamrogiewicz I, Jamrogiewicz R. Analysis of the influence of parenteral cancer chemotherapy on the health condition of oral mucosa. *Contemp Oncol.* 2015 Mar 26;19(1):77–82.
267. Ambrus JL, Ambrus CM, Mink IB, Pickren JW. Causes of death in cancer patients. *J Med.* 1975;6(1):61–4.
268. Schlander M, Hernandez-Villafuerte K, Cheng C-Y, Mestre-Ferrandiz J, Baumann M. How Much Does It Cost to Research and Develop a New Drug? A Systematic Review and Assessment. *Pharmacoeconomics.* 2021 Nov;39(11):1243–69.
269. World Health Organisation. 2021 Antibacterial agents in clinical and preclinical development: an overview and analysis. WHO reports. 2022;
270. Baym M, Lieberman TD, Kelsic ED, Chait R, Gross R, Yelin I, et al. Spatiotemporal microbial evolution on antibiotic landscapes. *Science.* 2016 Sep 9;353(6304):1147–51.
271. Bernacchia L, Paris A, Gupta AR, Moores AA, Kad NM. Identification of the Target and Mode of Action for the Prokaryotic Nucleotide Excision Repair

Inhibitor ATBC. Biosci Rep [Internet]. 2022 May 12; Available from: <http://dx.doi.org/10.1042/BSR20220403>

272. Bernacchia L, Gupta A, Paris A, Moores AA, Kad NM. Combining cancer chemotherapeutics with bacterial DNA repair inhibitors to develop novel antimicrobials [Internet]. bioRxiv. 2023 [cited 2023 Apr 17]. p. 2023.03.17.532951. Available from: <https://www.biorxiv.org/content/10.1101/2023.03.17.532951v1>
273. Kovalchuk I. Chapter 38 - Conserved and Divergent Features of DNA Repair: Future Perspectives in Genome Instability Research. In: Kovalchuk I, Kovalchuk O, editors. Genome Stability. Boston: Academic Press; 2016. p. 651–66.
274. Mazloun N, Stegman MA, Croteau DL, Van Houten B, Kwon NS, Ling Y, et al. Identification of a chemical that inhibits the mycobacterial UvrABC complex in nucleotide excision repair. Biochemistry. 2011 Mar 1;50(8):1329–35.
275. Ianiro G, Mangiola F, Di Rienzo TA, Bibbò S, Franceschi F, Greco AV, et al. Levothyroxine absorption in health and disease, and new therapeutic perspectives. Eur Rev Med Pharmacol Sci. 2014;18(4):451–6.
276. Sue LY, Leung AM. Levothyroxine for the Treatment of Subclinical Hypothyroidism and Cardiovascular Disease. Front Endocrinol . 2020 Oct 21;11:591588.
277. DrugBank [Internet]. DrugBank. Available from: <https://go.drugbank.com/drugs/DB00890>
278. Sikkema SH, Sevringhaus EL. Dienestrol; another synthetic estrogen of clinical value. Am J Med. 1947 Mar;2(3):251.
279. Schreiber E, Alfageme O, Garcia T, González N, Sirvent JJ, Torrente M, et al. Oral exposure of rats to dienestrol during gestation and lactation: Effects on the reproductive system of male offspring. Food Chem Toxicol. 2019 Jun;128:193–201.
280. Mahdy AM, Webster NR. Perioperative systemic haemostatic agents. Br J Anaesth. 2004 Dec;93(6):842–58.
281. DrugBank [Internet]. DrugBank. [cited 2023 Oct 20]. Available from: <https://go.drugbank.com/drugs/DB06692>
282. McMullan V, Alston RP. III. Aprotinin and cardiac surgery: a sorry tale of evidence misused. Br J Anaesth. 2013 May;110(5):675–8.

283. Jumper J, Evans R, Pritzel A, Green T, Figurnov M, Ronneberger O, et al. Highly accurate protein structure prediction with AlphaFold. *Nature*. 2021 Aug;596(7873):583–9.
284. Varadi M, Anyango S, Deshpande M, Nair S, Natassia C, Yordanova G, et al. AlphaFold Protein Structure Database: massively expanding the structural coverage of protein-sequence space with high-accuracy models. *Nucleic Acids Res*. 2022 Jan 7;50(D1):D439–44.
285. DrugBank [Internet]. DrugBank. [cited 2023 Oct 20]. Available from: <https://go.drugbank.com/drugs/DB12411>
286. Bhalla S, Fattah FJ, Ahn C, Williams J, Macchiaroli A, Padro J, et al. Phase 1 trial of bemcentinib (BGB324), a first-in-class, selective AXL inhibitor, with docetaxel in patients with previously treated advanced non-small cell lung cancer. *Lung Cancer*. 2023 Aug;182:107291.
287. Zhu C, Wei Y, Wei X. AXL receptor tyrosine kinase as a promising anti-cancer approach: functions, molecular mechanisms and clinical applications. *Mol Cancer*. 2019 Nov 4;18(1):153.
288. Wang X, Lim HJ, Son A. Characterization of denaturation and renaturation of DNA for DNA hybridization. *Environ Health Toxicol*. 2014 Sep 11;29:e2014007.
289. Petty NK, Ben Zakour NL, Stanton-Cook M, Skippington E, Totsika M, Forde BM, et al. Global dissemination of a multidrug resistant *Escherichia coli* clone. *Proc Natl Acad Sci U S A*. 2014 Apr 15;111(15):5694–9.
290. Bhat S, Muthunatarajan S, Mulki SS, Archana Bhat K, Kotian KH. Bacterial Infection among Cancer Patients: Analysis of Isolates and Antibiotic Sensitivity Pattern. *Int J Microbiol*. 2021 Jan 7;2021:8883700.
291. Coltescu A-R, Butnariu M, Sarac I. The importance of solubility for new drug molecules. *Biomed Pharmacol J*. 2020 Jun 30;13(02):577–83.
292. Chen Z, Min MR, Parthasarathy S, Ning X. A Deep Generative Model for Molecule Optimization via One Fragment Modification. *Nat Mach Intell*. 2021 Dec;3(12):1040–9.
293. Pelham HR, Jackson RJ. An efficient mRNA-dependent translation system from reticulocyte lysates. *Eur J Biochem*. 1976 Aug 1;67(1):247–56.
294. Krieg PA, Melton DA. Functional messenger RNAs are produced by SP6 in vitro transcription of cloned cDNAs. *Nucleic Acids Res*. 1984 Sep 25;12(18):7057–70.

295. Shimizu Y, Inoue A, Tomari Y, Suzuki T, Yokogawa T, Nishikawa K, et al. Cell-free translation reconstituted with purified components. *Nat Biotechnol.* 2001 Aug;19(8):751–5.
296. Shimizu Y, Ueda T. PURE technology. *Methods Mol Biol.* 2010;607:11–21.
297. Hawkins EM, Valley MP, Scurria MA, Unch J, Good T, Good D, et al. ONE-Glo™ Luciferase Assay System: New Substrate, Better Reagent [Internet]. Promega; 2007. Available from: <https://france.promega.com/resources/pubhub/promega-notes-2007/one-glo-luciferase-assay-system-new-substrate-better-reagent/>
298. Olivier NB, Altman RB, Noeske J, Basarab GS, Code E, Ferguson AD, et al. Negamycin induces translational stalling and miscoding by binding to the small subunit head domain of the Escherichia coli ribosome. *Proc Natl Acad Sci U S A.* 2014 Nov 18;111(46):16274–9.
299. Vazquez-Laslop N, Thum C, Mankin AS. Molecular mechanism of drug-dependent ribosome stalling. *Mol Cell.* 2008 Apr 25;30(2):190–202.
300. Joazeiro CAP. Ribosomal Stalling During Translation: Providing Substrates for Ribosome-Associated Protein Quality Control. *Annu Rev Cell Dev Biol.* 2017 Oct 6;33:343–68.
301. Chung SS, Bidstrup EJ, Hershewe JM, Warfel KF, Jewett MC, DeLisa MP. Ribosome Stalling of N-Linked Glycoproteins in Cell-Free Extracts. *ACS Synth Biol.* 2022 Dec 16;11(12):3892–9.
302. Sitron CS, Brandman O. Detection and Degradation of Stalled Nascent Chains via Ribosome-Associated Quality Control. *Annu Rev Biochem.* 2020 Jun 20;89:417–42.
303. Imataka H. Single-molecule imaging with a tagged ribosome to explore translation. *J Biochem.* 2012 Oct;152(4):293–5.
304. Wang L, Wasserman MR, Feldman MB, Altman RB, Blanchard SC. Mechanistic insights into antibiotic action on the ribosome through single-molecule fluorescence imaging. *Ann N Y Acad Sci.* 2011 Dec;1241(1):E1-16.
305. Gaba A, Wang H, Fortune T, Qu X. Smart-ORF: a single-molecule method for accessing ribosome dynamics in both upstream and main open reading frames. *Nucleic Acids Res.* 2021 Mar 18;49(5):e26.
306. Gross P, Laurens N, Oddershede LB, Bockelmann U, Peterman EJG, Wuite GJL. Quantifying how DNA stretches, melts and changes twist under tension. *Nat Phys.* 2011 May 22;7(9):731–6.

307. Bernacchia L, Paris A, Gupta A, Charman RJ, McGreig J, Wass MN, et al. Identification of a novel DNA repair inhibitor using an in silico driven approach shows effective combinatorial activity with genotoxic agents against multidrug-resistant *Escherichia coli*. *Protein Sci.* 2024 Apr;33(4):e4948.
308. Revitt-Mills SA, Wright EK, Vereker M, O’Flaherty C, McPherson F, Dawson C, et al. Defects in DNA double-strand break repair resensitize antibiotic-resistant *Escherichia coli* to multiple bactericidal antibiotics. *Microbiologyopen.* 2022 Oct;11(5):e1316.
309. Agirrezabala X, Schreiner E, Trabuco LG, Lei J, Ortiz-Meoz RF, Schulten K, et al. Structural insights into cognate versus near-cognate discrimination during decoding. *EMBO J.* 2011 Apr 20;30(8):1497–507.